UNIVERSIDAD COMPLUTENSE DE MADRID
FACULTAD DE CIENCIAS FÍSICAS
Departamento de Física de la Tierra y Astrofísica

TESIS DOCTORAL

Thermaly-driven mesoscale flows and their interaction with atmospheric boundary layer trubulence

Flujos térmicos mesoescalares y su interacción con la turbulencia en la capa límite atmosférica

MEMORIA PARA OPTAR AL GRADO DE DOCTOR

PRESENTADA POR

Jon Ander Arrillaga Mitxelena

Directores

Carlos Yagüe Anguís
Jordi Vilà Guerau de Arellano

Madrid
Ed. electrónica 2019

THERMALLY-DRIVEN MESOSCALE FLOWS AND THEIR INTERACTION WITH ATMOSPHERIC BOUNDARY LAYER TURBULENCE

FLUJOS TÉRMICOS MESOESCALARES Y SU INTERACCIÓN CON LA TURBULENCIA EN LA CAPA LÍMITE ATMOSFÉRICA

Memoria de tesis para optar al grado de doctor presentada por

JON ANDER ARRILLAGA MITXELENA

Departamento de Física de la Tierra y Astrofísica
Facultad de Ciencias Físicas
Universidad Complutense de Madrid

Directores:
Carlos Yagüe Anguís (Universidad Complutense de Madrid)
Jordi Vilà Guerau de Arellano (Wageningen University & Research)

Madrid
Octubre de 2018

This PhD thesis has been funded by the Predoctoral Training Program for Non-Doctorate Researchers of the Department of Education of the Basque government (PRE_2014_1_145, MOD = B); the Spanish-government Projects ATMOUNT-II CGL2015-65627-C3-3-R (MINECO/ FEDER), CGL2012-37416-C04-02 and CGL2016-81828-REDT/ AEI; the GR3/14 Program (supported by UCM and Banco Santander) through the Research Group "Micrometeorology and Climate Variability" (No. 910437); and the GuMNet (Guadarrama Monitoring Network, www.ucm.es/gumnet) observational network of CEI Moncloa campus of International Excellence. Part of the research was developed during a visit to Wageningen University, supported by the EGONLABUR mobility grant from the Basque government (EP_2016_1_0048).

We would like to thank the Spanish Meteorology Agency (AEMET), the Basque Meteorology Agency (EUSKALMET), the Spanish Port Agency (Puertos del Estado) and the Royal Netherlands Meteorological Institute (KNMI) for the meteorological data provided. Thanks also to the Energy Research Centre from the Netherlands (ECN) for the CO_2 and ^{222}Rn data, and to OSI-SAF for the satellite full-resolution *Metop* data provided.

We are grateful to José Antonio Aranda Eguía for the useful information provided and Iñigo Calleja for his help with the layout of topographical maps. We thank all the members from the Guadarrama Monitoring Network (GuMNet), and especially his coordinator Dr. J.F. González-Roúco for their contribution in La Herrería; and *Patrimonio Nacional*, for the facilities given during the installation of the meteorological tower.

A mis referentes y guías en la vida,
ama y aita

AGRADECIMIENTOS

Parece que era ayer, cuando tímido y algo inseguro, comencé mis andaduras como doctorando. Cuatro años después, tras varias experiencias inolvidables y grandes ilusiones, pero también algunos duros golpes y achaques de salud, me veo infinitamente más fuerte, maduro y seguro de mí mismo. Parte de esa evolución personal se debe a mi propia entrega y dedicación para sacar adelante este proyecto. Pero otra parte, también, se la debo a ciertas personas que han facilitado que haya podido recorrer este duro camino, a las cuales he querido reflejar, de la manera más honesta posible, en las siguientes líneas. Espero no dejarme a nadie olvidado, y si es así, espero que pueda perdonarme.

En primer lugar quiero agradecer a mis dos directores de tesis. Carlos, por haber confiado en aquel inexperto joven de 22 años para dirigirle el trabajo de fin de máster, dándole la libertad para elegir lo que poco después se iba a convertir en proyecto de tesis. Tu pasión por la meteorología que transmites fue una gran inspiración para sumergirme en el mundo de la investigación. Siempre te estaré agradecido por motivarme en este camino y proporcionarme tantas facilidades para llegar hasta donde he llegado. Siempre has cuidado hasta el mínimo detalle. Me has dado la oportunidad de asistir a múltiples congresos y siempre te has asegurado de que todo saliese adelante y no me faltase de nada. Pero sobre todo, te agradezco tu flexibilidad, buen carácter, comprensión y tu preocupación por mi salud cuando ésta flaqueaba. Jordi, tú fuiste un gran descubrimiento durante mi primera estancia en Wageningen. Te preocupaste desde el primer momento de que estuviese bien acompañado, y te aseguraste de que la estancia fuera lo más agradable y científicamente fructífera posible. Pero ante todo, eres un gran motivador. Tu amplio conocimiento, rigor, insistencia y estimulación positiva constante fueron y han sido fundamentales para los resultados cosechados en aquella estancia y esta tesis. Me enseñaste a ser ambicioso en el duro proceso de la investigación y te estaré siempre agradecido por ello.

Durante estos cuatro años la compañía y buenos ratos con muchos de los doctorandos han hecho que la pendiente predoctoral haya sido menos pronunciada. Las EGUs, las AMEs, las comidas en la cafetería... Sin vosotros ni vosotras no habría sido lo mismo. En primer lugar, quiero agradecer a mis primeros *compis* de despacho y rivales del *Bolita Palmera*: a los troperos Iñigo y Jorge; y a los magojocacayeros Cahlo y Mariano, de quienes tanto he aprendido durante el máster y mi primera etapa de doctorado. Cahlo, ha sido y sigue siendo un placer trabajar y asistir a congresos contigo. Mariano, gracias por ser mi compañero de viajes, confidencias y tan buen amigo. Gracias también a los *compis* del Elvira Zurita: Antonio, Ade, Jesús, Rober, Julián, Cristina y Marta. A los tan especiales visitantes de Senegal: Ibrahima, Coumba, Adama y

Moussa. A mis *compis* de comidas y confesiones Lara y Javi. También a los *compis* de volley + cervezas: José Manuel, Sara, Alberto, Mercedes, Enós, Fernando y Cristina. Saioa, gracias por ser tan buena anfitriona en Roma. Gracias también a las vecinas de despacho: Izarra, Marta R, y Serena. También a vosotros Juanje y Maialen, gracias por los buenos momentos durante las AMEs y vuestras visitas a la UCM.

Gracias también al resto de compañeros por las conversaciones en la cafetería, los congresos y lo que he aprendido de vosotros: Elsa, Belén, Ana, Javi P, Luis Di, Luis Du, Fátima, Maurizio, Marisa, V. Carlos e Irene. Tere, ha sido un placer tenerte de compañera de faenas docentes. A los que os he conocido mejor en vuestro regreso: Blanca, Marta y Álvaro. Gracias también Encarna por tu afable cercanía. Gracias Kike por los buenos momentos en las AMEs. Gracias Goyo por las reuniones de grupo. Y Rosa, por los laboratorios de geólogos. Y por supuesto, gracias Salva y Lucía por ser tan resolutivos, accesibles y hacer el día a día en el departamento más fácil.

During my stay in Wageningen University I met great people. First, I would like to thank the PhD students for many nice experiences with them: the soil-drilling competition, the BBOS, the *Beerdjeklaas*... Milesker Xabi y Alba por acogerme tan bien y hacerme sentir como en casa. Thanks Imme, Martin, Aris, Marie, Natalie, Stijn, Anna-Lena, Auke, Thomas, Arjan, Peter, Gerbrand and Folmer. Thanks also to Ingrid, Chiel, Laurens, Gert-Jan, Oscar, Caroline and Kees. And outside the university, thanks Daniel and Leo for the fun we had; the colleagues from Bransz; and Aniek, Dagmar and Laura for being so nice and cheerful flatmates.

Además de los compañeros de universidad, todo esto no habría sido posible sin la presencia de algunas otras personas fundamentales. Gracias Marina por escucharme y apoyarme, por las noches de desconexión y por haber estado siempre ahí. Y gracias Inés, por tus buenos consejos y por tu fiel amistad. A mi compañera de piso y amiga Ana, gracias por los buenos años juntos. Y a ti también Jose, por esas largas conversaciones. A los amigos de Bilbo, porque la distancia nunca fue un obstáculo en nuestra relación. Martin, Iñigo y Nerea: tengo tanto que agradeceros que es difícil reflejarlo aquí. Gracias por ser tan buenos amigos desde hace tanto tiempo, estéis donde estéis siempre os sentiré cerca. Y al resto del grupo: Diego, Álvaro, Asier, Leire, Jon, Paula, Ibon, Gotzone y Oihane gracias por las aventuras en Formentera, Tarifa, Barcelona y las noches bilbaínas..., y las que nos quedan. Milesker guztiagatik. Marta, tú has sido mi amiga fiel e incondicional desde los 3 años... Gracias por todo. Akiertxo, gracias a ti también por las risas, las juergas interminables y por los buenos momentos en tus visitas madrileñas. Y no me olvido de mis compañeras y amigas durante los primeros años de carrera en Leioa: Oihane, Ainhoa, Irene y Jasone... Eskerrik asko por los buenos momentos y por hacer más amenos aquellos dos años en la UPV.

Durante esta etapa, además, ha habido dos personas muy importantes que me han aguantado, acompañado y apoyado. Rafa, gracias por ser tan buena persona y por haberme cuidado tanto. Olivier, gracias por las aventuras y los buenos momentos que hemos vivido.

Y finalmente un pilar fundamental: mi familia. Ama, tú siempre has hecho todo lo posible para que tuviésemos el mejor cuidado, con sudor, dedicación y mucho cariño. Aita, tú te has asegurado de que nunca nos falte de nada y nos has inculcado unos valores vitales. Siempre me habéis querido tal y como soy, y si he llegado hasta aquí es en gran parte gracias a todo lo que me habéis dado. Gracias Inma y Jose, por ser los mejores compañeros de vida que ellos podrían tener. Quiero agradecer también a mis hermanos: Asier, por cuidarme cuando lo necesitaba; y Nerea, por dejarte cuidar y por todo el cariño que nos das por ello. Tía Ainhoa y tita Helen, gracias por estar siempre ahí. A mis aitites y amamas, parte de mi crecimiento como persona os lo debo también a vosotros. Y al resto de la familia, mil gracias por todo. Para terminar, quiero dedicar unas líneas al tío Pedro. Aunque no puedas leerlo, me hubiese gustado compartir mi logro contigo, el único doctor de la familia. Ahora, me dispongo a tomar con orgullo el testigo.

CONTENTS

RESUMEN

FLUJOS TÉRMICOS MESOESCALARES Y SU INTERACCIÓN CON LA TURBULENCIA EN LA CAPA LÍMITE ATMOSFÉRICA

INTRODUCCIÓN

Los movimientos atmosféricos se clasifican de acuerdo a su escala espacial y temporal de mayor a menor en macroescalares, mesoescalares y microescalares. Entre los procesos mesoescalares encontramos los flujos térmicos, producidos por contrastes térmicos horizontales en escalas que abarcan entre 1 y 100–200 km aproximadamente, y que ocurren en forma de circulaciones cerradas. Estos flujos juegan un papel crítico en la transferencia de energía entre la macroescala y microescala. En esta tesis investigamos las brisas marinas (SBs) y de montaña (MBs). Además de ser ubicuas, juegan un papel fundamental en el complejo decaimiento de la turbuencia que tiene lugar durante la transición vespertina (AET) de la capa límite atmosférica (ABL). Íntimamente relacionado con la interacción entre los flujos mesoescalares y la turbulencia en la ABL, la concentración de escalares relevantes como el CO_2 puede verse significativamente alterada por el establecimiento de circulaciones térmicas. Modelos mesoescalares tales como el *Weather Research & Forecasting* (WRF) muestran deficiencias en reproducir el decaimiento de turbulencia durante la AET y la influencia de los flujos mesoescalares en el balance de CO_2.

OBJETIVOS

Los objetivos principales de la tesis se recogen en los siguientes puntos:

- Analizar los forzamientos locales y de gran escala que influyen en la formación y desarrollo de los flujos térmicos.
- Arrojar luz sobre las interconexiones entre los flujos térmicos y la turbulencia en la ABL durante la AET.
- Cuantificar el impacto de los flujos mesoescalares en la dinámica de la ABL y la variabilidad de CO_2 y ^{222}Rn asociada.
- Evaluar la precisión del modelo WRF en simular las características de la SB y su interacción con la turbulencia en la ABL durante la AET.

DATOS Y METODOLOGÍA

La estrategia de investigación llevada a cabo en esta tesis combina bases de datos observacionales y simulaciones numéricas mediante el modelo mesoescalar WRF. Nos centramos en tres emplazamientos, cada uno de ellos representando un escenario distinto para la formación de circulaciones térmicas: la costa vasca (España), para analizar la SB sobre terreno complejo; CESAR (Países Bajos), donde exploramos la SB sobre terreno llano; y La Herrería (España), donde investigamos los vientos catabáticos junto a una abrupta ladera montañosa. El modelo suministra una perspectiva espacial adicional no proporcionada por las observaciones, y permite la evaluación de su precisión en reproducir los flujos térmicos. Asimismo, uno de los aspectos claves de la tesis es el uso de un algoritmo sistemático basado en criterios objetivos para seleccionar eventos mesoescalares y producir una estadística robusta.

RESULTADOS

Primero caracterizamos el fenómeno de SB en la costa vasca mediante una comparación observacional de dos emplazamientos topográficamente distintos. Las simulaciones numéricas mediante el modelo WRF proporcionan una perspectiva más amplia, y permiten evaluar la influencia del establecimiento de la SB en variables atmosféricas y la turbulencia asociada.

La investigación de las SBs se continúa con el análisis de una base de datos observacional de 10 años en CESAR. Tras aplicar el algoritmo de selección mesoescalar, analizamos 102 días de SB que tienen lugar a diferentes horas a lo largo de la AET, y los clasificamos de acuerdo a las condiciones de turbulencia en superficie. Encontramos que el impacto de la SB en la dinámica de la ABL y su estructura térmica son opuestos dependiendo de las características turbulentas en superficie. Nuestros resultados revelan además el papel determinante de la dirección de SB en el transporte de vapor de agua, CO_2 y ^{222}Rn. Por otro lado, empleamos simulaciones numéricas mediante el modelo WRF abarcando el mismo periodo de 10 años para reproducir las características principales de la SB, los factores que influyen y su impacto en la turbulencia durante la AET. Encontramos que el flujo de calor sensible es considerablemente sobrestimado, y probablemente en consecuencia, la intensidad de la SB es magnificada.

Finalmente, exploramos el papel de los flujos catabáticos en la dinámica y características turbulentas de la SBL mediante observaciones en La Herrería. Cuarenta eventos catabáticos son seleccionados durante un periodo de verano empleando el algoritmo de selección mesoescalar. Encontramos una relación directa entre la intensidad máxima de los flujos catabáticos y las características turbulentas de la SBL. Relacionando la dinámica de los regímenes de la SBL con el balance de CO_2, estimamos la contribución de los diferentes forzamientos a la variabilidad de este gas de efecto invernadero.

CONCLUSIONES

Las conclusiones principales de la tesis se resumen a continuación:

- La formación y desarrollo de la SB están particularmente limitados por el viento sinóptico. Los flujos catabáticos no están sólo influidos por el viento sinóptico, sino también por el balance de energía superficial mediante alteraciones en la humedad de suelo.
- La interacción entre los flujos térmicos y la turbulencia en la ABL ocurre de forma bidireccional. Debido a las distintas escalas espaciales y factores determinantes, la interconexión tiene lugar de una manera diferente para la SB y los flujos catabáticos.
- El impacto de los flujos térmicos en la variabilidad del CO_2 viene marcado principalmente por cambios en los flujos turbulentos inducidos por el paso del frente de brisa, y la advección horizontal, la cual puede ser considerablemente grande para flujos catabáticos intensos.
- WRF reproduce los principales impactos de la SB adecuadamente, aunque la gran sobrestimación del flujo de calor sensible produce perturbaciones frontales más intensas. Por otro lado, se da un aumento de la aceleración de la AET en comparación con las observaciones.

ABSTRACT

THERMALLY–DRIVEN MESOSCALE FLOWS AND THEIR INTERACTION WITH ATMOSPHERIC BOUNDARY LAYER TURBULENCE

INTRODUCTION

Atmospheric motions are classified according to their spatial and time scales from largest to smallest into macroscales, mesoscales and microscales. Among mesoscale motions we find the thermally-driven flows, which are driven by horizontal thermal contrasts in scales between around 1 and 100–200 km, and occur in the form of closed circulations. They have a critical role in transferring energy between the macroscales and microscales. In this thesis we investigate sea breezes (SBs) and mountain breezes (MBs). Apart from being ubiquitous, they play a fundamental role in the complex turbulent decay during the afternoon and evening transition (AET) of the atmospheric boundary layer (ABL). Intimately linked with the interaction between mesoscale flows and ABL turbulence, relevant scalars such as CO_2 can also be significantly affected by the onset of thermally-driven circulations. Mesoscale models such as Weather Research & Forecasting (WRF) have shown deficiencies in reproducing the turbulent decay during the AET and the influence of mesoscale flows on the CO_2 budget.

OBJECTIVES

The main objectives of this thesis can be outlined in the following bullet points:

- Analysing the large-scale and local forcings influencing the formation of thermally-driven flows, and developing an objective algorithm to select the mesoscale events.
- To shed light on the interconnections between thermally-driven flows and ABL turbulence during the AET.
- Quantifying the impact of mesoscale flows on the dynamics of the ABL and the associated variability in CO_2 and ^{222}Rn.
- To evaluate the performance of the WRF model in simulating the characteristics of SB phenomena and their interaction with ABL turbulence during the AET.

DATA AND METHODOLOGY

The research strategy followed in this thesis combines observational meteorological databases and numerical simulations from the WRF mesoscale model. We focus on three observational sites, each of them representing a distinct scenario for the formation of thermally-driven circulations: the Basque Coast (Spain) to analyse the SB over complex terrain; the CESAR site (Netherlands), where we explore the SB over flat terrain; and La Herrería site (Spain), to investigate katabatic winds nearby a steep mountainous slope. The model adds a spatial insight not provided by the observations and allows to evaluate its performance in reproducing the thermally-driven winds. Furthermore, one of the key aspects of this thesis is the development of a systematic algorithm based on objective criteria to select mesoscale events and produce robust statistics.

RESULTS

First we characterise SB phenomena at the Basque Coast by comparing observations from two topographically contrasting sites. Numerical simulations from the WRF model provide a more precise insight, and allow to evaluate the influence of the SB onset on atmospheric variables and the associated turbulence.

The investigation of SB phenomena is continued with the analysis of a 10-year observational database from the CESAR site. After applying the mesoscale selection algorithm, we analyse 102 SB days taking place at different times along the AET, and we classify them according to the surface-turbulence conditions. We find that the impacts of SB flows on the ABL dynamics and its thermal structure are contrasting depending on the encountered turbulent characteristics. Our findings furthermore reveal the determinant role of the SB direction in the transport of water vapour, CO_2 and ^{222}Rn. Numerical simulations from the WRF model spanning the same 10-year period are employed to analyse its performance in reproducing the main characteristics of the SB, their influencing factors and the impact on ABL turbulence during the AET. We find that the sensible-heat flux is greatly overestimated, and probably as a consequence, the simulated SB intensity is magnified.

Finally, the role of katabatic flows in the dynamics and turbulent features of the SBL is explored by employing observations from La Herrería site. Forty katabatic events are selected from a summer database by using the mesoscale selection algorithm. We find a direct relationship between the maximum intensity of the katabatic flows and the turbulent characteristics of the SBL. By relating the dynamics of the SBL regimes with the CO_2 budget, we estimate the contribution of the different forcings in the variability of this greenhouse gas.

CONCLUSIONS

The main conclusions of the thesis are summarised below:

- The formation and development of the SB is particularly constrained by the synoptic wind. Katabatic winds are not only influenced by the synoptic wind, but also by the surface-energy balance through alterations in soil moisture.
- The interaction between the thermally-driven winds and ABL turbulence occurs in a bidirectional way. Given the distinct spatial scales and influencing factors, that interconnection takes place differently for SB flows and katabatic winds.
- The impact of thermally-driven flows on the variability of the CO_2 is mainly explained by changes in turbulent fluxes induced by the breeze-front passage, and horizontal advection, which can be significantly large for intense katabatic flows.
- WRF reproduces the main impacts of SBs adequately, although the great overestimation of the sensible-heat flux produces sharper frontal disturbances. On the other hand, an enhanced acceleration of the AET is simulated comparing with observations.

1 INTRODUCTION AND OBJECTIVES

This snapshot was taken shortly before sunset on 11 August 2018 in Punta Galea, Getxo (Basque coast, Spain). This cliff area is located in a corner of the Estuary of Bilbao, and gets its name from the word 'gale' due to its exposure to severe weather coming from the Atlantic Ocean. The picture faces to the west, and shows the meteorological station of Punta Galea managed by Euskalmet, the Cantabrian Sea and the wind farm from the Port of Bilbao, the first offshore wind park put into operation in Spain. The cover picture was also taken from this cliff area, slightly towards the west. A moderate sea breeze was still blowing at the moment of sunset.

1.1 ABOUT THE DIFFERENT SCALES IN THE ATMOSPHERE

The air in motion, i.e. the *wind*, is present all over the earth. It is driven by circulations of all sizes within the atmosphere. The smaller motions are for instance responsible for the particular turning of smoke when it comes out of a chimney, or the whirls that form at the corner of a building. The turning of smoke or whirls, however, can be blurred by regional-scale circulations, such as urban circulations within a city or sea breezes in a coastal area. At the same time, those regional circulations are constrained by pressure differences induced by larger scales, of even up to the planetary scale.

In meteorology, atmospheric processes have traditionally been classified according to their spatial and time scales from largest to smallest into macroscales, mesoscales and microscales. This division was initially motivated by observations from, *inter alios* Van der Hoven (1957), who provided a spectral analysis of horizontal wind-speed variance near the surface, showing two pronounced peaks at around 4 days and 1 min. The first of the peaks is representative of synoptic or large-scale weather patterns (within the macroscale), whereas the second is associated with turbulent motions (microscale). Next to the first peak, a secondary maximum centred at approximately 10 h can be identified, associated with the intermediate scales, i.e. *mesoscale*, although they were included within the synoptic scales in Van der Hoven (1957). Roughly in between the mesoscale and microscale, the presence of a minimum of energy or spectral gap was postulated. Subsequent observed spectra of the horizontal wind speed, temperature and turbulent kinetic energy at different emplacements close to the ground and under different synoptic and geographical conditions, have corroborated the presence of such a spectral gap (Panofsky, 1969; Hess and Clarke, 1973; Smedman-Högström and Högström, 1975; Babić et al., 2017). Not only near the surface, but Vinnichenko and Dutton (1969) observed the spectral gap away from the ground in the free atmosphere, and differing from the spectra close to the ground, measured a -5/3 slope.

However, knowledge regarding the precise form and range of the spectral gap remains vague and subjective up until now. Factors such as stability (Smedman-Högström and Högström, 1975), the presence of mesoscale circulations (Babić et al., 2017), and the modulation of the synoptic forcing (Večenaj et al., 2010) contribute to its variability, to the point where its existence is even questioned. By way of example, Schalkwijk et al. (2015) analysed the power spectrum from observations and large-eddy simulations close to the surface, and found that the gap between the mesoscale and microscale was not as obvious as that reported in previous studies. Furthermore, Hess and Clarke (1973) observed the spectral gap for the horizontal components of the wind, but they reported that no gap was present for the vertical component of the wind.

Provided that mesoscale motions are intense enough, their energy is comparable with the turbulent eddies from the microscale, and the spectral gap is narrowed down as a consequence. Babić et al. (2017), for instance, found that the occurrence of mesoscale phenomena such as slope winds contributed to shift the low-frequency

edge of the spectral gap towards higher frequencies. An illustrative representation of a typical observed spectrum for the horizontal wind speed near the surface is shown in Fig. 1.1. The energetic contribution of mesoscale thermally-driven circulations (see Sect. 1.3) is also included, considering that their variance ranges roughly between 1–12 h. In any case, the reader should bear in mind that this representation is based on observed spectra from Van der Hoven (1957) and Babić et al. (2017). Hence, it is not universal, and its form can substantially vary depending on many factors, some of which were introduced above. It is just intended to be an illustrative example of the different atmospheric scales of relevance for this thesis.

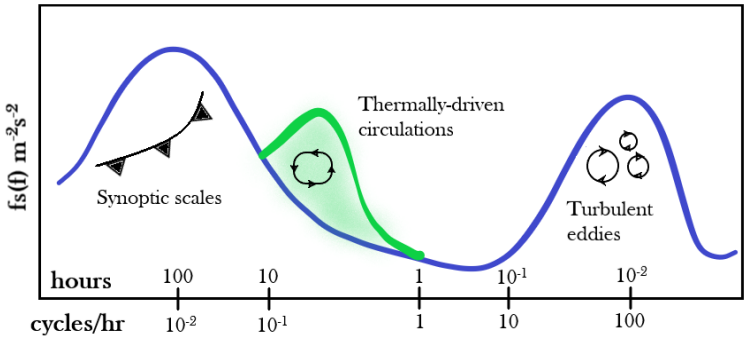

Figure 1.1: Schematic plot illustrating a typical spectrum of the horizontal wind speed close to the ground (blue solid line), and the contribution of the thermally-driven mesoscale circulations (green). Representative values are taken from Van der Hoven (1957) and Babić et al. (2017).

Further knowledge about the spectral gap is fundamental for choosing an appropriate averaging time for the turbulent fluxes of momentum, heat and other scalars that characterise the microscale motions. As a matter of fact, the election of the averaging time for eddy-covariance measurements and the presence of secondary circulations driven by surface heterogeneities, can be partly responsible for the closure problem in the surface-energy balance (Charuchittipan et al., 2014). Hence, a better understanding of the contribution of the thermally-driven circulations to the spectra results of high relevance. Moreover, they have a critical role in transferring energy between macroscale and microscale motions (Atkinson, 1981). The processes that encompass the meso and microscales occur in the atmospheric boundary layer, which is further detailed in Sect. 1.2. Microscale processes are not only important in terms of energy, but they can be directly responsible for the incorrect short-range weather forecasts (Baklanov et al., 2011). Furthermore, Hong (2010) pointed out that slight changes in the boundary-layer parameterisation could significantly affect the global and regional forecasts of precipitation, or even the intensity of tropical cyclones.

On the other hand, the large-scale forcing influences significantly the characteristics of the atmospheric boundary layer. Provided that the synoptic forcing is weak, the

diurnal evolution of the atmospheric boundary layer shows a marked cycle, characterised by contrasting daytime and night-time phases. Indeed, the turbulent behaviour of the nocturnal boundary layer is particularly sensitive to synoptic wind (e.g. Van de Wiel et al., 2012a; van der Linden et al., 2017). Transitions within the nocturnal regime are defined for certain values of that synoptic wind, but the direct implication of mesoscale circulations is generally missed, which act as a *bridge* between the larger and smaller scales.

In this thesis we aim at improving the comprehension and quantification of the interconnections between the different scales; in particular on the role of large scales in the formation of thermally-driven mesoscale phenomena, and the complex two-way interaction occurring between the latter and turbulent eddies in the atmospheric boundary layer. In order to clearly shape the scope of this thesis, first some fundamental concepts and contextualisation need to be introduced in the following Sects. 1.2 and 1.3. The research interest and objectives of the thesis are set out in Sect. 1.4. Finally, Sect. 1.5 presents the thesis outline.

1.2 THE ATMOSPHERIC BOUNDARY LAYER

The *atmospheric boundary layer (ABL)* is the region of the lower troposphere directly influenced by the surface and the forcings involved in it. These forcings include the heating/cooling of the ground, frictional drag and momentum exchange, and the interchange of scalars such as water vapour, CO_2 and anthropogenic pollutants (Stull, 1988).

The response of the ABL to those forcings occurs on time scales smaller than 1 h, mainly driven by turbulent transport processes. *Turbulence* is chaotic and hardly mathematically determined; instead, given its randomness, it is statistically described. Turbulent motions take place by means of irregular swirls called *eddies*, which have variable sizes and energy, because the mechanisms underlying their formation are different. The two main mechanisms that produce turbulence are *buoyancy* (convective turbulence) and *wind shear* (mechanical turbulence). The former is associated with developing thermals due to the differential surface heating from the sun, which gives rise to large and energetic eddies. Their motions can generate wind-shear areas, which produce smaller eddies in turn, so that energy is transferred from larger to smaller eddies in a process named as energy cascade (for further information we refer the reader to Stull (1988) or Arya (2001)). Smaller eddies are also generated due to wind shear produced by frictional drag or the existence of low-level jets.

One of the main importances of the ABL lies in the fact that human activities are carried out in it. Many other reasons make the investigation of the ABL relevant, particularly regarding some important practical applications: the forecasting of maximum and minimum temperatures (Blay-Carreras et al., 2015), the onset of fog (Román-Cascón et al., 2016a,b) and the formation of low-level clouds (Kalthoff et al., 2018),

frost deposition (Bonin et al., 2013), the diffusion and transport of pollutants (Seibert et al., 2000), or the land-atmosphere exchange of important scalars such as CO_2 (Pérez-Landa et al., 2007) and ^{222}Rn (Arnold et al., 2009). In addition, the thermally-driven mesoscale phenomena that are investigated in this thesis develop within the ABL and are actually constrained by its extent. Thus, the formation of thermally-driven winds and turbulence generation, as well as their diurnal evolution, are closely interrelated (Zardi and Whiteman, 2013)

One of the most distinctive features of the ABL is its marked diurnal evolution, particularly when incoming solar radiation is intense and synoptic forcing is virtually quiescent. Shortly after sunrise, provided that clear skies allow the radiative heating of the surface, large eddies form, which start producing the growth of the ABL. These eddies cause additionally the mixing of the ABL, giving rise to a *mixed layer (ML)* or *convective boundary layer (CBL)*, which reaches up to 2–3 km in some areas in the early afternoon. Later on, when net radiation (R_{net}) at the surface begins to decrease, convection associated with large eddies starts to decay, leaving a residual layer in place. This stage of the diurnal cycle of the ABL is referred to as the *afternoon transition (AT)*. Immediately after, once R_{net} turns negative, the *evening transition (ET)* of the ABL takes place, which gives rise to the formation of the *stable boundary layer (SBL)* at the bottom of the residual layer. The whole transition from daytime convective to night-time stable conditions is called the *afternoon and evening transition (AET)* of the ABL, and is characterised by the complex decay of turbulence particularly in areas of complex terrain (Lothon et al., 2014; Darbieu et al., 2015; Sastre et al., 2015; Nilsson et al., 2016). Definitions of these transitions vary between the different studies. In this thesis we follow the definition from Nadeau et al. (2011) and Lothon et al. (2014), so that the shift from the AT to the ET is delineated by the sign change of the sensible-heat (SH) flux.

A better understanding of the AET is necessary for a more accurate representation in mesoscale numerical models, which fail in reproducing precisely the transition periods (Lee et al., 2007; Couvreux et al., 2016). In particular, the complexity of the terrain and the generated nocturnal downslope flows produce sporadic enhancements of turbulence during the AET, inducing side effects such as the increase of local particulate-matter concentrations (Fernando et al., 2013). The frontal structure of downslope flows, and local-stability and turbulence conditions during the ET are closely interrelated, as reported in Papadopoulos and Helmis (1999). The increase of mechanical turbulence during the AET was also reported in a tropical coastal region (Jensen et al., 2017b). These findings, among others, reveal the importance of the complex interaction between thermally-driven mesoscale phenomena and turbulence during the AET of the ABL, which has overall received little attention and hence motivates one of the main objectives of this thesis.

To illustrate the relevance of that statement, we show in Fig. 1.2 the diurnal cycle of the ABL in Cabauw (Netherlands), on a day marked by the onset of the sea-breeze circulation during the AT. The evolution in time of the vertical distribution of aerosol

backscatter is represented in Fig. 1.2a, on a day characterised by well-mixed conditions within the ABL and the development of a prototypical CBL. Around 2 h before sunset, the convective regime was abruptly interrupted by the arrival of a well-formed sea-breeze front. In addition to the changes in state variables, the sea-breeze flow advected a distinct aerosol layer. The mixing-layer height (MLH) estimates, represented by black dots, identify the collapse of the CBL. The wind-vector evolution obtained from the wind profiler is represented in Fig. 1.2b, which shows the veering of the wind from the SW to N-NW around 1700 UTC, confirming the onset of the sea breeze at this location.

To better understand the synergies between thermally-driven circulations and turbulence in the ABL, the former are more specifically introduced, before heading to the main motivation of the thesis.

1.3 THERMALLY–DRIVEN CIRCULATIONS

Under quiescent synoptic forcing and fair-weather conditions, i.e. clear or partly cloudy skies, horizontal thermal contrasts in spatial scales ranging between roughly 1 and 100–200 km become relevant. Given these circumstances, local pressure gradients not associated with synoptic scales develop, giving rise to the formation of mesoscale circulations. They are produced by horizontal thermal contrasts, and are thus known as *thermally-driven circulations* or *breezes* (Barry, 2008). Although they are primarily manifested as near-surface flows, they are typically part of larger and closed circulations. These circulations are theoretically explained by a baroclinic-generation mechanism through the Bjerknes circulation theorem (we refer the reader to Thorpe et al. (2003) for additional information).

The above-mentioned horizontal thermal contrasts develop mainly in regions close to large water bodies (seas and lakes), on heterogeneous surfaces and nearby topographical features. In this thesis we investigate two mesoscale phenomena: sea breezes (Sect. 1.3.1) and mountain breezes (Sect. 1.3.2). In addition to being ubiquitous, their onset can be highly relevant during the AET as represented in Fig. 1.2. A closer look into these two phenomena is approached hereunder.

1.3.1 Sea breezes

Provided that large-scale forcings are weak and insolation important, the air heats up faster and more intensely over the land than over the sea, due to the greater heat capacity of the latter. This differential heating generates a thermal contrast at coastal regions during daytime, which creates a pressure-gradient force (PGF) directed from sea to land. The baroclinic instability that is established acts as the *engine* responsible for the onset and development of the *sea-breeze (SB) circulation* (Miller et al., 2003).

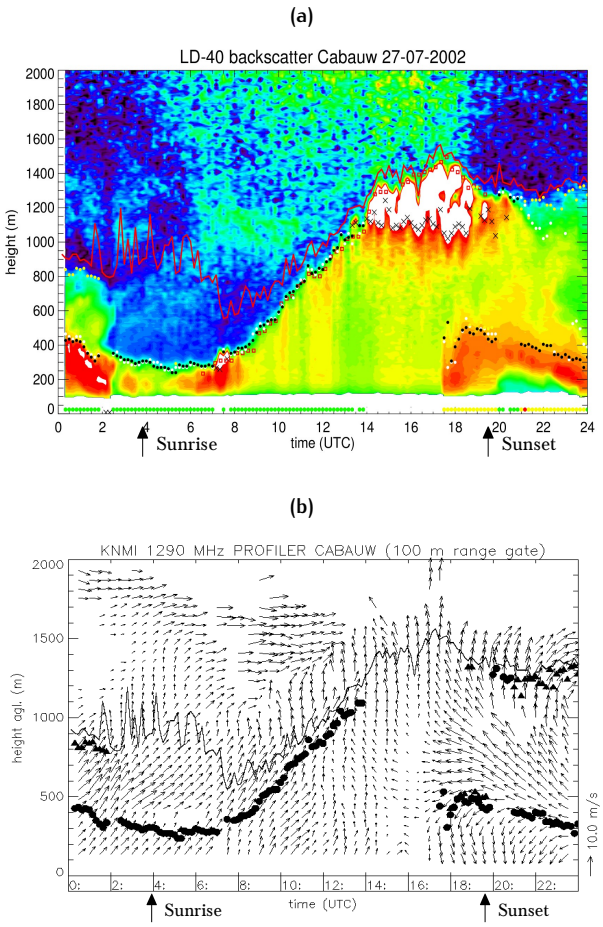

Figure 1.2: (a) Evolution in time of the aerosol backscatter obtained from the LD40 ceilometer in Cabauw on 27/07/2002. Black circles indicate the MLH estimates. (b) Wind-vector evolution obtained from the wind profiler in Cabauw for the same day. MLH estimates from the LD40 ceilometer are also included with black circles. For further specifications about the figures we refer the reader to de Haij et al. (2007), from which the figures were obtained. *Reproduced by kind permission of the authors.*

During night-time, the PGF is reversed and the SB circulation is replaced by a land-breeze (LB) circulation with the opposite direction. Even under a similar temperature difference in magnitude (not in the sign) between the land and the sea, the LB is considerably weaker than the SB (Pearson, 1975) and its extent is limited to the near-shore area. Anyway, this thesis just focuses on the SB circulation.

The SB has been widely studied due to its influence on air quality and pollution (Clappier et al., 2000; Talbot et al., 2007; Borge et al., 2008; Soler et al., 2011; Wang et al., 2013), the generation of wind energy offshore (Steele et al., 2013; Archer et al., 2014), the formation of convective systems and severe weather (Azorín-Molina et al., 2014; Comin et al., 2015), and the forecasting of maximum temperatures in locations close to the shore during hot spells (Meir et al., 2013). Besides, around 40% of the population lives within 100 km of the coast, and therefore its understanding and adequate representation in mesoscale numerical models is highly relevant.

A complete diagram illustrating the main components of the SB system, and the principal forcings and factors that affect its formation and development are represented in Fig. 1.3.

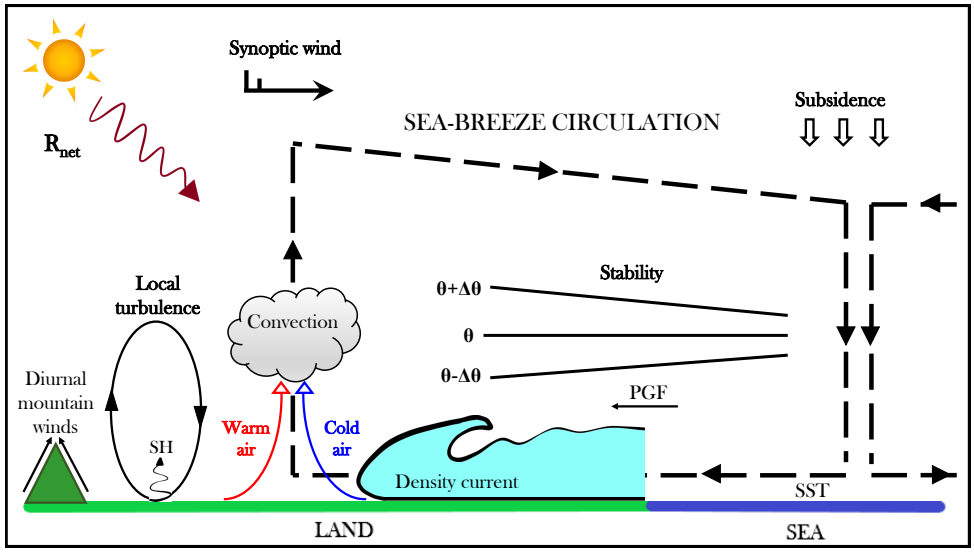

Figure 1.3: The SB system: the SB circulation, and the main influencing factors and forcings. R_{net} represents the net radiation, SH the sensible-heat flux, θ the potential temperature, PGF the pressure-gradient force and SST the sea-surface temperature.

The lower part of the SB circulation is commonly denominated the SB or onshore flow, i.e. directed from sea to land. Upward motions inland, downward motions offshore (over the sea) and the return flow above, close the mesoscale cell. The onshore flow of the SB circulation is also called the *gravity* or *density current*. Gravity currents form when a dense fluid passes through a less dense surrounding, and appear in the lower atmosphere commonly as thunderstorm outflows and SB flows (Simpson, 1994). The onset of the SB occurs when the forehead of the density current or *the sea-breeze front* (SBF) arrives, which resembles a minor cold front. The passage of the SBF is characterised primarily by a sudden shift to an onshore wind direction and the stationarity of the wind vector in this last direction for few hours. These patterns

serve as indicators of the SB occurrence and are consequently implemented in the SB selection algorithm described later in Chapter 2. Depending on the distance from the shore and the background atmospheric conditions, sudden drops in temperature and sharp increases in humidity take place occasionally. At the frontal boundary marine and continental air masses converge, generating updraughts which are responsible for turbulence production and subsequent convective clouds. By way of example, Helmis et al. (1987) observed vertical velocities of 1–1.5 m s^{-1} in sharp fronts, which could reach up to 2 m s^{-1} with an offshore ambient flow.

Two of the most important factors affecting the formation and development of the SB circulation are the synoptic forcing and local turbulence, which evidences the high relevance of the interconnections between distinct atmospheric scales. Their interactions are one of the main focuses of this thesis, and are therefore more deeply detailed below. Previous studies have investigated the role of other features depicted in the schematic diagram of Fig. 1.3. For instance Tang (2012) observed an intensification of the SB circulation with decreasing sea-surface temperature (SST), whereas most numerical simulations point towards a negligible influence of the SST (Crosman and Horel, 2010). Moreover, many studies reveal the complexity of the interaction between the SB and flows driven by orographic features near the coast: Azorin-Molina et al. (2011) and Cuxart et al. (2014) observed the intensification and further penetration of the SB induced by upslope flows, while Asai and Mitsumoto (1978) found the opposite effect when the slope was covered in fog or clouds. Other factors of geographical origin such as the coastline curvature (Arritt, 1993) and the Coriolis force (Zhong and Takle, 1992; Talbot et al., 2007), that are not depicted in Fig. 1.3, exert visible influence too. The latter gains relevance in the late phase of the SB circulation, driving its clockwise rotation and limiting its inland penetration. Its role over complex topography is however unclear (Cuxart et al., 2014).

As stated and represented in Fig. 1.3, one of the factors that more importantly affect the formation of the SB circulation is the synoptic forcing. If the synoptic flow close to the surface is offshore (directed from land to sea) and intense enough, it can prevent the inland propagation of the gravity current. The threshold value for the offshore ambient wind speed above which the SB circulation does not manifest inland varies in a range between 6 and 11 m s^{-1}, depending on the location and the sea-land temperature gradient (Crosman and Horel, 2010). Many studies have addressed the influence of the synoptic flow on the SB, although some gaps and contradictions remain. For instance, Frizzola and Fisher (1963) and Mestayer et al. (2018) observed weaker and shallower SBs with an opposing offshore synoptic flow, whereas Azorín-Molina and Chen (2009) and Gahmberg et al. (2010) found that the onset of the SB is more intense with an offshore than with an onshore synoptic flow, due to the increase of the sea-land thermal contrast. More precisely, the SB is broadly classified into four quadrants according to the direction of the synoptic flow with respect to the coastline: pure, synoptic, backdoor and corkscrew (Miller et al., 2003). Pure and synoptic SBs develop when the ambient flow is perpendicular to the shoreline: blowing from land

to sea in the former and the opposite in the latter. As regards the two remaining types, they develop when the main component of the synoptic wind is parallel to the coastline: the corkscrew with low pressure over land and high pressure over the sea, and the backdoor just the opposite. The former is characterised by an area of divergence at the coast, which intensifies this type of SB even more than the pure breeze (Steele et al. (2013)), while in the backdoor there is an area of convergence which weakens it. For further details we refer to Table I in Mestayer et al. (2018).

At the high-frequency sector of the spectrum (see Fig. 1.1), the SB has an important interconnection with microscale atmospheric motions, i.e. with turbulent processes. The advance of the cold gravity current over the heated land causes the development of the thermal internal boundary layer (TIBL): an unstable layer within the ABL that appears at the coast and grows in depth with distance inland. Its depth can be estimated with the transition from unstable to neutral/stable in the temperature profile (Anthes, 1978), as well as with an abrupt drop of turbulence (Raynor et al., 1979). Bechtold et al. (1991) and later Cuxart et al. (2014) observed that after the onset of the SB, turbulence is confined within the TIBL close to the surface, resulting in a fumigation of low-level pollutants in this layer (Talbot et al., 2007). The gravity current usually propagates far inland around 50-60 km (Miller et al., 2003), where the TIBL converges with the CBL. Occasionally, it reaches further inland: as far as 100 km in The Netherlands (Tijm et al., 1999), or for instance, Soler et al. (2014) observed the arrival of marine density currents at the CIBA site (Spain) which is located 200-km away from the sea. SBs have been detected even further inland, for example by Hu and Xue (2016), who found that the SBF reached Dallas (Texas, USA) at midnight, as far as 400 km inland. The arrival of the SBF led to a collapse of the urban-heat island, and the breakdown of the night-time surface inversion in rural areas. So depending on local-turbulence conditions, the impact of SBFs can be rather distinct.

The acceleration of the inland propagation of SBFs after the decay of the CBL is a relevant aspect that is not as yet well represented by mesoscale numerical models (Crosman and Horel, 2010). Convective mixing within the CBL leads to frontolysis, and consequently to the slowing down of the propagation of SBFs (Grisogono et al., 1998). When daytime convection is weakened, however, the SBFs are reinforced again, and subsequently, the SBFs in the late afternoon and evening accelerate (Atkins and Wakimoto, 1997). Although most SB studies focus on areas close to the coastline as far as 25 km inland (Atkins and Wakimoto, 1997; Borne et al., 1998; Talbot et al., 2007; De Tomasi et al., 2011; Calmet and Mestayer, 2016), in many locations further inland the arrival of the SBF takes place during the AET of the ABL.

Only a few investigations of the ABL transition under SB conditions have been performed. Jiménez et al. (2016b) characterised the morning transition between the LB and the SB using both modelling and observations. They found that the transition occurs in four steps, but the model is unable of capturing the observed evolution of the thermal profile. Cuxart et al. (2014) discovered that the SB below 200 m above ground level (agl) is the result of the equilibrium between the pressure gradient and

turbulence. They analysed the terms of the turbulent kinetic energy budget during the different stages of a SB case through numerical simulations. However, little attention has been paid to analysing the challenging interplay of the SB with local turbulence and scalar transport when the frontal passage occurs in the late afternoon and evening.

With regard to the impact on scalars, some previous studies have demonstrated the important role of the SB circulation. For example Pérez-Landa et al. (2007) measured lower CO_2 concentrations during the SB stage in Valencia (on the Mediterranean coast of Spain), since the shallow marine air mass was affected by the uptake by plants. However, as pointed out by Ahmadov et al. (2007), the measurements of pollutants at coastal sites are not always representative of a large-scale footprint, but are so for the characteristic recirculation of the SB. This statement is indeed backed by a few studies: e.g. Gangoiti et al. (2001) linked the recirculation of tropospheric O_3 to LB/SB circulation patterns, and Millán et al. (1991) found that the tracers released in the morning returned with the SB of two days later.

As occurs for the CO_2, mesoscale footprints can become of great significance to explain the variability of ^{222}Rn. This gas is naturally emitted, and for that reason is widely used as an inert tracer of air masses on different scales (e.g. Arnold et al., 2009), and is also useful as an indicator of vertical mixing. It is constantly emitted by terrestrial surfaces, and continental air masses therefore contain greater concentrations of ^{222}Rn. Zahorowski et al. (2008), for instance, found that offshore flows produce higher ^{222}Rn values, whereas air masses with an oceanic origin give rise to considerably smaller values. Concentrations of this gas are influenced by both local emissions and horizontal advection. For instance Ho and Measday (2005) stress the challenge of modelling the effect of the SB at coastal sites due to the *recycling* of the air. Other processes can also be relevant for ^{222}Rn as discussed by Hernández-Ceballos et al. (2015), who document the case of SB-LB cycles driving ^{222}Rn concentrations above 20 Bq m^{-3} in Huelva (Spain), due to the presence of phosphosypsum piles upstream of the city on pure SB days.

1.3.2 Mountain breezes

Thermally-driven slope winds, diurnal mountain winds or *mountain breezes (MBs)* develop in mountainous areas, when the large-scale flow is weak and skies are clear, allowing greater incoming solar radiation during daytime and larger outgoing longwave radiation during night-time (Zardi and Whiteman, 2013). Under this situation wind direction is reversed twice per day: thermally-driven slope winds flow upslope during the day and downslope during the night (Atkinson, 1981; Whiteman, 2000; Poulos and Zhong, 2008). The thermal disturbances that produce them have different scales and origin: from local hills and shallow slopes (Mahrt and Larsen, 1990), to large basins and valleys which extend horizontally up to hundreds of kilometers (Barry, 2008). The different scales, however, are not independent; for instance, local downslope flows converge at the bottom of the valleys generating larger-scale flows

(Jiménez and Cuxart, 2014), which in turn influence the mountain-plain circulations (Duine et al., 2017). Figure 1.4 shows the different patterns that MBs exhibit. Note that a return flow with opposite direction is represented above the slope winds, i.e. completing the thermally-driven wind circulation.

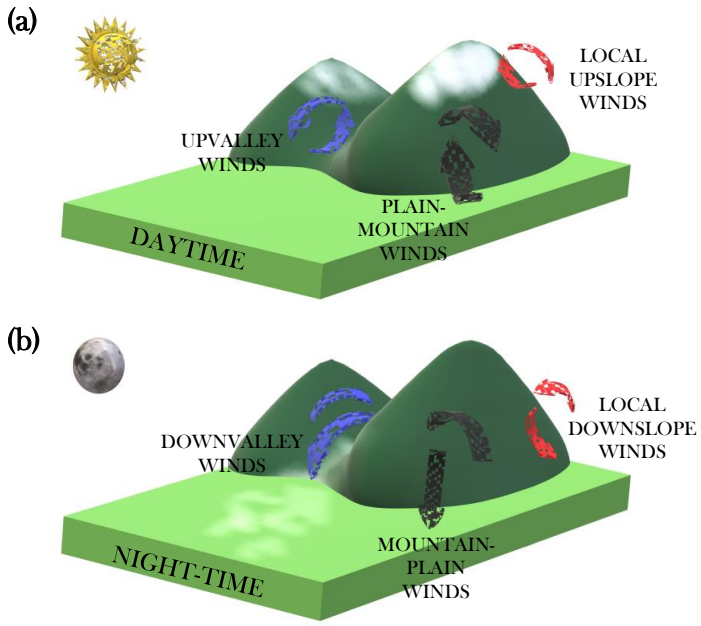

Figure 1.4: Representation of the MBs during daytime (a) and night-time (b). Adapted from (Whiteman, 2000).

Mountainous sites have struck the attention of many studies for plenty of reasons: in particular due the influence on fog formation (Hang et al., 2016; Prtenjak et al., 2018), diffusion of pollutants (Baumbach and Vogt, 1999), and also due to the important role that slope flows play in the thermal and dynamical structure of the ABL and its morning and evening transitions (Whiteman, 1982; Sun et al., 2006; Lothon et al., 2014; Lehner et al., 2015; Román-Cascón et al., 2015; Jensen et al., 2017a). Understanding atmospheric exchange processes over mountainous terrain is beneficial for a large variety of applications; such as ecology, hydrology urban planning and climate change amongst others (De Wekker et al., 2018).

In this thesis, we focus on the thermally-driven local downslope winds (hereinafter *katabatic flows*), given their leading role during the AET of the ABL. Despite the term *katabatic* is also used for referring to other non-thermally-driven winds (Zardi and Whiteman, 2013), by following Barry (2008) we use it to refer to downslope winds driven by local thermal disturbances (i.e. not by the basin or valley). A sketch of the

forces involved and the surface energy balance (SEB) terms during the katabatic stage is shown in Fig. 1.5. Shortly before sunset, when R_{net} becomes negative, the surface and the adjacent air layer start to cool down. A hypothetical air mass A is therefore colder ($T_2 < T_1$) and consequently denser ($\rho_2 > \rho_1$) than the air mass B, situated more distant from the slope. A PGF from A to B is induced as a consequence, which added to the negative buoyancy, results in a katabatic flow.

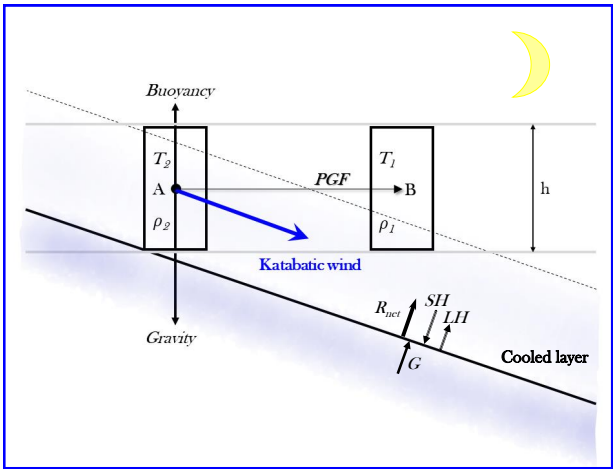

Figure 1.5: Schematic representation of the forces involved and the main components of the SEB (R_{net}= net radiation, SH = sensible-heat flux, LH = latent-heat flux and G = soil-heat flux) during the katabatic stage. The direction of the arrows from the SEB terms represents cooling of the air adjacent to the surface when the arrows are outgoing, and heating when they are incoming. Adapted from Barry (2008).

Several external factors have been documented to affect katabatic winds: the steepness of the slope and the distance to the mountain range (Horst and Doran, 1986), the canopy layer (Sun et al., 2007), spatial variations in soil moisture (Banta and Gannon, 1995; Jensen et al., 2017a), and the direction and intensity of the background wind (Fitzjarrald, 1984; Doran, 1991). However, most of the investigations analysing the influence of those external factors are carried out using numerical simulations, and there is a lack of observational studies to validate them. By way of example, Banta and Gannon (1995) carried out numerical simulations using a two-dimensional model and found that katabatic flows are weaker over a moist slope than over a dry one. They quantified a greater downward longwave radiation and soil conductivity under moister conditions, which gives rise to a reduced surface cooling. However, Jensen et al. (2017a) found an opposite correlation, which they attributed to the sensitivity of the soil-moisture parameterisation in the numerical simulations. As a matter of fact, Sastre et al. (2015) showed with a numerical experiment in contrasting sites that soil-moisture differences do not affect the AT and ET values with the same intensity,

but depending on the site. With respect to the background flow, by using a one-dimensional model Fitzjarrald (1984) observed that the onset time of katabatic winds is affected by the retarding effect of the opposing synoptic flow and reduced cooling rates.

On the other hand, knowing whether a certain night katabatics will be weak or intense enables us to predict how turbulence in the nocturnal boundary layer (NBL) will behave. Although most of the times we refer to the NBL and SBL indistinctly, we cannot assure that stable conditions are always present during night-time, and hence we employ the term NBL. It is well known that under weak ambient wind, turbulence is weak, patchy and intermittent (Van de Wiel et al., 2003, 2012b; Mahrt, 2014), giving rise to the so-called *very stable boundary layer (VSBL)*. On the contrary, when the ambient wind is strong, shear production increases substantially and turbulence is continuous, producing near-neutral conditions in the NBL (Mahrt, 1998; Sun et al., 2012; Van de Wiel et al., 2012a), and the so-called *weakly stable boundary layer (WSBL)*. Being able to foresee the occurrence of these two regimes has been in the eye of many studies, and some attempts have been made to characterise the transition between the regimes using parameters such as the geostrophic wind (van der Linden et al., 2017), local (Mahrt, 1998) and non-local scaling parameters (van Hooijdonk et al., 2015), and the observed wind speed (Sun et al., 2012). More or less explicitly, continuous turbulence in the NBL has been linked with a stronger background wind (e.g. > 5–7 m s^{-1} in Van de Wiel et al. (2012a)) and low-level jets (Sun et al., 2012).

In addition to the impact on the turbulent features and dynamics of the NBL, as occurs in the case of the SB, katabatic winds may have an influence in the concentration of scalars of high relevance such as the CO_2 at coastal areas (Cristofanelli et al., 2011; Legrand et al., 2016) and mountainous regions (Sun et al., 2007). Advection driven by katabatic winds can indeed dominate the CO_2 transport; for instance, Sun et al. (2007) found that downslope flows transported CO_2-rich air from the Rocky mountains. Not only advection, but local turbulence fluxes can also be influenced by the katabatic winds: Sun et al. (2006) observed an anomalous positive CO_2 flux just after sunset, suggesting that it was due to the sudden transition from upslope to downslope flow. Being able to better quantify the influence of mesoscale flows on the CO_2 budget can help to reduce the large discrepancy from modelling studies in reproducing the land-atmosphere exchange for this gas (Rotach et al., 2014).

1.4 MOTIVATION AND OBJECTIVES

In previous sections we have explained the relevance of a deeper understanding regarding the thermally-driven circulations and their interactions with atmospheric processes of different scales. It is therefore necessary to provide new quantitative insights. Enhanced knowledge about mesoscale phenomena is essential for a better assessment of air quality in coastal and mountainous areas, the impact on deep-convection gener-

ation and fog formation, and the budget of relevant scalars such as CO_2. Additionally, a better performance of mesoscale models in reproducing these phenomena brings important consequences: more precise forecasting of extreme-precipitation events, minimum and maximum temperatures and wind speed. The latter, for instance, is fundamental for an optimum choice of the location of wind farms.

Below, we present the main motivating aspects and the related objectives of this thesis. We additionally pose the overarching research questions associated with each objective.

- Most of the observational studies investigating mesoscale phenomena focus on individual events, from which global conclusions concerning the influence of local, regional and large-scale forcings are hardly inferred. Besides, the selection of the events in most of the cases is based on subjective criteria, and the use of thresholds for the large-scale wind and thermal contrast to foresee the onset and development of the mesoscale circulation remains unclear (Mestayer et al., 2018).

  OBJECTIVE 1: The first goal of this thesis is thus to investigate the factors affecting the formation of thermally-driven winds, and to develop an algorithm to select mesoscale events of interest, which is easily implementable and based on objective criteria for evaluating the distinct forcings. The algorithm is described in Chapter 2 and employed all along the thesis, after being correspondingly adapted to the different thermally-driven circulations studied and the locations employed. The associated research question is the following:

  > ***What are the main large-scale and local factors influencing the formation and development of thermally-driven flows?***

- The nature and turbulent characteristics of the NBL depend partly on the precedent decay of turbulence throughout the AET. As illustrated in Fig. 1.2, the onset of mesoscale flows can be disruptive during the AET, but few studies have addressed this matter. At the same time, local-turbulence conditions are influential for the density currents: SBFs, for instance, accelerate in the late afternoon due to the collapse of convective mixing and the subsequent sharpening of the fronts. Moreover, the time of arrival of the density current is highly determinant for assessing the subsequent impacts on atmospheric variables such as temperature and wind speed, since they depend on the local stability encountered by the mesoscale flow.

  OBJECTIVE 2: The second aim of the thesis is therefore focused on shedding light on the relevant interconnections between mesoscales and microscales during the AET. Chapter 3 approaches the interaction of SB events with turbulence over complex terrain. A deeper inspection on this aspect is carried out in Chapters 4 and 5 over flat terrain, by using respectively comprehensive observational and numerical databases. The role of katabatic events of variable intensities in

inducing different regimes in the NBL is eventually explored in Chapter 6. The following research question is posed:

> ***How does the interconnection between turbulence and the thermally-driven flow take place during the AET?***

- Thermally-driven circulations have important implications for local weather patterns, and the diffusion and advection of anthropogenic pollutants as well as naturally-emitted scalars within the ABL. The arrival of the mesoscale flow at different times of the day has contrasting implications in terms of dynamics, and depending on the origin of the thermal disturbance and the extent of the circulation, it can additionally affect the transport of scalars.

  OBJECTIVE 3: First, in Chapter 4 we aim at determining the impact of well-formed SBFs on the dynamics of the ABL. Directly related, we analyse the influence on the variability of a naturally emitted gas (^{222}Rn), and on the variability of a partly natural and partly anthropogenic gas (CO_2). Later in Chapter 6, we evaluate the impact of katabatic flows on the variability of CO_2. Directly connected with the previous research question, we tackle the following:

  > ***How does the complex turbulence-mesoscale interaction affect the structure and dynamics of the ABL as well as the associated variability in CO_2 and ^{222}Rn?***

- As pointed out in the review from Crosman and Horel (2010), the main reason for the inaccurate performance of mesoscale models in reproducing the SB is related with an erroneous treatment of turbulence in the ABL. As a matter of fact, numerical models are unable of replicating the observed acceleration of the SBFs in the early afternoon induced by the convective decay. Incrementing the horizontal resolution or increasing the complexity of the ABL parameterisation schemes does not solve this issue.

  OBJECTIVE 4: Hence, the last objective of this thesis is to evaluate the performance of numerical models in simulating SB phenomena, targeting in particular the deficiencies of the model in reproducing the turbulent decay during the AET, with the goal of throwing light on the aspects to improve for a better replication of afternoon and evening SBFs and their implications. First, we evaluate the performance of the WRF model in reproducing the SB over complex terrain in Chapter 3, focusing on two events arriving at different times of the day. Finally, using the same mesoscale model, numerous SB events arriving during the AET over flat terrain and the impacts on local turbulence are evaluated in Chapter 5. This objective is summarised in the following research question:

  > ***How does the WRF model reproduce the characteristics of SBFs and their interaction with turbulence in the ABL during the AET?***

A diagram sketching the conceptual scope of this thesis is shown in Fig. 1.6.

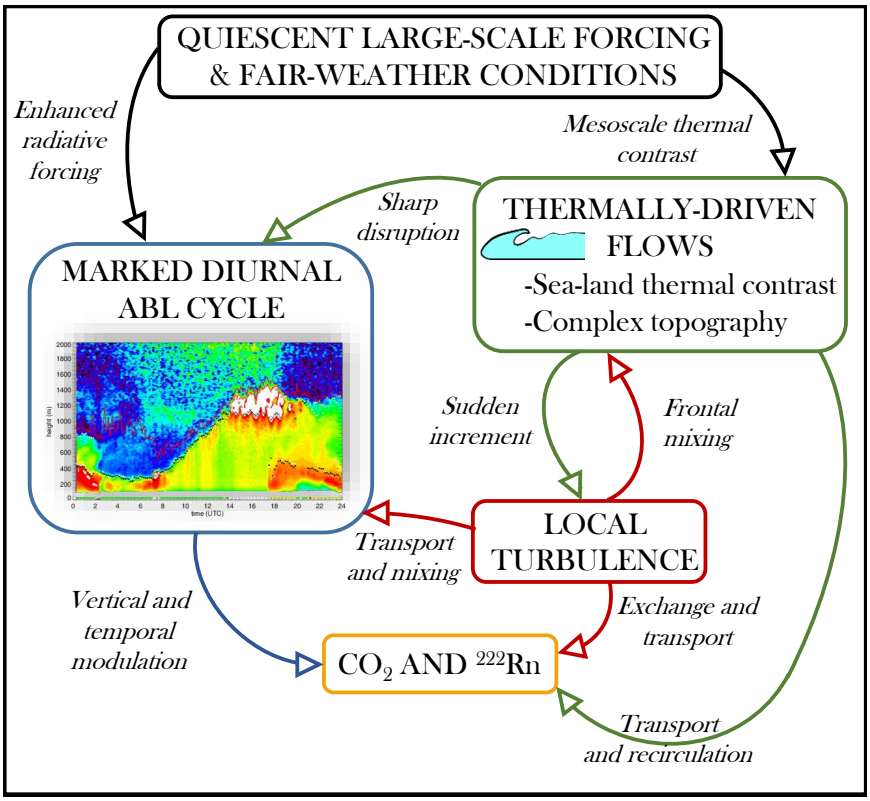

Figure 1.6: Conceptual sketch illustrating the physical approach of the thesis.

1.5 THESIS OUTLINE

As outlined in the previous section, the general purpose of this thesis is the analysis of the disturbances associated with SB events and katabatic flows, their interaction with local turbulence in the ABL and their implication in the diffusion and transport of relevant scalars. Hereunder, the in-chapter distribution is presented:

Chapter 2. In this chapter we introduce the different observational data employed, we describe the usage of micrometeorological data and we detail the configuration of the mesoscale model for performing the numerical simulations. The algorithm for selecting mesoscale phenomena of interest is additionally described.

Chapter 3. We commence the investigation of the thesis with an entangled scenario for thermally-driven circulations: a coastal area with complex terrain. We employ observational data from one summer and numerical simulations of a few events from

the WRF model. The SB events are selected using the algorithm from Borne et al. (1998).

Chapter 4. With the goal of exploring pure SB phenomena and their two-way interaction with smaller scales in the ABL during the AET, we move to a flat region located further away from the coastline. A comprehensive 10-year observational database and the selection algorithm developed in this thesis are employed to produce robust statistics of the mesoscale phenomena of interest.

Chapter 5. The performance of the WRF model in reproducing the observed SB events from Chapter 4 and their influencing factors is investigated in here. The simulations, moreover, enable to draw conclusions that are not inferred solely from the observations.

Chapter 6. The research of this thesis is concluded by inspecting katabatic winds in a relatively flat area nearby a mountainous feature. The research strategy followed for investigating SB phenomena is applied, but the implications of these mesoscale phenomena differ from those of the SB.

Chapter 7. We finalise this thesis by presenting the most relevant conclusions, a final thought and the future prospects.

An illustrative summary of the research strategy is presented in Fig. 1.7.

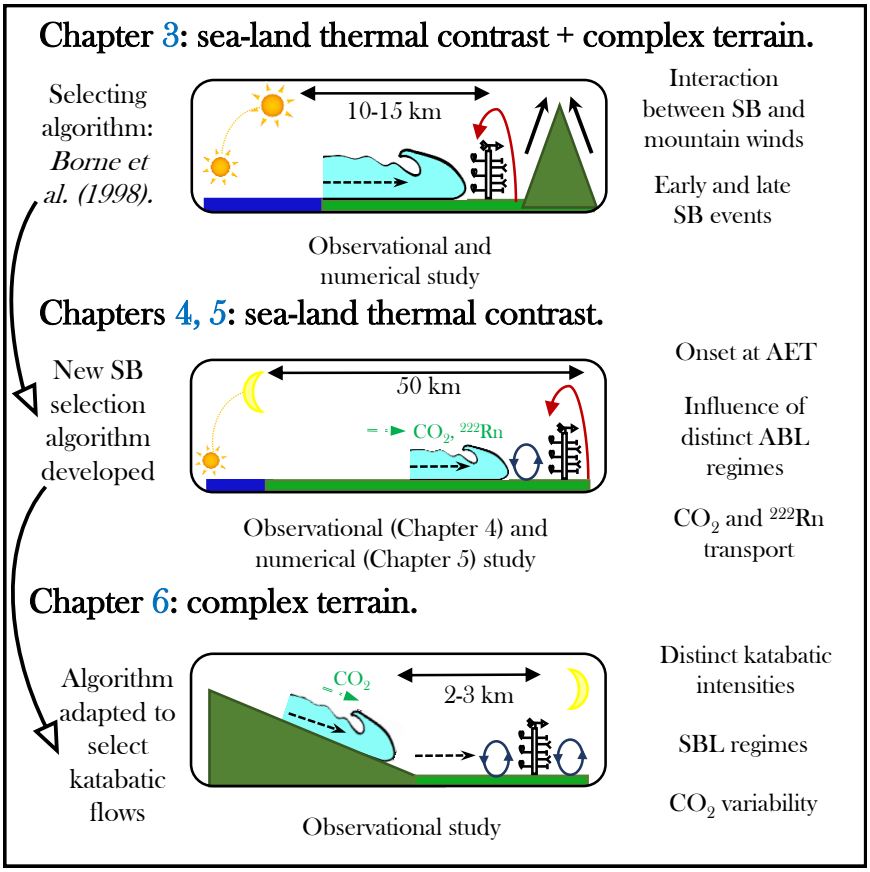

Figure 1.7: Illustrative sketch of the research strategy.

2 DATA AND METHODOLOGY

This picture was taken in Villasana de Mena (320 m above sea level (asl), Spain) on 14 May 2018 at 1400 LT, located very close to the Peña Angulo mountain range, which peaks up to an altitude of 1200 m. The particular wind vane shown was designed in 1947, and despite its maritime look, it witnesses countless wind-direction shifts caused by the diurnal mountain winds that form on synoptically quiescent and fair-weather days.

2.1 PREFACE

The objectives of this thesis are carried out by employing large meteorological databases in order to produce robust statistics. In particular, the research strategy followed combines both meteorological observations from different emplacements and numerical simulations from the WRF mesoscale model. The model adds a spatial insight not provided by the observations, and besides, allows to evaluate the performance of this mesoscale model in simulating the thermally-driven circulations. A summary of the observational data and the model version used in each chapter (if any) are provided in Table 2.1.

Furthermore, one of the most important features of this thesis is the use of a systematic algorithm based on objective criteria to select the mesoscale events of interest. This method allows to produce robust statistics out of the selected events. On the other hand, to explore the interconnection of these mesoscale phenomena with turbulence, micrometeorological data require a specific post-processing so that they provide a precise and complete characterisation of the turbulent features in the ABL. Further specifications about the observational data employed and the methodology followed are provided below.

Table 2.1: Summary of the observational data and numerical simulations employed in each chapter.

Chapter(s)	Site	Period	Model Version
3	Basque coast (Spain)	01/07/2013–31/08/2013	WRF 3.5.1
4, 5	CESAR (Netherlands)	01/01/2001–31/12/2010	WRF 3.4.1
6	La Herrería (Spain)	22/06/2017–26/09/2017	–

2.2 OBSERVATIONAL DATA

We focus on three observational sites in this thesis, each of them representing a distinct scenario for the formation of the thermally-driven circulations to be analysed. The location of the sites are shown in Fig. 2.1. The first region is the Basque coast, washed by the Cantabrian sea at the N of Spain, which is characterised by a complex coastal orography. This region manifests mesoscale thermal contrasts associated with the sea-land gradient and sloping terrain. Therefore, we start the investigation with the most complete scenario in Chapter 3, to narrow down to each specific phenomenon in the subsequent chapters. We continue the investigation in the CESAR site located at around 50 km from the sea in a flat and relatively homogeneous area. Thus, we analyse in Chapters 4 and 5 pure SB phenomena arriving mostly in the afternoon or evening. Finally, the last region explored in Chapter 6 is La Herrería site, which is

located nearby a steep slope in a mountainous area of central Spain. Hence, in this last chapter we investigate pure katabatic phenomena. Further details about the three sites are supplied hereunder.

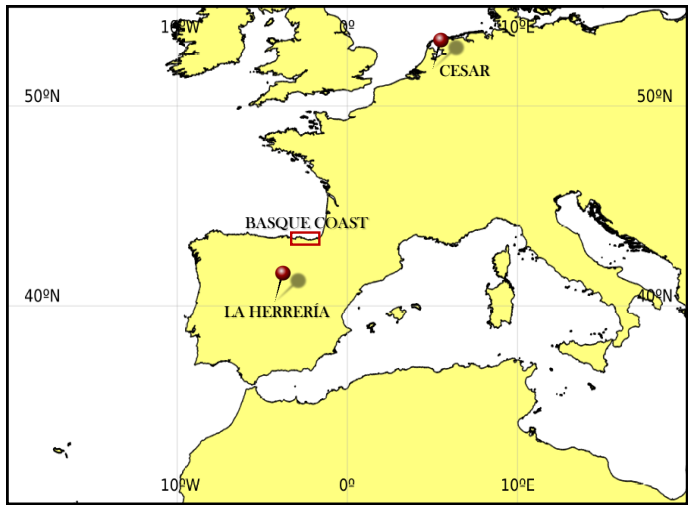

Figure 2.1: Map showing the location of the three meteorological sites investigated in the thesis.

2.2.1 Basque coast

The characteristics of SB phenomena are first explored in the Basque coast, which is situated in the eastern Cantabrian coast at the N of Spain. It is a region characterised by complex topography, i.e. it is composed by unevenly distributed mountains (of up to 1000 m) and valleys. Topography of the region of study is shown in Fig. 2.2a, together with the location of the chosen stations/buoys that provide meteorological data. Figure 2.2b illustrates the four domains of the modelling configuration (which is further detailed in Sect. 2.3.2 and Chapter 3), and the topography of the model for the inner domain.

Meteorological data from two surface meteorological stations [Spanish Meteorological Agency (AEMET)] are analysed. The station of Sondika (43.29°N, 2.91°W, 42 m asl) corresponds to the airport of Bilbao (ICAO code LEBB), and is located in an open valley facing the sea with its axis in the NW-SE direction. The second one, Azpeitia (43.17°N, 2.27°W, 180 m asl), is located in a closed valley surrounded by mountains of approximately between 400–1000 m elevation, with a narrow stream located to the N-NE of the town, through which Urola river runs towards the sea. Sondika is situated at a distance of 12 km from the sea and at 4.5 km from the city centre of Bilbao, and Azpeitia is within a distance of 14 km from the shore. At both stations wind is

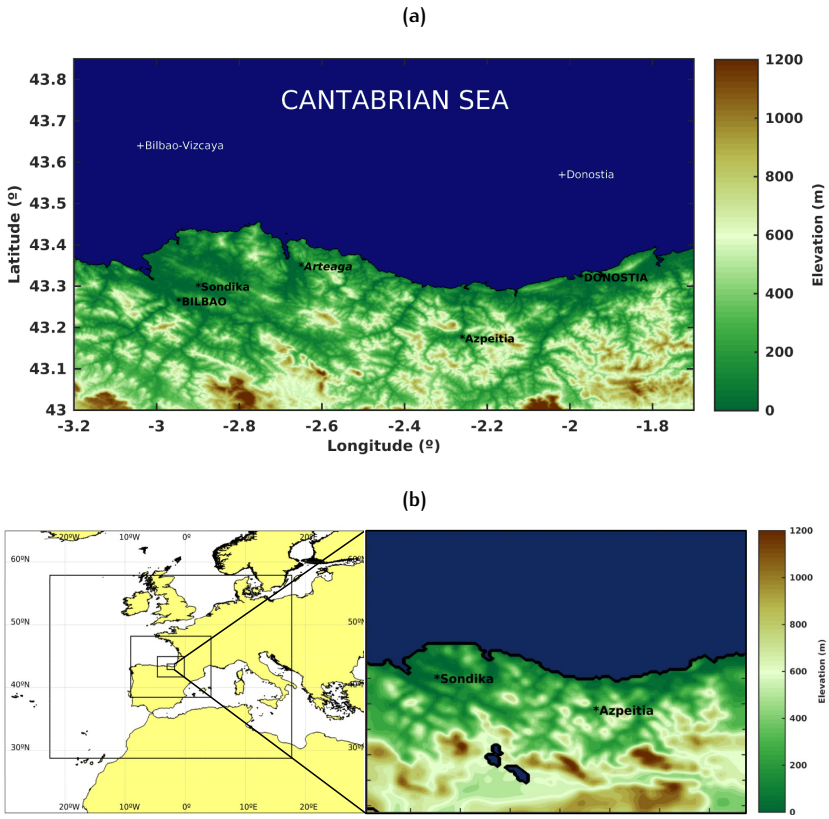

Figure 2.2: (a) Topography of the region of study. Surface meteorological stations, the principal cities (in capital letters) and the radiosonde station of Arteaga (in italics) are shown in black; buoys are shown in white. The source of topography data is ASTER GDEM, which is a product of METI and NASA. The coastline is plotted using GSHHS data. (b) Map depicting the four nested domains (left) and the topography of the model for the inner domain (right), which covers the Basque coast.

measured at 10 m agl and temperature at 1.5 m agl. The weather station in Azpeitia is a Thies automatic station, whereas the one corresponding to Sondika is a synoptic complete weather station with data since 1947, rated as very reliable by AEMET.

Apart from surface stations over land, buoys are used for measurements offshore: Bilbao-Vizcaya (Puertos del Estado) and Donostia (Euskalmet) buoys close to Sondika and Azpeitia respectively. Temperature and wind are measured at 3 m agl in both, with a sampling time of 10 min, although hourly means are given. In addition, radiosonde data are available in Arteaga (43.35°N, 2.66°W, 19 m asl, Euskalmet, see Fig. 2.2a) once a day at 1200 UTC and in case of temporal gaps, data from Santander

radiosondes (43.49°N, 3.80°W, 59 m asl, AEMET) are employed, for which data are available at 0000 and 1200 UTC. Santander (not shown in Fig. 2.2) is located approximately 80 and 130 km towards the W from Sondika and Azpeitia.

2.2.2 CESAR

Contrasting with the complex terrain of the Cantabrian coast, the Cabauw Experimental Site for Atmospheric Research (CESAR) is located on a flat and homogeneous area (Van Ulden and Wieringa, 1996), approximately in the centre of The Netherlands (51°58′N, 4°56′E, -0.7 m asl, see Fig. 2.3). The North Sea is about 50 km W-NW of Cabauw, while the Markermeer, a shallow freshwater lake adjacent to the IJsselmeer lake, lies to the N-NE at approximately the same distance. Since the latter is very shallow (between 5–7 m depth), its temperature is closely coupled to air temperature (Mooij et al., 2008): thus, the North Sea is the main potential driver of SB circulations on the Dutch coast. Figure 2.3 shows the spatial differences of the satellite-measured sea-surface temperature (SST) for a few consecutive SB days. It can be seen that the SST of the Markermeer and IJsselmeer are significantly higher than in the North Sea. However, the Markermeer and IJsselmeer lakes play an important role in the propagation of SBs as shown in Chapter 4.

The area between Cabauw and the sea consists mainly of flat grassland (Tijm et al., 1999), even though the densely populated metropolitan areas of Amsterdam-Utrecht and Rotterdam-The Hague are relatively close to the N-NE and W-SW respectively. In any case, the topography of the surrounding area is very flat, and therefore mesoscale flows are unaffected by topography and the density currents that spread inland are driven purely by SBs, making this area an ideal site for the investigation of this phenomenon.

The CESAR site consists, first, of a 213-m tower located in a topographically flat agricultural area, free of surrounding obstacles (Beljaars and Bosveld, 1997), although the roughness length varies with wind direction (Verkaik and Holtslag, 2007). The soil is significantly wet throughout the year, with the water table lying about 1 m below the surface. The soil type in the southerly region of the tower is mainly river-clay, while N of the tower it is peat or peat on clay (Van Ulden and Wieringa, 1996). Most of the ground is covered by grass or canals.

The Cabauw in-situ observational program that has been under way since 2000, allowed for the performance of several variable and flux measurements along the meteorological mast, covering the physical and dynamical aspects of the lowest part of the ABL. Apart from the 213-m mast, auxiliary masts and devices are available. Further specifications about the measurements utilised in our analysis are provided in Chapter 4.

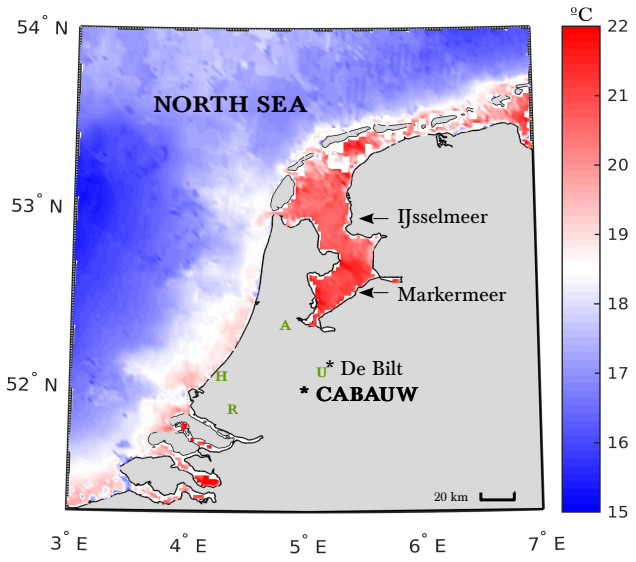

Figure 2.3: Map of the coast in the region under study in the Netherlands and the mean observed SST for the 28/06/09–02/07/09 period, in which four consecutive SB days were observed. The average SST was computed considering the values at 1000 UTC and 2000 UTC. The SST was obtained from satellite full resolution Metop data (L3P AVHRR, EUMETSAT/OSI SAF 2015). The location of Cabauw and De Bilt observational sites, as well as the seas are shown. The location of the largest cities within the surrounding area are indicated with initials: A (Amsterdam), U (Utrecht), R (Rotterdam), H (The Hague).

2.2.3 La Herrería

The last explored emplacement is La Herrería Site, which is is located beside La Herrería Forest (40.582° N, 4.137° W, 920 m asl), from which the name is adopted. La Herrería is located at the foothills of the Guadarrama Mountain Range in central Spain, approximately 50 km NW of the city of Madrid (see Fig. 2.4a). The site chosen is a key aspect of the study for various reasons explained below.

First, it is placed at around 2 km from the steep slope of the Guadarrama mountain range (see Fig. 2.4b), which has a slope angle of around 25° in the main katabatic direction (295°; approximately W-NW, from which the most intense katabatic winds blow). The closest peak, Abantos, is 1763 m high, and the summit Peñalara is at 2420 m asl; both pointed in Fig. 2.4a. Second, it is close to a highly vegetated area to the W, being also close enough to the small urban areas of San Lorenzo de El Escorial to the NW and El Escorial to the E-SE. In addition, it is relatively close to the large metropolitan area of Madrid, where concern regarding high pollution levels has increased in the last

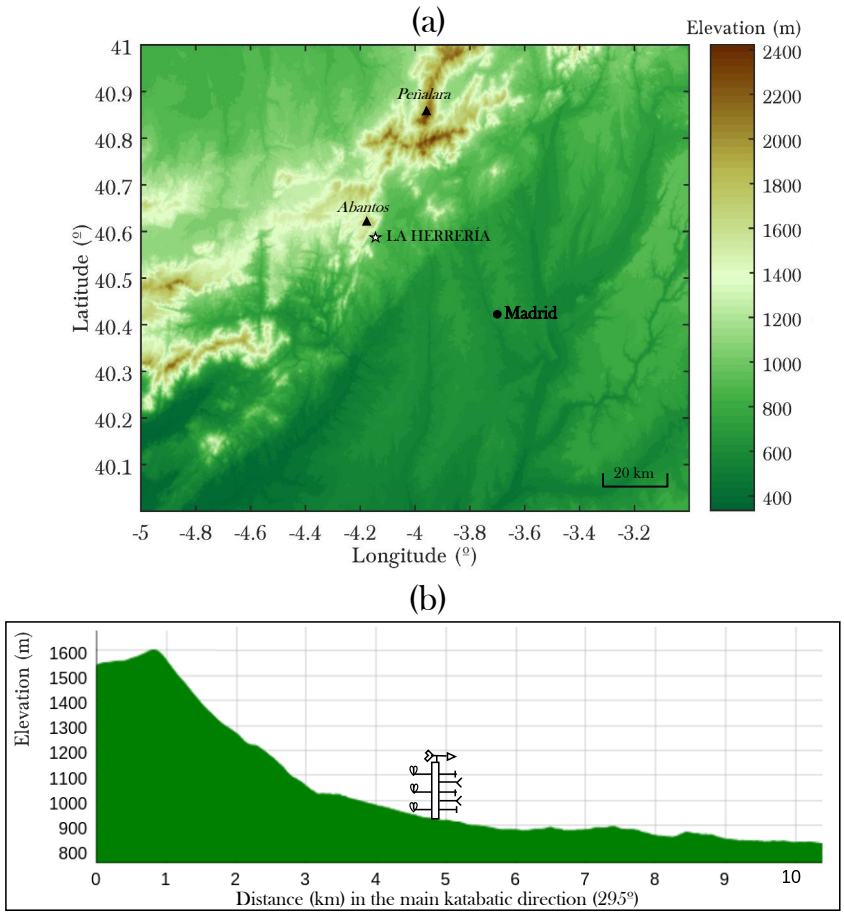

Figure 2.4: (a) Topography of the area surrounding La Herrería site, which is indicated with a star. The position of the city of Madrid, and Abantos (1763 m) and Peñalara peaks (2420 m) are also pointed out. The source of topography data is ASTER GDEM, which is a product of NASA and METI. (b) Topographical profile in the main katabatic direction from La Herrería, depicted ~5 km around in both directions. It is obtained from the *Geocontext-Profiler* tool.

years (Borge et al., 2016, 2018). The diffusivity of pollutants is highly affected by the presence of down-basin winds in the city (Plaza et al., 1997), which develop from converging katabatic flows at the centre of the basin. Besides, the generation of katabatic drainages causes fog formation in the centre of the Iberian Peninsula, affecting visibility, amongst others, in Madrid-Barajas Adolfo Suárez airport (Terradellas and Cano, 2007). Understanding the factors that modulate katabatic winds in this region is there-

fore of high importance. Third, the analysis is carried out during summer, a season that is characteristically very dry and warm in central Spain, even at the mountainous areas (Durán et al., 2013). The soil is particularly dessicated at the end of the season, which makes it different from other mountainous areas in Europe such as the Pyrenees or the Alps. Due to this dessication, small amounts of precipitation can significantly impact the SEB. This sets up a striking framework to explore the role of soil moisture in the SEB and the impact on the intensity of katabatic flows. During night-time, developing katabatic flows are affected by a moisture-limited SEB scenario, which involves more energy available for cooling up of the surface. And finally, the area surrounding the station is located in an relatively flat area (its slope angle is of around 2°) immediately besides the mountain range (see Fig. 2.4b), which allows the formation of strong surface thermal inversions. These inversions are sporadically eroded by the arriving katabatic flows, providing an interesting scenario for the investigation of the distinct SBL regimes.

Regarding the vegetation and land use, the observational site is placed in a pasture grassland with scattered 3–4 m high shrubs, and the soil is composed of granite and gneiss. At around 2 km towards the SW, a broadleaved deciduous forest is found, and at the same distance to the NW, approximately where the steep slope starts, a mixture of needle-leaved evergreen tree cover and mosaic-tree and herbaceous cover. During the katabatic stage, the footprint can reach horizontally up to 200 m, lying within the fetch of the station (Arrillaga et al., 2016a). Nevertheless, under very stable conditions the footprint may increase substantially, which could induce uncertainty in the estimation of the turbulent fluxes and a possible impact of the urban area located to its NW. In any case, the direct implications of the urban area are negligible given the little traffic and the non-existent industrial activity.

Eddy-covariance and meteorological measurements are carried out using a 10-m high fixed tower. Data from aspirated thermometers, radiometers, cup anemometers, a wind vane and IRGASON (Integrated CO_2 and H_2O Open-Path Gas Analyser and 3D Sonic Anemometer) devices among others are recorded. La Herrería tower is part of the Guadarrama Monitoring Network (GuMNet, 2018), which aims at providing observational meteorological and climatological records to deepen into scientific research in the mountainous area of the Guadarrama mountain range. The measurements employed are detailed in Chapter 6.

2.3 METHODOLOGY

A description of the post-processing of meteorological data, the numerical modelling from the WRF mesoscale model and the background and criteria of the mesoscale selection algorithm are presented in this section.

2.3.1 Analysis of meteorological data

Prior to analysing the observational data employed in this thesis, meteorological data require quality-control processing. Additionally, diverse considerations and corrections need to be applied to micrometeorological data. Since each observational database requires a different post-processing, specifications are provided in the respective chapters. Thus, in this section, we describe the main common considerations related to the post-processing of the observational data.

Turbulent parameters and fluxes are calculated from measurements by sonic anemometers and IRGASON devices when available, which incorporate an infrared gas analyser. Turbulent quantities have been determined by calculating the variances and covariances of the turbulent part of the variables after applying the Reynolds decomposition, i.e. the eddy-covariance (EC) technique (Foken et al., 2005). Ideally, the averaging time should be located at the centre of the spectral gap that separates the mesoscales and microscales. But as discussed in the introduction, the precise form of this gap varies depending on several factors, and in some cases it is even imperceptible. Hence, the choice of the averaging window is, to some extent, subjective. Although it is important for a precise estimation of the turbulent parameters and the derived calculations, in this thesis we did not pursue the investigation of the spectral gap and its implications. Instead, we fixed an average time of 10 min, which is considered standard for micrometeorological datasets (Mauritsen and Svensson, 2007).

Most of the turbulent parameters calculated in this thesis are based on the determination of the SH flux (H), friction velocity (u_*) and the turbulent kinetic energy (TKE), which are computed as follows:

$$H = \rho c_{pd} \overline{w'\theta'}, \tag{2.1}$$

$$u_* = \left[(\overline{-u'w'})^2 + (\overline{-v'w'})^2 \right]^{1/4}, \tag{2.2}$$

$$\mathrm{TKE} = (1/2)(\overline{u'^2} + \overline{v'^2} + \overline{w'^2}), \tag{2.3}$$

where ρ is the air density, c_{pd} the specific heat of the dry air at constant pressure, u', v', w' the perturbation part of the wind components, and θ' the perturbation part of the potential temperature.

Along the thesis many other turbulent parameters are defined and calculated. Since they are relevant within the understanding of each chapter, they are introduced in the corresponding parts. In any case, it must be noted that for all the turbulent calculations, the *Monin-Obukhov Similarity Theory (MOST)* has been considered (Monin and Obukhov, 1954; Foken, 2006). This theory describes quantitatively the main turbulent features of the surface layer, i.e. the part of the ABL adjacent to the surface within which the turbulent fluxes of heat and momentum are considered to be constant. Particularities and assumptions regarding the application of this theory are given correspondingly in the following chapters.

To better characterise the surface layer, the vertical profiles of the virtual potential temperature and the wind are fitted to a logarithmic profile by the method of least squares. In this way, the vertical gradients are estimated in a more precise manner by calculating the derivatives. This method is applied to the generic scalar variable $\psi(z)$ in the following form (see Johansson et al. (2001); Steeneveld et al. (2005)):

$$\psi(z,t) = \alpha(t) + \beta(t)\ln(z) + \gamma(t)\ln^2(z) + \delta(t)\ln^3(z). \tag{2.4}$$

2.3.2 WRF model

The *Weather Research & Forecasting (WRF)* model is a numerical mesoscale model that is used both for operational and research purposes (Skamarock et al., 2008). In particular, in this thesis we have solely employed the Advanced Research WRF (ARW) dynamical core, which is based on the following governing equations and physical and numerical assumptions. First, fully compressible and Euler non-hydrostatic equations, which are conservative for scalar variables. Second, terrain-following vertical coordinates and a horizontal Arakawa C-grid staggering. Lastly, prognostic variables include: velocity components, perturbation potential temperature and geopotential, and surface pressure of dry air. Optionally, the TKE and a variety of scalars can be forecasted.

Moreover, the core performs a dynamical downscaling from the coarse resolution of global models to the finest spatial resolution of the modelling configuration, which can be increased up to the lowest grid-size limit of the mesoscale range (roughly about 1 km). The downscaling, instead of being abruptly carried out, it is commonly made by means of nested domains, which allow for a smoother transition. In particular, the two-way nesting option has been set up in the model configuration for a bidirectional communication between the domains. To allow for a robust stabilisation of the model, a 24-h spin-up time has also been fixed in the different experiments carried out.

The WRF model has been shown to be an effective tool to simulate the thermally-driven circulations addressed in this thesis. For example Sastre et al. (2015) and Ribeiro et al. (2018) successfully simulated katabatic flows and SBs with WRF. The model is continuously under progress, since the wide spectrum of applications that encompasses and the research behind, contribute to its progressive improving and development. In this thesis, versions 3.4.1 and 3.5.1 are employed to perform the numerical simulations. Depending on the research purposes, one configuration proves to be more satisfactory than another, and hence some settings of the model vary throughout the thesis. Regardless, specifications about the settings of the numerical experiments are provided in the corresponding chapters.

Physical processes that have a characteristic length below the grid resolution need to be parameterised in the model. Hereinafter we introduce some basic specifications of the schemes tested in this thesis. In particular, we explore some of the physical parameterisations of high relevance for an adequate representation of turbulent processes:

ABL parameterisations. On the other hand, we test an option that forces or nudges the model towards time- and space-interpolated analyses: the *grid-analysis nudging*. For further information about other schemes and settings of the model, Skamarock et al. (2008) or specific articles can be consulted. In spite of not being investigated in this thesis, other physical parameterisations can also be of relevance for the representation of turbulent processes in the ABL, such as the land-surface model (LSM), as demonstrated in the studies from Román-Cascón et al. (2012) and Sastre et al. (2014).

ABL parameterisations

These parameterisations solve for turbulent features of scales below the grid spacing. Two distinct ABL parameterisation schemes are tested in this thesis:

Yonsei State University (YSU): it is a first-order closure scheme with a counter-gradient term to account for non-local gradients (Hong et al., 2006). Within the ML, the turbulent-diffusion equation for a generic variable C is defined as:

$$\frac{\partial C}{\partial t} = \frac{\partial}{\partial z}\left[K_c\left(\frac{\partial C}{\partial z} - \gamma_c\right) - \overline{(w'c')}_h\left(\frac{z}{h}\right)^3\right], \tag{2.5}$$

where K_c is the eddy diffusivity of C, γ_c is a non-local gradient term incorporating the contribution of large eddies, $\overline{(w'c')}_h$ is the flux at the inversion layer, and h is the ABL height. The last term represents the explicit treatment of the entrainment flux. The ABL top is determined from the critical bulk-Richardson number: $R_c = 0$; so that the flux at that level is minimised.

In stable conditions the second and third therms on the right-hand side of Eq. 2.5 are not included in the turbulence diffusion equation. The formulation of K_c is distinct for heat and momentum, and for stable, neutral or unstable conditions (for further details we refer to Hong and Pan (1996)).

Mellor-Yamada-Janjic (MYJ): it is a one-and-a-half order prognostic TKE-closure scheme, with local vertical mixing (Mellor and Yamada, 1982; Janjić, 1994). Hence, it does not incorporate the second and third terms from Eq. 2.5. The eddy-diffusivity coefficients are more complex than for YSU:

$$K_c = l_M q S_c \,, \tag{2.6}$$

where l_M is a master length scale defined following Blackadar (1962), $q = (\overline{u'^2})^{0.5}$ u' being the turbulent fluctuation velocity and S_c is the generic form of the dimensionless stability functions of heat and momentum. They are determined after the governing equation of the TKE is iteratively solved (we refer to Mellor and Yamada (1982) and Janjić (1994) for further specifications). In this scheme, the ABL top is defined at the level where the TKE decreases below the threshold value of 0.2 $m^2\ s^{-2}$.

The ABL scheme is bound to the *surface-layer scheme*. YSU is used together with the MM5 surface-layer scheme (Beljaars, 1994), and MYJ with the Eta scheme (Janjić, 1996). MM5 uses stability functions (Paulson, 1970; Dyer and Hicks, 1970; Webb, 1970) to calculate the surface-exchange coefficients of momentum, heat and moisture. Eta, instead, is based on MOST and includes parameterisations of the viscous sub-layer.

Grid-analysis nudging

This type of nudging forces the model towards a series of analysis (which are space- and time-interpolated) for each grid-point (Skamarock et al., 2008), providing the model a four-dimensional data assimilation . It is usually employed for the dynamic initialisation (spin-up), or for boundary conditions in nested-domains. Hence, this method adds an extra tendency term to the equation of the nudged variable α in the following way:

$$\frac{\partial \alpha}{\partial t} = F(\alpha) + G_\alpha W_\alpha (\hat{\alpha}_0 - \alpha), \tag{2.7}$$

where $F(\alpha)$ is the normal tendency term due to physics, advection etc., $G(\alpha)$ represents an inverse time scale that controls the nudging strength, $W(\alpha)$ is an additional weight in time or space which serves to limit nudging and $\hat{\alpha}_0$ is the time- and space-interpolated analysis field.

Model-performance indicators

The accuracy of the model simulating the observed variables is evaluated using various scores. In this thesis we use the mean bias error (MBE) and the root mean square error (RMSE). These statistical scores are computed as follows:

$$\mathrm{MBE} = \frac{1}{n} \sum_{i=1}^{n} (m_i - o_i), \tag{2.8}$$

$$\mathrm{RMSE} = \sqrt{\frac{1}{n} \sum_{i=1}^{n} (m_i - o_i)^2}, \tag{2.9}$$

where m_i and o_i represent respectively the modelled and observed n values of the variables. In the case of wind direction those expressions cannot be employed due to the circular character of this variable. Thus, the difference Δd_i is calculated following its definition in Jiménez and Dudhia (2013), so that the values are in the range [-180°, 180°]. This allows the calculation of a normalised RMSE in the following way:

$$\mathrm{RMSE}_n = \frac{1}{180} \sqrt{\frac{1}{n} \sum_{i=1}^{n} (\Delta d_i)^2}, \tag{2.10}$$

which has the value 0 when the model is equal to observations and 1 when the difference is the largest possible.

2.3.3 Mesoscale Selection Algorithm

Many studies addressing the analysis of SB and katabatic phenomena zoom in single events, which in many cases are subjectively selected. That strategy, however, hampers the investigation of the forcings affecting their characteristics, and the assessment of the interaction with turbulence during the AET of the ABL. Hence, we pursue the analysis of mesoscale phenomena in an objective and consistent manner. For that, we develop a robust method to select mesoscale events systematically from the available databases, based on objective criteria that assure that the changes in the meteorological variables are exclusively due to SBF passages. These criteria combine synoptic and surface features.

Our algorithm is firstly based on the objective filters defined in Borne et al. (1998), which were developed after an empirical study in a relatively flat area in the western Swedish coast. Their method underestimates the number of SB events, but conversely, provides an unambiguous database. Some other analyses make also use of distinct objective filters to detect SB events, but most are manually applied. For instance, Wichink Kruit et al. (2004) selected SB days by requiring a minimum thermal contrast of at least 5 °C between the observed temperature over land and the SST. Other requirements included a maximum wind-speed threshold of 1 m s^{-1} at sunrise, and an earlier enhancement of the onshore component at the shore than further inland. On the other hand, Azorin-Molina and Lopez-Bustins (2008) employed the semi-diurnal pressure oscillation to select the SB events. A review of the criteria used to detect SB occurrences is carried out in Azorin-Molina et al. (2011).

Before developing our own algorithm, we apply the method from Borne et al. (1998) in Chapter 3 due to its ease and convenience. It is executed in an automated manner, employing merely data from individual standard meteorological stations and large-scale conditions from radiosonde data. This algorithm identifies SB events when a noticeable wind shift and an immediate period of constant wind direction occurs during daytime, not due to synoptic forcing, and a predefined sea-land thermal-contrast threshold is exceeded. To be selected as a SB day, the conditions determined by six different filters must be met.

The first three filters impose conditions for the synoptic wind, which is determined from radiosonde records at 700 hPa in Arteaga (see Fig. 2.2a). Filter 1 rejects days in which the synoptic-wind direction varies more than 90° in 24 h. The second filter excludes days in which the synoptic wind speed variation is larger than 6 m s^{-1} in 12 h. Radiosonde data from Santander are required for this filter. In the third filter a maximum limit for the synoptic wind at 1200 UTC is fixed: 11 m s^{-1}.

The last three filters evaluate surface conditions. The fourth filter requires that the sea-land thermal contrast is greater than 3 °C. The difference is computed considering

the daily maximum air temperature over the sea (measured at buoys) and over land (measured at surface stations). Filter 5 selects days with an hourly veering of the wind greater than 30° in the time range between 1 h after sunrise and 5 h before sunset. The sixth filter rejects days in which the average hourly variation of the wind direction during 5 h after the veering of the wind is not at least six times smaller than the magnitude of the veering *per se*. With this last filter, the wind direction constancy is assured.

As will be explained in Chapter 3, this method manifests some issues regarding the level at which the synoptic wind is considered and the lack of a predefined onshore direction. For that reason, and taking the method from Borne et al. (1998) as a starting point, we develop a new selection algorithm. We build it in a way that is applicable for selecting SB phenomena, and extendible to other regions, as is the case of the CESAR site. Later, it is adapted to select katabatic occurrences at La Herrería site. Table 2.2 presents the algorithm used to filter the SB events in Chapters 4 and 5, and the katabatic occurrences in Chapter 6. The corresponding objective criteria are explained in detail below.

Table 2.2: Mesoscale selection algorithm. The first column indicates the filter number; the second column the physical justification of each of the filters; and the third and fourth columns, respectively for the SB and katabatic events, the criteria to be fulfilled in order to pass each of the filters. Specific SB criteria are shown in blue, for katabatics in green and the coincident criteria, however, in black.

Filter	Physical justification	Criteria (SB)	Criteria (katabatics)
1	Weak large-scale winds	$V_{850} < 6\ \mathrm{m\,s^{-1}}$	$V_{850} < 6\ \mathrm{m\,s^{-1}}$
2	No synoptic cold fronts	$(\Delta\theta_{e,850}/\Delta t) > -1.5\,^{\circ}\mathrm{C/6h}$	$(\Delta\theta_{e,850}/\Delta t) > -1.5\,^{\circ}\mathrm{C/6h}$
3	Non-rainy events	$pp < 0.1\ \mathrm{mm}$	$pp < 0.5\ \mathrm{mm}$
4	Thermal contrast	$\Delta T_{sea,land} > 2\,^{\circ}\mathrm{C}$	–
5	Frontal passage	$\Delta\alpha_{10'} > 45^{\circ}$ & $(\overline{\Delta\alpha_{10'}})_{2h} < 15^{\circ}$ or $\Delta\alpha_{10'} > 22.5^{\circ}$ & $(\overline{\Delta\alpha_{10'}})_{2h} < 5^{\circ}$	$\alpha \in [250^{\circ}\text{–}340^{\circ}]_{2h}$

- Filter 1 eliminates the days with strong large-scale winds. In coastal areas, when the large-scale wind is offshore and above a certain threshold, the SB airflow may not reach land (Simpson, 1994). When the wind is onshore, the SB component is masked by the large-scale wind and therefore very difficult to detect as an isolated phenomenon (Miller et al., 2003). For these reasons, several studies have defined an upper threshold for the synoptic wind speed above which the SBF passage is blocked. Numerical studies set that value within the range of 6–11 m s^{-1} (Crosman and Horel, 2010). Since our aim is to remove all days with strong large-scale winds, we choose the lowest value, i.e. 6 m s^{-1}. In order to derive the large-scale wind, we use data from reanalysis at 850 hPa, because at that level the lower branch of the SB cell is unlikely to be detected (the typical

maximum ABL depth in a SB day is around 1000 m). For instance, according to Atkinson (1981) the highest altitude at which the SB is detected is around 1.5 km. When computing the mean large-scale wind speed for each day, we only take into consideration the reanalysis values at 0600, 1200 and 1800 UTC, since the value at 0000 UTC does not affect the development of the SB circulation. For katabatic events we use the level of 850 hPa too, since at the reanalysis grid point in which the synoptic flow is analysed the 850-hPa level is approximately at a height of 800 m agl: sufficiently close to the surface as to be representative of the synoptic wind at the surface level, and far enough as to be out of the influence of katabatic flows. However, we just consider the values at 1800 UTC, since they are the ones affecting katabatic development.

- Filter 2 discards the days that display a synoptic cold-front passage during daytime. Cold fronts have features that resemble those observed in SBFs or sometimes in katabatic flows; for instance, a sudden veering of the wind and a sharp drop in temperatures. Indeed, synoptic fronts that pass when the intensity of the large-scale winds is below the defined threshold of Filter 1, could be filtered as SB or katabatic occurrences. In addition, cold fronts are generally linked to rough weather, which of course is not the best scenario for the formation of thermally-driven circulations. Synoptic fronts are hard to define objectively, and their depiction in weather pressure charts is actually rather subjective. However, Hewson (1998) defines synoptic fronts objectively using the horizontal gradient of the equivalent potential temperature and the wet-bulb potential temperature, amongst other ways. Considering that both the latent heat of vaporisation and the specific heat at constant pressure for dry air ($l_v(15°C) = 2.46\times10^6$ J kg^{-1} and $c_{pd}(15°C) = 1005$ J kg^{-1}K^{-1} respectively) are constant, we can assume the following for the tendency of the equivalent potential temperature θ_e:

$$\frac{\Delta\theta_e}{\Delta t} \simeq \frac{\Delta\theta}{\Delta t} + \frac{l_v}{c_{pd}}\frac{\Delta r}{\Delta t}, \tag{2.11}$$

where θ is the potential temperature and r the water-vapour mixing ratio, both obtained from reanalysis data at 850 hPa, for the above-mentioned reasons. Taking into account the values of the horizontal gradients given by Hewson (1998) and a V_{850} of 5 m s^{-1}, which is regarded as adequate to describe the propagation speed of the cold fronts (bearing in mind that the cases in which $V_{850} > 6$ m s^{-1} are discarded), the days in which θ_e falls more than 1.45°C in 6 h (either from 0600 to 1200 or from 1200 to 1800 UTC) are regarded as being characterised by the passage of a synoptic cold front, and were therefore eliminated from the selection. We emphasise that the correctness of this filter was checked for a number of days in contrast with the fronts depicted in Met Office surface pressure charts, and produced convincing results.

- Filter 3 rejects the days in which precipitation greater than a predefined threshold is recorded. Most of the days in which precipitation occurs have already been rejected by the previous filters, but some of them are characterised by fair-weather conditions, which may trigger convective-cloud development, and in some cases, storms. Such afternoon storms could produce gravity currents which may also be misinterpreted as thermally-driven flows, and we therefore need to discard them. Even if these days include the passage of the SBF or katabatic flows, they would pollute the pure event that we finally wish to analyse. Precipitation that occurs during the night does not affect the SB formation and passage; hence, we only consider precipitation measured between 0600 and 2200 UTC to select SB events. The predefined threshold is of 0.1 mm for SB events and of 0.5 mm for katabatic flows, since as observed, the SB circulation is more sensitive to the formation of weak and scattered showers.

- Filter 4 is just applicable for SB phenomena, and assures that a certain sea-land temperature gradient is exceeded, as it is needed to trigger the circulation of SBs. The filter is designed to the specific case of the SB in Cabauw (Chapters 4 and 5), and thus needs to be adapted to be applicable in other coastal emplacements. Since we need the values of the air temperature over the sea, we employ 2-m ERA-Interim reanalysis data at 1200 UTC. At that time of the day, the land is sufficiently warm, and due to the distance from Cabauw to the sea (~ 50 km), the SBF has not usually reached Cabauw. The value of 2 °C was derived from the tenth percentile of all the SB days in the Basque coast, obtained from the observational data. Many other authors use higher thresholds to select SB days: 3 °C in Borne et al. (1998) or 5 °C in Wichink Kruit et al. (2004). However, they use the SST to compute the gradient, which is demonstrated to have a bias with respect to the air-temperature over the sea in Chapter 3. As a proxy for the air temperature offshore in Chapter 4, the ERA-Interim reanalysis value at a grid point over the North Sea (52.5°N, 4.25°E) is chosen, at approximately 20 km from the shore. Over land the grid point closest to Cabauw (52°N, 5°E) is picked, both sites at 2 m asl.

- Finally, the last filter (Filter 5), requires a clear frontal signal in order to be finally selected as a SB or katabatic day. The frontal requirement is specific to the location (topography, distance to the sea etc.), and the characteristics of the SB or katabatic flows. In the case of the SB, we require a veering in the wind $\Delta\alpha$ to an onshore direction (i.e. blowing from sea to land) between 1000 and 2000 UTC, and one of the two conditions described in Table 2.2 must be met. The wind has to be maintained in the onshore direction for at least 2 h without oscillating too much around the wind direction after the shift. For the case of Cabauw we define the onshore range taking into account the coastline orientation: [225°–45°]. With respect to the time range, [1000–2000 UTC], we fix it given the mean wind roses at different times (not shown). This filter is an adaptation of the last filter

defined in the algorithm of Borne et al. (1998), which is applied to the SB study in the Basque coast (Chapter 3). The criteria are rather strict, since we demand a certain degree of confidence regarding the filtering of clear SBF passages.

In the case of katabatic winds, this filter is based on specific criteria for katabatic flows in La Herrería site, and was defined after a thorough inspection of the wind behaviour around sunset on days passing the first three filters. An event is selected as *katabatic* when wind direction at 10 m is roughly perpendicular to the mountain-range axis, i.e. within the range [250°–340°], for at least 2 h at a time between 1600 and 2400 UTC.

3 CHARACTERISATION OF SEA-BREEZE EVENTS OVER COMPLEX TERRAIN

We investigate the behaviour of the SB along the north coast of Spain by using observations of two topographically contrasting sites and simulations from the WRF model. An objective and systematic selection method is used to select SB days from a database of two summer months. Its performance is evaluated and possible improvements are proposed. We find that the direction and intensity of the SB are significantly affected by the topography of the region. In fact, the estimated SB intensity shows an opposite relationship with the cross-shore temperature gradient for both sites. Numerical simulations reproduce the onset of the SB, but some characteristics are not adequately simulated: wind speed is generally overestimated, the diurnal evolution of the temperature is smoothed and the interaction with terrain-induced flows is not correctly represented. Additionally, four sensitivity experiments are performed with the WRF model modifying the ABL scheme, as well as the grid-analysis nudging for an anomalous case study. As the two simulations with nudging reproduce an unreal (not observed) SB, this day turns out to be of great interest: it allows to evaluate the influence of the passage of the SBF on atmospheric variables and the associated turbulence. With regard to the ABL scheme, the best model scores are obtained for the scheme that does not use a TKE closure.

The main contents of this chapter are published in:
Arrillaga, J.A., Yagüe, C., Sastre, M., and Román-Cascón, C. A characterisation of sea-breeze events in the eastern Cantabrian coast (Spain) from observational data and WRF simulations. *Atmos. Res.*, 181:265-280, http://dx.doi.org/10.1016/j.atmosres.2016.06.021, 2016.

3.1 INTRODUCTION

As explained in the introduction of this thesis the SB phenomenon has been broadly studied due to its influence among others on air quality and pollution, severe weather and wind-energy generation offshore. In this chapter we explore the characteristics of this mesoscale phenomenon on the Cantabrian coast of Spain, particularly on the Basque coast. The SB and its characteristics are well studied on the Mediterranean coast of Spain (Ramis and Romero, 1995; Azorín-Molina and Chen, 2009; Soler et al., 2011; Ponce de León and Orfila, 2013), but not so in the Cantabrian coast, perhaps due to a lower prevalence of fair-weather conditions during the summer period. However, it was found that the SB was one of the main drivers of pollution episodes in the industrialised metropolitan area of Bilbao (Alonso et al., 2000). In addition, the eastern Cantabrian coast is characterised by the complex topography, which has been proved to impact significantly the evolution of the SB circulation (Crosman and Horel, 2010), even in the tropics during the winter and pre-monsoon seasons (Muppa et al., 2012). Therefore, this region allows to analyse the features of the SB over complex topography and their interaction with terrain-induced flows. A robust method is required to select SB events objectively and distinguish them from the flows induced by the complex topography. The research questions we address in this first analysis of the thesis are these that follow:

RQ 3.1: *How is the SB circulation affected by the complex terrain and the flows induced by it?*

RQ 3.2: *How is the vertical and temporal distribution of meteorological and turbulent variables altered for SBFs arriving at different times of day?*

OUTLINE Section 3.2 describes the observational data employed. Section 3.3 presents the configuration of the numerical experiments. The obtained results are discussed in Sect. 3.4 and finally, the main conclusions of the work are summarised in Sect. 3.5.

3.2 OBSERVATIONS

The region of study of this work is located on the eastern Cantabrian coast (north of Spain), more precisely on the Basque coast. Further information about this area of study and the observational data employed is provided in Sect. 2.2.1.

The period chosen for this study spans two summer months (July and August) in 2013 mainly for two reasons: firstly, it corresponds to the driest and synoptically most stable season in this region (Font Tullot, 2000); and secondly, the strong surface heating in these months enhances the sea-land temperature gradient and so the SB perturbation. In particular, due to the prevalence of high pressure over Great Britain in July,

this month was drier and synoptically more stable than the climatological mean. August, however, was very close to the climatology for this month. This analysis could be extended in the future for a longer time period in order to establish a climatology of the SBs in the area of study.

With the aim of obtaining a reliable database, the objective SB selection method from Borne et al. (1998) is employed (details are given in Sect. 2.3.3)

3.3 WRF MODEL

The numerical experiments are performed using the WRF model version 3.5.1 (Sect. 2.3.2). A summary of the model configuration employed is shown in Table 3.1.

Table 3.1: WRF model setting and sensitivity tests.

WRF configuration and physics	Value
Central point	43.33°N, 2.41°W
Horizontal resolution (km)	4 nested domains (27; 9; 3; 1)
Vertical resolution	35 eta levels (default)
Time step	180 s
Initial and boundary conditions	NCEP FNL Global Analysis Data (6 h)
Longwave physics	RRTM (Rapid Radiative Transfer Model)
Shortwave physics	Dudhia
Microphysics	WSM-3-class
Surface physics	Noah LSM
Sensitivity tests	ABL scheme (YSU/MYJ) + grid analysis nudging/no nudging

Four nested domains are used in each simulation (see Fig. 2.2b), with the two-way nesting option active. The inner domain covers the entire Basque coast with a horizontal grid resolution of 1 km and 100 x 100 grid points. The remaining domains have 120 x 120 grid points and the grid spacing increases by a factor of three up to the outer domain, which has a horizontal resolution of 27 km. For each simulation the model is run for 48 h, the first 24 h being considered as spin-up time. The simulated time never exceeds 24 h to avoid the possible influence of simulated conditions precedent (Steele et al., 2013). The vertical levels are the default 35 eta levels with 7 in the lowest km (0, 59, 145, 259, 399, 578, 805 m), and top pressure of 50 hPa. Additionally, we update the SST, despite it is not usually required for short simulations.

The model is initialised using 1° x 1° (~ 100 x 100 km²) resolution NCEP FNL Operational Global Analysis data and four sensitivity experiments are performed varying the ABL scheme as well as the grid analysis nudging option (see Table 3.2). Firstly, the effect of changing the ABL scheme from the YSU to MYJ, which are based on dif-

ferent turbulence representation, is explored. The ABL scheme option is bound to the surface-layer Scheme: MM5 for YSU and Eta scheme for MYJ.

Table 3.2: Sensitivity simulations with the WRF model.

Simulation	ABL scheme	Grid analysis nudging
Sim. 1	YSU	NO
Sim. 2	MYJ	NO
Sim. 3	YSU	YES
Sim. 4	MYJ	YES

Then again, the sensitivity to selecting the grid analysis nudging option is considered. For further information about this setting and the different physics behind both ABL schemes we refer the reader to Sect. 2.3.2. We use a value for $G(\alpha)$ of $3{\cdot}10^{-4}$ s^{-1} in this experiment. The four nudged variables are u, v, T and q, but only the wind is nudged for all the vertical levels including the ABL. This nudging configuration has been used in some previous works (Stauffer and Seaman, 1990; Stauffer et al., 1991; Liu et al., 2012), leading to a greater reduction of the modelling bias. We apply the nudging during the first 24 h of the simulation, and hence, for a smooth pre-forecast period which acts as initial condition for our simulation.

The accuracy of the model simulating the observed variables is evaluated using both the MBE and the RMSE scores, which are introduced in Sect. 2.3.2.

3.4 RESULTS AND DISCUSSION

3.4.1 Observed SB characteristics

After applying the SB selection method to the observational data, 14 and 21 SB days are obtained in Azpeitia (complex topography) and Sondika (valley facing the sea) respectively, of which 10 are in common. Bearing in mind that both stations are approximately at the same distance from the sea (~ 12–14 km), it suggests that complex topography hinders the detection of SBs due to the influence of other local winds. A summary of the selected SB days by each filter is shown in Table 3.3. We find that Filter 5 accepts all the input days. Since the first three filters assure synoptically stable conditions, under which SBs and MBs cause an inversion of the wind direction from night-time to daytime, a turn of the wind larger than 30° is observed. On the other hand, the sixth filter is the main filter responsible for the rejection of the candidate SB days: in Azpeitia rejects almost 50% of the days that pass Filter 5, but in Sondika, instead, only 30%. This filter together with Filter 4, rejects wind turns caused by topographically induced winds and assures that SB conditions are fulfilled. However, it seems that many possible SBs could be declined due to a lack of wind-direction

constancy, which apparently is harder to attain in Azpeitia, probably due to the orographic barrier caused by the surrounding mountains. This is also reflected in the observed low wind speed. In addition, local terrain-induced flows alter the resultant wind speed, particularly in this location, even though the main forcing is the SB.

Table 3.3: Summary of the selected SB days by each filter of the selection method in (a) Sondika and (b) Azpeitia. The first three filters are common for both stations. By way of example, the fourth filter in Sondika (a) gets 35 candidate days from Filter 3 and accepts 30 of them, which implies a partial acceptance percentage of 86%. Taking into account the number of accepted days (30) out of the whole period (62), the absolute acceptance percentage is obtained (48%).

(a) Sondika

Filter	Input days	Output days	Partial acceptance (%)	Absolute acceptance (%)
1	62	51	82	82
2	51	47	92	76
3	47	35	74	56
4	35	30	86	48
5	30	30	100	48
6	30	21	70	34

(b) Azpeitia

Filter	Input days	Output days	Partial acceptance (%)	Absolute acceptance (%)
1	62	51	82	82
2	51	47	92	76
3	47	35	74	56
4	35	27	77	44
5	27	27	100	44
6	27	14	52	23

Once the SB database is available, we explore their main characteristics. The onset of the SB is characterised by a turn of the wind to an onshore wind direction. This direction is influenced by the synoptic wind (Miller et al., 2003), topography (Papanastasiou et al., 2010), coastline curvature (Steele et al., 2013) and the Coriolis force (Crosman and Horel, 2010). Figure 3.1 shows the wind rose at both locations for the obtained SB days. The predominant SB direction in Sondika (Fig. 3.1a) is in the fourth quadrant (270°–360°). The most intense SBs blow from the NW in this site, coinciding with the direction of the valley in which the station is located (see Fig. 2.2) and with the orientation of the nearest shoreline, where the maritime flow penetrates inland. But

as previously mentioned the synoptic flow influences the SB direction, and in the case of Sondika results in a wind blowing from the first quadrant (0°–90°) when the E component of the large-scale wind is more intense. This occurs with a low pressure system over land and a high pressure system over the sea, i.e. forming a corkscrew SB. However, this type of SB is not very common in Sondika due to the orientation of the valley, which hampers the penetration of the corkscrew SB towards Sondika and the surroundings of the city of Bilbao. In fact only 3 SB days of this type are obtained from the analysed period, even if the predominant synoptic situation (high pressure over Great Britain and the thermal low pressure over the Iberian Peninsula) over almost the entire month of July was likely to form them. In few cases the wind started blowing from the NE and later shifted to NW, being maintained in the second direction for the period of time required by the selection method.

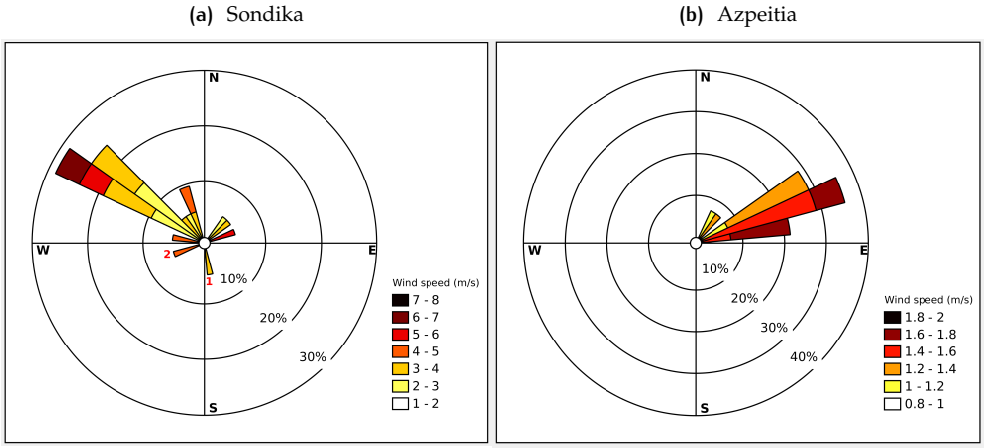

Figure 3.1: Wind rose for the obtained SB days in (a) Sondika and (b) Azpeitia. The wind speed is represented with colours. Red numbers in (a) label two days with offshore wind direction that passed the selection method.

By contrast, in Azpeitia the wind blows only from the first quadrant on the obtained SB days (Fig. 3.1b). In particular, the most intense SBs blow from the E-NE even though the Urola valley is located to the N-NE of the location (Fig. 2.2). In addition, the nearest shoreline (in which the Urola river flows into the sea) is orientated with its perpendicular axis favouring the winds from the N-NW. As mentioned above, synoptic conditions in July favoured the formation of corkscrew SBs, but it is not the only reason. Azpeitia is located in a closed valley surrounded by mountains of relatively high elevation (400–1000 m). Hence, the SB interacts with the valley circulation resulting in an E-NE wind direction. Additionally, the SB intensity in Azpeitia is considerably weaker than in Sondika due to the barrier effect of the surrounding mountains.

On the other hand, two days passed the selection method in Sondika with an offshore SB direction (pinpointed in Fig. 3.1a with red numbers), which is inconsistent with the definition of the SB. The day pinpointed with a "1" corresponds to 31 July. On this day the wind direction was offshore (from the S, i.e. from land to sea) during daytime, and passed the selection method due to a wind turn from onshore to offshore and to the maintenance of this final S direction for some hours. However, this day turned out to be a a late-sea-breeze (LSB) day of great interest to analyse and simulate with the WRF model. It is explored in detail in Sect. 3.4.3. Moreover, the day labelled in Fig. 3.1a with a "2" corresponds to 28 July. This day passed the selection method again incorrectly due to a slight turn in the wind from SW to W-SW, probably synoptically influenced. Therefore, at least 2 days are incorrectly identified as SB days due to the employed selection method, which does not assure that the final wind direction (after the observed turn) is onshore. This issue motivates the adaptation of the last filter to assure that the wind during 5 hours after the turn is onshore.

Another important aspect of the SBs is related to the intensity of the perturbation that causes them, i.e. the magnitude of the sea-land temperature gradient. Mathews (1982) developed a forecast rule by representing the recorded strength of the SB as a function of the sea-land temperature contrast. Fitting a regression line resulted in:

$$|U| = 5\sqrt{\Delta T}, \tag{3.1}$$

where U is the magnitude of the SB component in knots (not the observed wind) and ΔT the sea-land temperature difference in °C. In this work we propose a new formulation for the SB intensity:

$$u_{SB} = |\boldsymbol{u} - \boldsymbol{U}_*|\,, \tag{3.2}$$

where u_{SB} is the estimated intensity of the SB, $\boldsymbol{u}$ the observed surface wind at 10 m after the turn and $\boldsymbol{U}_*$ represents an estimation of the surface large-scale wind. The latter is estimated considering 0.25° x 0.25° ERA-Interim reanalysis data at surface: in particular, taking the nearest grid points from Azpeitia and Sondika that are located far enough from the shore to avoid the influence of the SB. The grid point (43°N, 3°W) is used to estimate the large-scale wind in Sondika (43.29°N, 2.91°W) and (42.75°N, 2.25°W) in Azpeitia (43.17°N, 2.27°W).

Figure 3.2 shows the estimated SB intensity (Eq. 3.2) *versus* the square root of the sea-land temperature gradient for both Sondika (red) and Azpeitia (blue). The above-mentioned non-SB (NSB) days that passed the selection method in Sondika are not included. The results show an opposite trend for both locations: in Sondika the SB is more intense when the temperature contrast between the air over the sea and over the land increases, and the opposite in Azpeitia. Student-t-tests with a confidence level of 95% show that the linear correlation is statistically significant in Sondika. The analysis has also been performed for u_{SB} *vs* ΔT (not shown), resulting in a similar correlation value. On the other hand, the linear correlation apart from being negative is not statistically significant in Azpeitia. This behaviour can be associated with the

closed-valley effect produced by the surrounding orography of this station, which acts as a barrier for the onshore flow. From Fig. 3.1b we found that the SB intensity in Azpeitia is very weak. The complex topography of the region induces upslope and upvalley flows that interact with the SB and the synoptic flow. Thus, the resultant wind is influenced by local forcings other than the SB, and thereby the relationship between the SB intensity and the cross-shore temperature gradient is opposite than expected. In any case, estimating the SB intensity is a complicated task since it is highly influenced by the atmospheric stability, topography and soil conditions amongst others (Atkinson, 1981; Miao et al., 2003).

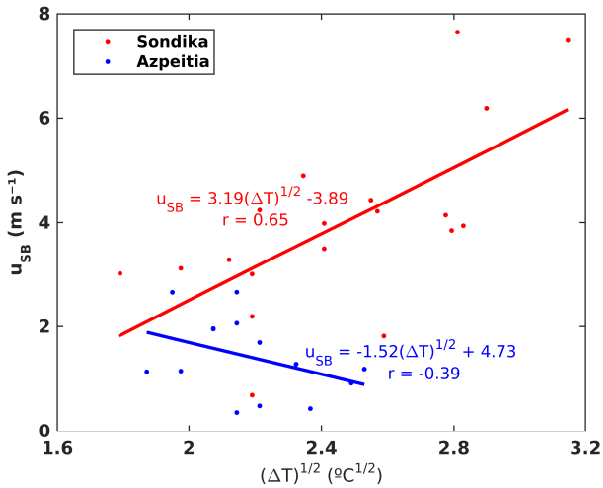

Figure 3.2: Observed SB intensity (u_{SB}) *versus* the root-square of the sea-land temperature gradient ($(\Delta T)^{1/2}$). Dots represent the estimated SB intensity for each value of the observed temperature gradient, and lines represent the corresponding linear fitting. Alongside each line, the corresponding equation and linear correlation coefficient are shown.

3.4.2 SB case study: 6 July

We choose a day selected as a SB day in both locations in order to analyse a prototypical SB situation: 6 July. Meteorological conditions were strongly favourable for SB: clear sky and synoptic stability. In particular, the anticyclone over Great Britain (Fig. 3.3a) inducing easterly large-scale winds made the situation prone to the formation of corkscrew SBs. The radiosonde for this day in Arteaga at 1200 UTC (Fig. 3.3b) shows the thermal inversion strengthened by the presence of subsidence motions at approximately 1700 m asl, typical of anticyclonic situations. Additionally, the wind is light and blowing from the E/NE in the lower atmosphere.

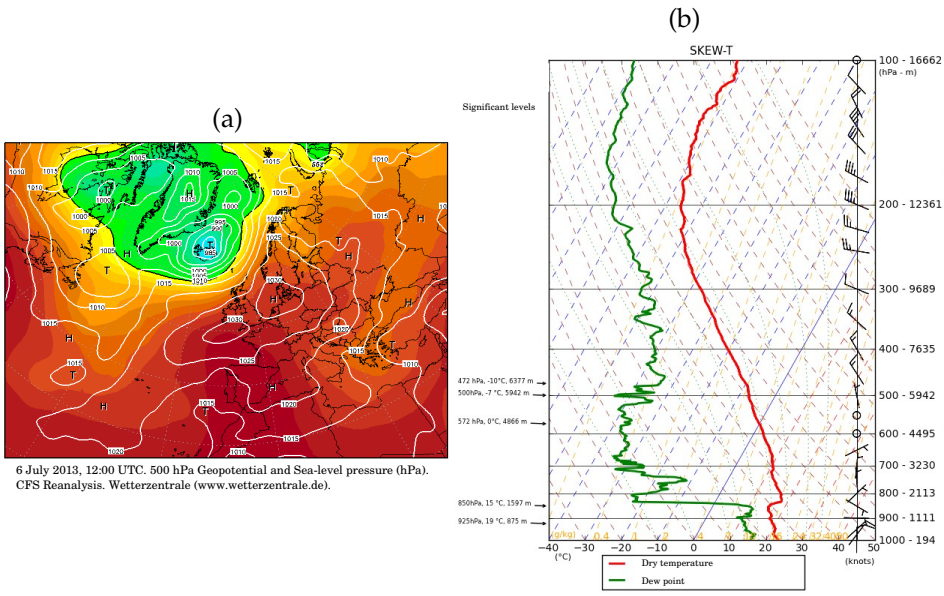

Figure 3.3: (a) Sea-level pressure (white lines) and geopotential height (contours) at 500 hPa from CFS (Climate Forecast System) Reanalysis (Wetterzentrale), and (b) Upper-air sounding from Arteaga (EUSKALMET) on the 06/07/2013 at 1200 UTC.

The observed vertical profile from the radiosonde is compared to the simulated profile in Fig. 3.4. The configuration of the model is shown in Table 3.1, with the YSU ABL scheme and without considering the nudging option for this particular event. The simulated period begins on 5 July at 0000 UTC and finishes on 7 July at 0000 UTC (the first 24 h correspond to the spin-up time). The observed wind vectors are plotted every 100 m (except for the value closest to the surface, i.e. at 28 m), and the simulated wind vectors at the vertical levels of the model up to 2500 m. The observed temperature profile shows an inversion roughly between 100 and 200 m asl, indicating the top of the TIBL. From the simulated near-surface temperature we infer that the model does not reproduce the observed surface heating properly, and partly as a result, the TIBL is not adequately reproduced. Besides, the SB direction is not well represented: the reported wind is from the N-NW close to the surface whereas a NE wind is simulated. Furthermore, between the observed temperature inversion at 1100 m and the subsidence inversion at 1700 m, a layer of E/SE wind in observed, which complies with the definition of the return flow in the SB circulation cell. However, this offshore-wind layer could be also linked to slope flows induced by the complex terrain, as observed by other authors (Banta et al., 1993). The model simulates an E/SE flow as well but significantly below (at between 500 and 1200 m).

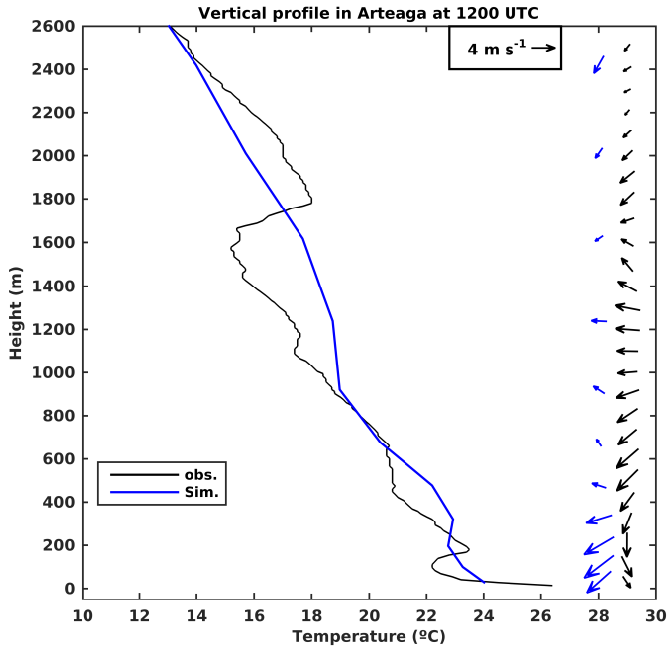

Figure 3.4: Vertical profiles of temperature and wind vectors in Arteaga, on 06/07/2013 at 1200 UTC. Observations are represented in black and the simulation in blue. The observed profile corresponds to that from Fig. 3.3.

We compare the observed and simulated wind vectors and temperature at the surface meteorological stations of Sondika and Azpeitia in Fig. 3.5. These variables are represented for the daytime period (0600–2100 UTC), when the SB onset and termination occur. In the early morning when the land-sea temperature gradient is negative in Sondika (Fig. 3.5b: observed temperature over the Bilbao-Vizcaya buoy is greater than in Sondika) or still slightly positive, a light (~1-2 m s^{-1}) LB from the SE blows in this location coinciding with the axis-direction of the valley (Fig. 3.5a). This LB, however, is not reproduced by the model (in blue) due to the positive land-sea temperature gradient. In fact, the simulated air temperature over the sea has a significant negative bias (of roughly 3 °C). Temperature in the model is calculated at 2 m asl while observations at buoys are recorded at 3 m asl, but this does not explain the large bias (Fig. 3.5b). During daytime, however, the temperature over land is also underestimated by the model and therefore the bias of the simulated land-sea temperature gradient decreases.

The SB onset occurs around 1000 UTC in Sondika, identified by the NW wind direction and the slowing down in the temperature increase. A similar SB onset time is observed in the work of Jiménez et al. (2016a) in the island of Mallorca (Spain). In that work they analyse the morning transition between the LB and the SB and they

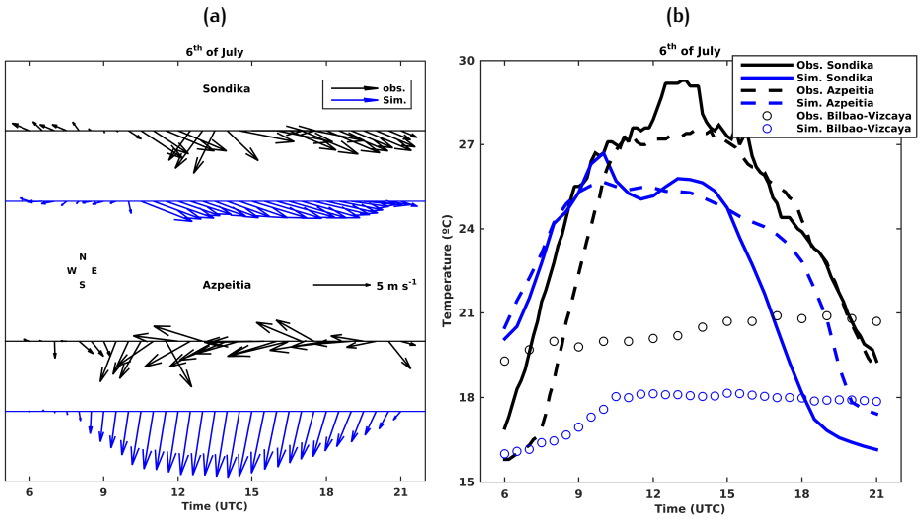

Figure 3.5: Observed and simulated wind-vector and temperature evolution on the 06/07/2013 from 0600 to 2100 UTC. (a) 10-m wind vectors: observations in black and simulation in blue. (b) Air-temperature evolution: the solid curve represents the 1.5-m temperature in Sondika, the dashed curve in Azpeitia and the circles at the Bilbao-Vizcaya buoy. Simulated values at 2 m are shown in blue. Observed wind vectors are plotted every 30 min.

obtain that the SB onset occurs approximately 4 h after sunrise. In the case of Sondika there is a short lapse of time (1200–1330 UTC) in the early afternoon during which the wind blows from the N-NE, producing a temperature increase of around 2–3 °C. This suggests that it is a SB of different origin (from the NE) that travels over a longer continental surface, and is consequently warmer. The model does not simulate the irruption of this warmer SB. Instead, the wind blows constantly from the NW. Partly for that reason the maximum temperature is significantly lower in the model than in the observations. However, the negative bias also both over the sea and in Azpeitia during daytime suggests that the model is underestimating the temperature probably due to a wrong representation of the surface heating and its influence on the air just above.

In Azpeitia the wind blows from the N-NW prior to the onset of the SB (from the E/NE). At that moment the land-sea temperature gradient is negative or nearly zero, and therefore the N-NW flow is induced by the upslope and upvalley flows formed in the closed valley (Fig. 3.5a). Note that the temperature over the buoy of Donostia is not shown in Fig. 3.5b, since it is very similar to the temperature over the buoy of Bilbao-Vizcaya. This is also the case for the simulated temperature. With the arrival of the E-NE flow temperature stops increasing, indicative of the onset of the SB. The model,

however, does not reproduce the onset of this easterly flow. Instead, it reproduces a wave-like behaviour for the wind speed and a slight clockwise rotation for the wind direction (from the N-NW at the beginning and from the NE in the end). This result indicates that the model does not reproduce the features related to the complex terrain in the region of Azpeitia: the flows induced by the closed valley and their interaction with the SB.

Table 3.4 gives the model-performance scores for this event (calculated considering the period from 0600 to 2100 UTC), and reflects the underestimation of the temperature particularly in Sondika. Wind speed is slightly underestimated as well, but it is significantly overestimated in Azpeitia. Wind direction has a certain deviation from the observations, larger in Azpeitia.

Table 3.4: Values of the statistical indexes used for model validation in the case study (06/07/2013) for Sondika and Azpeitia. Values of the MBE and RMSE have been computed for temperature, wind speed and wind direction. A normalised RMSE ($RMSE_n$) is calculated for the wind direction, i.e. it has the value 0 when the model is equal to observations and 1 when the difference is the largest possible (180°).

LOCATION	Sondika	Azpeitia
Temperature (°C)		
MBE	-2.29	-0.21
RMSE	3.40	2.96
Wind speed (m s^{-1})		
MBE	-0.67	+2.38
RMSE	0.92	2.79
Wind direction		
$RMSE_n$	0.30	0.38

We conclude from the variables represented in Table 3.4 that the WRF model is not able to reproduce properly the influence of the surface heating and the complex terrain on the SB. On the one hand, despite the resolution of the inner domain is of 1 km the topography of the model is smoothed compared to the real one (Fig. 2.2). On the other hand, the influence of the topography at local scale needs to be improved in the model.

Figure 3.6 represents maps with simulated 10-m wind and 2-m temperature in the region of study (zoomed in the inner domain) for 6 July at 0700 UTC (when the SB has already been initiated at the coastline), and at 1400 UTC (when the SB intensity is maximum). Wind vectors at 10 m agl are plotted with 3-km grid spacing, since the horizontal resolution of 1 km in the smallest domain is too high for representing

the whole domain. Contour lines of elevation are plotted every 200 m to represent topography.

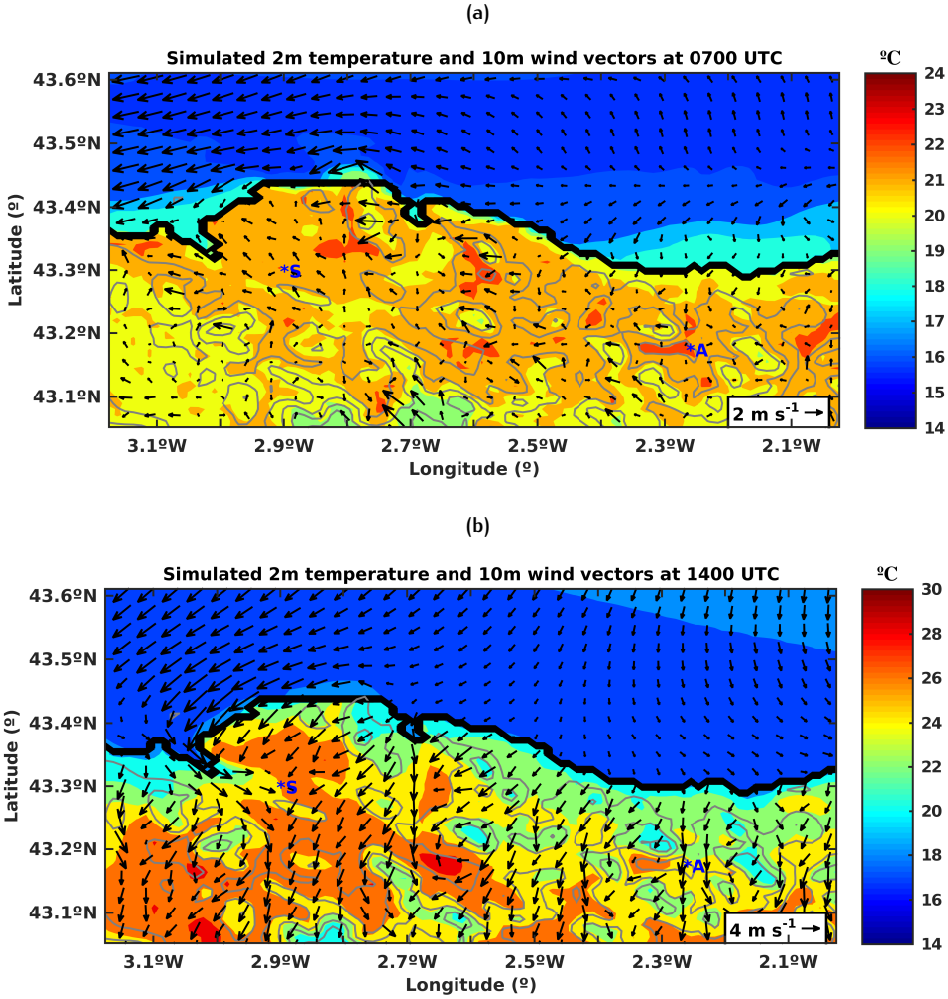

Figure 3.6: Simulated 2-m temperature and 10-m wind vectors in the region of study (zoomed in the inner domain of the model) at 0700 UTC (a) and 1400 UTC (b) on the 06/07/2013. The thick black line delimits the coastline and the thin grey curves represent contour lines of altitude every 200 m. The location of Sondika is represented by "S" and Azpeitia by "A". Note that the temperature and wind-vector scales are different between (a) and (b).

At 0700 UTC the wind blows from the NE over the sea, especially in the western part of the domain and from the SE or almost calm inland (Fig. 3.6a). A light SB is reproduced in some parts of the coast (particularly in the eastern part), which prevents the temperature increase by the incoming fresher air from above the sea. Later at 1400 UTC, the maximum SB intensity is achieved and the onshore flow is extended throughout the area (Fig. 3.6b). The model simulates a rather intense SB blowing from the NE in the coastline located NW of Sondika, parallel to the direction of the shoreline. But when it enters the valley in which Sondika and the city of Bilbao are located it turns to NW and weakens. Furthermore, this NW wind brings cooler air keeping temperatures below 24 °C, whereas temperatures reach up to 26–27 °C to the N of Sondika, where NE winds blow. Hence, this second NE SB system is overheated when penetrates onshore, after overpassing the topography located in its way from the sea. From Fig. 3.5 we stated above how the observations represent the irruption of the NE flow in Sondika in the early afternoon, resulting in a temperature increase. Since the model does not simulate this irruption, it could indicate that the simulated NE SB is weaker than the real one. In Azpeitia the model simulates a N SB blowing with an intensity of approximately 5 m s^{-1}, contrasting to the observed weak SB from the E/NE (Fig. 3.5a). This suggests that the easterly forcing induced by the synoptic situation (see Fig. 3.3a), which helps form the corkscrew SBs, might be underestimated.

As an overall behaviour, the model reproduces the modulation of the wind due to the orography, i.e. it blows along the axis of valleys in an onshore direction and surrounds mountains in its way. Besides, the temperature is lower in valleys in which the onshore flow is channelled, whereas it reaches higher values in valleys in which the onshore flow is weakened due to the presence of mountainous barriers. Furthermore, friction influences the intensity of the SB at the shoreline. The SB is weakened when wind blows perpendicular to the coastline and remains intense when wind blows parallel to it.

To analyse the vertical structure of the SB at both locations, temporal evolution of the vertical profiles of the meridional wind component (N-S), the virtual potential temperature and mixing ratio, and the vertical velocity from the WRF simulation are represented in Fig. 3.7. The magnitude of the N-S component of the wind gives the approximate intensity of the sea SB, since the main component of the onshore flow on the Cantabrian coast is N. The onshore flow is represented in blue, and in red the offshore flow. The arrival of the SB is reproduced at 1000 UTC in Sondika (Fig. 3.7a) and the gravity current associated with the onshore flow reaches a depth of approximately 800 m agl. The termination of the SB is unclear due to the weak intensity of the N-S wind. In fact, the onshore flow is weakened due to the collision of the above-mentioned two SB systems in the region of Sondika: the NW SB and the SB from the NE. The onset of the onshore flow is accompanied by the appearance of a light offshore flow approximately at between 1000 and 1300 m agl (considering the calm-wind zone as well this layer would be slightly thicker). This offshore flow seems to be consistent with the definition of the return flow of the SB circulation and with

the formerly commented observed offshore layer in Arteaga between 1100 and 1700 m (see Fig. 3.4). Furthermore, the onset of the SB in Sondika produces a slight decrease of the virtual potential temperature and an increase of the water vapour mixing ratio particularly noticeable between 600 and 800 m agl. In fact, its vertical gradient above the density current increases significantly. Moreover, the arrival of the SBF generates an increase of vertical draughts. Prior to the onset of the SB, light downdraughts are observed in the first 500 m agl around 0900 UTC (Fig. 3.7e), whereas with the SB onset the collision of marine and continental air masses generates updraughts of up to 0.2 m s^{-1}. Later, downdraughts of the same magnitude are reproduced for a longer time period.

The simulated SB cell in Azpeitia (Fig. 3.7b) is more intense than in Sondika. In addition, the onshore flow is established earlier, approximately at 0800 UTC, and develops its maximum intensity between 1100 and 1600 UTC. The depth of the gravity current reaches hardly 500 m, but it has to be taken into account that the altitude of this region is of around 200 m asl. This value goes along with the ones given by other authors: Lyons (1972) found a mean height of 500 m agl for the density current, but it could extend up to 1000 m agl. In addition, a S wind layer is detected over the maritime flow at between 800 and 1400 m agl. The termination of the SB takes place between 2000 and 2100 UTC. The evolution of virtual potential temperature and water vapour mixing ratio are slightly different from Sondika, mainly due to the altitude difference between both locations. Besides, the arrival of the SBF does not produce significant updraughts in Azpeitia. Instead, a constant and light upward vertical velocity is reproduced during the SB phase due to the influence of the surrounding slopes in the closed valley. At the end of the SB stage, updraughts of up to 0.4 m s^{-1} are simulated at around 500 m agl, while very close to the surface vertical velocity is negative. This can be explained by the development of katabatic flows. Updraughts are caused by the sum of: first, the interaction between the residual SB and katabatics; and second, the convergence of katabatic/downvalley flows at the center of the closed valley (Bodine et al., 2009).

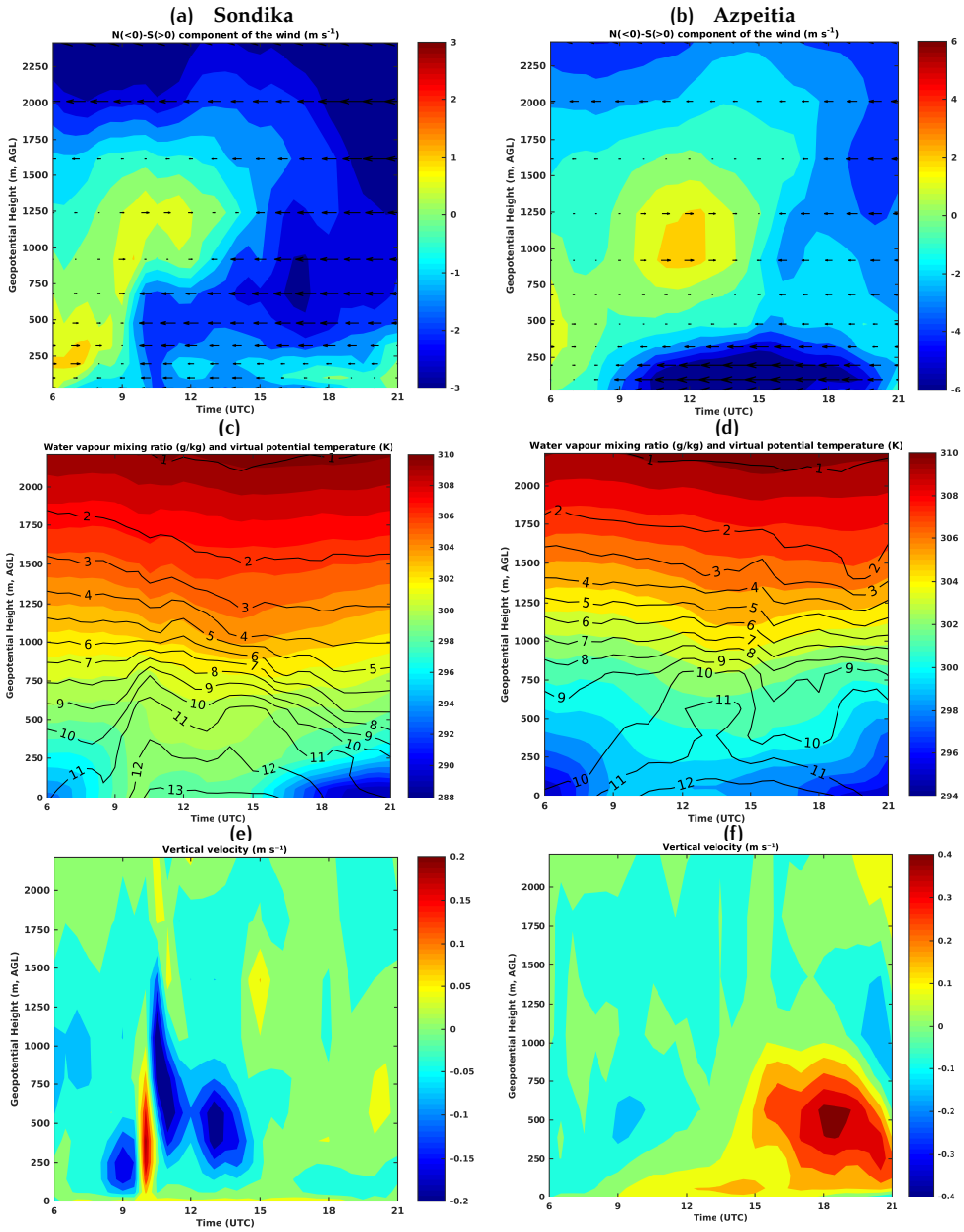

Figure 3.7: Time evolution of the vertical profiles of (a,b) the N-S component of simulated 10-m wind vectors, (c,d) virtual potential temperature (contours) and water-vapour mixing ratio (black lines), and (e,f) vertical velocity, on the 06/07/2013 from 0600 to 2100 UTC . Negative values (blue) correspond to onshore winds and positive values (yellow-red) to offshore winds in (a) and (b).

3.4.3 Anomalous case: 31 July

As explained in Sect. 3.4.1, 31 July passed the selection method erroneously in Sondika due to a shift indication to an offshore wind direction. Further inspection, however, let us classify it as a LSB day: an event in which the onset of the SB occurs after the weakening of the convective mixing in the ABL in the late afternoon. This type of situation occurs when the synoptic flow is offshore (blowing from the S in the Cantabrian coast) and intense enough to prevent the onset of the SB during daytime. However, when the heating of the surface weakens and convective mixing in the ABL disappears, the intensity of the wind decreases while the thermal gradient between air masses is still large, allowing a sudden establishment of the SB. The eastern part of the Cantabrian sea (particularly the Basque coast) is more vulnerable than the western part to warm advections from the Iberian Peninsula in summer, due to the barrier of the Cantabrian Range in the second. In some cases, temperature differences of around 15 °C are observed between both parts of the Cantabrian coast. This generates a mesoscale pressure difference superimposed on the existing synoptic pressure differences, producing a Coastal Trapped Disturbance (Skamarock et al., 1999) that advances and intensifies along the Cantabrian coast. The local name of this phenomenon is *galerna*, famous for the cause of tragedies in this sea. It is characterised by a sudden shift of the wind from S to W/NW with gusts that can exceed 100 km h^{-1}, an abrupt decrease of temperature and an increase of relative humidity, and a prominent worsening of sea conditions. Anyway, this phenomenon is not the focus of this work but one should be careful of not getting confused when studying SBs in the Cantabrian coast.

Figure 3.8 presents reanalysis data and radiosonde observations for this day. Reanalysis maps reveal the presence of a high pressure system over Central Europe and low pressure at the W of Ireland, but the pressure gradient is weak over Spain (Fig. 3.8a). Southerly winds are responsible for the warm-air advection ($>$ 20 °C at 850 hPa) in northern Spain, apparent in the dry-temperature curve (the red one in Fig. 3.8b)) of the radiosonde in Arteaga.

A determinant factor in generating SBs is the formation of a mesoscale low on the Cantabrian coast. In this case study, the presence of a mesoscalar low in the middle Cantabrian coast can be noticed (Fig. 3.8a), which induces a maritime flow in the western Cantabrian and a weak continental flow in the eastern Cantabrian. Despite those conditions inhibit the onset of the SB on the Basque coast, the formation of local and shallow SBs is possible. Indeed, a shallow and weak SB is intuited from the radiosonde of Arteaga (Fig. 3.8b), which shows the existence of an inversion close to the surface in which temperature increases 2 °C with height. Its base is located at 100 m agl, and its top at approximately 350 m agl. Within the upper 100 m of the inversion the wind is very light and turns from onshore to offshore with height. These features can be better identified from Fig. 3.9, in which vertical profiles of observed and simulated temperature and wind vectors at 1200 UTC in Arteaga are compared.

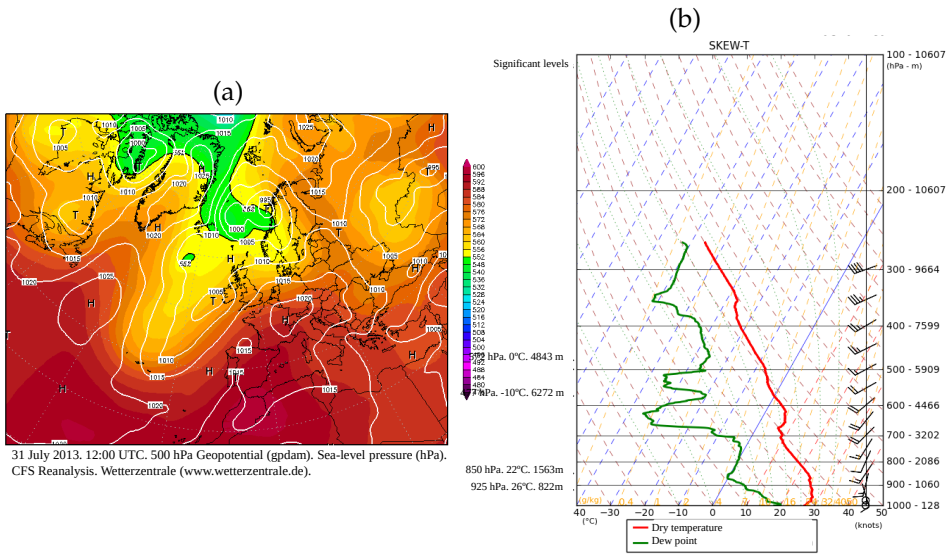

Figure 3.8: (a) Sea-level pressure (white lines) and geopotential height (contours) at 500 hPa from CFS (Climate Forecast System) Reanalysis (Wetterzentrale), and (b) Upper-air sounding from Arteaga (Euskalmet) on the 31/07/2013 at 1200 UTC.

Sensitivity tests with the WRF model provide very useful information about the behaviour of the SB for this case study. The simulated period begins on 30 July at 0000 UTC and finishes on 1 August at 0000 UTC. In Fig. 3.9 the observed radiosonde is shown in black, in blue Sim. 1 (YSU without nudging), in red Sim. 2 (MYJ without nudging), in grey Sim. 3 (YSU with nudging) and in green Sim. 4 (MYJ with nudging). The observed shallow SB in Arteaga is not reproduced by any of the simulations. Furthermore, the model simulates warm S winds and a typically convective thermal profile in the lower atmosphere, contrasting to the observed inversion at 100 m agl due to the light SB (almost calm). Above roughly 500 m agl the model reproduces the observed S-SW wind, even though its intensity is overestimated by the four simulations (particularly close to 2000 m asl). Close to the surface, the two simulations that consider grid analysis nudging (Sim. 3 and Sim. 4) reproduce a lower wind speed than the other two simulations. Hence, the use of the nudging option introduces a non-negligible variability in the wind profile. This result is quite relevant for what is shown below.

Figure 3.10 shows the evolution of wind vectors and air temperature in Sondika, both the observed ones at surface meteorological stations (black) and those corresponding to the four different simulations. The analysis of this anomalous case is not carried out for Azpeitia, since this day is not filtered by the selection method nor is the LSB phenomenon observed.

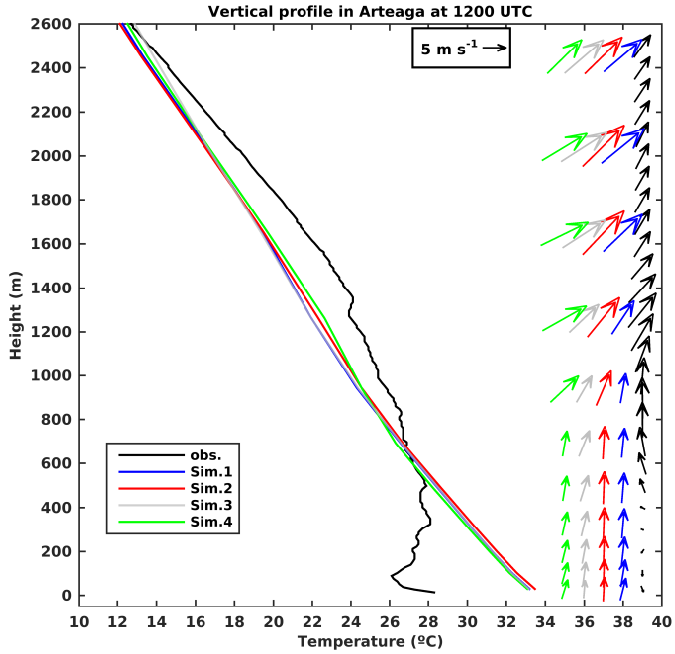

Figure 3.9: Vertical profiles of temperature and wind vectors in Arteaga, on the 31/07/2013 at 1200 UTC. Observations are represented in black and in colours the different simulations: using the YSU ABL scheme and no-nudging (Sim. 1) in blue, MYJ and no-nudging (Sim. 2) in red, YSU and nudging (Sim. 3) in grey and MYJ and nudging (Sim. 4) in green.

A sudden turn of the wind to a light NW (almost calm) can be seen around 1000 UTC in the observations for this day in Sondika (Fig. 3.10a, black), which 30 min. later turns back to SE. That shift is responsible for the incorrect filtering by the selection method. The short-lasting turn is also noticeable in the simulations but a few hours before. During the central hours of the day, S winds blow strong enough to block the onset of the SB, making temperatures reach unusually high values (maximum of 40 °C) as shown in Fig. 3.10b. WRF smooths the temperature curve, simulating lower maximum and higher minimum temperatures than the observations. However, account has to be taken of the different heights at which values are given: temperature observations are taken at 1.5 m whereas the model gives the temperature value at 2 m. This could introduce differences between both, but the weaker cooling during the night in the model, which can be seen in the four simulations, is partly linked to the underestimation of the LB which brings cool air from the land.

On the other hand, the two simulations considering the grid analysis nudging simulate the onset of the SB at around 1300–1400 UTC, several hours prior to the observed

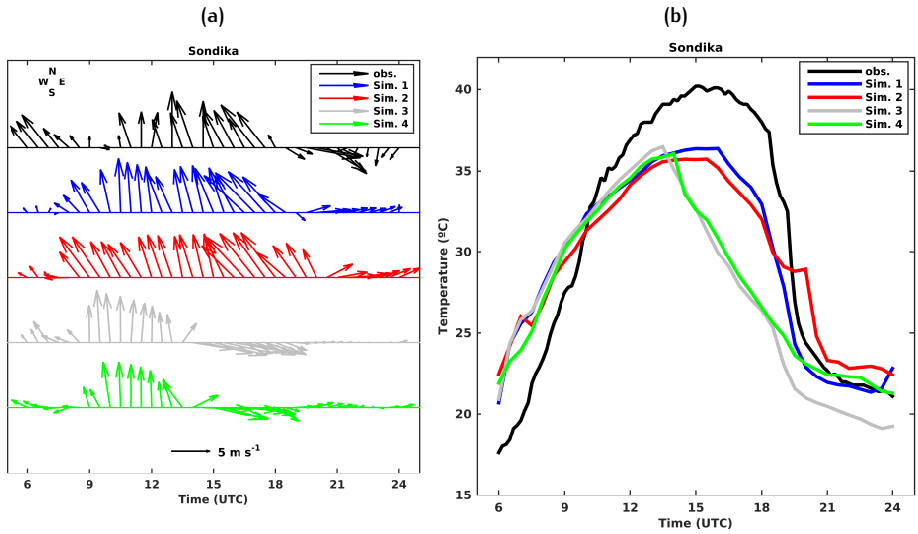

Figure 3.10: Observed and simulated wind-vector (a) and air-temperature (b) evolution, on the 31/07/2013 from 0600 to 2400 UTC in Sondika. Observations are represented in black and outputs from the WRF model in colours: using the YSU ABL scheme and no-nudging (Sim. 1) in blue, MYJ and no-nudging (Sim. 2) in red, YSU and nudging (Sim. 3) in grey and MYJ and nudging (Sim. 4) in green. Observed wind vectors are plotted every 30 min.

LSB onset. That erroneous onset is manifested as an abrupt shift to NW, which makes temperatures descend sharply. Hence, the model stays far from the observations for both simulations (Sim. 3 and Sim. 4). In the observations, the turn to an onshore direction takes place when S winds weaken during the ET of the ABL, allowing the onset of the LSB circulation after 1800 UTC (Fig. 3.10a). The observed wind is weak at the beginning of the onshore flow, but an hour later it intensifies and shifts to W/NW, causing a sharp temperature decrease. This situation is phenomenologically reproduced in Sim. 1 (blue); the onset occurs almost simultaneously and the evolution of the temperature is similar to observations. There is only a slight difference in the LSB direction: NW in observations and W (or even W/SW) in Sim. 1. From wind vectors in Fig. 3.10a it may seem that the final direction is not onshore, but maps of simulated wind and temperature in the region (not shown here) show the marine-air intrusion. Thus, the simulated W/SW wind is due to an issue from the model solving local topography and the wind channelling.

The weakening of the S wind during the ET is hardly noticeable in Sim. 2 (red), and the onset of the LSB occurs around 2000 UTC, when the SBL is already established. Consequently, the evolution of temperature is different from observations. For this

simulation, the LSB is reproduced with a W/SW direction as well. Besides, this simulation reproduces the strongest wind profile at Arteaga (Fig. 3.9). The configuration of Sim. 2, with regard to the ABL and surface-layer schemes, fixes a minimum value of 0.1 $m^2 s^{-2}$ for the TKE. This could explain the overestimation of the wind speed for this simulation.

The skill of the simulations is also evaluated using statistical scores. The values of these scores are computed during the 24 h of the simulations and presented in Table 3.5 for temperature, wind speed and wind direction.

Table 3.5: Values of the statistical indexes used for model validation in the anomalous case study in Sondika. The MBE and RMSE have been computed for the four simulations and for three variables: temperature, wind speed and wind direction (normalised for this variable).

SIMULATION	Sim. 1	Sim. 2	Sim. 3	Sim. 4
Temperature (°C)				
MBE	-0.48	+0.11	-1.82	-1.05
RMSE	2.95	3.47	5.14	4.90
Wind speed ($m s^{-1}$)				
MBE	+0.12	+1.10	+0.13	+0.77
RMSE	1.50	1.98	1.76	1.77
Wind direction				
$RMSE_n$	0.35	0.39	0.43	0.43

The simulation which has lowest errors for the three variables and is consequently closer to observations is Sim. 1. As explained before, it reproduces the onset of the LSB but substantially smooths the temperature evolution (RMSE is close to 3 °C). Simulations that consider nudging simulate a non-observed SB and for that reason the bias increases. From the positive values of the MBE for the wind speed, we conclude that WRF overestimates the wind speed. This overestimation has also been observed by other authors (Papanastasiou et al., 2010; Ponce de León and Orfila, 2013; Román-Cascón et al., 2012). However, the wind profiles shown in Fig. 3.9 demonstrate that the use of grid analysis nudging in the pre-forecast period reduces the overestimation of the wind before the onset of the SB (or LSB in the corresponding case). The weakening of the opposing offshore wind (in Sondika blowing from the S-SE) enables the onset of the SB for the two simulations that consider nudging. In other words, the force that counteracts and blocks the onset of the SB is reduced.

The grid analysis nudging is generally used to force the outputs of the model towards reanalysis data and in this way reduce their bias with respect to observations. However, in our case gives rise to a worse phenomenological simulation of the SB from

the model, and consequently a worsening of model error scores. From these results, it can also be concluded that the limit of opposing wind speed for which the SB is not established is higher in the model than in reality. For that reason, the nudging and other options that modify the outputs of the model should be cautiously used, since they can affect the simulation of certain mesoscale phenomena.

Even though the simulations considering nudging produce an unreal (not observed) onset of the SB in Sondika, they prove to be of high interest since they allow us to study the passage of the SBF by comparison with the simulations not considering nudging, which reproduce a situation closer to observations. In this way, we can explore the influence of the SB in meteorological variables. In addition, simulations with the MYJ ABL scheme (Sim. 2 & Sim. 4) give a turbulent variable: the TKE. Simulations with the YSU and MM5 ABL and surface-layer schemes respectively, do not reproduce significant differences with respect to the MYJ and Eta schemes beyond the above-mentioned ones, and for that reason are not shown hereinafter.

Figure 3.11 shows the evolution of the N-S component of the wind, virtual potential temperature, water-vapour mixing ratio, vertical velocity, TKE and ABL height in Sondika for the simulations with the MYJ ABL and Eta surface-layer schemes. The onset of the SB circulation is observed in Sim. 4 (nudging, Fig. 3.11a) at 1400 UTC approximately. It reaches its maximum intensity 2 h later at 300–400 m agl, but the gravity current extends up to 800–900 m agl due to the existence of a SB head at the frontal part of the density current. After 1700 UTC, however, its intensity and depth decrease substantially. Conversely, in Sim. 2 (no-nudging) the offshore wind prevails during the day, but its intensity decreases after 2000 UTC and allows the establishment of a LSB. This small circulation extends up to only 200 m agl and its intensity is low comparing to a conventional SB.

Virtual potential temperature has been used in several works to detect the presence of the SBF through its horizontal gradient (e.g. Chang et al., 1982; Bechtold et al., 1991; Chemel and Sokhi, 2012). In Sim. 4, a drop of 7–8 K in no more than 3 h indicates the passage of a well-formed SBF (Fig. 3.11c), and at the same time the mixing ratio increases 4 g kg^{-1} at the surface, due to the transition from the typical hot and dry air mass from the Iberian Peninsula to the humid and mild maritime air mass from the Cantabrian Sea. The passage of the SBF produces a transition from a well-mixed to a stably-stratified lower atmosphere. In Sim. 2 the drop of the virtual potential temperature is more abrupt (Fig. 3.11d), but it has to be taken into account that it coincides with night-time and the cooling of the surface. The increase of the mixing ratio is also abrupt: 4 g kg^{-1} in approximately 1 h.

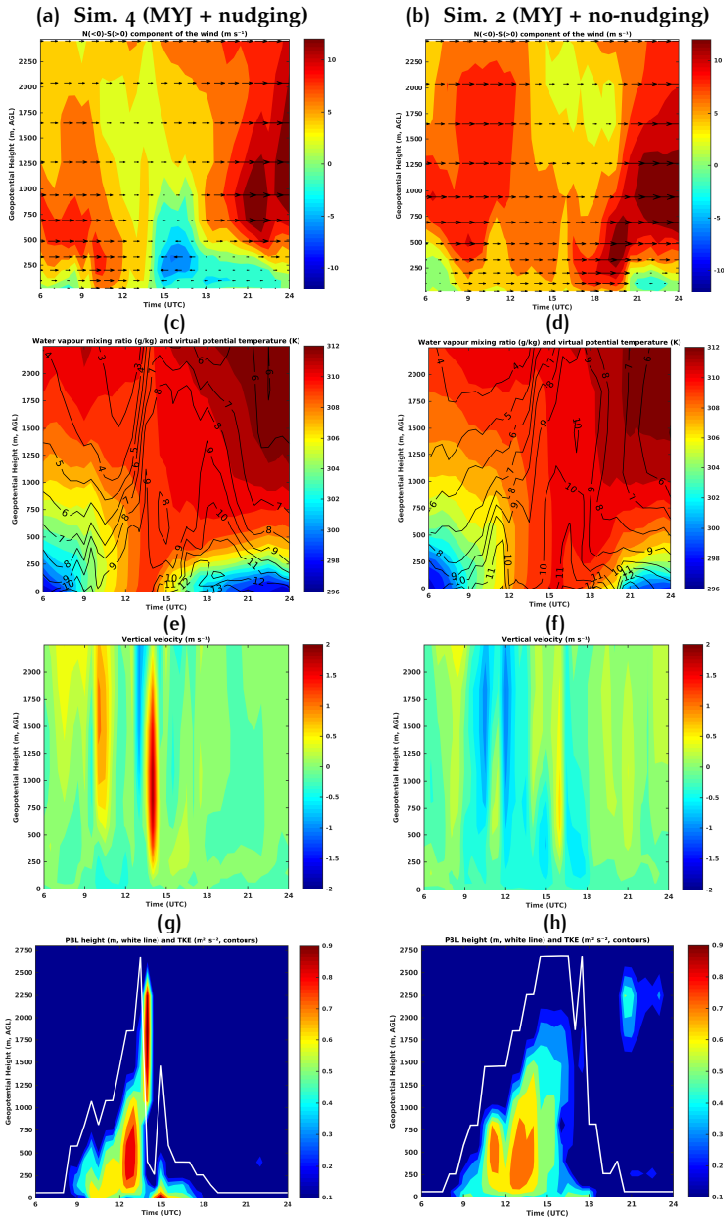

Figure 3.11: Time evolution of the vertical profiles of (a,b) N-S component of simulated 10-m wind vectors, (c,d) virtual potential temperature (contours) and water-vapour mixing ratio (black lines), (e,f) vertical velocity and (g,h) TKE (in contours) and ABL height (white line), in Sondika on the 31/07/2013 from 0600 to 2400 UTC. The outputs correspond to Sim. 4 (a,c,e,g) and Sim. 2 (b,d,f,h).

Additionally, the arrival of the SBF in Sim. 4 is marked by the formation of strong updraughts, with an intensity of up to 2 m s^{-1} at between 500 and 1500 m agl (Fig. 3.11e). Those updraughts are generated due to the collision of the contrasting air masses and their intensity is comparable to that observed in sharp frontal zones with offshore ambient winds (Helmis et al., 1987). After the passage of the SBF, no significant vertical motions are observed, indicating the stabilisation of the lower atmosphere. In Sim. 2, however, the passage of the SBF generates rather weaker updraughts (Fig. 3.11f). On the one hand the intensity of the LSB is much lower; and on the other, the SBL inhibits vertical motions. The intense updraughts of Sim. 4 affect turbulence production too, depicted in the TKE evolution in Fig. 3.11g. The arrival of the SBF produces a TKE generation of up to 0.9 m^2s^{-2} at a height between 1500 and 2250 m agl approximately, related to the above-mentioned updraughts. That increase of TKE lasts for a short time and immediately after turbulence is confined close to the surface, giving more evidence of the breaking down of the CBL. Besides, the MYJ ABL scheme computes the ABL height (white line) considering a TKE threshold (see Sect. 2), and for that reason, a sharp decrease of the ABL height is observed with the arrival of the SBF. In Sim. 2, instead, the CBL is maintained until its typical diurnal end, with the ABL depth being greater than 2000 m agl (Fig. 3.11h). With the onset of the LSB, in contrast to Sim. 4, turbulence is not confined at the surface, but is slightly generated at between 2000 and 2500 m agl.

Finally we analyse the differences in the SH and LH fluxes between a scenario with the SB (Sim. 4, MYJ + nudg.) and another with the LSB (Sim. 2, MYJ + no-nudg.) in Fig. 3.12. We did not include the simulations with the YSU ABL scheme; on the one hand, in Fig. 3.11 we only compare the simulations using the MYJ scheme and on the other hand, the values of the fluxes are very similar. The difference between the magnitude of both fluxes is noticeable: the maximum of LH is close to 600 W m^{-2} whereas SH does not exceed 70 W m^{-2}. We calculate the ratio between them, i.e. the Bowen ratio (β), and its value is slightly greater than 0.1: representative of a tropical-wet-forest ecosystem (Chapin et al., 2011). In the simulations for other SB days (not shown) SH reaches peak values of between 150-200 W m^{-2}, while LH reaches up to 400-450 W m^{-2}. In those cases, β is roughly between 0.35 and 0.5, representative of temperate forest and grassland, i.e. closer to the real ecosystem type. For that reason, the simulated values of SH and LH fluxes for this day are anomalous. Since all simulations use the same surface-physics scheme (Noah LSM, see Table 3.1), the simulated unusual values of the turbulent fluxes for the present case study are not related to soil conditions, but to the warm- and dry-air advection mentioned before, producing an increase of LH and a decrease of SH. The difference between the two simulations is important as well, especially for SH in the afternoon. On the one hand, the establishment of the SB in Sim. 4 increases the value of SH (comparing to Sim. 2) due to the drop of the air temperature. On the other, in Sim. 2 the advected air is warmer than the air just above the surface. Consequently, SH lowers down to negative values (almost -100 W m^{-2} at 1800 UTC) in Sim. 2. The value of LH in Sim. 4 prior to the onset of the SB is around

50 W m^{-2} greater than in Sim. 2. However, the arrival of the SB in Sim. 4 moistens the air, and as a result LH in this simulation decreases and after 1600 UTC is lower than in Sim. 2.

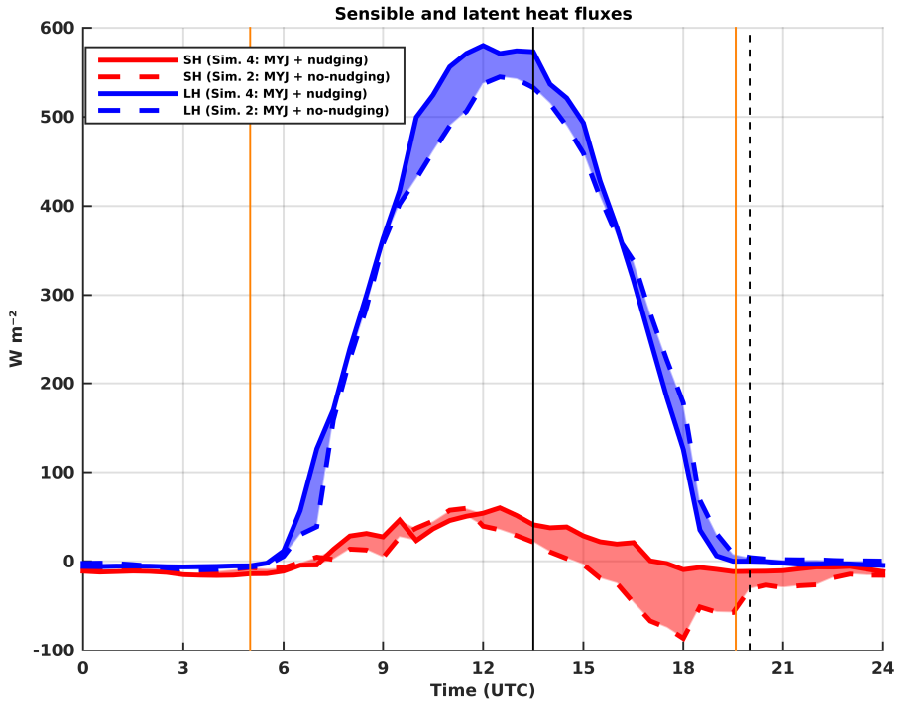

Figure 3.12: Time evolution of SH and LH fluxes in Sondika on the 31/07/2013. Dashed curves correspond to Sim. 2 and solid curves to Sim. 4. Shaded areas represent the differences between both simulations. Orange vertical lines indicate sunrise and sunset times, black-solid line the SB onset for Sim. 4 and the black-dashed line the SB onset for Sim. 2.

3.5 SUMMARY AND CONCLUSIONS

This work analyses SB characteristics on the Basque coast, a region with complex topography washed by the Cantabrian Sea in the North of Spain. Observations from two contrasting locations are employed: Sondika, located in a valley facing the sea; and Azpeitia, in a closed valley. Besides, simulations from the WRF mesoscale model complement the observations.

Two offshore-wind days in Sondika are incorrectly identified by the SB selection method. For that reason, the selection method should be modified for future studies: on the one hand, including an extra filter to assure that the final wind direction is onshore; and on the other, adapting it to reject situations dominated by flows induced by the complex topography or by a strong synoptic forcing.

A SB day selected in both locations is analysed from observations and a simulation with the WRF model. It reproduces the onset of the SB in Sondika, although it does not represent correctly the interaction between the existing two SB systems in the region. In Azpeitia, the model reproduces a SB with a stronger wind speed and a different direction. The main reason for the worse simulation in this location is linked to the misrepresentation of the topography. In fact, the observed closed-valley circulation, a mesoscale phenomena with a smaller length scale, and its interaction with the SB flow are not reproduced. Besides, the comparison of the simulated and observed wind profiles shows that surface heating and its influence on the lower atmosphere are not properly reproduced by the model.

The WRF model is evaluated using four sensitivity experiments for one of the offshore-wind days that passed the selection method incorrectly, which proves to be a LSB day. In general, the temperature evolution is smoothed and wind speed overestimated. The use of the grid analysis nudging reduces the overestimation of the wind speed, but in return gives rise to an unreal onset of the SB. This reveals that the threshold value of the ambient offshore wind that blocks the inland propagation of the SB is higher in the model than in reality. Regarding the ABL scheme and the corresponding surface-layer schemes, YSU + MM5 provides the best results and MYJ + Eta, which uses a TKE closure, fails to reproduce correctly the onset time of the observed LSB during the ET of the ABL.

By comparing SB and LSB situations, we find that the generated updraughts and production of turbulence due to the passage of the SBF are greater when the onset of the SB occurs during diurnal convective conditions. In a LSB event, i.e. when the onset takes place during the ET of the ABL, the stable stratification of the SBL inhibits vertical updraughts and the increase of turbulence. These relationships between the mesoscale flow and turbulence are studied in more detail by exploring a greater number of events over flat terrain in Chapter 4.

To sum up, in this analysis we have learnt about the characteristics of the SB over complex terrain, and their interaction with the MBs induced by that complex orography. In the following chapters, we aim at shedding more light on the interaction between the SB and turbulence during the AET of the ABL. For that, we investigate the SB in an area in which the influence of the terrain in terms of thermal forcing is negligible.

4 IMPACTS OF SEA-BREEZE FRONTS ON LOCAL TURBULENCE AND SCALAR TRANSPORT

We investigate sharp disruptions of local turbulence and scalar transport due to the arrival of SBFs. To this end, we employ a comprehensive 10-yr observational database from the CESAR site. SB days are selected from the mesoscale selection algorithm, that accounts for large-scale conditions and a clear frontal signal associated with the land-sea contrast. Among those SB days (102 in all, 8.3%), based on the value of the SH flux at the SB onset, we identify three ABL regimes: convective, transition and stable. In the convective regime, the thermally-driven CBL is just slightly altered by a small enhancement of the wind shear when the SBF arrives. Regarding the transition regime, we find that the AT of the ABL is accelerated. This is quantified by estimating the contributions of shear and buoyancy to the TKE. Other relevant disruptions are the sharp reduction in ABL depth ($\sim$250 m h^{-1}) and the sudden increase in average wind speed ($>$ 2 m s^{-1}). In the stable regime the arrival of the SB leads to disturbances in the wind profile at the surface layer. We observe a deviation of more than 1 m s^{-1} in the observed surface-layer wind profile compared to the profile calculated using MOST. Our findings furthermore reveal the determinant role of the SB direction in the transport of water vapour, CO_2 and ^{222}Rn. The return of continental air masses driven by the SB circulation generates sharp CO_2 increases (up to 14 ppm in half an hour) in a few SB events. We suggest that the variability in ^{222}Rn evolution may also be influenced by other non-local processes such as the large-scale footprint from more remote sources.

The main contents of this chapter are published in:
Arrillaga, J.A., Vilà-Guerau de Arellano, J., Bosveld, F., Klein Baltink, H., Yagüe, C., Sastre, M., and Román-Cascón, C. Impacts of afternoon and evening sea-breeze fronts on local turbulence, and on CO_2 and radon-222 transport. *Q.J.R. Meteorol. Soc.*, 144:990-1011, https://doi.org/10.1002/qj.3252, 2018.

4.1 INTRODUCTION

In the previous chapter, we have shown that over complex terrain the arrival time of the SBF determines how turbulence in the ABL will react to the mesoscale disturbance. However, as highlighted in the introduction of this thesis, little is known about the impact of the SB during the AET of the ABL, and at the same time, how the SBF itself reacts to the complex decay of turbulence that takes place. On the other hand, the application of the objective filtering method from Borne et al. (1998) has revealed some weaknesses, and therefore a new systematic and objective algorithm is developed based on that method, to select SB phenomena unequivocally.

Hence, in this chapter we aim to shed light on the role of the SB during that critical stage within the diurnal cycle of the ABL, studying not just a single, but numerous SB events. To that end, we use a 10-year comprehensive observational database from the CESAR site, and we apply the SB selection algorithm developed in this thesis to those data. Since Cabauw is located sufficiently far away from the coast ($\sim$ 50 km) and in a topographically flat area, it is an ideal site to investigate the role of pure SB phenomena during the AET. Figure 1.2 has been presented in the introduction as an illustrative instance of the challenges of our study. The specific research questions that underlie in this analysis are the following:

RQ 4.1: *What is the impact of the SB on the lower atmosphere under the different ABL regimes? How do the AT and ET respond to the SBF?*

RQ 4.2: *How are the vertical and temporal distribution of scalars affected by maritime air-mass advection?*

OUTLINE We first describe the comprehensive database employed in Sect. 4.2. Section 4.3 discusses the main features of both local conditions and SB phenomena in Cabauw. Section 4.4 analyses the response of the ABL to the SB and quantifies the interaction with local turbulence for the different ABL regimes. In order to complete the dynamic description, the impact of the SB on scalar distribution is assessed in Sect. 4.5. We finish with the main conclusions of this analysis.

4.2 OBSERVATIONAL DATA

This study is based on a detailed analysis of 10 years of measurements from the CESAR site. We focused on the warm period (May, June, July and August), since in these months the local forcings and mesoscale have a more noticeable influence in the ABL (Jiménez et al., 2016b). Table 4.1 gathers the measured variables explored in this work, specifying the measurement devices employed, vertical levels and periods. For further

information about technical aspects and other specifications of the CESAR site we refer the reader to Bosveld (2017).

Table 4.1: Technical specifications about the measured variables and fluxes employed in this thesis. Within the whole analysed period some instrumentation changes have been carried out (see footnote of the table).

Variables	Height (m, agl)	Instrument	Period
Air Temperature	1.5, 10, 20, 40, 80, 140, 200	KNMI Pt-500 element	01/2001-04/2010
		EPLUSE Pt-1000 element	04/2010-12/2010
Dew point temperature	1.5, 10, 20, 40, 80, 140, 200	Vaisala HMP243	01/2001-04/2010
		EPLUSE 33 polymer sensor	04/2010-12/2010
Wind direction	10, 20, 40, 80, 140, 200	KNMI wind vane	01/2001-12/2010
Wind speed	10, 20, 40, 80, 140, 200	KNMI cup anemometer	01/2001-12/2010
Turbulent fluxes	3	Kaijo-Denki sonic anemometer	01/2001-09/2006
$(\overline{u'w'}, \overline{v'w'}, \overline{w'T'},$	5	Gill R3 sonic anemometer	09/2006-12/2010
$, \overline{w'CO_2'}, \overline{w'q'})$*		IFM open-path sensor	01/2001-11/2005
		LiCor 7500 open-path sensor	11/2005-12/2010
Atmospheric pressure	10	Paroscientific 1016B-01	01/2001-12/2010
Rain	surface	KNMI rain gauge	01/2001-12/2010
CO_2 concentration	20, 60, 120, 200	LiCor-7000 non-dispersive infrared analyser	01/2001-12/2010
Radon concentration	20, 200	ANSTO, two-filter technique	11/2005-12/2010
Aerosol backscatter	surface	Vaisala-Impulsphysik LD-40 ceilometer	**
Radar backscatter	surface	Vaisala LAP-3000 wind profiler	01/2001-12/2010

* The averaging period of the turbulent fluxes is 10 min.
** LD40 ceilometer has been continuously operational only since April 2006 in Cabauw. The CT75 ceilometer in Cabauw and the LD40 ceilometer in De Bilt have been operational during the whole period (01/2001–12/2010). Further details are specified in the text.

One of the novelties in this analysis is the integration of the ABL depth from the estimation of the MLH. First, we analyse the MLH from a 10-year perspective, which is estimated from the aerosol backscatter measured by the LD40 ceilometer, mainly due to its continuing operational availability that provides robust and continuous databases. This device makes use of the Light Detection and Ranging (LIDAR) principle and is generally used to detect cloud bases. Moreover, the MLH can be estimated on the basis of strong vertical falls in the backscatter signal. The methodology employed to estimate the MLH is described in Appendix A. For the SB cases, we employ MLH estimates derived from the radar backscatter profiles measured with the LAP-3000 wind profiler at Cabauw. This is a Doppler radar that is more reliable for detection of the MLH in the case of well-developed CBLs, which occur quite frequently on SB days. Unlike the estimates from the LD40 ceilometer for the 10-years period, the profile es-

timates are manually edited by inspection of the daily time-height radar backscatter data. The methodology employed to estimate the MLH based on the wind profiler is also detailed in Appendix A.

4.3 LOCAL SCALE AND MESOSCALE IN CABAUW

Before studying the complex interplay between the mesoscale phenomena and local turbulence, we first explore the average local conditions in Cabauw during the warm period, followed by the main characteristics of the selected SB events. Following the process of narrowing these down, we filter the clear SBF passages that occurred during this period and we explore their general aspects.

4.3.1 Ten-year analysis of the ABL

We start by evaluating the role of local SH and LH fluxes in the diurnal evolution of the potential temperature θ and specific humidity q (from 1.5 to 200 m) for the warm period of the 10 years, as shown in Fig. 4.1. The 10-year averages are calculated for each of the variables; in the case of the SH and LH fluxes, the averages are computed from series of observations that contain gaps, instead of using gap-filled data. Closely related to the fluxes and state variability, we show the ABL-depth estimation in De Bilt. In this study we employ the ABL depth as the metric that integrates both local and mesoscale effects.

The vertical lines represented in Fig. 4.1a indicate the limits of the three ABL regimes that are defined according to the value of the SH flux in the SB onset. We distinguish between three different ABL regimes: convective, transition and stable. The first is defined when the SH flux at the onset fulfils the following conditions: $H_{\text{onset}} > 0.5H_{\text{max}}$, where H_{max} is the diurnal maximum H value; the stable regime when $H_{\text{onset}} < 0$ and the transition regime in the rest of the cases, i.e. when $0 \leqslant H_{\text{onset}} \leqslant 0.5H_{\text{max}}$. Employing this classification, we explore how the impact of the arrival of the SBF varies depending on the local-turbulence conditions. Prior to that analysis, we study the mean local conditions in Cabauw within the warm period, i.e. before filtering for the SB days.

First, the SEB in Cabauw is mainly radiation-limited due to the moisture surplus: the average β reaches a value of $\simeq 0.35$ (Chapin et al., 2011), typical of irrigated grasslands, at the moment of maximum heating. The soil is very wet in the area of Cabauw and during the warm period a substantial evaporation ($\text{LH}_{\text{max}} \sim 200$ W m^{-2}) takes place. The LH flux begins to increase before both SH and buoyancy fluxes are positive: thus, specific humidity (Fig. 4.1c) starts to increase before θ rises (Fig. 4.1b). Moreover, the evaporated water is mixed within a shallow boundary layer until 2–3 h after sunrise, which explains the morning peak observed in the specific humidity at around 0700

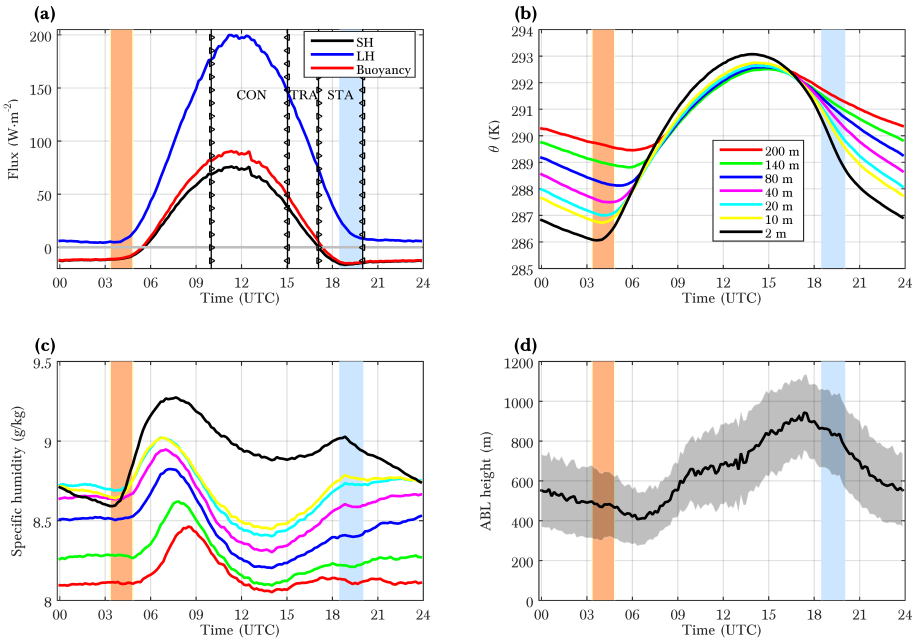

Figure 4.1: Ten-year mean of the diurnal evolution during the warm period (MJJA) of (a) the surface SH, LH and buoyancy fluxes; (b) potential temperature at the different vertical levels; (c) specific humidity at the different vertical levels and (d) estimation of the MLH in De Bilt and its standard deviation (shaded). Only detections with a weak or good quality index are selected for the estimation of the MLH. Shaded vertical bars indicate the sunrise and sunset time ranges for MJJA, in orange and blue respectively. Vertical lines with triangle markers in (a) delimit the SH values for the three ABL regimes defined in Sect. 4.3 (convective, transition and stable). Local summer time is UTC + 2.

UTC at lower levels. Later on, when thermal turbulence is strong enough to produce convection and the growth of the ABL, drier air from higher levels is entrained. The maximum value of the surface heat fluxes is recorded at around 1200 UTC.

The evolution of the ABL depth is mainly driven by the buoyancy flux and the strength of the capping inversion. However, the MLH measurements from the ceilometer are also influenced by other factors, and the estimation of the ABL depth is therefore more challenging. For instance, during the morning and early afternoon, the signal-to-noise ratio level of the ceilometer is lower than at the end of the day, which explains the significant reduction in the rising trend between 1000 and 1300 UTC (just 50 m in 3 h), in addition to the fact that the ceilometer fails to detect the top of the well-mixed convective layers. In fact, the mean daily maximum MLH lies at around 900 m. The measurement uncertainty for daytime clear-sky ABLs is around 75–100 m (de Haij

et al., 2007). Furthermore, the mesoscale phenomena, in the form of SBFs in Cabauw, have a significant influence on the physics and dynamics of the lower atmosphere in the afternoon and evening, being in a two-way interaction with turbulence.

However, the large-scale forcing masks the arrival of the SBF in many cases, which does not occur on every day of the warm season. On the other hand, the arrival of the SB density current takes place at a different time depending on the day, and therefore the time averages do not capture the real effect of the SB. We therefore need to conduct an objective and systematic SB filtering by using the algorithm described in Sect. 2.3.3. This method enables us to disentangle the clear mesoscale frontal passages independently, as well as their impact on the ABL. Once we have identified the onset of the SB, we group the different events together, taking the arrival of the SBF as a reference.

4.3.2 SB phenomena

We first present the performance of the systematic algorithm in selecting the SB events (Table 4.2) by showing the percentage of the total number of days that pass each of the filters. The specific SB criteria of each of the filters are described in Table 2.2. Moreover, Fig. 4.2 displays the wind roses at two times of day for each day that passed the individual filters of the algorithm: 1200 UTC and 1800 UTC. The first time is chosen for two reasons: it is roughly the time at which LH and SH fluxes have their maximum values and additionally, in most of the cases the SB onset has not taken place yet at Cabauw. With respect to the second time, it is close to sunset (the average SH flux is negative at this moment) and the SBF passage has already occurred in most of the cases.

Table 4.2: Performance of the SB algorithm when applied to the 10-year observational database. First column indicates the filter number; second column, the physical justification of each of the filters; and third column, the absolute percentage of the days that pass each of the filters. From a total of 1230 days entering Filter 1, 102 days finally passed Filter 5. See Sect. 2.3.3 for description of the criteria.

Filter	Physical justification	Acceptance percentage (%)
1	Weak large-scale winds	31.1
2	No synoptic cold fronts	26.5
3	Non-rainy events	21.7
4	Thermal contrast	17.0
5	Marked veering to an onshore direction	8.3

The wind roses before the filters were applied are shown at the top of Fig. 4.2. The 10-m wind measurement is employed. At 1200 UTC the predominant direction is SW, which is climatologically the most frequent and synoptically influenced (Sluijter

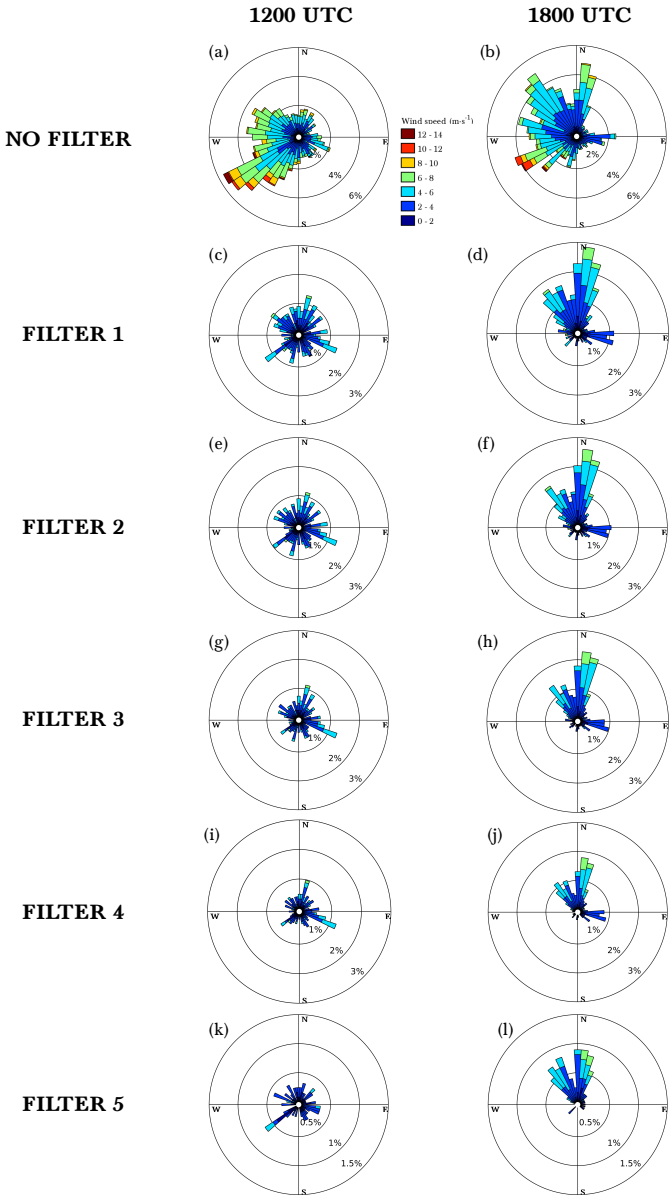

Figure 4.2: Wind roses for the warm period (MJJA) after application of each filter, at 1200 UTC (left) and 1800 UTC (right). The scale of the circles represents the percentage of days from all the days that fell within the study period.

et al., 2011). However, there is a clear predominance of all the westerly winds, which are affected by the sea-land temperature difference. It is likely that at this stage, the near-coastal diurnal acceleration (NCDA) introduced in Jiménez et al. (2016b) accelerates the W component of the wind. A complete analysis of the contribution of the mesoscale phenomena in the wind diurnal variability was discussed in their study, but focusing on the NCDA. Jiménez et al. (2016b) analysed the rapid propagation of the inland wind-shift in the morning, which is directly related to the growth of the ABL onshore. However, we focus here on a distinct mesoscale phenomenon: sharp/clear SBF passages characterised by significant contrasts of temperature, humidity and wind speed, which are associated with the sea-land temperature gradient and take place in the afternoon/evening.

As shown in Fig. 4.2b, two main wind directions emerge at 1800 UTC: NW and N-NE, which are linked to the two main SB directions. Filter 1 leads to many days being discarded (~ 69%), since The Netherlands is usually affected by large-scale perturbations throughout the year. Of the days that remain, most of them show a wind direction linked to either one of the two above-mentioned SB directions at 1800 UTC (Fig. 4.2d). At 1200 UTC, most of the SW-flow occurrences are excluded, and there is no any main direction at this time. After applying all the filters, we end up with 8.3% of the total amount of days being pure SB days, 102/1230 in total.

As stated, two main directions characterise the SB phenomena in Cabauw: NW and N-NE. Given the geographical location of Cabauw (see Fig. 2.3), the former originates in the North Sea whereas the second seems to come from the closed Markermeer and IJsselmeer Seas. However, according to the satellite-derived SST, the latter seas are significantly warmer than the North Sea, and are therefore less prone to the formation of SB circulations. This suggests that the N-NE SBs are probably generated in the North Sea (N of the IJsselmeer) and subsequently propagated over these closed and shallow seas. On the other hand, the two SB directions are driven by different large-scale pressure patterns: for instance the N-NE SB develops under a high-pressure system over the N of the Netherlands, which induces a E-NE flow. The synoptic horizontal pressure gradient is therefore primarily responsible for the different SB directions.

Figure 4.3 shows the time of onset histogram of the SB for the filtered days, in coloured bars for the different months, and in black lines for the different wind directions just after the SB onset. Most of the SB passages take place between 1400 and 1900 UTC. This means that our dataset is adequate to study the role of the SB during the AET. In fact, the AT lies within the above-defined transition regime (SH $>$ 0), and the ET within the stable regime (SH $<$ 0). Moreover, the distribution of onset times differs from month to month. First, June is the month with the highest number of SB days (35% of the warm period), followed by July (26%), May (23%) and August (16%). June and July have longer periods of daylight, and they present a clear increase in the time of onset of the SB from 1500 to 1600 UTC onwards. In contrast, in August and particularly May, the increase is less clear and the differences between the time-range

frequencies are smaller. On the other hand, the clear increase in the frequency of arrival of the SBF between 1400 and 1900 UTC could be a consequence of the acceleration of the inland propagation of SBFs that takes place in the late afternoon/early evening due to reduced convection, as has been suggested by some authors (e.g. Atkins and Wakimoto, 1997; Crosman and Horel, 2010). In any case, since we only analyse measurements at Cabauw that issue is not addressed in this study.

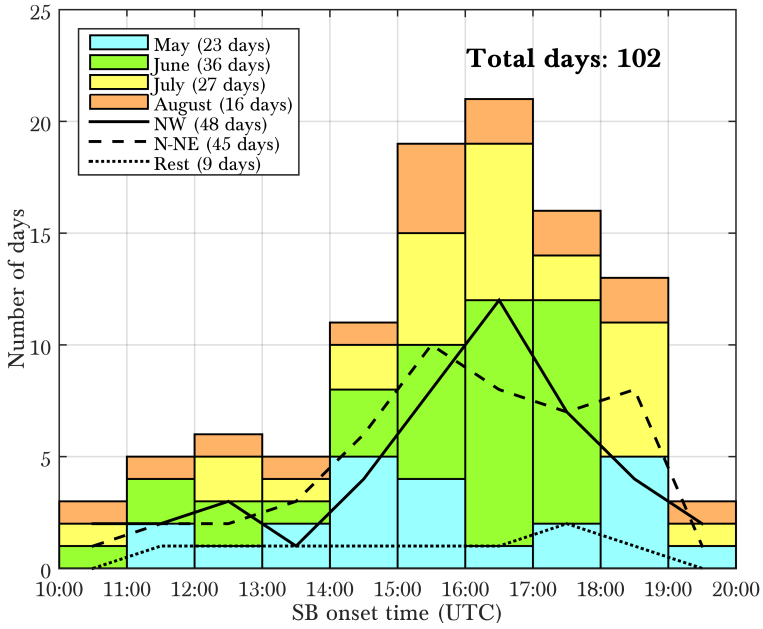

Figure 4.3: Histogram of times of onset of SB for the individual months (bars) and SB directions just after the onset (lines). The range for defining NW SBs is [290°–350°] and for N-NE SBs, [350°–45°]. The other directions are included in the 'Rest' group.

We separate the wind direction just after the onset into three different categories: NW, when it lays between 290° and –350°, N-NE between 350° and –45° and the latter value for remaining events (mainly W-SW). In 47% of the cases the wind blows from the N-NE, from the NW in 44% and 9% from other directions in the remainder. For the SB events in which the onset occurs with the wind from the N-NE or NW, we find a clear frequency increase for the aforementioned time range (1400–1900 UTC). The remaining events are almost equally spaced along the hours of daylight. There is a secondary peak in the N-NE SB distribution between 1800 and 1900 UTC which may be due to the Coriolis force, but at the same time the frequency of N-NE SBs is higher than the NW SBs between 1000 and 1300 UTC. Hence, although the influence of the Coriolis force in veering the wind clockwise has been reported in a few studies (Miller

et al., 2003), we do not have enough evidence to support that statement and the role of Coriolis is still unclear.

The wind roses at 10 and 200 m agl at the moment of the SB onset are shown in Fig. 4.4. The most intense SBFs at 10 m are those coming from the NW, which squares with the fact that the SST of the North Sea is colder than those of the inland seas (see Fig. 2.3). However, at 200 m the wind rose shows strong SBFs from the NE (with a wind speed of up to 7–9 m s^{-1}), particularly between 22.5° and 45°. Furthermore, in a few cases the wind direction was offshore, i.e. between 45° and 225° at that height, indicating that while the SBF had reached the level of 10 m, it had not yet arrived at 200 m.

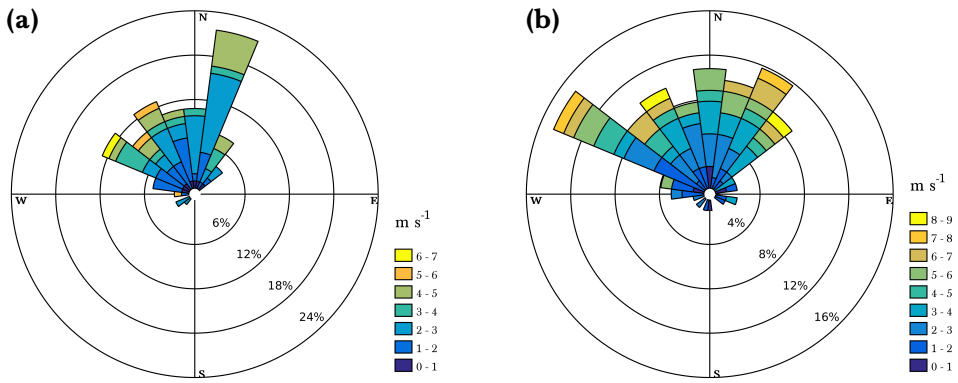

Figure 4.4: Wind roses of the wind speed at (a) 10 m agl (a) and 200 m agl (b) at the moment of the SB onset. The scale of the circles represents the percentage of days out of the total number of SB days.

Despite the peak of SB events occurring during the afternoon/evening, the onset of mesoscale fronts takes place under distinct ABL regimes, which are defined at the beginning of this section. The onset of SBs may occur either when the SH flux is around its maximum value (convective regime), when it is decreasing (transition regime) or even when it is already negative (stable regime). A chart showing the distribution of the SB events in the three regimes is shown in Fig. 4.5. In Sect. 4.4 we analyse how the SBF impacts the ABL for the different regimes and we focus particularly on the challenging interconnection with local turbulence. Finally in Sect. 4.5 we explore another important aspect of the SB phenomenon: the impact of the different directions of the SBs on the advection of relevant state variables such as potential temperature and specific humidity, and scalars like CO_2 and ^{222}Rn.

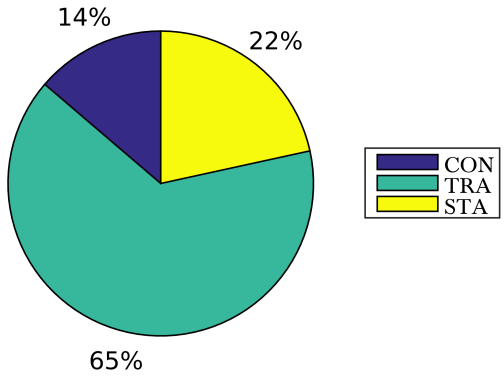

Figure 4.5: Percentages of the three ABL regimes for the occurrences of SBs: convective regime (CON), transition regime (TRA) and stable regime (STA).

4.4 SEA BREEZE–TURBULENCE INTERACTION IN THE ABL

Before dealing with the complex mesoscale-microscale interactions under each of the ABL regimes, we investigate the effect of the arrival of the SBF on the dynamic aspects of the ABL.

4.4.1 How does the ABL respond to the arrival of the SBF?

Figure 4.6 shows the impact of the SBF on the wind speed (a), potential temperature (b), specific humidity (c) and ABL depth (d) for the three ABL regimes. For each of the regimes, we represented the mean of all the events normalised with respect to the onset of the SB. With t = 0 being the first post-onset measurement, negative abscissa values indicate pre-frontal time, while positive values identify post-frontal measurements. First, the wind speed confirms that the algorithm is capable of filtering out clear SBFs. It is interesting to observe that, during the short delay before the arrival of the SBF, a slight reduction in wind speed occurs due to the collision of the continental and maritime air masses, which is particularly evident in the convective regime. Under this regime, indeed, the trend of increasing wind speed is slightly altered by the SBF and the wind shear between the observational levels displays a slight increase. The change in the trend is evident in the potential temperature and even more so in the specific humidity. Before the SBF passage, q diminishes as convection entrains drier air from above the ABL; after the onset of SB, however, a moister air mass is advected and its value increases by over 0.5 g kg^{-1} in 10 min, especially at lower levels.

The behaviour of the lower atmosphere under the other two regimes is different. Under the transition regime, the wind speed after the SBF undergoes an abrupt increase particularly at higher levels, from less than 3 m s^{-1} up to more than 5 m s^{-1} within 2

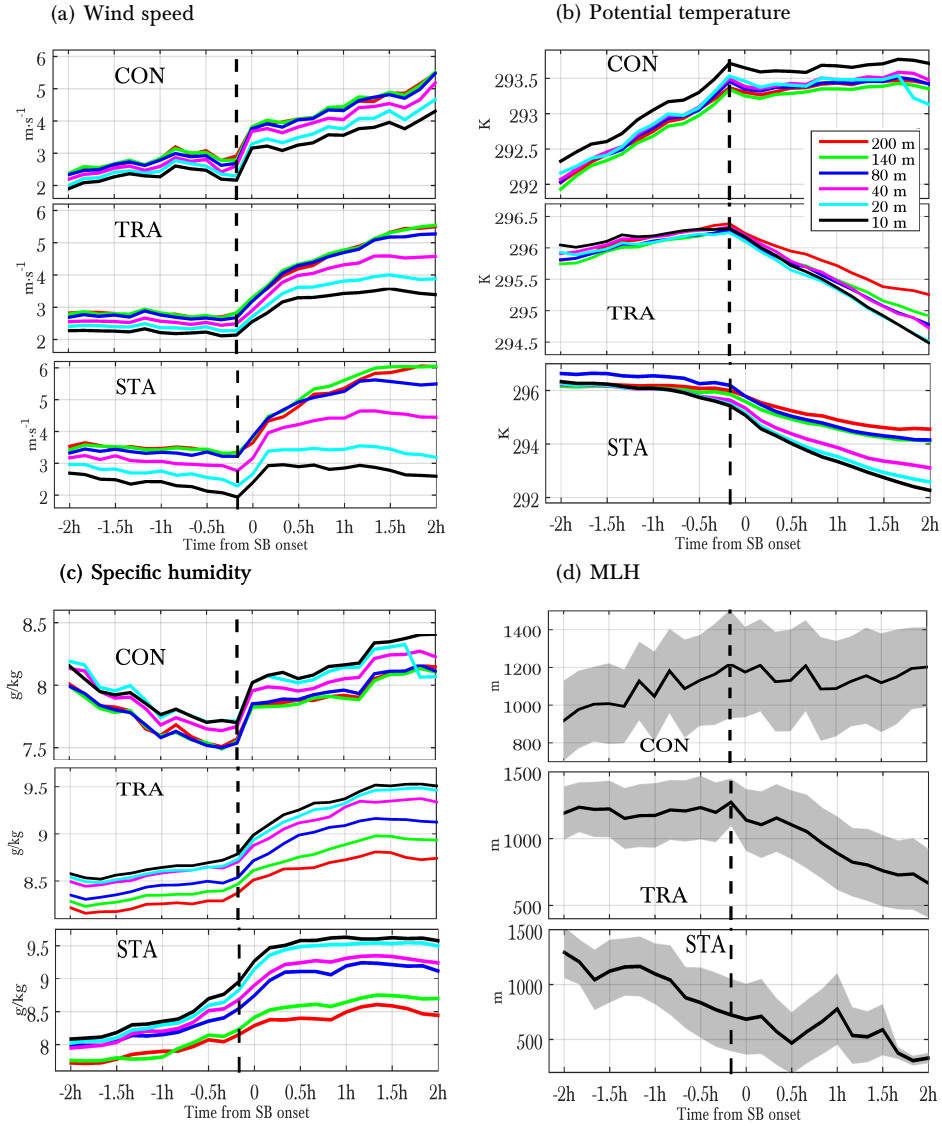

Figure 4.6: Evolution in time of the average (a) wind speed, (b) potential temperature, (c) specific humidity and (d) MLH between 2 h before and 2 h after the onset of SBs for each of the ABL regimes. The mean for each regime was calculated normalising all the events with respect to the SB onset. The dashed vertical line identifies the 10-min measurement just before the onset; thus, the onset of SBs occurs between the dashed line and time = 0.

h. The most significant aspect, however, is the rapid increase in shear after the SBF: the difference between 10 and 200 m is less than 1 m s^{-1} before the onset and slightly over 2 m s^{-1} 2 h later. We perform a more thorough quantification of the shear term in the following subsection. Moreover, the evolution of the potential temperature for this regime shows the transition from unstable to nocturnal stable conditions (from $\Delta\theta_{200\text{-}10} \simeq 0$ K before the SB onset to $\simeq 1$ K 2 h after it), and the stratification of the specific humidity increases as well (from $\Delta q_{10\text{-}200} \simeq 0.45$ g kg^{-1} before the onset to $\simeq$ 0.8 g kg^{-1} 2 h after it). This suggests that the arrival of the SBF produces an acceleration of the ABL AT (SH > 0). Within the stable regime, however, the ABL ET (SH $<$ 0) is also evident from the clear stratification of all the variables until the typical NBL conditions are clearly met (see for instance Figs. 4.6b-c 2 h after the arrival of the SBF). Nevertheless, the rise in wind speed particularly at higher levels (80, 140 and 200 m) prevents the formation of a highly stable NBL. In order to determine whether those features were actually due to the effect of the SB or were merely aspects of the ET under the stable regime, we compare SB and NSB days in Sect. 4.4.2.

With respect to the ABL depth (Fig. 4.6d), which is regarded as the variable that integrates local and non-locally forced processes, we infer it from the estimates of the MLH derived from LAP3000 wind profiler/RASS after a thorough manual editing. The passage of the SBF usually tends to result in a decrease in the MLH, while at the convective regime the MLH displays a sudden change in trend, evidenced by zero growth or even a slight fall after the SB onset. The effect of the SB is more evident under the transition regime, in which the MLH decreases substantially after the onset ($\sim$ 250 m/h), further reinforcing the hypothesis regarding the acceleration of the AT.

4.4.2 Quantifying the interaction with local turbulence

We now explore the complex interaction between mesoscale and local turbulence by employing scaling arguments appropriate for each ABL regime. We particularly stress the way in which the onset of the SB alters the transition to nocturnal stable conditions, depending on the degree of stability that the lower atmosphere has already reached.

We first present Fig. 4.7, which shows the response of local surface turbulence to the passage of the SBF. The buoyancy flux, which is the measurement of the sonic-temperature flux, is displayed in (a), and the CO_2 surface flux in (b). We also include u_* (c), and the TKE and the variance of the vertical component of the wind (σ_w^2) in (d). u_* is derived from the 10-m wind speed, the measured SH and the wind-direction dependent roughness length (Beljaars and Bosveld, 1997; Verkaik and Holtslag, 2007).

Both the buoyancy and the CO_2 fluxes are scarcely affected by the onset of SBs. Only in the stable regime does the trend appear to be slightly altered by the SBF, producing a sharper decrease in the buoyancy flux. On the other hand, u_*, TKE and σ_w^2 are affected by the passage of the front. For instance, u_* falls before the arrival of the SBF, particularly in the convective regime (Fig. 4.7a). As we have already observed for the evolution of the wind speed (see Fig. 4.6a), the collision of the maritime and

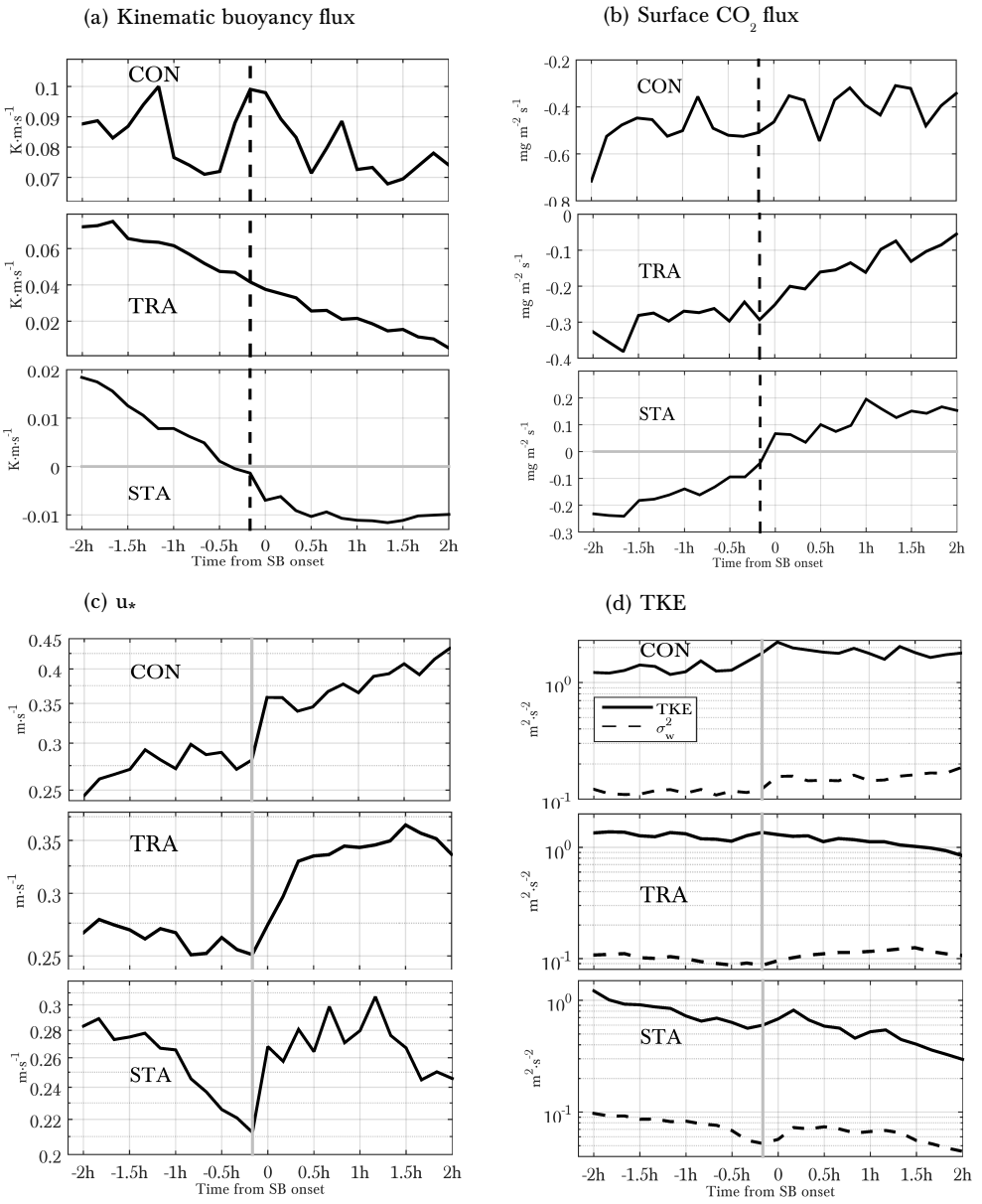

Figure 4.7: Evolution in time of the average (a) kinematic buoyancy flux, (b) surface CO_2 flux, (c) u_* (d) TKE and σ_w^2 between 2 h before and 2 h after the onset of SBs under each of the ABL regimes. The onset is indicated by dashed black vertical lines in (a) and (b), and solid grey vertical lines in (c) and (d).

continental air masses produces a moment of calm. After the passage of the front, u_* undergoes a sudden increase, especially under the stable and transition regimes: in the latter it increases by 40% within 2 h, and in the stable regime, it increases almost by 50% in 1 h, but decreases just afterwards. The TKE rises after the front, partially due to the increase in the vertical component σ_w^2 (Fig. 4.7d). For example, the latter increases from 5 x 10^{-2} to 7 x 10^{-2} m^2 s^{-2} in the stable regime and from 12 x 10^{-2} to 16 x 10^{-2} m^2 s^{-2} in the convective regime just after the onset.

Assuming horizontal homogeneity and zero subsidence, the governing equation of the TKE (= $\overline{e}$) takes the following form (Stull, 1988):

$$\frac{\partial \overline{e}}{\partial t} = \frac{g}{\theta_v}(\overline{w'\theta_v'}) - (\overline{u'w'})\frac{\partial u}{\partial z} - (\overline{v'w'})\frac{\partial v}{\partial z} - \frac{\partial}{\partial z}(\overline{w'e'}) - \frac{1}{\rho}\frac{\partial}{\partial z}(\overline{w'p'}) - \epsilon, \tag{4.1}$$

where the term on the left-hand side denotes the trend, and the terms on the right are, from left to right, buoyancy, shear (two terms), TKE transport, pressure correlation and dissipation.

We have already explored how the surface turbulence is affected, but we lack validated flux measurements at the vertical levels of the tower for our 10-year period. However, based on the first-order closure we can infer the turbulent fluxes at the different levels by calculating the vertical gradients of measured variables:

$$\overline{w'\theta_v'} = -K_H \frac{\partial \theta_v}{\partial z}, \tag{4.2}$$

$$\overline{u'w'} = -K_M \frac{\partial u}{\partial z} \qquad \overline{v'w'} = -K_M \frac{\partial v}{\partial z}, \tag{4.3}$$

where θ_v is the observed 10-min averaged virtual potential temperature and u and v the 10-min mean horizontal wind components. The eddy diffusivities of heat and momentum K_H and K_M depend on the stability of the ABL. Since during the AET of the ABL we are close to neutral conditions, we can assume that both coefficients are constant (Stull, 1988). For our purpose and for the sake of simplicity, we consider both coefficients to be =1. As a result, we obtain alternative buoyancy and shear terms (hereafter referred to as B_* and S_*) along the tower levels:

$$B_* = \frac{g}{\theta_v}\frac{\partial \theta_v}{\partial z}, \tag{4.4}$$

$$S_* = \left(\frac{\partial u}{\partial z}\right)^2 + \left(\frac{\partial v}{\partial z}\right)^2. \tag{4.5}$$

To explore the impact of the SBF and to quantify the acceleration of the AT taking place in the transition regime, we calculate the temporal derivatives of both B_* and S_* as follows:

$$\frac{dB_*}{dt} = \frac{\partial \theta_v}{\partial z}\left(-\frac{g}{\theta_v{}^2}\frac{d\theta_v}{dt}\right) + \frac{g}{\theta_v}\frac{d}{dt}\left(\frac{\partial \theta_v}{\partial z}\right), \tag{4.6}$$

$$\frac{dS_*}{dt} = \frac{d}{dt}\left\{\left(\frac{\partial u}{\partial z}\right)^2 + \left(\frac{\partial v}{\partial z}\right)^2\right\}. \tag{4.7}$$

The temporal derivatives were computed using finite differences, while the vertical gradients of θ_v and the wind components u and v were derived from the method of least squares (see Eq. 2.4). The time-dependent coefficients were estimated at every observational measurement, i.e. every 10 min, and the vertical gradient $\partial\psi/\partial z(z,t)$ was computed at the intermediate levels: 15, 30, 60, 110 and 170 m agl. Since this method is sensitive to missing data (Steeneveld et al., 2005), we did not calculate the coefficients for the cases in which any of the vertical measurements were lacking.

In Fig. 4.8, we represent dB_*/dt (a) and dS_*/dt (b) for the three ABL regimes at three intermediate levels: 30, 110 and 170 m. The 15-m and 60-m levels were excluded from the plot for the sake of simplicity: the first showed larger values than at other levels but its trend was equal to the 30-m level, whereas the second displayed behaviour intermediate between 30 m and 110 m. We also depict the trend of the temporal derivatives through regression lines, both before and after the onset of the SBs. Moreover, by exploring the second temporal derivatives of B_* and S_*, we infer whether the changes in both contributions occurred in an accelerated or decelerated manner. Note that in order to smooth the temporal series, 30-min moving means were employed. Starting with the convective regime, the influence of the SB at higher levels is virtually non-existent. At the lowest level, i.e. at 30 m agl, however, dB_*/dt increases just after the onset, and starts to decrease immediately afterwards. The increasing trend of S_* is positive after the arrival of the SBF, but the dispersion of points implies that this trend is not particularly significant. A further analysis within the convective regime is discussed later.

In the case of the transition regime, the significance of the trends is stronger, particularly for B_*. The onset of the SB represents a minimum in the temporal evolution of dB_*/dt, as its trend is negative before and positive after the onset at the three vertical levels. This indicates that before the onset the lower atmosphere is decelerating towards a more stable state ($d^2B_*/dt^2 < 0$), whereas after the onset that acceleration becomes positive ($d^2B^*/dt^2 > 0$), being slightly larger at the lowest level ($d^2B_*/dt^2 \simeq +8.5\times10^{-6}$ $s^{-3}/1h$). On the other hand, dS_*/dt behaves differently at the lower and higher levels. Before the SB, S_* at 30 m increases at a steady rate ($dS_*/dt \simeq 2\times10^{-5}$ s^{-3}), while it scarcely changes at 110 and 170 m. After the onset of the SB, however, S_* at 30 m increases more rapidly ($d^2S_*/dt^2 \simeq 1\times10^{-4}$ $s^{-3}/1h$). It also increases at the

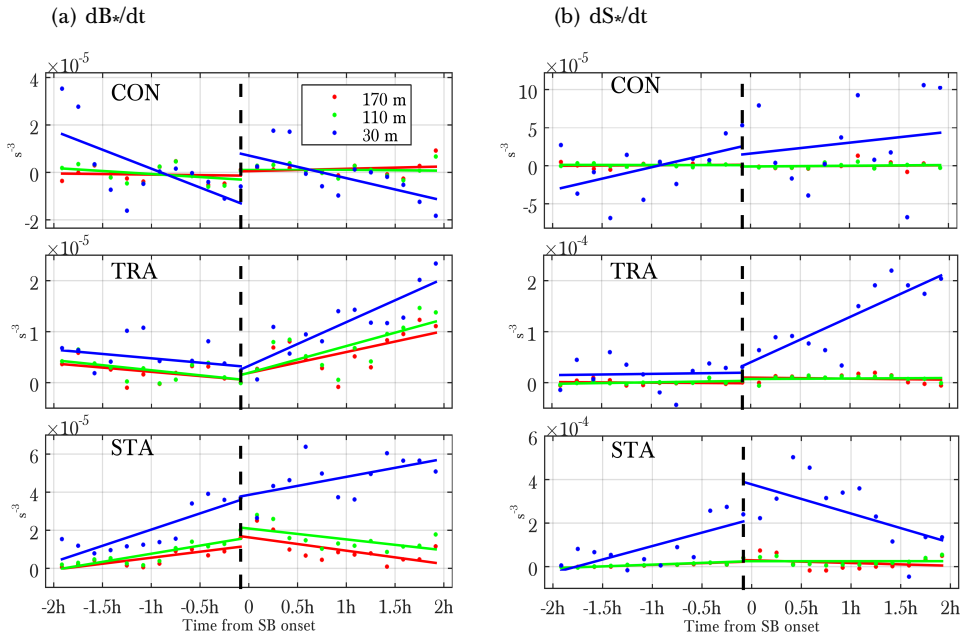

Figure 4.8: Mean evolution of the temporal derivative of B_* (a) and S_* (b) between 2 h before and 2 h after the SB onset for each of the ABL regimes at three intermediate vertical levels. The onset of SBs is identified by a dashed vertical line. Dots represent the mean observed values every 10 min, while the regression lines are included to depict the trend before and after the onset. Note that 30-min moving means were calculated in order to smooth the time series.

higher levels, but at a roughly constant rate ($dS_*/dt \simeq 1\times10^{-5}$ s^{-3}). Accordingly, we can unequivocally conclude that the arrival of the SBF in Cabauw accelerates the ABL AT when the convective regime is already decaying. In other words, the stabilisation of the lower atmosphere occurs more rapidly in the afternoon once the SB is established. Most of the SB studies have focused on early-afternoon SB cases and the interaction with convective turbulence (for instance Antonelli and Rotunno (2007); Comin et al. (2015)), but do not deal with the transition to stable nocturnal conditions. The role of katabatic flows as they interact with local turbulence during the AET has certainly been observed and even modelled (e.g. Sun et al., 2006; Sastre et al., 2015; Lampert et al., 2016), but such acceleration of the stabilisation process has not previously been documented. Moreover, the density currents arriving in Cabauw are unaffected by the topography, and we can be sure that this particular situation can only be attributed to the SB phenomenon.

With respect to the stable regime, the state that precedes the SB is different from that in the other regimes, and B_* increases more rapidly at the three vertical levels (for

instance $d^2B_*/dt^2 \simeq +1.5\times10^{-5}$ s^{-3}/1h at 30 m), which is consistent with the fact that the *SH* flux is negative or close to being so. Note that this pre-SB situation is what results after the arrival of the SBF in the transition regime. Comparing this situation with the transition regime; in the stable regime, the reaction of the lower atmosphere to the passage of the maritime gravity current is far from being identical: the SB produces a deceleration of dB_*/dt. At 110 and 170 m dB_*/dt decreases shortly after the onset, while at the lowest level the rising rate is merely reduced by around $+0.5\times10^{-5}$ s^{-3}/1h. The shear term, S_*, continues to increase but more slowly, largely during the first 20-30 min after the onset. These results suggest that the ET could be somewhat slowed down, contrasting with the AT. Therefore, whether the SH flux is positive or negative is a key factor in determining the reaction of the lower atmosphere to the SB.

We have already shown that the SB produces an acceleration of the ABL AT, but the effect on the stable and convective regimes is still unclear. We therefore explore both regimes in detail below.

Stable regime

The clear increase in the wind speed and surface turbulence in the stable regime (see Figs. 4.6 and 4.7), invites to conjecture that the equilibrium profile within the surface layer could somehow be disrupted by the arrival of the density current. We further explore this possibility in Fig. 4.9, where we compare the evolution through time of the wind-speed difference between 80 and 10 m using both the similarity relations within the surface layer and the real observed differences, after the passage of the SBF. If both differences are similar, the wind profile is in equilibrium with local turbulence. If not, it means that an external factor brings it out of equilibrium: in this case the SB.

We assume the turbulent fluxes in the surface layer to be constant with height and dependent on gradients and the stability parameter $\zeta = z/L$ through universal dimensionless functions, where z is the height agl and L is the Obukhov length defined as:

$$L = \frac{-{u_*}^3\ \theta_v}{\kappa g\ \overline{w'\theta_v'}}, \tag{4.8}$$

where u_* is the friction velocity, θ_v is the virtual potential temperature measured at each height, κ is the Von Kármán constant (=0.4), g is the gravity acceleration (=9.81 m s^{-2}) and $\overline{w'\theta_v'}$ is the θ_v flux. Since we are considering that $\theta_v = T_v + 0.0098z$, we can assume that $\overline{w'\theta_v'} \simeq \overline{w'T_s'}$, where T_s is the sonic temperature, which is almost equal to virtual temperature. According to MOST, the turbulent fluxes can be expressed in terms of the corresponding gradients, which are assumed to be proportional to the universal functions of ζ. For the specific case of the resultant wind speed U, we assume that:

$$\frac{\kappa z}{u_*}\frac{\partial U}{\partial z} = \Phi_M(\zeta). \tag{4.9}$$

The relationship between the gradient function (Φ_M) and the stability profile function Ψ_M is:

$$\Phi_M = 1 - \zeta \frac{\partial \Psi_M}{\partial \zeta}. \tag{4.10}$$

By integrating Eq. 4.9 between two vertical levels z_1 and z_2, we get the following equivalence:

$$U(z_2) - U(z_1) = \frac{u_*}{\kappa}\left\{ \ln\left(\frac{z_2}{z_1}\right) - \Psi_M(\zeta_{z_2}) + \Psi_M(\zeta_{z_1}) \right\}. \tag{4.11}$$

Under stable conditions ($\zeta > 0$), Holtslag and Bruin (1988) proposed an empirical form for Ψ_M given by:

$$\Psi_M(\zeta) = -b\left(\zeta - \frac{c}{d}\right)\exp(-d\zeta) - a\zeta - \frac{bc}{d}, \tag{4.12}$$

with $a = 1$, $b = 2/3$, $c = 5$ and $d = 0.35$.

On the other hand, in order to determine whether the disruption of the equilibrium in the profile is caused by the arrival of the SBF rather than by the decoupling of the different layers in the NBL, we compare the SB days in the stable regime with NSB days. Before selecting the NSB cases, we first computed the time-lag between the sign change of the SH flux (t_0) and the SBF arrival (t_{SBF}) for the 22 SB days under the stable regime: t_{SBF} - t_0. Then, among the days that passed Filter 4 of the algorithm but were rejected by Filter 5 (see Table 4.2), we selected those ones when the wind was offshore (i.e. within the range 45°–225°) at least between t_0 for those days and the last t_{SBF} of the SB days. To this end, we selected 31 NSB days that fell under the stable regime that we knew for certain that were not affected by the SB. Just as we normalised all the SB events with respect to the SB onset in order to compute the averages, we also normalised the NSB events with respect to an artificial SB onset. To do so, we created 22 new events for each NSB day, shifting their time dimension by the quantity t_{SBF} - t_0 obtained from the 22 SB days. In this way, we normalised the NSB days with reference to an artificial SB onset so that SB and NSB days would be comparable under the *modus operandi* followed in this work.

Employing Eq. 4.11 we estimate the wind-speed difference between the observational levels of 80 and 10 m agl for both the SB and NSB days, and we represent them together with the REAL observed differences in Fig. 4.9, after the appropriate normalised averages. For the NSB days the observed ΔU follows the MOST ΔU, and indicates that without the perturbation of a mesoscale flow the wind profile is controlled by the local turbulence. However, on SB days the wind profile departs from MOST lead by the flow disturbances due to the arrival of the SBF, and is therefore no longer controlled by local turbulence. A representative example is the difference between the average MOST and REAL ΔU of up to 1 m s^{-1} 10 min after the arrival of the

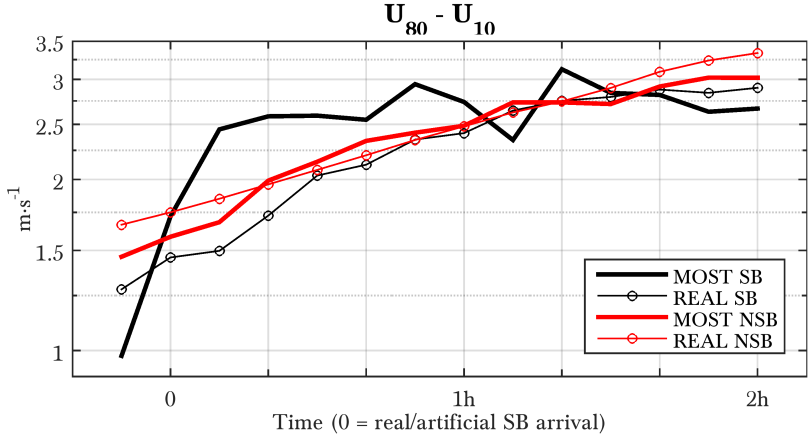

Figure 4.9: Evolution between the time value before the onset and 2 h after it of the average wind-speed difference between 80 and 10 m for the SB days and the NSB days under the stable regime: the solid line represents the wind-speed difference calculated using MOST theory under stable conditions ($\xi = z/L > 0$, see Eq. 4.11), and the line with circles represents the observed difference (REAL). The events were averaged by being normalised with respect to the SB onset in the case of the SB days and with respect to the artificial SB onset for the NSB days.

SBF. The difference is thereafter reduced progressively, suggesting that the equilibrium is gradually being restored.

We further explore how local turbulence is modified by the SBF under the stable regime by calculating the mean shear capacity (SC) again for the SB and NSB cases, in this case at the five intermediate vertical levels. This dimensionless quantity was first introduced by van Hooijdonk et al. (2015) and it compares the measured shear with the minimum shear to maintain a continuously turbulent state (i.e. a WSBL), which is given by the energy demand at the surface. It is used to predict the regime transition from the WSBL to the VSBL, or vice versa. Derived from the TKE budget equation (Eq. 4.1) by ignoring the transport terms, the SC is defined as:

$$SC = \left\{ \frac{(\kappa z)^2 \left(\frac{\partial U}{\partial z}(z)\right)^3}{g/\theta_0 \, |\overline{w'\theta'_v}|} \right\}^{1/3}, \tag{4.13}$$

where θ_0 is a reference potential temperature (we set a constant value of 293 K), κ is the von Kármán constant (=0.4), z is the height agl, $\partial U/\partial z(z)$ is the wind shear, g the gravitational acceleration (9.81 m s^{-2}), and $\overline{w'\theta'_v}$ is the downward surface kinematic heat flux, since SC is defined only when $\overline{w'\theta'_v} < 0$. The wind shear was computed using the method of least squares according to Eq. 2.4, but in this case for the wind speed itself, not the horizontal-wind components as for dS_*/dt.

We represent the SC for both SB and NSB days between the time before the SB onset and 2 h after in Fig. 4.10. First, in the NSB cases (Fig. 4.10b) SC increases particularly at the intermediate levels of 30 and 60 m, for instance in the latter case from 2.25 before the artificial SB onset to 4.25 2 h after it. From observations at 20 m van Hooijdonk et al. (2015) found SC values that lay roughly between 2–3 and 3.5–5 for the VSBL and WSBL respectively. Hence, we can conclude that as an overall behaviour there is a tendency towards a continuously turbulent state in Cabauw on NSB days. This dimensionless number shows a distinct behaviour for the SB events. Interestingly, the SC displays a decrease at the very moment of the onset at the lowest (15 m) and highest levels (100 and 160 m), subsequently spreading to the 30- and 60-m levels. Moreover, there is a clear increase after the onset of about 1.5 at 160 m, followed by a fall of similar magnitude. These evolutions suggest that due to the disruption of the wind-profile equilibrium, the balance between the wind-shear profile and the surface SH flux is altered, until the momentum flux in the surface layer is able to restore the balance. In spite of the decrease of dS_*/dt (Fig. 4.8b), the ability of mechanical turbulence to sustain the turbulent steady state is increased, and there is a general trend towards a more continuously turbulent NBL in the SB cases.

Hence, our analysis shows that the ABL regime in which the onset of the SB occurs is critical to determine its impact. Whether the SH flux is positive or negative when the SBF arrives during the AET is actually fundamental, and involves contrasting consequences.

Convective regime

Finally, we explore how the characteristic convective scales of the well-mixed boundary layer are affected by the passage of maritime density currents. We explore two representative free-convection scaling factors (w_*/u_* and σ_w/w_*), and a time scale t_* in Table 4.3.

w_* is defined as the free-convection scaling velocity (Deardorff, 1972):

$$w_* = \left(\frac{g Z_i}{\theta_v} \overline{w'\theta_v'} \right)^{1/3}, \tag{4.14}$$

where in Z_i we substitute the MLH obtained from the wind profiler (see Fig. 4.6d), θ_v is the virtual potential temperature at 2 m, and $\overline{w'\theta_v'}$, in contrast to Eq. 4.13, is the upward surface kinematic heat flux, for which the sonic-temperature flux is employed as previously justified. w_* is only defined when $\overline{w'\theta_v'} > 0$, but under the convective-regime that requirement is always fulfilled within the range between 2 h before and 2 h after the SB onset. This velocity has widely been used as a convective scale (Deardorff, 1972; Moeng and Sullivan, 1994; Calmet and Mestayer, 2016): in Table 4.3 we present the calculated values of both the vertical-velocity standard deviation σ_w normalised by w_*, and w_* normalised by u_*. In addition, we calculated a representative time scale (t_*) for the eddies within the convective regime. Depending on whether the CBL is

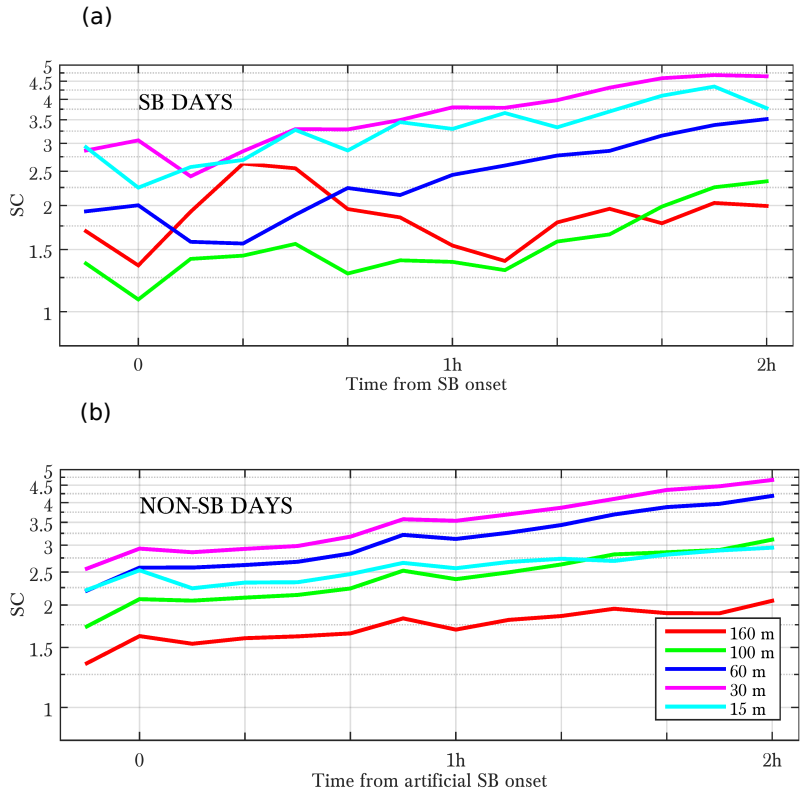

Figure 4.10: Mean evolution of the SC for SB days (a) and NSB days (b) in the stable ABL regime, between the time value before the real(a)/artificial(b) SB onset and 2 h after it. The averages are calculated as in Fig. 4.9.

buoyancy- or shear-driven the time scale is calculated as $t_{*_b} = Z_i/w_*$ or $t_{*_s} = Z_i/u_*$ respectively.

Table 4.3 shows the range of values for the above-mentioned scaling both during the 2-h period before and after the arrival of the SBF. The slight increase in the shear (see Fig. 4.8b) after the arrival of the SBF induces a slight decrease in w_*/u_* ranging from 0.6 to 0.8 (Table 4.3). This scaling factor is a measure of the buoyancy-driven turbulence relative to the shear-driven turbulence. When the stability parameter $-Z_i/L$ is very large, indicating the presence of a free-convection like state, then $w_* >> u_*$ (Wyngaard, 2010). Other studies, for instance Deardorff (1972) found that $w_*/u_* > 2.2$ for a CBL in a buoyancy-driven regime, whereas Moeng and Sullivan (1994) set that value at 1.6 for a regime in which both shear and buoyancy dominate. Therefore, we can assume that the SB does not bring the buoyancy-driven CBL down, although it shifts it closer to the shear- and buoyancy-driven regime. Moreover, the upper range

of σ_w/w_* increases to up to 1.3 after the SB as a consequence of the increase in σ_w. Most studies have found a value around 0.6 (e.g. 0.67 in Lenschow et al. (1980)) for a buoyancy-driven regime, which is within the range of values we observe. With respect to the representative time scale, we calculated it assuming a buoyancy-driven CBL ($t_* = Z_i/w_*$), and it represents the time needed for a thermal to rise. We obtain a range of values between between 15 and 30 min before the SB onset. After the onset, these values oscillate between 15 and 35 min, so we can conclude that the time scale of the eddies within the CBL is generally constant. Those values are close to those given for instance by Lenschow et al. (1980) (17 min) or Deardorff (1972) (15 min), which are representative of the turbulent scales within the CBL.

Table 4.3: Free-convection scales for the convective ABL regime between 2 h before and 2 h after the SB onset: w_*/u_*, σ_w/w_* and t_*. We show the range of values for all the days. Besides, representative values of buoyancy- and shear-driven CBLs (indicated with B and S respectively) obtained in other studies are introduced. Depending on the type of CBL, buoyancy or shear driven, the time scale is given as $t_{*_b} = Z_i/w_*$ or $t_{*_s} = Z_i/u_*$.

CABAUW	w_*/u_*	σ_w/w_*	t_*(min)
Before SB onset (2 h)	3.2–5.2	0.3–0.8	t_{*_b}: 15–28
After SB onset (2 h)	2.4–4.6	0.3–1.3	t_{*_b}: 15–35
OTHER STUDIES			
Deardorff (1972)	$>$ 2.2 (B)	0.6	t_{*_b}: 15
Lenschow et al. (1980)	-	0.67 (B)	t_{*_b}: 17
Moeng and Sullivan (1994)	3.6 (B)	0.63	t_{*_b}: 8
	1.6 (B + S)	-	t_{*_b}: 8–10
	0 (S)	-	t_{*_s}: 17
Calmet and Mestayer (2016)	3.3 (B)	-	-

4.5 IMPACT ON SCALAR TRANSPORT

Finally, we address another relevant aspect of the dynamic analysis related with RQ 4.2: the influence of the direction of the SB on the transport of scalars and state variables ($\psi(t)$). Figure 4.11 shows box plots of the change in their values during the onset for the three ABL regimes, given by $\Delta\psi = \psi(t_{\text{onset}}) - \psi(t_{\text{onset}} - 1)$, with respect to the wind direction $\alpha(t_{\text{onset}})$, gathered into six different subranges within the onshore range of (225°–45°).

First, we show the change in air temperature (Fig. 4.11a) and specific humidity (Fig. 4.11b) during the onset. To be consistent with the wind-direction measurements

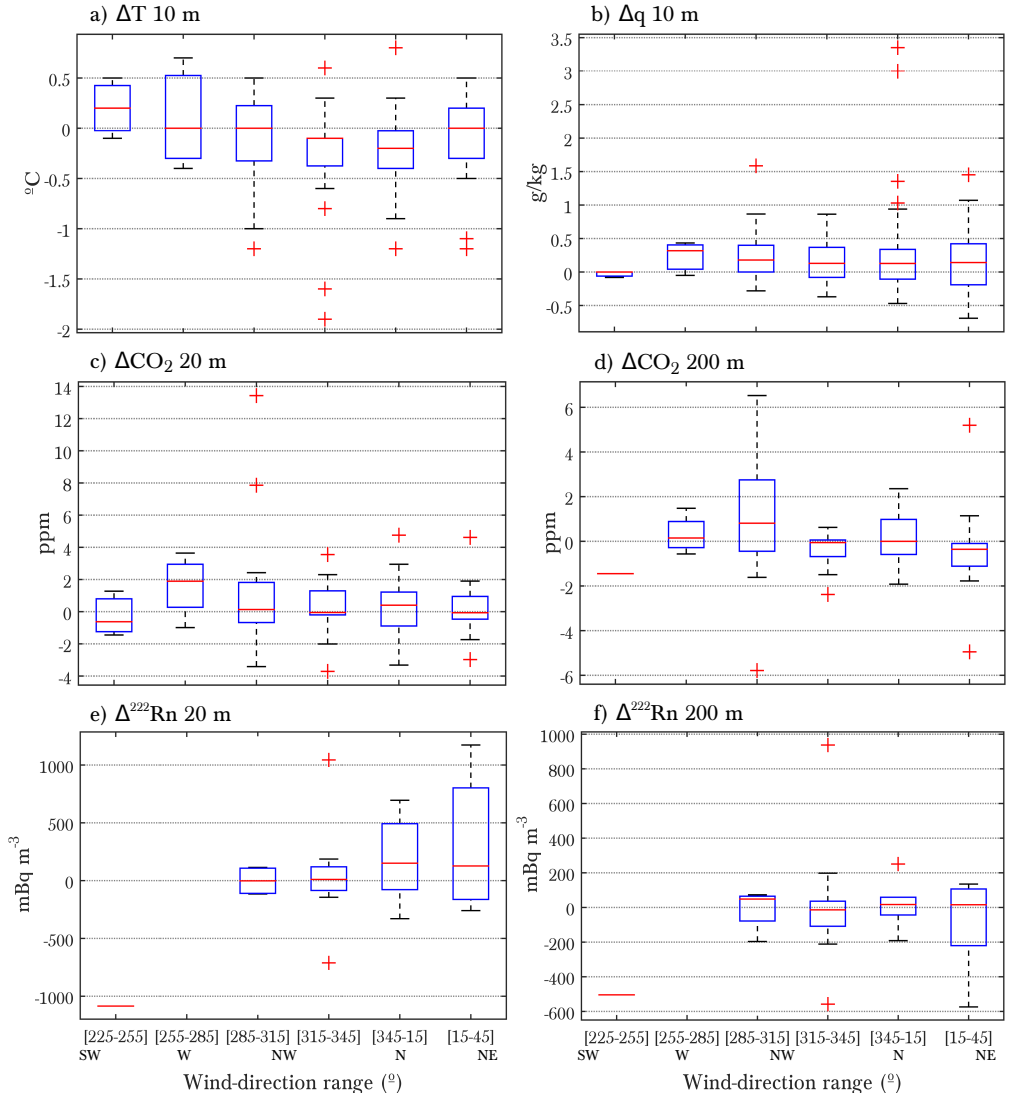

Figure 4.11: Box plots of the variation in individual variables for different wind-direction ranges: (a) air temperature at 10 m, (b) specific humidity at 10 m, CO_2 at 20 (c) and 200 m (d), and ^{222}Rn at 20 (e) and 200 m (f). The red horizontal line of the boxplots represents the median, the blue box delimits the first and third quartiles, the whiskers delimit the most extreme data points not considered to be outliers, and finally, the outliers are represented with red crosses.

which were taken at 10 m, the lowest height, we employed the 10-m measurements of both T and q. In some SB events, particularly from the N-NW, the temperature fall is significant, between 1 °C and 2 °C in only 10 min, although it slightly increases in a few of them. In fact, Fig. 4.6 shows how under diurnal convective conditions the cooling effect of the SB can be very slight or even absent. The specific humidity increases in most cases, being particularly significant for some N-NE SBFs (up to 3–3.5 g kg^{-1}). Besides, for those directions we also find the largest variance, and in fact, few q decreases are observed. To explain the significant increases, on the one hand the SST of the IJsselmeer and Markermeer is considerably higher than in the North Sea (Fig. 2.3), and the air over warmer seas has a greater q due to its higher evaporative capacity. Consequently, the SBs that pass over these enclosed seas bring a more humid air mass with them. On the other hand, N-NE SBs are generally driven by E-NE large-scale flows. Since air masses with an easterly origin are drier, the q jump that accompanies the onset of SBs is larger.

We also explore the role of the SB in modifying the evolution of scalars such as CO_2 and ^{222}Rn in Fig. 4.11 (c,d) and 4.11 (e,f) respectively. We analyse their concentrations at both 20 m and 200 m agl, since they are affected by distinct flux footprints and the amplitude of their diurnal cycle is also different. The measurements for these atmospheric compounds were performed every 30 min, while the wind direction was recorded every 10 min. The onset is defined taking into account the wind veering in Filter 5 of the SB algorithm, which is obtained from the 10-min wind direction. We therefore always define the SB onset for these scalars considering the next 30-min value, in order to be sure that the SB has already arrived.

No significant changes in CO_2 concentrations were observed at the onset of SBs, except for a couple of SBFs from the W-NW (285°–315°), in which a substantial jump (around 8 and 14 ppm) was measured at 20 m. In both cases the large-scale flow on the previous night had a continental origin and the SB arrived during the stable ABL regime. At 200 m, the greatest rises and falls of around 4–6 ppm are observed for both W-NW (285°–315°) and N-NE (15°–45°) ranges, coinciding with the directions of the main water bodies (see Fig. 2.3). Previous studies in The Netherlands found higher CO_2 concentrations during E-SE continental flows, for instance Super et al. (2017) and Casso-Torralba et al. (2008); the latter derived from measurements at Cabauw. Of the cities with more than 250.000 inhabitants in The Netherlands, the city of Amsterdam is located to its N-NW, Rotterdam the SW, The Hague to the W and Utrecht to the NE (see Fig. 2.3). The most plausible explanation for the observed jumps in CO_2 is the return of continental air masses rich in CO_2 through the SB circulation. Since the higher CO_2 concentrations are associated with offshore flows, they transport the CO_2 over the North Sea during the night. On the following day, if a SB circulation is formed and the SBF arrives in Cabauw, it may induce a sudden increase in the concentration of CO_2, particularly when surface conditions are stable, since the CO_2 is concentrated in the lower layers.

Regarding the ^{222}Rn, shown in Fig. 4.11 (e, f), we calculated the changes from 30 min before the onset until 1 h after: $\Delta\psi = \psi(t_{\text{onset}} + 2) - \psi(t_{\text{onset}} - 1)$, i.e. within 90 min. We chose a longer time step than for the CO_2 measurements because in this case the impact of the frontal passage in the ^{222}Rn transport is less sharp. In Cabauw, measurements are recorded at 20 and 200 m agl from 2006 on (see Table 4.1). ^{222}Rn was studied at Cabauw in 2007 by Zahorowski et al. (2008), who focused on diurnal, synoptic and seasonal time-scales. Measurements affected by the mainland European fetch, i.e. for winds blowing from between 50° and 220°, give rise to significantly higher ^{222}Rn concentrations. That range coincides approximately with the one we used to define the offshore flow in the SB algorithm (Sect. 2.3.3). Particularly high values are reported for SE flows at 200 m, while ^{222}Rn concentrations in air masses with oceanic footprints take low ^{222}Rn concentrations along. van der Laan et al. (2016) inferred the ^{222}Rn surface fluxes from 2007–2013 in Cabauw and the surrounding area, and found that the highest values corresponded to the SW wind direction, whereas the lowest were observed from the NE.

Given that mean diurnal cycle amplitudes at 20 m in spring and summer are about 1.3–1.4 Bq m^{-3} (Zahorowski et al., 2008), some SBF passages trigger significant changes in ^{222}Rn. In particular, some SBFs from the N-NE (15°–45°) induce a significant increase only at 20 m (Fig. 4.11e), whereas they lead to decreases at 200 m. Furthermore, one SB event from the N-NW (315°–345°) induces a large jump (~ 1 Bq m^{-3}) at both 20 and 200 m agl. There is also a single event from the W-SW marked in this case by a significant fall in ^{222}Rn of more than 1 Bq m^{-3} at 20 m, and of around 0.5 Bq m^{-3} at 200 m. These observations disagree with the estimates of van der Laan et al. (2016) for the surface fluxes of ^{222}Rn, and must therefore be explained by other processes than the nearby emissions. First, the increase in the wind speed enhances the dilution of ^{222}Rn and consequently produces a fall of its concentration (Ho and Measday, 2005; Vargas et al., 2015), but on the other hand, the transition from convective to stably stratified conditions builds up ^{222}Rn at lower levels. Another factor is linked to the origin of the air mass: oceanic backgrounds bring markedly smaller concentrations (Arnold et al., 2009). However, as commented above for CO_2, the SB circulation leads to the return of continental air masses, with the result that mesoscale footprints (~ 100 km) can become of great significance in explaining the variability of ^{222}Rn.

4.6 SUMMARY AND CONCLUSIONS

This study addresses SB phenomena and their complex interactions with the local turbulence and the transport of scalars. We have satisfactorily applied an objective and systematic algorithm to select the SB events from a comprehensive meteorological database of 10 years from the CESAR site. Validated and continuous data at different levels along the 213-m measurement tower, as well as the measured surface turbulent

fluxes, provide a complete snapshot of the lower atmosphere. Clear SBF passages were obtained, which are solely driven by mesoscale factors.

We find two main SB directions, driven by distinct large-scale pressure patterns and associated with the main nearby bodies of water: the North Sea and the IJsselmeer and Markermeer lakes. Most of the SBF arrivals occur in late afternoon/early evening (1400–1900 UTC), suggesting that, as observed by other authors, the weakening of thermally-driven convection accelerates the inland propagation of SBFs.

In order to explore how local turbulence interacts with the arrival of SBFs, we classify the SB events into three ABL regimes according to the value of the SH flux in the onset: convective, transition and stable regimes.

In the convective ABL regime, the local surface turbulence is virtually unaltered by the arrival of the SB. A slight enhancement of the shear contribution with respect to buoyancy is quantified, even though the thermally-driven regime is sustained. It appears that the convection itself weakens the SB disturbances.

Under the transition regime, the arrival of the SBF leads to a sudden jump in wind speed, a clear falling trend in the MLH, and an enhancement of u_*. Surface heat and CO_2 fluxes remain unchanged. Besides, the estimated shear and buoyancy terms increase more rapidly at the higher levels. We therefore conclude that the onset of the SB accelerates the AT, and that subsequently the nocturnal stable conditions arrive earlier.

A distinct behaviour is observed in the stable regime, when the SH flux and the vertical gradient of θ are already negative. As in the transition regime, the wind speed and u_* are sharply enhanced. In addition, the arrival of the SBF produces an increase in σ_w, which disrupts the surface-layer equilibrium. On the one hand, the increasing trend of the buoyancy – which is already negative – and shear contributions to the TKE are decelerated. On the other, on the basis of the observed and calculated wind-speed differences between two vertical levels based on MOST theory, we find that the onset of the SB brings the wind profile out of equilibrium with the surface. By comparison with NSB days within the stable regime we find that this disruption is due to the appearance of the SB. Furthermore, the evolution of the SC indicates that there is a tendency towards a weakly turbulent state on both SB and NSB days. However, in the case of the SB days the balance between the wind-shear profile and the downward SH flux breaks down, until the equilibrium is restored somewhat later.

As expected, the maritime density currents are accompanied by moister and colder air masses, even though the frontal discontinuities are constrained by forcings such as the local convective mixing. The SB flows from the lakes bring with them the sharpest jumps in humidity, while in case of the CO_2, the greatest increases take place for the SB from the North Sea and within the stable regime. Since the CO_2-rich air masses have a continental origin, we argue that those increases probably occur due to the return of continental air masses together with the SB circulation, bringing back the excess CO_2 previously advected by offshore flows, which is concentrated in the lower layers due to the stable conditions. In the case of ^{222}Rn, understanding the changes

in concentration is more challenging. We find considerable increases and decreases in ^{222}Rn for distinct SB directions both at 20 and 200 m, indicating that not only the footprint of the air masses, but also the recent history and return of continental air masses together explain the observed conditions.

Finally, we can point out that there is a two-way interaction between the SB and local turbulence. On the one hand, daytime convective mixing weakens the SB disturbances and slows down their inland propagation. On the other, depending on the local turbulence conditions the effect of the SB is distinct, occasionally giving rise in turn to sudden increases in turbulence.

Since our observations are spatially limited, subsequent studies in the form of large-eddy simulations (LES) should be conducted in order to describe turbulence explicitly and answer questions such as how turbulent convection affects the slowing down of the inland propagation of the SBFs. Furthermore, the ability of the mesoscale models to capture the observed challenging interaction between the SB and turbulence needs to be investigated, in order to obtain a better representation of the AET, the SB circulation and related atmospheric variables. This matter is investigated in the following chapter.

5 MODELLING SEA BREEZES AND THEIR INTERACTION WITH ATMOSPHERIC TURBULENCE

We analyse the performance of the WRF model in reproducing the main characteristics of the SB, their influencing factors and the impact on ABL turbulence. For that, we employ numerical simulations spanning the 10-year period from the observational study of Chapter 4 at the CESAR site. The fine resolution of 2 km and the replication of the observational vertical levels allows for the investigation of mesoscale-turbulence interactions for the three ABL regimes: convective, transition and stable. By applying the mesoscale selection algorithm to the numerical simulations, we find that 28% of the observational events are coincident with the SB events from the model. On the coincident days an average deviation of almost 4 h is found in the onset time of the SB, so that local turbulence conditions are contrasting for the same event of the simulations and the observations. Hence, the analysis of the simulated SB characteristics and impacts for the three ABL regimes is challenging. Firstly, we find that the maximum diurnal value of the SH flux is overestimated by more than 100%, which gives rise to an enhanced convective mixing. Partly and probably as a consequence, the intensity of the simulated SBFs is overestimated, as well as the associated increase in local turbulence (for instance u_* is overestimated by around 50% at the SB onset in the transition regime). Finally, the arrival of the SB yields an enhancement of the stable stratification. As a consequence, the AT and ET occur faster than under conditions solely dominated by local atmospheric turbulence.

The main contents of this chapter will be submitted as:
Arrillaga, J.A., Vilà-Guerau de Arellano, J., Jiménez, P. and Yagüe, C. The role of local turbulence and synoptic scales on sea-breeze features: using 10-year WRF and observations. *J. Geophys. Res. Atmos.*

5.1 INTRODUCTION

SB phenomena have been investigated in numerous studies by using multiple observations and numerical simulations from mesoscale models. Numerical experiments, indeed, have contributed to the understanding of these mesoscale phenomena, since they provide information about their vertical and spatial extent not covered by the available observations. Nevertheless, most numerical studies are based on individual analyses. Besides, some gaps remain in our knowledge of, for instance, the factors influencing the SB onset (Mestayer et al., 2018). As pointed out in the review by Crosman and Horel (2010), the main reason for the inaccurate performance of mesoscale models in reproducing the SB is related to an erroneous usage of turbulence in the ABL. Inconsistencies are also found regarding the transition phase from the SB to the LB. From a three-dimensional mesoscale model Zhong and Takle (1992) found that the Coriolis force is dominant during that transition, whereas Cuxart et al. (2014) observed that the contribution of the Coriolis term in the momentum balance is negligible. Their conclusions were based on both observations and numerical simulations, and they explained the constancy of the afternoon wind direction through the influence of local topography.

In this chapter we aim at assessing the performance of the WRF mesoscale model in reproducing the SB characteristics by analysing a large 10-year database. Additionally, combining observations and modelling introduces an important synergy in our analysis. We particularly address two of the most relevant factors in the SB formation and evolution as has been stated in the introduction of the thesis: the large scales and local turbulence. For that purpose, numerical simulations spanning the 10-year observational period from Chapter 4 are employed. Hence, the plan of action from the previous chapter is followed and numerous SB events are investigated together after applying the SB selection algorithm to the simulated data from WRF. This research strategy aims at answering the following questions:

RQ 5.1: *Which are the atmospheric variables producing discrepancy in the SB selection between observations and the WRF model?*

RQ 5.2: *How does the WRF model reproduce the afternoon and evening SBFs and their interaction with turbulence for the three ABL regimes?*

OUTLINE We first describe the configuration of the numerical experiments and the method employed to select the SB events from the WRF simulations in Sect. 5.2. The statistics from applying the algorithm to both databases (observations and simulations) is analysed in Sect. 5.3. Section 5.4 evaluates the simulated SB characteristics for the three ABL regimes and their impacts on local turbulence. The chapter is finalised with a general discussion and the future prospects.

5.2 METHOD

The observational data employed in Chapter 4 are compared with numerical simulations from the WRF model spanning the same 10-years period from the observational database. In order to carry out an objective comparison, the simulated data corresponding to missing observational data were removed from the 10-year dataset. Moreover, the 10-min observations were adapted to 1-h time resolution in order to be consistent with the time resolution of the numerical simulations. The adaptation was performed by choosing the hourly observational data, not by calculating hourly means, in order to avoid smoothing of the observed trends.

5.2.1 WRF model

The model (version 3.4.1, see Sect. 2.3.2) is configured with four nested domains which have a three-to-one spatial resolution. The outputs of the numerical experiments are recorded every hour, and the smaller domain of the model configuration is centred at the CESAR site, having a horizontal resolution of 2 km. The distribution of vertical levels is the standard one, except for the near-surface levels, which are forced to follow the observational levels (up to 200 m).

The runs are carried out every 48 h, with the first 24 h being the spin-up time. This strategy is adopted with the goal of not deviating considerably from the large-scale conditions prescribed from the ERA-Interim reanalysis at 0.75° x 0.75° resolution. Further specifications about the modelling configuration can be found in Jiménez et al. (2016b), where the numerical experiment is described. A summary of the model configuration is shown in Table 5.1.

The employed ABL scheme is YSU. As we concluded in Chapter 3 or as they did for instance in Challa et al. (2009) and Steele et al. (2013), this scheme provides an adequate and less biased representation of the SB compared to other ABL schemes. As we describe in Sect. 2.2.2, the soil in Cabauw is very wet. The land properties such as soil moisture have not been modified in the model, and climatological values have been used.

5.2.2 SB selection

SB days are selected from the WRF database by employing the SB algorithm described in Sect. 2.3.3. The same criteria are applied to observations and WRF simulations, which are specified in Table 2.2. In that way, the SB databases obtained from the model and the observations are comparable, since they are filtered based on objective filters. Besides, the comparison allows us to analyse which factors, either related with synoptic, regional or local scales, are responsible for the differences observed. For consistency, the filtering is carried out in both cases for the warm period (May, June,

Table 5.1: WRF model setting

WRF configuration and physics	Value
Central point	51.97°N, 4.93°E
Horizontal resolution (km)	4 nested domains (54; 18; 6; 2)
Vertical resolution	36 eta levels (6 in the first 200 m)
Initial and boundary conditions	ERA Interim (6 h)
Longwave physics	RRTM (Rapid Radiative Transfer Model)
Shortwave physics	Dudhia
Microphysics	WSM-6-class
Surface physics	5-layer model
ABL scheme	YSU

July, August). By exploring and contrasting the performance of each filter, we can gain further knowledge about the meteorological conditions for a better forecast of the SB formation in numerical weather prediction models.

5.3 FORCINGS AFFECTING THE SEA–BREEZE DETECTION

First, we systematically explore the performance of the different filters of the SB algorithm when applied to observations and WRF. We show in Table 5.2 the statistics of how each filter of the algorithm performs when applied to observations and WRF. All synoptic, mesoscale and local (with a spatial scale of few km or less) factors are responsible for the differences observed.

Table 5.2: Statistical evaluation of the SB algorithm applied to observations and numerical simulations (1230 days in total corresponding to the warm period). First column indicates the filter number; second column a short description of each filter; third column the variable evaluated; fourth column the number of days from the observational database that pass each filter; fifth column the number of days from WRF simulations that pass each filter; sixth column the coincident days between the observational and numerical databases; and finally, seventh column the percentage of the coincident days with respect to the observational database. Further specifications about the criteria of each filter can be found in Chapter 2.3.3.

Filter	Description	Variable	#(obs.)	#(WRF)	#(coinc.)	%(coinc.)
1	Synoptic wind	V_{850}	382	377	320	84
2	Synoptic fronts	$\Delta\theta_{e,850}/\Delta t$	326	329	253	78
3	Precipitation	pp	267	230	185	69
4	Thermal gradient	$\Delta T_{sea,land}$	209	229	143	68
5	Frontal passage	$\alpha_{10'}$	75	62	21	28

After applying the first two filters, which are related to the synoptic scales, only around 78% of the filtered days are coincident. This result reveals that simulated large-scale conditions are biased with respect to the observed large-scale conditions, giving rise to a discrepancy of almost a quarter in the SB detection. The third filter evaluates the daily precipitation in Cabauw, mainly occurring due to the convective mesoscale showers, since synoptic stability is assured via the previous two filters. The impact of the third filter is greater in WRF: it rejects 30% of the days, contrasting with the 18% from the observations. Conversely, the fourth filter, which rejects the days in which a minimum land-sea temperature difference of 2 °C is not exceeded, discards only 1 event in WRF (*vs* 68 in the observations). This result indicates that the land-sea temperature horizontal gradient is overestimated in the model, probably linked with the great overestimation of the SH flux from WRF, as will be shown later. Besides, the misrepresentation of the land-sea gradient could also be partly explained by discrepancies between the soil moisture given by ERA-Interim and the one fixed by WRF. The last filter, which evaluates the wind turn influenced by the SBF passage, turns out to be very selective when applied to the model and rejects around 73% of the days that pass the fourth filter. By analysing different meteorological variables at the moment of the onset we characterise the frontal passage in Sect. 5.4.

It is important to point out that fewer observed days (75 *vs* 102) result from the application of the SB algorithm comparing with the selected events in Chapter 4. That difference is explained by the adaptation of the observations to 1-h time resolution. The resultant 21 coincident events are the ones employed to carry out the verification of the model and the reproduced SB characteristics. From the 21 coincident days, 18 are within the 102 days from the 10-min observational study. Hence, the 21 coincident SB days may not be absolutely representative of the observed SB characteristics in Cabauw, which were presented in Chapter 4, but allow an objective and consistent comparison with the SB events reproduced by the WRF model.

5.4 ASSESSMENT OF THE MODEL PERFORMANCE

5.4.1 SB characteristics

We start contrasting the SB databases from WRF and the observations by clustering them together in histograms (Fig. 5.1). They illustrate the frequency of SB onset at different times of day, shown for different months and SB directions.

Comparing first the 75 observed (a) and the 62 simulated (b) SB events, we find that WRF does not reproduce the increase in the onset frequency between 1500 and 1900 UTC of the observed SB days. That increase was even more clearly observed in Fig. 4.3 when representing the 102 events from the 10-min observational study. The absence of the increase in the simulations may be linked with the fact that mesoscale models do not reproduce correctly the acceleration in the inland propagation of SBFs in the late

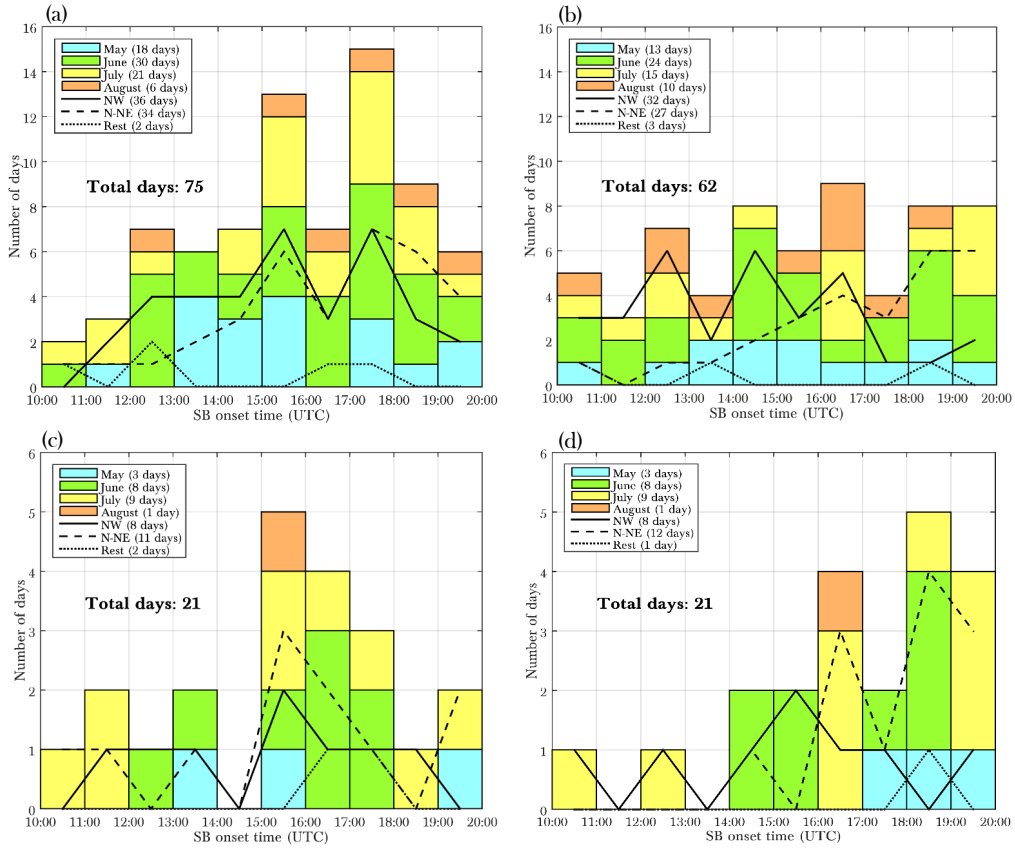

Figure 5.1: Histograms of onset times for the (a) 75 observed, (b) 62 simulated, (c) 21 coincident observed and (d) 21 coincident simulated SB days. The monthly distribution is shown in colours, and the wind-direction distribution in black lines. The frequency scale (y-axis) is the same between (a) and (b), and (c) and (d). Local summer time is UTC + 2.

afternoon, when convection is already decaying. According to Crosman and Horel (2010), we expect an acceleration of the SBF passage when convective turbulence starts to decay. Hence, in the model the distribution of SB-onset frequencies is more uniform throughout the day. The wind-direction distribution is different as well. Furthermore, we find an increase in the frequency of NE SB days and a decrease of the NW SB days at the end of the day for the simulated events. In Chapter 4 we concluded that the large scale was responsible for the observed distinct SB directions and not the Coriolis force. Besides, the area surrounding Cabauw is very flat, so the influence of topography in the SB direction can be considered as null. Hence, we can hypothesise that WRF

overestimates the relative weight of the Coriolis term in the momentum budget, which would explain the biased turn to NE SB directions.

Regarding the 21 coincident days (Fig. 5.1c and d), the maximum in the onset frequency is delayed in the model: it is observed between 1500 and 1800 UTC, but in the model takes place roughly between 1600 and 2000 UTC, clearly contrasting with the uniformity of the distribution for the 62 simulated days (Fig. 5.1b). From individual inspection of the coincident events we find that the onset time of SBs is overall delayed in the model: the onset-time bias is around 25 min. What is more, the delay or advance in few events is even greater than 5 h. We calculate a RMSE of the onset time of almost 4 h, indicating that the model has an important deviation in reproducing the exact onset time of the SB passage, as we define it in the SB algorithm. The lack of coincidence of the SB onset times can also be noticed from the monthly distribution. The increase of NE SBs between 1600 and 2000 UTC is also evident in the 21 coincident days from the numerical simulations.

We further explore the performance of the model in reproducing the observed SB direction and intensity by representing wind roses in Fig. 5.2. Focusing first on the observations, we find that the frequency of W-NW and NE SB directions decreases in Fig. 5.2a comparing to the 102 observed days in Fig. 4.4 at the same height. The frequency of the same directions also decreases for the 21 coincident days (Fig. 5.2c) particularly for the most intense events. Overall, the 21 coincident observed SB events are significantly weaker than the 75 observed days. Comparing the 62 simulated days (Fig. 5.2b) with the 21 coincident simulated days (Fig. 5.2d), we find a decrease of the NW SB cases (again the most intense ones). On the other hand, comparing the numerical simulations and observations on the 21 coincident days, we find that WRF overestimates the SB intensity, especially in the case of N-NE SBs. In addition, SB directions are slightly shifted towards the NW and NE in the model, underestimating the N SB frequency.

5.4.2 ABL regimes

In the previous section, we compared the onset features of all the SB days selected by the algorithm both from observations and numerical simulations. However, as discussed in Chapter 4, local-turbulence and stability conditions at the arrival time of the SBF are fundamental to understand the evolution of the AET of the ABL and the complex processes that occur within this stage (Lothon et al., 2014). Following the same procedure as in the previous chapter, a classification of the SB events into three ABL regimes (convective, transition and stable) is carried out from the value of the SH flux at the onset with respect to the diurnal maximum value. To show the differences in local forcings we compare LH and SH fluxes in Fig. 5.3. In the case of the latter, those differences have an impact on the regime classification.

WRF overestimates significantly the SH flux (more than 100% for the peak), and besides, it delays the evolution of both the SH flux and the LH flux on the SB days.

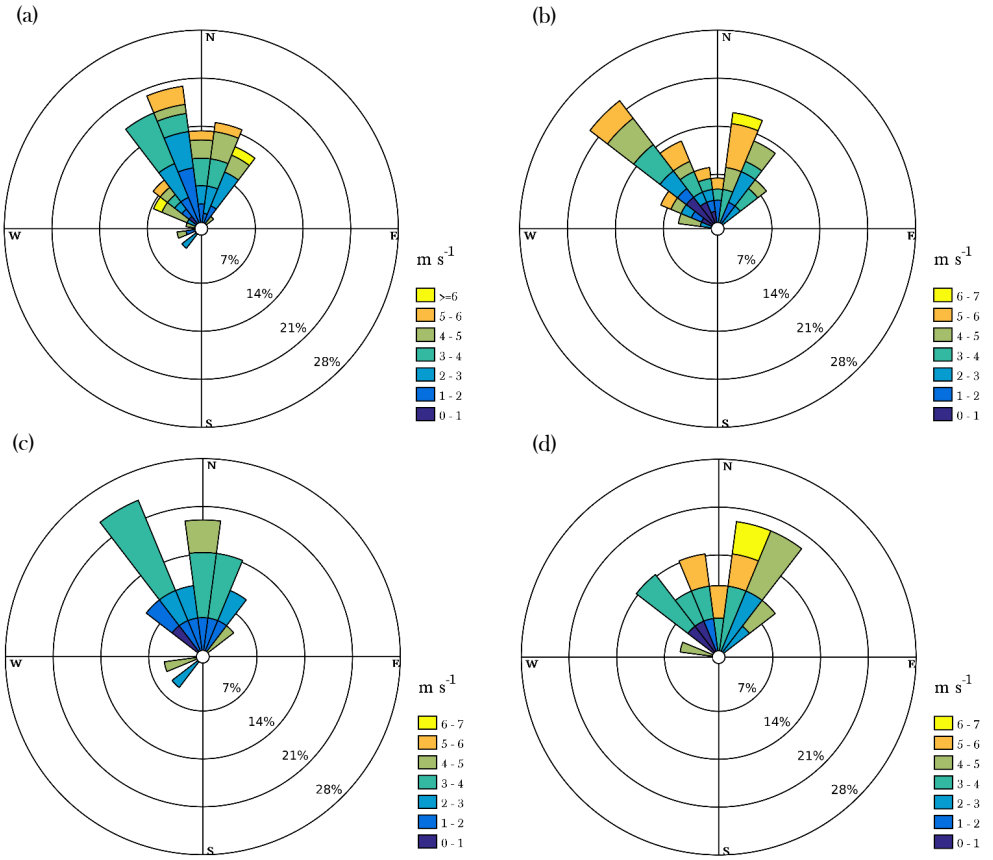

Figure 5.2: Wind rose at 10 m the moment of the SB onset for the (a) 75 observed SB days, (b) 62 simulated SB days, (c) 21 coincident days from observations and (d) 21 coincident days from WRF.

Regarding the rest of the terms of the SEB (not shown here), R_{net} is slightly overestimated during daytime (up to 15–20%), whereas G is adequately represented. Therefore, it seems there is a slight excess of the available energy reaching the surface in the model. Since climatological values are fixed for the soil moisture, it is important to note that the use of more updated yearly values would still give an overestimation of the SH flux despite reducing the difference. This strong overestimation of the SH flux was also observed in the simulations carried out in the area of Cabauw from the WRF model in Steeneveld et al. (2011), although the temperature profiles were adequately reproduced. However, it must be taken into account that measurements tend to underestimate the turbulent fluxes as reported for instance in Foken (2008). By comparing the standard deviation of observations and simulations, we find that during daytime,

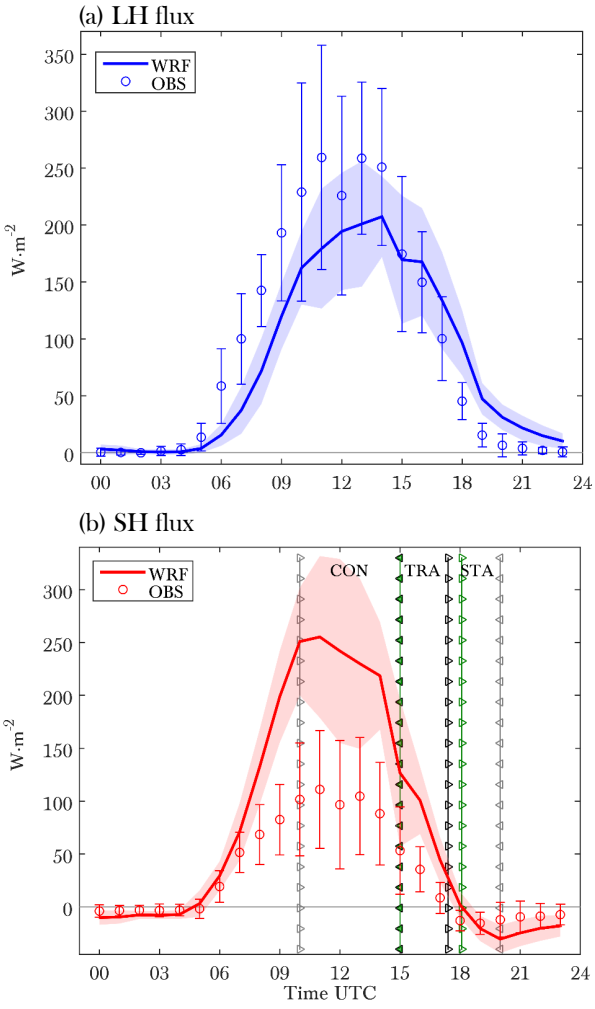

Figure 5.3: Time evolution of the average (a) LH and (b) SH flux and their standard deviation on the 21 coincident SB days, in circles for the observations and solid lines for the numerical simulations. Vertical lines with triangle markers in (b) delimit the SH values for the 3 ABL regimes (convective, transition and stable), in green for the model and in black for the observations. Grey vertical lines are coincident for the model and the observations.

in spite of having a wide range of variability, the evolutions of the SH are not overlapped. On the other hand, the model delays approximately 1 h the moment at which the SH reverses its sign. Even though the delay is more evident in the case of the LH

flux, it is more relevant in the case of the SH flux: the stable regime is established later in the model, and therefore, the SBF arriving in the simulation at the same time as in the observations would evolve dynamically in a different way. This can be an important source of bias when forecasting SB phenomena and the variables closely related to them. Hence, a better representation of surface and ABL processes is highly relevant in a mesoscale model.

We compare in Fig. 5.4 the average wind speed, potential temperature, specific humidity and the MLH for the model and observations in the 21 coincident SB days by classifying them into the three ABL regimes. As in the previous chapter, the mean for each regime was calculated normalising all the events with respect to the SB onset. First, it is noteworthy that from the 21 coincident days we find that 5 (5 in WRF) are within the convective regime, 12 (10 in WRF) in the transition regime and 4 (6 in WRF) in the stable regime. However, we only find regime coincidence in 1/5 of the cases in the convective regime, 6/12 in the transition regime and 1/4 in the stable regime, which makes the comparison more challenging. In any case, since the conditions for each regime are similar in terms of local turbulence, we compared all the 21 coincident days. Besides, due to the quality control of the MLH estimation from the wind profiler, 61% of data were missing, and therefore we just represent the simulated values coinciding with observed MLH data.

In general the impact of the SBF on the represented variables is different depending on the ABL regime, and numerical simulations from WRF differ from observations in how this impact is manifested. At this point it is necessary to note that a lack of similarity can be found in the observational results with respect to the results presented in the previous Chapter (for instance see Fig. 4.6). That is due to two main reasons: firstly, the time resolution in this study has been adapted to 1 h, so that the evolution of the different variables is smoothed; and secondly, we only show 21 events (from which 18 are coincident with the 102 employed in Chapter 4).

Starting with the convective regime, wind speed is underestimated by around 1 m s^{-1} prior to the SB onset. This fact could be explained by a stronger collision between continental and maritime air masses generating a more pronounced decrease in wind speed. This result indicates in any case that the reproduced SBF in the model is sharper, which is in agreement with the stronger SB intensity observed in Fig. 5.2d. Potential temperature is considerably overestimated (up to 2 K after the onset) and specific humidity underestimated (around 0.5 g kg^{-1}). The simulated specific humidity at 10 m is considerably biased with respect to the rest of the levels and the observed values, which is illustrating a remarkable bias from the WRF model in diagnosing this variable near the surface. With respect to the MLH, it is approximately between 400–700 m deeper in WRF, which could be partly influenced by the commented issues with the wind profiler in detecting the top of the mixing layer. In any case, the above commented biases in the model for the potential temperature, specific humidity and MLH can be explained by the great overestimation of the SH flux. A greater SH flux induces a greater warming of the lower atmosphere, greater convection and a stronger

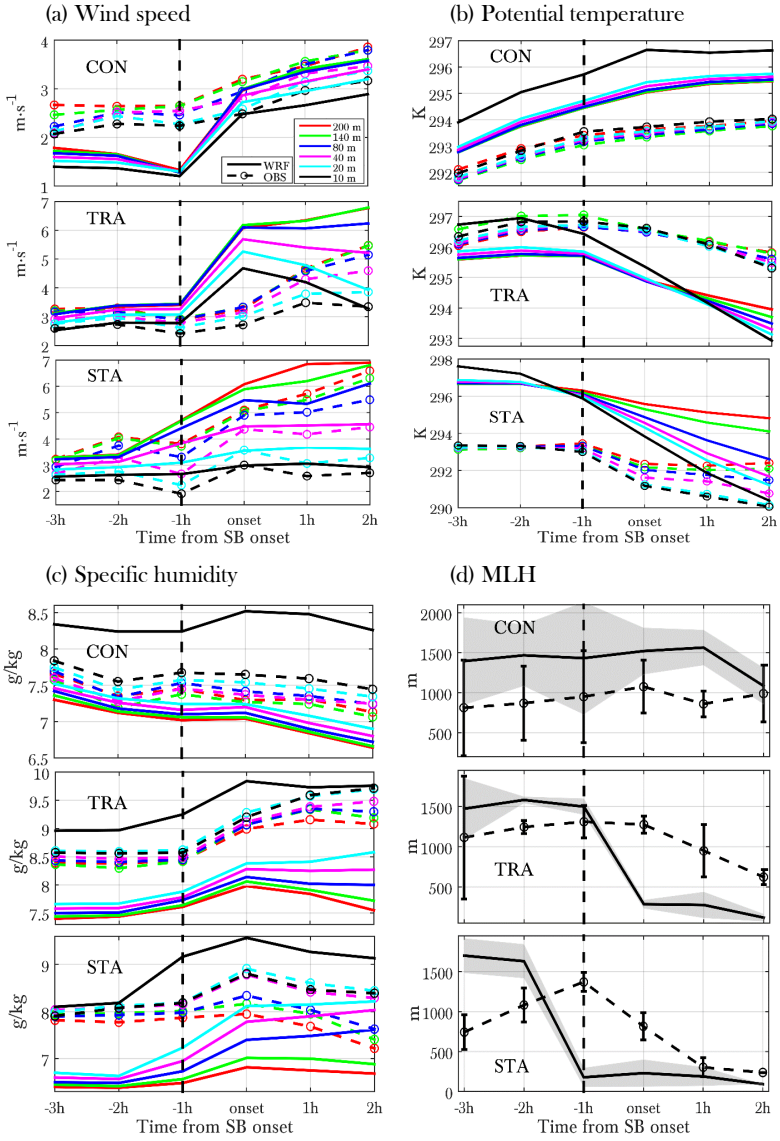

Figure 5.4: Time evolution of the average (a) wind speed, (b) potential temperature, (c) specific humidity and (d) MLH and its standard deviation between 3 h before and 2 h after the onset of the 21 coincident SB days for the three ABL regimes. The dashed vertical line identifies the 1-h measurement just before the onset, which occurs between the dashed line and time = 0.

vertical mixing with drier air above. Regarding the intensity of SBFs, the enhanced SH flux has a two-sided effect. On the one hand, the induced greater convection reduces the intensity of SBFs by increasing the mixing between the maritime and continental air masses. On the other hand, the greater SH flux over land sharpens the land-sea thermal contrast and consequently the intensity of the SBF. Since in our case SBFs are stronger in the model, it seems that the second effect dominates over the first.

With respect to the transition regime, both the SBF intensity and the stratification of the wind speed 2 h after the onset are slightly overestimated. The four variables analysed show a sharper transition in the model, from well-mixed conditions 2 h before the onset to an already stably stratified lower atmosphere 3 h after the onset. For instance, the vertical difference between 20 and 200 m for the specific humidity is of ~ 0.2 g kg^{-1} 2 h before the onset both in observations and WRF, and of ~ 0.6 g kg^{-1} in the observations and ~ 1.1 g kg^{-1} in the numerical simulations 3 h after the onset. The acceleration of the AT due to the SBF passage observed in the observational study from Chapter 4 is overstated in WRF. The transition from convective to stable conditions in the model takes place abruptly depending on the value of R_c, which could also explain the faster AT.

Finally, in the stable regime the stratification is already stable when the SBF arrives, but as occurred in the transition regime the stabilisation process is overestimated in the model. It can be particularly noticed from the evolution of potential temperature and specific humidity. The MLH shows a contrasting behaviour in the model comparing to the observations. Before the onset of the SB the observed MLH shows a peak (~ 1300–1400 m) despite the SH flux turns negative, whereas the model reproduces a shallow MLH, typical of the nocturnal regime (~ 200 m). As above commented, this difference can be partly associated with the issue from the wind profiler itself. On the other hand, the MLH is determined from different criteria in the observations and numerical simulations, which also increases the discrepancy. And finally, the parameterisations of the ABL are based on MOST formulation, and as we concluded in the previous chapter, it fails in reproducing the surface-layer wind profile just after the SB onset, which could also explain the considerable bias. In any case, we address the impact on turbulence in the next section.

5.4.3 Impact on turbulence

In order to explore the influence of the SB passage in turbulent characteristics during the AET of the ABL we investigate the evolution of the friction velocity in Fig. 5.5. The observational u_* employed considers a regional wind-direction dependent roughness length. In this way, the comparison with grid u_* from WRF is more optimal and less dependent on the local conditions around the 213-m tower in Cabauw (Beljaars and Bosveld, 1997; Verkaik and Holtslag, 2007)

In the convective regime the enhancement in u_* associated with the passage of the SBF is overestimated, which is in agreement with the evolution of the wind speed.

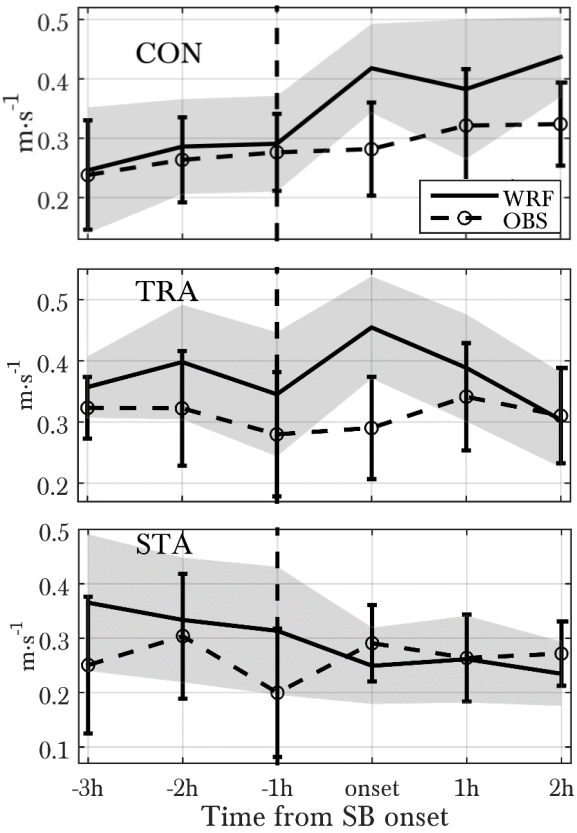

Figure 5.5: Time evolution of the average friction velocity and its standard deviation between 2 h before and 2 h after the onset of SBs for the 21 coincident SB days, separated in the three ABL regimes (convective, transition and stable). The dashed vertical line identifies the 1-h measurement just before the onset, which occurs between the dashed line and time = 0

However, the greater vertical mixing in the model compensates the underestimation of the wind prior to the SB onset, and hence the values of u_* are similar before the arrival of the SBF. The value of u_* is overestimated around 50% at the moment of the onset in the transition regime. In the previous chapter we proved how the increase of the shear induced by the SBF resulted in an acceleration of the AT, so that the stable stratification was established before. The increase of mechanical turbulence is greater in the model, which explains the sharper AT taking place in the numerical simulations (Fig. 5.4). However, the overestimation of local turbulence after the SB onset is not present in the stable regime, and the simulated u_* follows the observed one. In any case, the different variables represented in Fig. 5.4 indicate that the lower

atmosphere evolves in a distinct way once the stable conditions are achieved. As we concluded from Fig. 4.9 the onset of the SB in the stable regime brings the wind profile within the surface layer out of the equilibrium with local turbulence. Since the ABL parameterisations in WRF are based on MOST formulation, discrepancies can be expected in the evolution of distinct atmospheric variables during the ET when the SBF arrives within this stage.

5.5 DISCUSSION AND FUTURE RESEARCH

After evaluating the performance of the WRF mesoscale model in reproducing the main observed SB characteristics and their impacts on local meteorological and turbulence conditions in Cabauw, new research prospects emerge.

Firstly, by applying the SB selection algorithm to the variables from the numerical simulations, we have verified how several discordances exist regarding the correct representation of the relevant forcings for SB formation. The algorithm has enabled us to study whether these disagreements depend on the synoptic conditions or more local features. For instance, the SB filtering shows a discordance of around 25% in terms of large-scale conditions. Future research should be focused on investigating the large-scale conditions which give rise to a greater rejection of events. On the other hand, the last filter of the algorithm shows a great discrepancy when applied to the simulations contrasting to the observations. Further investigation exploring whether the wind-direction shift associated with the SBF passage is correctly represented in the model should be carried out. This information is highly valuable for a correct forecasting of SB phenomena in numerical weather prediction models.

Secondly, we have found a disagreement in the temporal distribution of SB directions, which suggests a connection with an overestimated magnitude of the Coriolis terms in the momentum budget. To shed light on this issue, hodographs of the wind components can be calculated to infer the influence of the Coriolis forcing in the wind-direction veering at the termination of the SB. Since the influence of the topography in driving additional thermally-driven circulations is negligible, large-scale pressure forcings could also be determinant to explain the veering of the wind.

Finally, during daytime WRF strongly overestimates the SH flux, which induces also an enhancement of the vertical mixing in the numerical simulations. This enhanced vertical mixing is probably responsible for the stronger SBFs reproduced in the model. This hypothesis could be supported by the analysis of temperature and wind fields in the coastal area. On the other hand, just the weakest observed SBFs are coincident with the simulated events that pass the selection algorithm. The intensity of these weak SBFs is overestimated in the model, and partly linked with it, the AT and ET of the ABL occur faster than in the observations. Next steps will pursue the investigation of ABL parameterisations and they performance when local turbulence is affected by the passage of the mesoscale flow.

6 WEAK AND INTENSE KATABATICS: INFLUENCE ON TURBULENCE AND CO_2 TRANSPORT

The role of katabatic flows in the dynamics and turbulent features of the SBL is investigated using observations from La Herrería Site. Forty katabatic events are selected from an observational database spanning the period of Summer 2017, by using an objective and systematic algorithm that is able to account for local and synoptic forcings. We subsequently classify the katabatic events into weak, moderate and intense according to the observed maximum wind speed. This classification enables us to contrast the main differences in dynamics and thermal structure. We find that the stronger katabatic events are associated with an earlier onset time of these flows. We relate it to very low soil-moisture values (< 0.07 m^3 m^{-3}, i.e. smaller than the median during the analysed period) and a weak synoptic wind (V_{850} < 6 m s^{-1}) having the same direction as the katabatic. The relative flatness of the area favours the formation of VSBLs characterised by a longwave radiative cooling of around 60-70 W m^{-2} and very weak turbulence (u_* < 0.1 m s^{-1}). They occur when katabatics are weak, and are occasionally associated with the formation of skin flows, that are manifested as weak jets (U < 1 m s^{-1}) at 3 m. Intense katabatics, instead, are characterised by a strong and increasing bulk shear (the maximum u_* is close to 1 m s^{-1}) that avoids the development of the surface-based thermal inversion, giving rise to the so-called WSBL. We identify the transition between the two regimes for a threshold katabatic wind speed of around 1.5 m s^{-1}, in agreement with the hockey-stick transition hypothesis. Our analysis is extended by calculating non-dimensional numbers to characterise the transition: the SC, R_B and z/L. On the other hand, by inspecting individual weak and intense events, we further explore the interaction between katabatic flows and turbulence, and the impact on CO_2 concentration. By relating the dynamics of the two regimes with the CO_2 budget, we are able to estimate the contribution of the different terms. For the intense event, indeed, we infer a horizontal transport of 67 ppm in 3 h driven by the katabatic advection.

The main contents of this chapter are under review in:
Arrillaga, J.A., Yagüe, C., Román-Cascón, C., Sastre, M., Maqueda, G, and Vilà-Guerau de Arellano, J. Weak and intense katabatic winds: impacts on turbulent characteristics in the stable boundary layer and CO_2 transport. *Atmos. Chem. Phys. Discuss.*, https://doi.org/10.5194/acp-2018-944, in review, 2018.

6.1 INTRODUCTION

In this chapter we investigate the main features of katabatic winds, their influencing factors and their role during the AET of the ABL affecting the turbulent characteristics of the SBL and the transport of CO_2. We first explore the influence of external factors, particularly how soil moisture and the large-scale wind affect the onset time and intensity of katabatic winds, from an observational analysis of several katabatic events. Our second aim is to investigate the direct implication of katabatic winds generated by the presence of steep topography on the occurrence of the two SBL regimes. A relevant aspect of our site is its location in a relatively small flat area nearby the mountain range. We therefore encounter a scenario different from other sites located at slopes where the SBL barely becomes very stable, since the shear production linked with the katabatic is large and continuous, and buoyant turbulence production may occur even when the stable stratification is present (Oldroyd et al., 2016). At out site, however, VSBLs associated with relatively strong surface-based thermal inversions take place occasionally. Besides, over flat or almost flat terrain universal scaling according to MOST can be applicable and corrections due to measuring over a slope are not required (Stiperski and Rotach, 2016). Finally, connected also to the dynamics of the SBL, we approach another relevant issue on this topic: the impact of katabatic winds on the CO_2 mixing ratio.

The main aspects motivating research in this study are summarised in the following research questions:

RQ 6.1: *Which are the external factors that modulate the onset of katabatic flows and yield to different intensities?*

RQ 6.2: *How does the interaction between katabatic winds and local turbulence occur and which is the implication on turbulent characteristics in the SBL?*

RQ 6.3: *What is the role of katabatic advection and local turbulent fluxes, associated with the distinct SBL regimes, in the variability of CO_2?*

OUTLINE We detail the observational data employed in Sect. 6.2. Section 6.3 describes the main characteristics of the katabatic events and analyses the influencing factors. We pursue the interaction with turbulence and the link with the different regimes in the SBL in Sect. 6.4. Section 6.5 deepens the analysis by inspecting two individual events in detail, and estimates the contribution of the horizontal transport to the variability of the CO_2. We finish with the relevant conclusions.

6.2 DATA

6.2.1 Observations

The analysis is carried out during the summer months, particularly in Summer 2017, which was very warm and very humid (AEMET, 2017) in this region, following a very warm and very dry spring. In any case, it was not a particularly rainy season and in fact, precipitation during Summer 2017 took place just over a few days, so that the dessicated soil experienced sharp moisture increases. As explained in Sect. 2.2.3, small amounts of precipitation in La Herrería can significantly impact the SEB, and as a consequence the intensity of katabatic flows.

EC and meteorological measurements (including CO_2) were carried out over the warmest and driest season of the year, when thermally-driven slope winds are strongest and weak large-scale winds prevail. In particular, measurements were recorded over an intensive campaign in Summer 2017 (22/06–26/09), with supplementary vertical levels. Table 6.1 gathers specifications about the devices and the variables employed in this study. The atmospheric non-turbulent variables have a sampling rate of 1 Hz, whereas turbulent variables of 10 Hz. All the variables employed in this analysis are averaged over 10 min.

Table 6.1: Technical specifications about the variables measured and the devices employed over the intensive Summer 2017 campaign.

Variable	Height (m, agl)	Instrument	Model
Air Temperature*	3, 6, 10	Aspirated thermometer	Young 41342
Wind speed	3, 6, 10	Cup anemometer	Vector A100LK
Wind direction	10	Wind vane	Vector W200P
Turbulent fluxes**	4, 8	IRGASON***	Campbell
Rain	surface	Pluviometer	OTT Pluvio²
Soil moisture****	-0.04	Reflectometer	CS655
Soil-heat flux	-0.04	Heat-flux plate	Hukseflux HFP01SC
Radiation components	2	4-component radiometer	Hukseflux NR01
CO_2 concentration	4, 8	IRGASON	Campbell

* The sampling rate of atmospheric non-turbulent variables is of 1 Hz.
** The averaging period of the turbulent fluxes is 10 min.
*** The sampling rate of turbulent variables is of 10 Hz.
**** The sampling rate of soil variables is of 10 min.

6.2.2 Katabatic-event selection

In order to select the katabatic events we follow the research strategy from the analysis of SB phenomena in the previous chapters. To that end, we perform an objective and

systematic detection by employing the algorithm described in Sect. 2.3.3 (see katabatic criteria in Table 2.2). In this way, we evaluate the characteristics and impacts of the katabatic flows in a more robust and objective way. Besides, the algorithm defines a benchmark which is the onset of the katabatic flow, enabling the clustering of different events and their analysis in a consistent way.

The katabatic flow usually lasts until sunrise, when a strong veering of the wind direction occurs. However, in this study we just focus on the first stage of these flows, since the main objective is to investigate their connection with the onset of the SBL (defined as when the SH flux, H, turns negative), and the different regimes associated. During the summer months, the katabatic onset usually takes place around 1800 UTC, i.e. before sunset, but it can be considerably advanced or delayed depending on a number of factors, which are investigated in Sect. 6.3.2. A wide variability in the onset time of the katabatic flow was also reported in the studies from Pardyjak et al. (2009) and Nadeau et al. (2013) for instance.

We identify the onset of the katabatic flow as the first value within the 2-h range of continuous katabatic direction. Having that onset time as a reference, we explore the characteristics of katabatic flows, their interaction with turbulence and the impact on CO_2 in the next sections.

6.3 CHARACTERISTICS OF THE KATABATIC FLOWS

Forty were selected as days with the formation of katabatic events from the analysed summer period with available data (94 days in total). The algorithm is very rigorous to ensure that the selected events are strictly thermally-driven downslope flows and not dynamically driven, since we just focus on the days with a weak large-scale wind in which there is a shift from the daytime upslope to the night-time downslope wind direction. The results presented hereinafter are related to these 40 katabatic events.

6.3.1 Wind direction and intensity

Fig. 6.1 shows the direction and intensity of the katabatic events over the 2-h period subsequent to the onset of the downslope flow. The mean katabatic direction is around 290–300° and the variation around this direction is small; the largest oscillations in the direction are observed for weak intensities. Within the database of the 40 events we find diverse cases depending on the maximum intensity of the katabatic flow. We represent in Fig. 6.2 the wind vertical profile at the time of the katabatic onset (a) and when the katabatic intensity is maximum (b) using box plots, which contain information about the frequency distribution at each observational level (3, 6 and 10 m). At the time of the onset the katabatic flow is weak at all levels (Fig. 6.2a); for instance the median at 10 m is slightly over 1 m s^{-1}. It can be noted that the median at 3 m is

similar to that at 6 m, and the first quartile is even smaller at 6 m. This occurs because prior to the identified onset at 10 m a very shallow katabatic or a skin flow is usually developed, and is only reflected at 3 m (as observed for instance in Román-Cascón et al. (2015)). This skin flow can be observed when turbulence is very weak and thermal stratification is very stable (Mahrt et al., 2001; Soler et al., 2002), and occasionally gives rise to a greater wind speed at 3 than at 6 m, and a few times even greater than at 10 m. However, when the katabatic flow is more intense, wind speed increases with height within the 10-m layer from the surface (for instance note that the third quartile is greater at 6 than at 3 m). A maximum jet is probably found above 10 m.

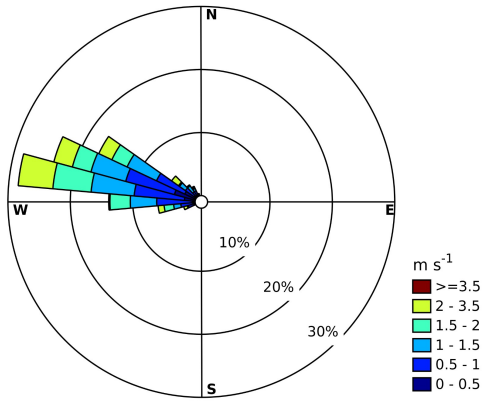

Figure 6.1: Wind rose at 6 m over the 2 h after the onset of the katabatic flow for the 40 selected events.

We represent in Fig. 6.2b the intensity distribution at all levels when the maximum event intensity at 6 m is observed. We find in this case that the distribution above the median is elongated at all levels. In fact, the level of 6 m is employed to classify katabatic events according to the their maximum intensity and the associated erosion of the surface-based thermal inversion. The reasons for employing the level of 6 m are outlined below. Firstly, red crosses pinpoint an event identified as an outlier due to its high intensity at all levels (e.g. $U > 6$ m s^{-1} at 10 m). Together with the wind maximum, the surface thermal inversion is very weak or non-existent, and the maximum of turbulence measured from the TKE and u_* is even greater than the daytime maximum of the typical diurnal cycle (generally $u_* \simeq 0.5$–0.7 m s^{-1}). We find in addition two other events with the above-mentioned features which are included within the right whisker. These three events are classified hereinafter as intense katabatics, and they all meet that the maximum 10-min wind speed at 6 m is greater than 3.5 m s^{-1}. It must be noted that this threshold is not very high, but in the context of a weak synoptic forcing and comparing to the rest of katabatic events, we can consider them to be relatively

(a) Onset

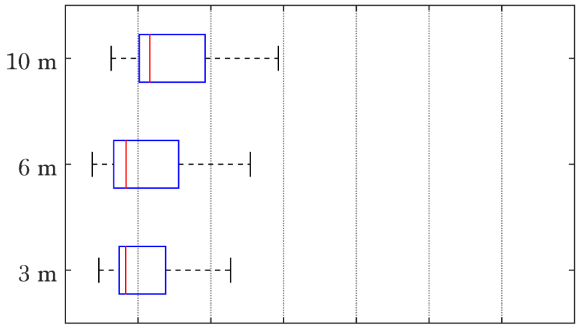

(b) Maximum intensity (considering values at 6 m).

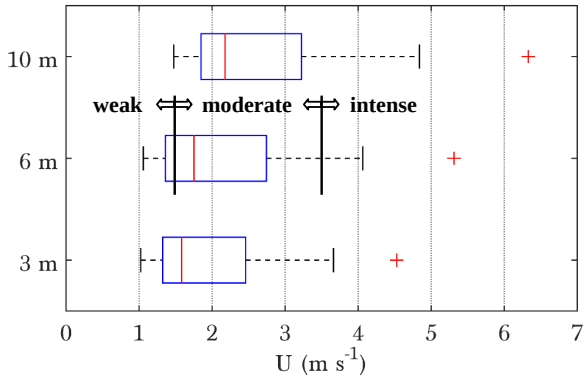

Figure 6.2: Box plots of the 10-min wind speed profile at 3, 6 and 10 m for the katabatic events, (a) at the time of the onset and (b) for the maximum value (from the onset till 2400 UTC) for each level. The red vertical line within blue boxes represents the median, the blue box delimits first and third quartiles, and whiskers delimit the most extreme points not considered outliers (red crosses). Black vertical lines pinpoint the limits for the wind speed at 6 m that separate weak, moderate and intense katabatics.

intense. Secondly, in some events turbulence is very low and the surface-based thermal inversion is not eroded ($u_* < 0.1$ m s^{-1}). They all occur when wind speed is very weak, and hence we classify as weak events (14 in total) those in which the maximum wind speed at 6 m is below 1.5 m s^{-1}. The cases in which the maximum wind speed at 6 m is between 1.5 and 3.5 m s^{-1} are classified as moderate katabatics (23 in total). A summary of the classification is shown in Table 6.2. We employ the level of 6 m for the classification, since at 3 and 10 m the events showing different features cannot be so

clearly detached. Flocas et al. (1998) for instance studied katabatic flows at a similar height (7 m), since the influence of the large-scale wind was minimised at this level.

Table 6.2: Classification of katabatic types according to their maximum 10-min averaged wind speed at 6 m from the onset until 2400 UTC.

Type	Definition
Weak	$U_{max} < 1.5$ m s^{-1}
Moderate	1.5 m s^{-1} $\leqslant U_{max} \leqslant$ 3.5 m s^{-1}
Intense	$U_{max} > 3.5$ m s^{-1}

This classification is employed in the following sections to better illustrate the differences between the katabatic events, and the very distinct way in which they interact with local turbulence (in particular this is addressed in Sects. 6.4 and 6.5).

6.3.2 Factors influencing intensity

Once the katabatic events are classified according to their maximum intensity, we explore the factors that induce different intensities. Fig. 6.3 shows a histogram with the difference between the onset time of the katabatic flow and sunset time (it ranges from 1810 UTC in September to 1940 UTC in June), for different intensities in colours, and in lines for a different static stability of the thermal profile at the moment of the onset. The static stability was estimated by fitting the virtual potential temperature at the different vertical levels (surface, 3, 6 and 10 m) to a logarithmic profile, as explained in detail in Appendix B. The surface radiometric temperature was calculated from the upward longwave radiation by employing the Stefan-Boltzmann law.

From the classification introduced in Appendix B and particularising for the moment of the katabatic onset, we infer the relationship between the earlier or later onset of the katabatic wind, static stability at the onset and the intensity of the flow. On the one hand, intense katabatics develop when the onset takes place prior to 2 h before sunset and the thermal profile in the first 10 m is still unstable. On the other, weak katabatics occur when the onset takes place later than 2 h before sunset and the profile is neutral or stable. Moderate katabatics, however, can occur either earlier or later independently of the static stability.

Linked with the three different static stabilities, we explore the influence of the TKE at the onset of katabatic flows from Fig. 6.4a. By representing the maximum katabatic intensity at 6 m with respect to the TKE at the onset, two main groups result. In one of them TKE is very low at the onset (of the order or smaller than 0.1 m^2 s^{-2}), which includes all the weak katabatics. This group is associated with a later onset of the katabatic flow (Fig. 6.3), when the the thermal profile is already neutral or stable and $R_{net} < 40$ W m^{-2} always; it is in fact negative in more than 80% of the cases. On the other group, TKE is about one order of magnitude greater and includes all the intense

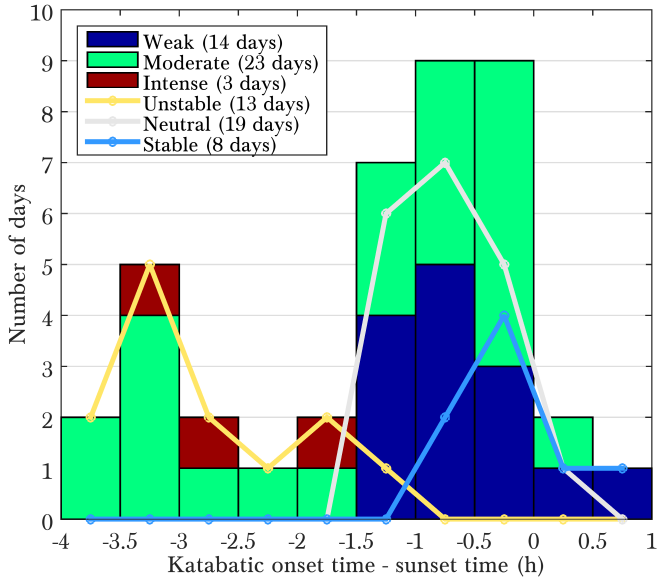

Figure 6.3: Histogram of the difference between the katabatic onset time and sunset time, for the three groups of intensities (bars) and for different thermal stratification at the moment of the onset (lines).

events, which are related with an earlier katabatic onset, when the thermal profile is already unstable. R_{net} is in fact always > 80 W m^{-2} at the onset.

This result implies that there is a strong relation between katabatic flows and turbulence, which is essential to fully understand their nature and development. This aspect is further addressed in Sect. 6.4. Regarding the moderate katabatics, we separate them into two subgroups: $U_{max} \leqslant 2.5$ m s^{-1} (triangles pointing downward) and $U_{max} > 2.5$ m s^{-1} (triangles pointing upward). Even though the weaker moderate katabatics are mostly related with the stable and neutral thermal profile and the more intense moderate with an unstable profile, the opposite occurs also in few of the cases. This result suggests the existence of external factors affecting the earlier or later onset of katabatic winds. For the reasons outlined in the introduction, we investigate two factors: soil moisture and the large-scale wind.

To explore the influence of the soil moisture, we define an index that provides a measure of the relative dessication of the soil over the summer. This soil-moisture index is defined as the ratio between the observed liquid water volume and the maximum value throughout the analysed period (0.14 m^3 m^{-3}): $SM_i = SM/SM_{max}$. We separate the events into drier ($SM_i \leqslant 0.5$) and moister ($SM_i > 0.5$) cases. On the other hand, to explore the influence of the large-scale wind ($V_{850,18}$: at 850 hPa at 18 UTC) despite

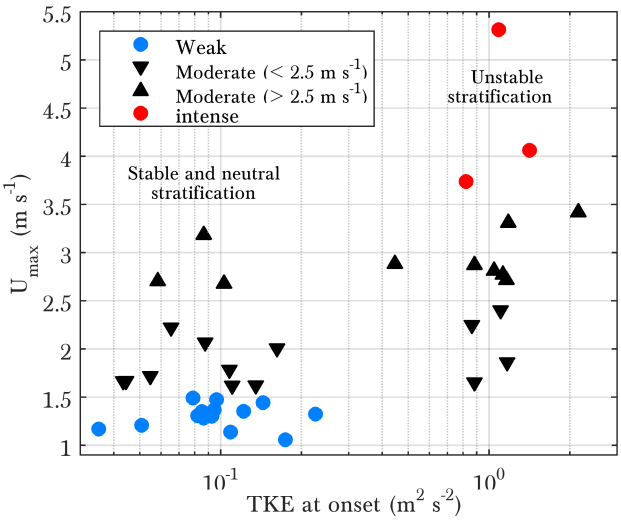

Figure 6.4: Maximum wind speed (U_{max}) at 6 m for each katabatic event *versus* TKE at 8 m at the moment of the katabatic onset. Note that moderate katabatics are divided into two subgroups.

its low intensity required by the selection algorithm, we separate the katabatic events into very weak ($V_{850,18} \leqslant 3.5$ m s^{-1}) and weak ($V_{850,18} > 3.5$ m s^{-1}) synoptic forcing.

The influence of the large-scale wind speed and direction, and soil moisture are investigated in Fig. 6.5. The maximum katabatic intensity at 6 m together with the direction of the synoptic wind are represented in wind-rose form for the above-mentioned drier (a,b) and moister (c,d) cases, and for a very weak (a,c) and weak (b,d) synoptic forcing. The synoptic wind is estimated from the NCEP reanalysis wind speed employed in the selection algorithm, by choosing the grid point at 850 hPa closest to La Herrería (40.5° N, 4° W) at 18 UTC. At that point, the 850-hPa level is approximately at 800 m agl, sufficiently close to the surface as to be representative of the synoptic wind at the surface level, and far enough as to be out of the influence of katabatic flows.

We find that intense katabatics (orange-reddish) develop when the soil is drier, the large-scale wind is weak and blowing from the N-NW (Fig. 6.5b). This direction is perpendicular to the mountain range axis (Fig. 2.4a), and approximately coincident with the katabatic direction (Fig. 6.1). However, under those conditions we find weak katabatics (dark blue) when the large-scale wind blows from parallel or opposite directions (S or E-NE for instance), although most of the weak katabatics occur mainly when the soil is moister and the synoptic forcing is very weak (Fig. 6.5c). Weak katabatics establish primarily for W-SW and S-SE large-scale winds, but they can also occur

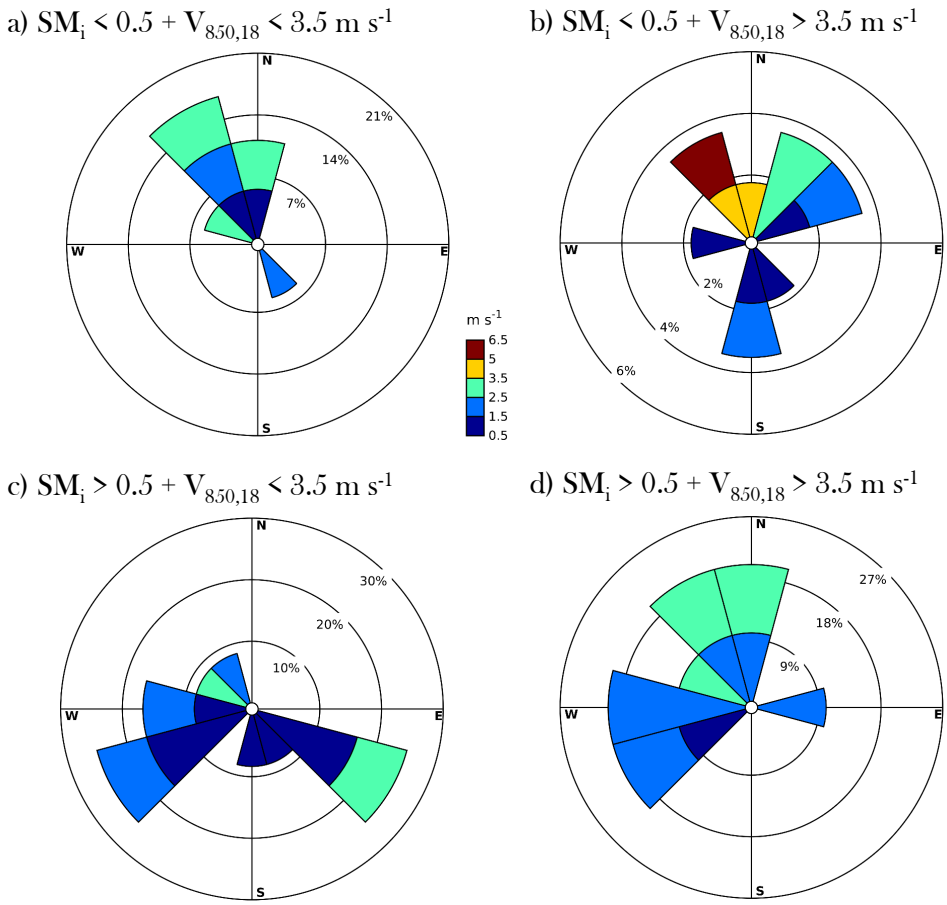

Figure 6.5: Wind roses representing the maximum katabatic wind speed at 6 m in colours, for different directions from the NCEP-reanalysis wind at 850 hPa, at the closest grid point to La Herrería (40.5°N, 4°W) at 18 UTC. Wind roses are shown for different values of the soil-moisture index (SM_i) and the reanalysis wind speed ($V_{850,18}$) (a-d). Note that the frequency scale of the wind roses is variable.

for N-NW winds when their intensity is very weak (Fig. 6.5a). Overall, the intensity of katabatics increases with decreasing soil moisture, and increasing synoptic forcing with a N-NW direction.

To study the role of the soil moisture and the relative dessication of the soil in the SEB, we represent the observed average G and longwave-radiative loss (LWU–LWD) during the katabatic stage with respect to the SM_i in Fig. 6.6. To better show the trends of the scatter plots, an eighth-order polynomial fit has been added. In particular, we find that above a fourth-order polynomial fit the bimodal behaviour of the

scatter in maintained. While from the fourth- up to the seventh-order polynomial the goodness of the fit barely improves, the scores increase for the eighth-order polynomial fit, confirming the bimodal nature of the correlation. Both G and $LWU–LWD$ show two maxima for high and low SM_i, at around 0.9 and 0.25–0.4 respectively. However, whilst the correlation is statistically significant with a confidence level of 95% in the case of G *vs* SM_i, the confidence level has to be lowered down to 90% in order to be statistically significant in the case of $LWU–LWD$ *vs* SM_i. That worse correlation in Fig. 6.6b is reflected in the lower value of r^2.

The peak for low SM_i is more pronounced in both plots, and implies that the cooling of the soil is stronger when the relative dessication is higher, since the average G is positive (opposing $G < 0$ for the secondary peak) and the longwave-radiative loss is greater. However, when the soil moisture increases considerably after precipitation has occurred ($SM_i \simeq 0.9$), the cooling of the soil can also be enhanced, inducing an enlarged thermal contrast between the slope and the overlying air layer, and therefore contributing to the intensification of the katabatic flow. The contrasting findings from Banta and Gannon (1995) and Jensen et al. (2017a) for the impact of the soil moisture in the katabatic intensity could be explained by this complex correlation.

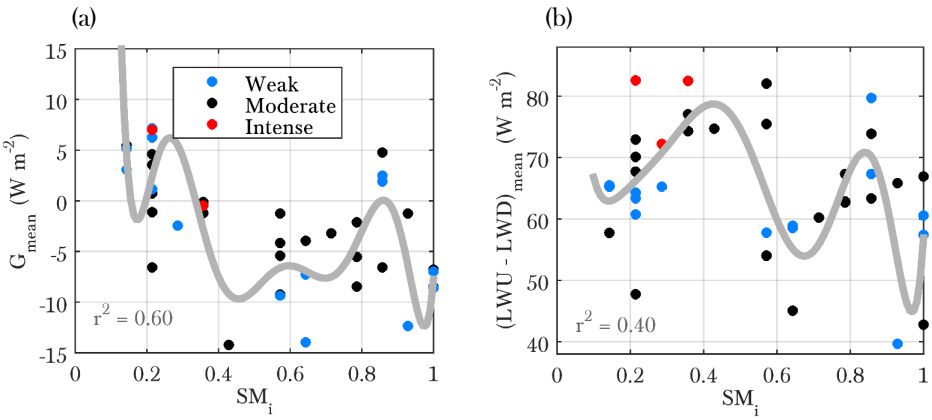

Figure 6.6: (a) Average soil-heat flux (G) and (b) longwave-radiative loss ($LWU–LWD$) during the katabatic stage (from the onset until 2400 UTC) *vs* the soil-moisture index (SM_i). The grey line represents the eighth-order polynomial fit of the data. The square of the multiple correlation coefficient (r^2) for the fit is included.

Overall, we find that the combination of low soil moisture and synoptic wind direction coincident with the downslope direction (N-NW) induces an earlier onset of katabatic flows, when stratification is still unstable and convective turbulence relatively strong, which facilitates the development of intense katabatic flows. If those conditions are not met, the onset occurs later when stratification is already neutral or stable, which limits the intensification of katabatic flows. Nevertheless, sharp enhance-

ments in the soil moisture due to precipitation can give rise to a stronger cooling of the soil and an earlier onset of the katabatic flow. To understand the evolution of katabatic flows after their onset we explore their interaction with turbulence in the next section.

6.4 INTERACTION BETWEEN KATABATICS AND TURBULENCE

Thermal stratification and the associated turbulence at the moment of the onset modulate the intensity of the katabatic flow. If the katabatic flow arrives when the stratification is still unstable and the surface thermal inversion (hereinafter measured from $\Delta\theta_v$) is not formed yet, the shear associated with the katabatic flow increases, and the downslope flow strengthens progressively. Later, due to the radiative energy loss ($R_{net} < 0$) the stable stratification is already established ($\Delta\theta_v > 0$). Given that turbulence associated with wind shear is already high, the negative H strengthens ($H < 0$) and after a while compensates the energy loss at surface, impeding the development of the surface-based thermal inversion and inducing near-neutral stability conditions (Van de Wiel et al., 2012b). In that way, intense katabatics give rise to a WSBL. On the other hand, if the katabatic wind arrives later and thermal stratification is already neutral or stable, the increase of shear is limited by the stable stratification itself. Thus, even the maximum sustainable heat flux does not compensate the radiative energy loss. Consequently, the bottom of the SBL cools down, which contributes to enhance the stable stratification. This positive feedback occurring under weak katabatics suppresses turbulence and gives rise to a VSBL (Van de Wiel et al., 2012a). For moderate katabatics, any of the two regimes can occur depending on the onset time and the SEB. These mechanisms are explored below by means of measured variables and calculated non-dimensional relevant parameters.

6.4.1 Turbulence regimes in the SBL

Figure 6.7 shows the temperature stratification $\Delta\theta_v = \theta_v(10\text{ m}) - \theta_v(3\text{ m})$ and the turbulence velocity scale V_{TKE} *vs* U at 6 m. In this and subsequent figures we only represent the 10-min average values (just until 2400 UTC) in which the wind direction is katabatic and H is negative, so that the katabatic flow is present and the SBL is already established. V_{TKE} is calculated as the square root of the TKE (see Eq. 2.3). By representing $\Delta\theta_v$ *vs* U we find a contrasting relationship for weak and intense katabatics (Fig. 6.7a). Weak katabatics give rise to a strongly stratified SBL ($\Delta\theta_v$ up to 2 K), whereas intense katabatics are linked with very weak or almost non-existent surface-based thermal inversions. Interestingly, for a few 10-min values with similar wind speed ($U \simeq 1$–1.5 m s^{-1}) the thermal stratification is very different between weak and intense katabatics, which suggests the existence of distinct regimes in the SBL. On the other hand, we find for very weak wind speed ($U < 1$ m s^{-1}) a large variability of

thermal stratification, that occurs because around the onset of katabatics the thermal inversion is still absent or very weak in most of the cases. At the upper limit, however, $\Delta\theta_v$ tends to zero when wind speed increases its value. Moderate katabatics show both types of behaviour, with the transition taking place for $U \simeq 1.5$ m s^{-1}.

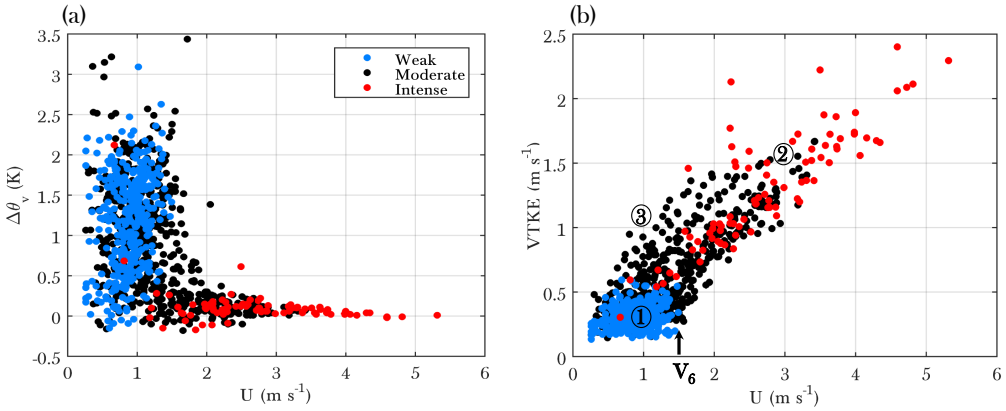

Figure 6.7: (a) Temperature stratification ($\Delta\theta_v$) and (b) turbulence velocity scale (V_{TKE}) at 8 m *versus* wind speed (U) at 6 m. The numbers pinpoint the SBL regimes defined in Sun et al. (2012): (1) weak turbulence driven by local instabilities, (2) intense turbulence driven by the bulk shear, and (3) moderate turbulence driven by top-down events. The threshold wind-speed (V_6) at which the HOST transition occurs is indicated too.

By representing the turbulence strength V_{TKE} *vs* U at 6 m we confirm the sharp transition for $U = 1.5$ m s^{-1} (Fig. 6.7b). Weak katabatics are associated with very weak turbulence ($V_{TKE} < 0.5$ m s^{-1}) that hardly increases with wind speed, while turbulence for intense katabatics is considerably greater and increases linearly with U. This behaviour was first observed in Sun et al. (2012), and defined as the HOckey-Stick Transition (HOST) in Sun et al. (2015). They identified three turbulence regimes in the SBL depending on the relationship between turbulence and wind speed. In regime 1 turbulence is very weak and generated by local shear; in regime 2 turbulence is strong and generated by the bulk shear U/z (hence the linear relationship with wind speed); and finally, in regime 3 turbulence is moderate and mainly generated by top-down turbulent events. The three regimes are pinpointed in Fig. 6.7b. The threshold value for the wind speed depends on height, and sets the value above which the abrupt transition from regime 1 to regime 2 occurs. Since in our case $z = 6$ m, it is indicated as V_6 in the figure. Weak katabatics are clearly associated with regime 1 and intense katabatics, instead, with regime 2. Moderate katabatics can give rise to either the three of the regimes. We just show the relationship for $z = 6$ m, and HOST in our case occurs for $V_6 = 1.5$ m s^{-1}, which is significantly lower than the value at that height from Sun et al. (2012) ($\simeq 3$ m s^{-1}) over relatively flat and homogeneous terrain (Poulos et al., 2002). Besides, V_6 coincides with the threshold value we anticipated for defining weak

katabatics (Table 6.2). We measure a slope of ~0.5 for V_{TKE} *vs* U for regime 2, while is of ~0.25 in the results from Sun et al. (2012).

In Fig. 6.8 we explore how katabatic intensities and turbulence strength are manifested in terms of SH flux. The downward H (i.e. when the SBL is already established: $H < 0$) is represented with respect to U at 6 m in Fig. 6.8. The smallest H values are observed for weak katabatics, when $U < 1$ m s^{-1}. The highest values take place for moderate katabatics when U lies between 1.5–2.5 m s^{-1}. We find a few data from some intense katabatics in which H is nearly 0 for that wind-speed range, when the thermal inversion is still very weak. For intense katabatics the peak is reached at $U \simeq 3$ m s^{-1}, and above that intensity H decreases, since it is limited by the neutral stratification. One of the key questions is whether this heat flux is able to compensate the surface radiative loss. This matter is addressed later in Sect. 6.5.1 by analysing the time evolution of the SEB on individual events.

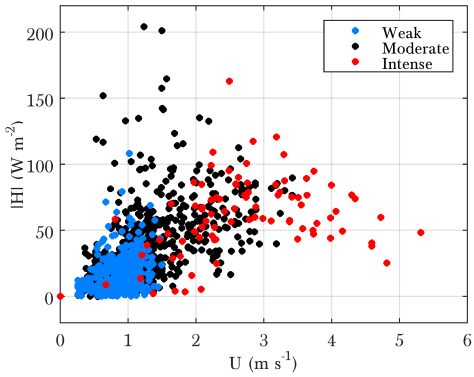

Figure 6.8: Absolute value of the SH flux (H) *vs* wind speed (U) at 6 m.

6.4.2 Regime transition from non-dimensional parameters

We have observed in Sect. 6.4.1 that the nocturnal regime can be predicted from the katabatic intensity at 6 m. In fact, by knowing in advance its maximum value during the night we can foresee whether the katabatic wind will give rise to a VSBL or a near-neutral regime within the SBL. In Fig. 6.9 we characterise the regime transition from relevant non-dimensional numbers by representing V_{TKE} at 4 and 8 m as a measure of turbulence intensity with respect to three nondimensional parameters, both local and non-local. As stated in Sun et al. (2016), MOST is only applicable in a thin layer above the surface (up to approximately $z = 10$ m) during SBL conditions. Since our measurements do not exceed that height, we can assume that MOST is valid in the subsequent calculations.

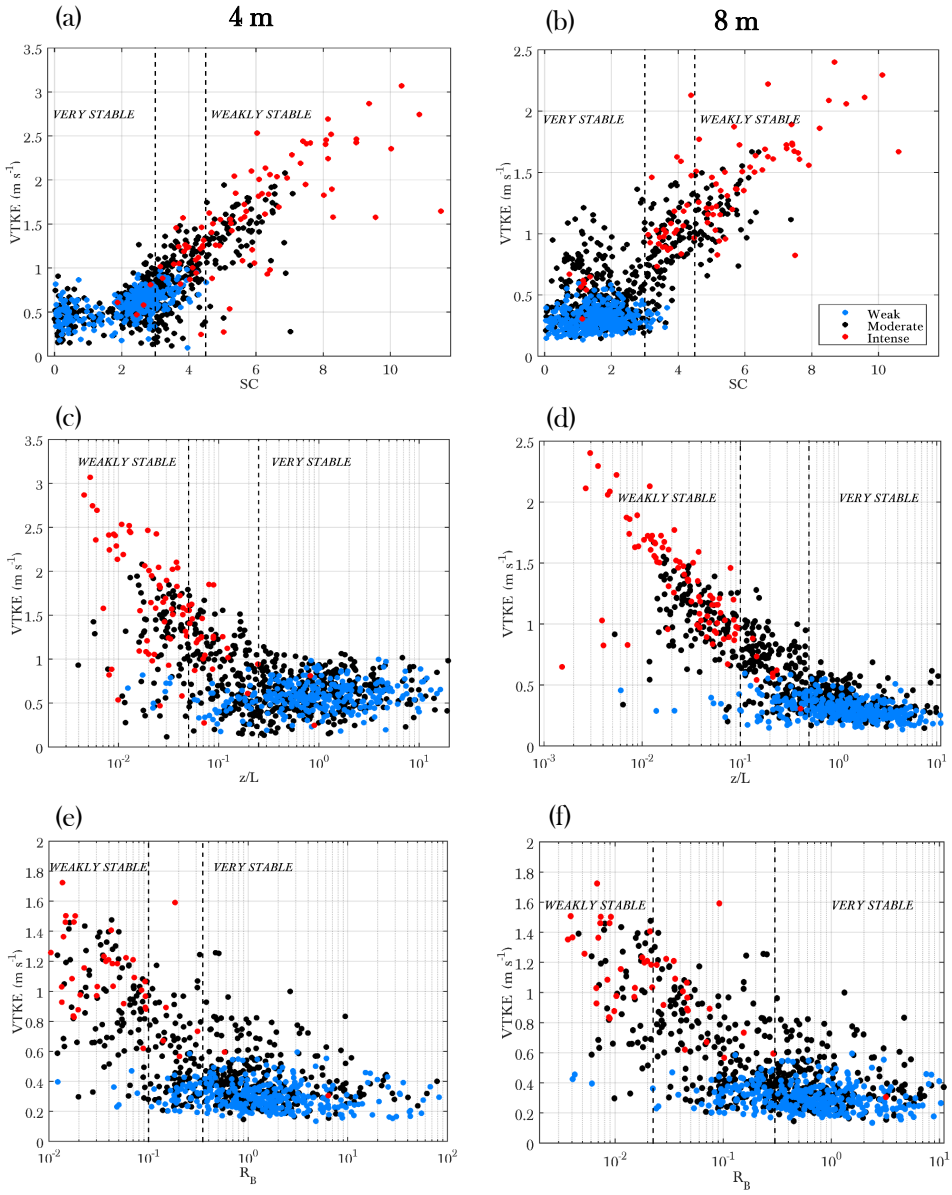

Figure 6.9: V_{TKE} at z = 4 and 8 m as a function of different non-dimensional parameters: SC (a,b), z/L (c,d) and R_B (e,f). The colour legend is shown in Fig. 6.7. Vertical dashed lines represent the values of the non-dimensional parameters that delimit the very stable and weakly stable regimes in the SBL.

First, we investigate the use of a non-local parameter: the SC. This dimensionless quantity was introduced in Chapter 4 (Eq. 4.13), and it compares the measured shear with the minimum shear required to maintain a continuously turbulent state, which is given by the heat-flux demand (HFD) at the surface. The HFD is calculated from the SEB as $HFD = R_{net} - G - LH$. Since turbulence responds to the bulk shear instead of the local shear for a wind speed $U > V_6 = 1.5$ m s^{-1}, we re-define the SC in this study as:

$$\begin{aligned} SC(U < 1.5\ \mathrm{m\ s^{-1}}) &= \left\{ \frac{\rho c_{pd} (\kappa z)^2 \left(\frac{\partial U}{\partial z}\right)^3}{g/\theta_v(z)\ |HFD|} \right\}^{1/3}, \\ SC(U > 1.5\ \mathrm{m\ s^{-1}}) &= \left\{ \frac{\rho c_{pd} (\kappa z)^2 \left(\frac{U}{z}\right)^3}{g/\theta_v(z)\ |HFD|} \right\}^{1/3}. \end{aligned} \tag{6.1}$$

θ_v is the virtual potential temperature, κ is the von Kármán constant (=0.4), z is the height agl, $\partial U/\partial z$ is the local shear, U/z the bulk shear, g the gravitational acceleration (9.81 m s^{-2}), ρ is the air density, c_{pd} the specific heat at constant pressure (= 1005 J kg^{-1} K^{-1}) and $|HFD|$ is the absolute value of the HFD at surface, since SC is defined only when $\overline{w'\theta_v'} < 0$. $\partial U/\partial z$ was computed by fitting the wind measurements at 3, 6 and 10 m to a log-linear profile as in Eq. 2.4.

van Hooijdonk et al. (2015) observed over flat and homogeneous terrain that independently of the measurement height they could define a SC value ($\simeq 3$) for which the transition from very-stable (low SC values) to weakly-stable conditions (higher SC values) occurred. In this work we calculate the SC at 4 and 8 m (Fig. 6.9a and b respectively), and we find two transitions (indicated with dashed vertical lines): the first at SC = 3 above which both SBL regimes are almost equally found, and the second at SC = 4.5, over which the SBL is always weakly stable. The observed transition is independent of height, but we are unable to select a single value for separating the weakly stable and very stable regimes. Instead, the shift between the regimes seems to occur along a transition regime, within which both intense a weak katabatics are observed. The transition is directly related with the HOST hypothesis, given that the SC is predominantly dominated by wind shear. As a matter of fact, the hockey-stick shaped plot of Fig. 6.9b resembles Fig. 6.7b, except that the regime transition is sharper for the SC: intense and weak katabatics cluster into two clearly distinct regimes according to the dependence on local or bulk shear. The transition is less sharp at 4 m, since at this level local and bulk shear are closer than at 8 m.

Two other local non-dimensional numbers are investigated: z/L and R_B. They are frequently employed in the literature as stability parameters and turbulence-production indicators, with local significance. As occurs for the SC, when representing V_{TKE} *versus* z/L and R_B at 4 and 8 m the transition occurs over a range of values. This transition region was also observed by Mahrt (1998). He found at 10 m that $z/L = 0.065$ is the limit for the WSBL and $z/L = 1$ for the VSBL. We set respectively these values at 0.05 and 0.25 at 4 m (Fig. 6.9c), and 0.1 and 0.5 at 8 m (Fig. 6.9d), the latter coinciding

with the value found by Högström (1996). This threshold appears to be very strong, since above it no intense katabatics are found. The regime transition is fuzzier for R_B, in particular the threshold for the WSBL is difficultly identified (Figs. 6.9e and f). However, it should be taken into account that by definition this non-dimensional parameter estimates wind shear from finite differences in height. It does not consider whether wind shear is produced by bulk or local shear, and it will be closer from one or the other depending on the vertical-level separation. In any case, we find that at $\sim R_B$ = 0.3–0.35 turbulence production has decayed so that the VSBL is established, between the measured critical values for the gradient Richardson number Ri_c = 0.25 and bulk Richardson number R_C = 0.5 (Stull, 1988). Among the three non-dimensional parameters, SC seems to be the sharpest and most adequate in foreseeing the regime transition.

6.5 ANALYSIS OF REPRESENTATIVE KATABATIC EVENTS

So far we have explored all the selected katabatic events together, and learnt about their main characteristics and connection with the SBL regimes. However, in order to better understand the mechanism behind the complex interaction between the katabatic flow and turbulence in the SBL, we target the analysis of individual events.

6.5.1 Inspecting individual events

We choose a weak and an intense event, so that their contrasting features are revealed. The weak event is 13 August and shows the presence of a skin flow and a VSBL. In short, the synoptic situation was marked by the Azores high and a thermal low over the Iberian Peninsula inducing a weak S flow, which is related with a weaker katabatic intensity (Fig. 6.5). The intense event is 27 July, and this day the synoptic situation was also characterised by the Azores high, but in this case with a weak NW forcing, associated with greater katabatic intensity. In addition to the strong turbulence associated with the intense katabatic flow, it is chosen due to its particular influence on the CO_2 transport, which is explored in Sect. 6.5.2.

To determine how turbulence in the surface layer responds to both katabatic events, we start our analysis showing u_* in Fig. 6.10a. The onset of the intense katabatic takes place around 1640 UTC during the AT of the ABL. After this time, u_* continues increasing slowly up to 0.5–0.6 m s^{-1} at 8 m when the SBL is already developed at around 2000–2100 UTC, and even up to 0.9 m s^{-1} later, exceeding the value associated with the diurnal peak. For the weak event the values of u_* at around 1600–1700 UTC are similar to the intense event, but by the time the katabatic flows arrives (at 1830 UTC, coinciding with the moment at which R_{net} turns negative), u_* has already decreased down to 0.1–0.15 m s^{-1}. Except for some sporadic bursts at 8 m, probably induced

by isolated top-down turbulence turbulent events, u_* is maintained below 0.1 m s^{-1}, revealing the presence of the VSBL.

Vertical profiles of U and θ_v are shown below (Figs. 6.10 (b-g)) at three relevant stages: at the moment of the katabatic onset, when R_{net} turns negative and finally at 2100 UTC when the SBL is well formed. The measurements and the logarithmic fitting of the discrete observed profiles for both variables are shown. As stated in previous sections, intense katabatics arrive earlier in La Herrería when the stratification is still unstable, which is clearly inferred from Fig. 6.10c. In contrast, the weak katabatic arrives when R_{net} turns negative and the stratification is already stable. The wind profile for the weak event at the moment of the onset shows a low-level jet below 3 m associated with a skin flow ($U < 1$ m s^{-1}), while U is stronger and increases linearly with height between 3 and 10 m for the intense event. U continues increasing in the intense event, exceeding 2 m s^{-1} at 6 m when R_{net} turns negative and 3 m s^{-1} at 2100 UTC. This intensification of the katabatic flow shows a different pattern from for instance Grachev et al. (2016). Based on observations from the MATERHORN field campaign, they reported that the wind profile is stationary in time during the katabatic flow. By the time $R_{net} < 0$, as a consequence of the flow intensification, the layer between 3 and 10 m is well mixed ($\Delta\theta_v \simeq 0$) despite the fact that the surface is already cooling down ($\theta_s < \theta_3$). On the contrary, U stays below 1 m s^{-1} throughout the entire weak katabatic event, and the stable stratification sharpens progressively (for instance $\Delta\theta_v \simeq 2$ K at 2100 UTC).

In order to shed more light on the possible factors inducing such a behaviour of the lower SBL in both cases, we explore the time-evolution of the measured shear at 4 and 8 m, $\Delta\theta_v$ and the SEB for the weak and intense katabatic event in Fig. 6.11. When the onset of the weak katabatic flow takes place, wind shear is weak (< 0.1 s^{-1}), $\Delta\theta_v > 0$ and the heat fluxes ($H + LH + G$) are unable to balance the radiative loss. As a consequence of the negative imbalance, the surface-based thermal inversion intensifies (up to 2 K) limiting the increase of wind shear: it is mostly below 0.05 s^{-1} after the onset at 4 m. The limitation of wind shear confines H (see the low values in Fig. 6.8), intensifying the thermal inversion in turn and producing a positive feedback in which the VSBL is set up. For the intense katabatic, however, the onset takes place when $\Delta\theta_v < 0$ and $R_{net} \simeq 200$ W m^{-2}. Wind shear increases particularly at 8 m, without being limited by the stable stratification. By the time R_{net} turns negative slightly before 1900 UTC, wind shear is already very high ($\simeq 0.5$ s^{-1}) and due to the turbulent mixing, $\Delta\theta_v$ is maintained always below 0.2–0.3 K. In fact, 2–3 h after the onset the heat fluxes balance the radiative loss and the thermal gradient is almost completely destroyed between 3 and 10 m, limiting the thermal inversion to a thin layer close to the surface (below 3 m). This indicates the presence of near-neutral conditions and the set up of the WSBL.

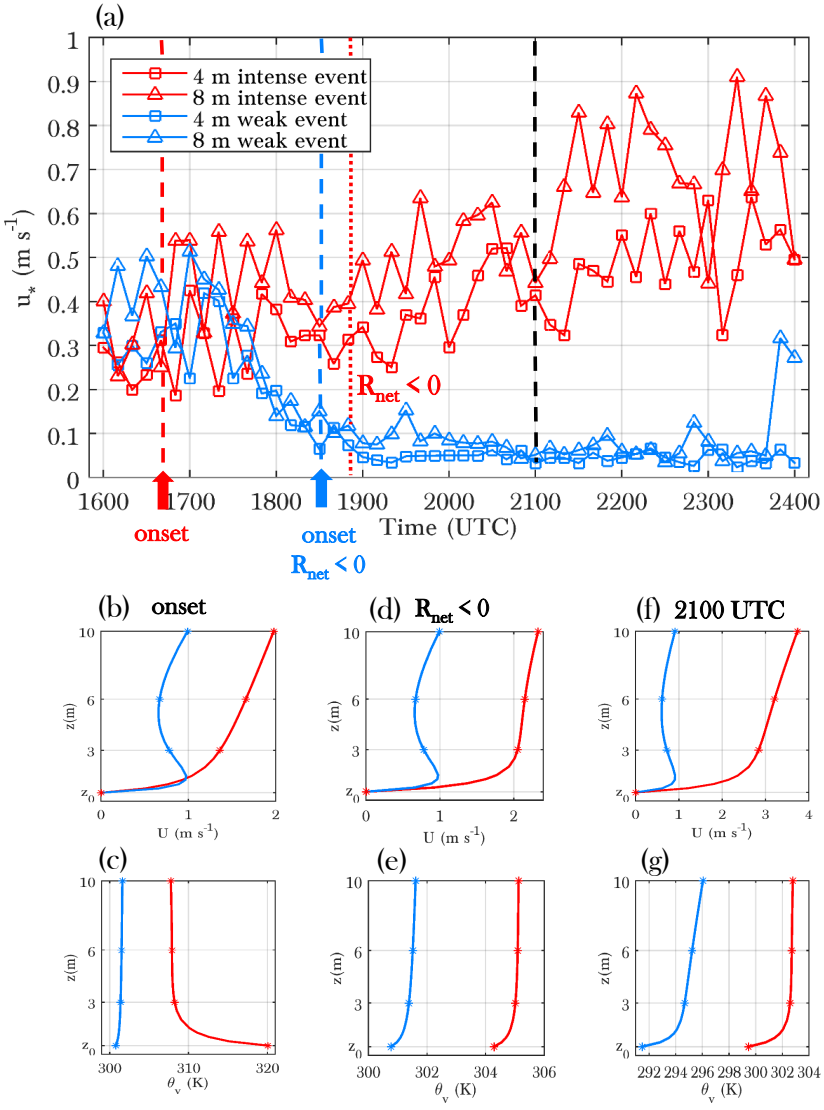

Figure 6.10: (a) Time evolution of the friction velocity (u_*) at 4 and 8 m for the weak-katabatic and the intense-katabatic event. The coloured arrows and the tied dashed vertical lines indicate the respective onset times, the red pointed line the time at which R_{net} turns negative for the intense event, and the dashed black vertical line is represented at 2100 UTC, i.e. when the SBL is already well developed for both events. (b-g) Vertical profiles of the wind speed (U) and virtual potential temperature (θ_v) at the onset time (b,c), when R_{net} turns negative (d,e), and at 2100 UTC (f,g).

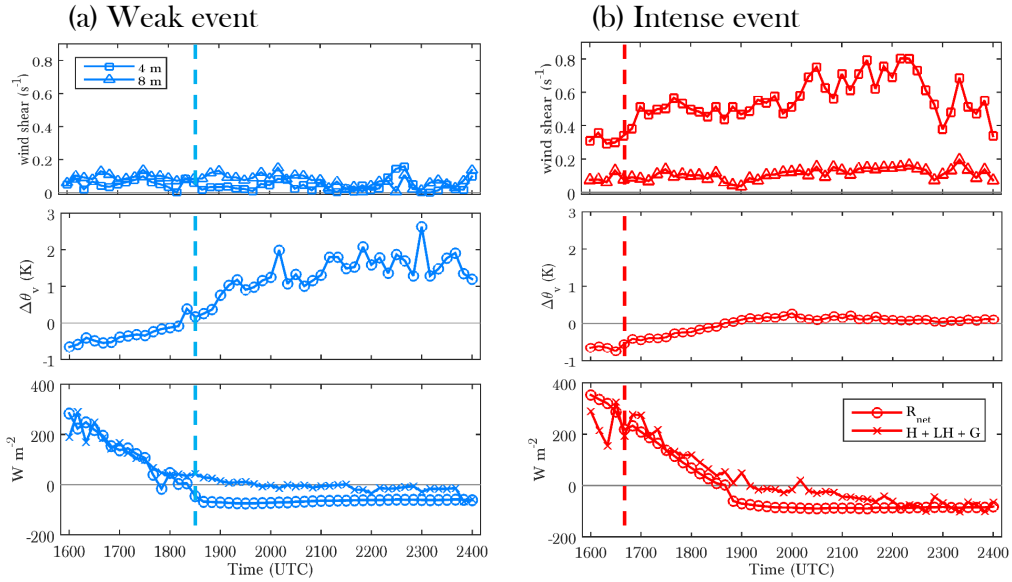

Figure 6.11: Time evolution of the wind shear at 4 and 8 m, thermal stratification ($\Delta\theta_v$) and the terms from the surface energy balance for the weak (a) and the intense (b) events. The vertical dashed line indicates the onset time of the katabatic flow.

6.5.2 Impact of katabatic flows and turbulence on CO_2

We finally explore the role of the transport produced by the katabatic flow and the associated different turbulent patterns within the SBL on a relevant scalar: the CO_2. The mixing ratio of CO_2 and the vertical turbulent fluxes are represented in Fig. 6.12 for the weak and intense katabatic events. The CO_2 mixing ratio is normalised with respect to the daily mean. By so doing, we aim to reduce the uncertainty due to possible biases. In Fig. 6.12b the measured turbulent fluxes at 4 and 8 m, and the estimated soil respiration flux (R_s) are represented. Since the soil respiration is an important CO_2 source term near the surface, we decided to include it in the analysis. It has been calculated following Lloyd and Taylor (1994) and Jacobs et al. (2007a):

$$R_s = R_{10}\left(1 - f(SM)\right)\left(\exp\left(\frac{E_0}{283.15R^*}\right)\left(1 - \frac{283.15}{T_s + 273.15}\right)\right), \tag{6.2}$$

where $R^* = 8.31{\cdot}10^{-3}$ kJ K mol^{-1} is the universal gas constant, E_0 is the activation energy (we employ a value of 53.30 kJ mol^{-1}) and T_s is the soil temperature which has been estimated from the upward longwave radiation. R_{10} is the reference soil-respiration value at 10° C under no water-stress condition, and it can vary significantly from site to site (Jacobs et al., 2007b); in this case, we consider a value of $R_{10} = 0.10 \pm 0.02$ mg

m^{-2} s^{-1} given the dry-soil conditions. Finally, (1 - *f(SM)*) is a water-stress correction (Jacobs et al., 2007a) where:

$$f(SM) = C\frac{SM_{max}}{SM + SM_{min}}, \tag{6.3}$$

with C(=0.0016) being a constant, and SM the observed soil moisture at 4-cm depth. SM_{max} and SM_{min} are the respective recorded maximum (= 0.14 m^3 m^{-3}) and minimum (= 0.01 m^3 m^{-3}) soil-moisture values throughout the summer.

The normalised CO_2 mixing ratio at 4 and 8 m for the weak and intense events has the same values at 1600 UTC before the surface thermal inversion is set up. It is therefore of great interest comparing these particular weak and intense events having the same initial mixing ratios but contrasting subsequent dynamical and stability conditions. During the weak event the CO_2 starts increasing at around 1730 UTC when the turbulent fluxes at 4 and 8 become positive. Slightly after the onset, which coincides with the set up of the SBL as reported in Sect. 6.5.1, the CO_2 starts to accumulate close to the surface until 2000 UTC approximately, due to the dominance of the soil flux over photosynthesis and dynamic transport. Later on, the balance between the divergence of the turbulent fluxes and the horizontal transport explains the variability of the scalar.

The CO_2 for the intense katabatic shows a contrasting evolution. The onset occurs almost 2 h before the weak event, and the diurnal positive vertical CO_2 gradient is reduced beforehand. Due to strong turbulence, the vertical CO_2 fluxes reach values of up to 0.2–0.3 mg m^{-2} s^{-1} slightly after the establishment of the SBL (see Fig. 6.10) at around 1900 UTC, following closely the estimated values of the soil respiration. From that moment and until 2200 UTC, the vertical gradient of the CO_2 is almost null, but the concentration increases around 6 ppm at both levels (note that it cannot be inferred from the normalised concentration in Fig. 6.12a). Considering in addition that the divergence of the vertical fluxes is mostly positive in that time range ($(\overline{w'CO_2'})_{8m} > (\overline{w'CO_2'})_{4m}$), the increase of the CO_2 concentration is explained by the non-local horizontal transport associated with the intense katabatic flow. From the null vertical gradient of CO_2 between 4 and 8 m and of θ_v between 3 and 10 m (see Fig. 6.10g), we can assume that the layer between 4 and 8 is well mixed, and since w close to the ground is nearly zero, vertical advection can be neglected. From this assumption we can additionally infer the horizontal transport in that layer between 1900 UTC and 2200 UTC following the methodology from Casso-Torralba et al. (2008) based on well-mixed layers.

We based our analysis on the one-dimensional governing equation for CO_2 in between 4 and 8 m. We therefore neglected the effects of soil CO_2. In short, after applying the Reynolds decomposition and averaging of the velocity fluctuations, and by considering the continuity equation we get Eq. 6.4 for the average CO_2 in the layer between 4 and 8 m. The wind has been aligned in the mean 10-min direction. We additionally

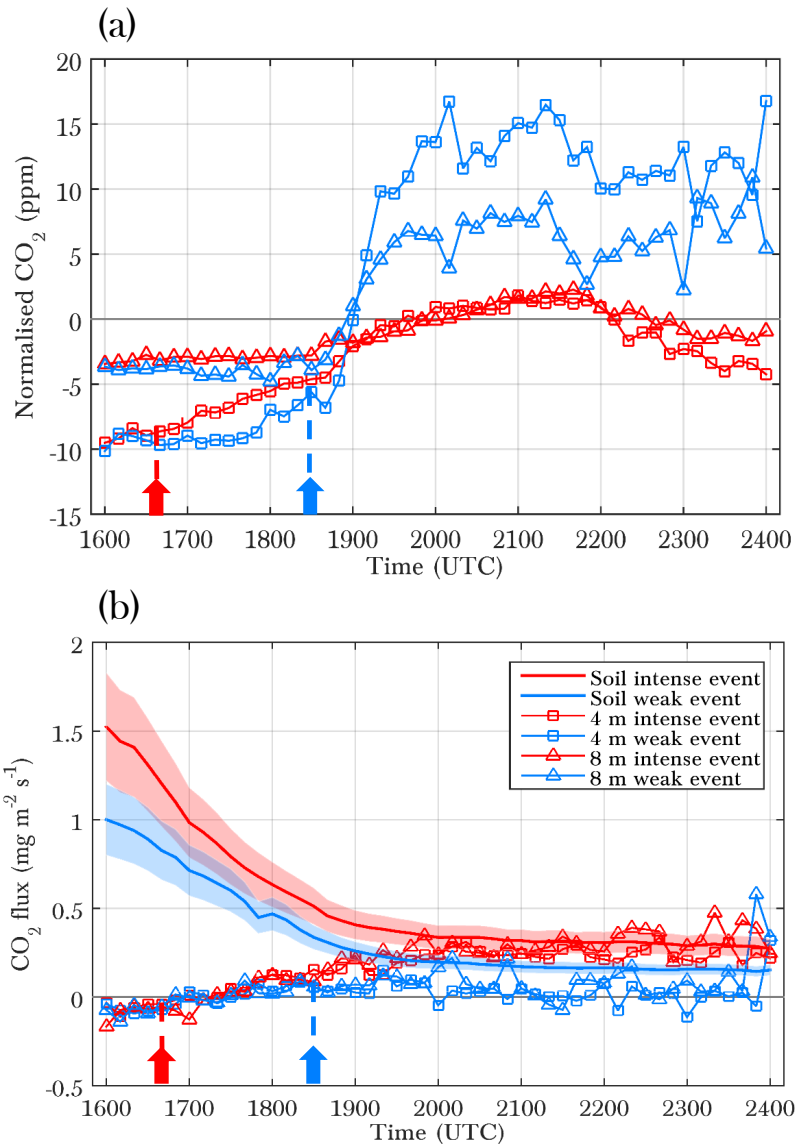

Figure 6.12: Time evolution of the normalised CO_2 mixing ratio (a) and vertical turbulent fluxes (b) at 4 and 8 m agl for the weak (blue) and intense (red) events. In (b) we include in solid lines the soil-respiration estimation and the 20% uncertainty of R_{10} (see Eq.6.2) in shaded. The onset of the katabatic flow is indicated from faced arrows of respective colours.

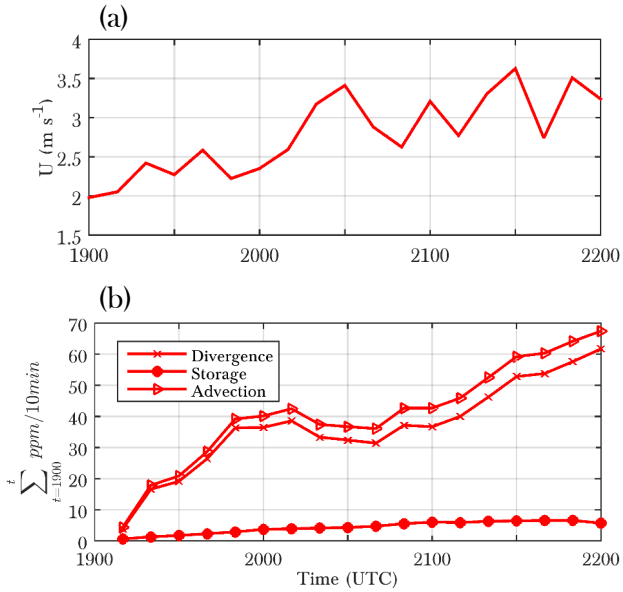

Figure 6.13: Time evolution between 1900 and 2200 UTC for the intense katabatic event, of (a) the wind speed (U) at 6 m, and (b) the different terms of the CO_2 budget from Eq. 6.4. Note that the cumulative sum from 1900 UTC is represented in (b), and that the advection term, which is negative, is shown in absolute values.

neglect the horizontal turbulent flux divergence, since under near-neutral conditions the flux-fetch condition in the katabatic direction is met in our emplacement.

$$\frac{\partial \overline{CO_2}}{\partial t} + \overline{u}\frac{\partial \overline{CO_2}}{\partial x} + \frac{\partial \overline{w'CO_2'}}{\partial z} = 0. \tag{6.4}$$

The first term represents the storage, the second advection and the third the divergence of the turbulent fluxes in the layer between 4 and 8 m. Since the layer is well mixed, we assume linearity of the turbulent fluxes with height (Casso-Torralba et al., 2008). Integrating Eq. 6.4 in time we get to the following equivalence for the horizontal-transport term:

$$\int_{1900}^{2200} \overline{u}\frac{\partial[\overline{CO_2}]}{\partial x}dt = -\int_{1900}^{2200} \frac{\partial[\overline{CO_2}]}{\partial t}dt - \int_{1900}^{2200} \frac{\Delta\overline{w'CO_2'}}{\Delta z}dt \tag{6.5}$$

The time evolution of the three terms is shown in Fig. 6.13, together with the katabatic speed evolution. Since the horizontal gradient of the CO_2 concentration increases upwind of the katabatic flow, the sign of the advective term is negative (note that it is represented in absolute values). After the corresponding calculations in Eq. 6.5, we

obtain that a horizontal transport of 67 ppm over 3 h induced by the intense katabatic flow compensates for the loss due to the vertical divergence (around 61 ppm in 3 h), resulting in an increase of the CO_2 storage of 6 ppm. This positive CO_2 advection is probably induced by the presence upwind of a land use composed of forest, mosaic trees and shrubs towards the katabatic direction, which accumulates greater CO_2 concentrations close to the surface during the night due to increased plant respiration and soil flux. Intense katabatics, as demonstrated in previous sections, induce strong wind shear and considerable mixing of the lower SBL, which together with the strong flow, contribute to cause important transport of scalars such as the CO_2.

6.6 SUMMARY AND CONCLUSIONS

Forty katabatic events of different intensities and with contrasting impacts on the turbulent characteristics of the SBL and on the CO_2 transport and mixing were investigated. Measurements were carried out in a relatively flat area with a relatively dessicated soil at the foothill of a high mountain range in central Spain during one summer. Observations of energy fluxes (heat and momentum), CO_2 and other meteorological variables were recorded in a tower at various vertical levels up to 10 m. A systematic algorithm was employed in order to select unambiguously thermally-driven downslope winds, by using objective filters to account for large-scale and local forcings.

The selected katabatic events were classified into three groups according to the observed maximum katabatic intensity until midnight: weak, moderate and intense. By clustering them into these three groups, we were able to analyse the factors that produce different intensities, and their relationship with the different turbulent patterns in the SBL.

Weak katabatics form when the maximum wind speed is kept below 1.5 m s^{-1}. They particularly take place when the large-scale wind opposes the katabatic flow and soil moisture is greater than the summer median, which in general induces a smaller radiative cooling. These factors give rise to a delayed arrival of the katabatic flow, when the stratification is already neutral or stable, which limits the increase of the wind shear. A positive feedback between the weak turbulence and the progressive cooling of the surface, which induces a more stable stratification, explains the formation of the very stable regime. A skin flow below 3 m and intermittent but weak turbulence are sporadically observed.

Intense katabatics are found when the maximum wind speed exceeds 3.5 m s^{-1} at 6 m agl. They mostly occur when soil moisture is lower than the summer median, the large-scale wind blows in the katabatic direction and its speed is greater than 3.5 m s^{-1} at 850 hPa. These factors induce an earlier katabatic onset, when the stratification is still unstable. Wind shear can therefore increase without being damped by the stable stratification. By the time the SBL is formed, wind shear is considerably high (up to 0.5 s^{-1}), and the layer between 3 and 10 m is maintained well mixed. Given the

strong turbulence, the downward heat flux is finally able to compensate the radiative cooling at the surface, and therefore the thermal inversion is limited to a very thin layer close to the surface. In this way, near-neutral conditions are reached and the WSBL is established.

Moderate katabatics lie between weak and intense katabatics, and their impact on the SBL regime and the associated turbulence is not so clearly assessed. Among all the moderate ones, the weakest events mostly approach the weak katabatics and the strongest events the intense katabatics, although the boundary for the transition between the regimes in this case in unclear.

Our findings show that the regime transition in the SBL is defined by using various values of dimensionless parameters. The transition occurs over a certain range which depends on the observational height for z/L and R_B, and is independent of that height in the case of the SC. The latter is the best in predicting the regime transition, as long as the HOST transition is taken into consideration for the corresponding wind-speed threshold. We found, indeed, that the wind speed is the most precise variable for representing the regime transition: above a wind speed of 1.5 m s^{-1} at 6 m, it is the bulk shear which dominates the turbulence production, and the thermal inversion is eroded significantly, giving rise to a regime transition.

Finally we inspected individual intense and a weak katabatic events, and their contribution to the CO_2 budget. For the weak event, minimal turbulence levels contribute to the accumulation of CO_2 close to the surface, and its concentration is sensitive to slight changes in the turbulent fluxes. For the intense event, instead, turbulence is considerably greater and consequently the layer between 4 and 8 m is well mixed. Under these conditions, we estimated the contribution of the horizontal transport in the katabatic direction, which is of around 67 ppm in 3 h, contributing to the increase in the storage of this scalar.

To sum up, we have been able to characterise the ET and diagnose the turbulent characteristics of the SBL during the night by measuring the maximum intensity of the katabatic flow, which depends on external factors such as the large-scale wind and soil moisture. In particular, the influence of the latter in the SEB needs further investigation. Being able to predict these external factors more precisely is therefore of high interest to better forecast the night-time turbulence and regime transition. However, sudden turbulent bursts and collapses, and the interaction with gravity waves have not been explored in this work, which can also be relevant in producing perturbations in the SBL and regime transitions. Future studies should tackle with those features and a better performance of numerical models in reproducing them.

7 CONCLUSIONS AND OUTLOOK

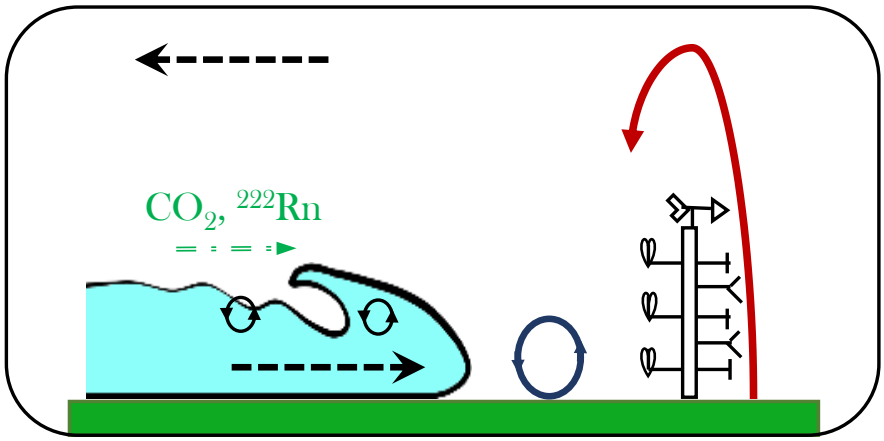

In this thesis we have dealt with the analysis of frontal disturbances in the form of density currents associated with SB phenomena and katabatic flows. The main large-scale and local factors affecting their formation and development, their interconnection with ABL turbulence during the afternoon and evening transition and their implication in the variability of CO_2 and ^{222}Rn have been analysed. In this last chapter, we first present the main conclusions derived from the obtained results in Chapters 3 to 6, and we close the thesis with a final thought and the future prospects.

7.1 GENERAL CONCLUSIONS

The main conclusions drawn from the investigation of the foremost matters of this thesis are hereunder listed. Each matter is associated with the objectives presented (in the same order) in Sect. 1.4.

THERMALLY-DRIVEN FLOWS: FORMATION AND CHARACTERISTICS (OBJECTIVE 1)

- We have successfully developed a systematic selection algorithm that provides an objective and reliable database of well-defined thermally-driven mesoscale flows. It discriminates between the large-scale conditions being or not favourable for the formation of these flows. By defining a frontal passage from the wind direction it also provides their onset time, which is valuable to cluster the potential mesoscale events together and investigate the impacts of their arrival on the ABL.
- The main external forcings affecting the characteristics and development of the thermally-driven winds analysed in this thesis are distinct primarily due to their different spatial scales. SB flows cover an average regional scale of around 100 km and are particularly constrained by the synoptic wind. Katabatic winds range in scales of up to 5–10 km and are not only influenced by the synoptic wind, but also by the partitioning of the different terms from the surface energy balance through alterations in the soil moisture.

TURBULENCE-MESOSCALE INTERACTION IN THE ABL (OBJECTIVE 2)

- The interconnection between the thermally-driven flows and local turbulence occurs in a bidirectional way. Given the different spatial scales and influencing factors, that interaction is described for SB and katabatic flows independently.
- The propagation speed of the SBFs is limited by thermal convection, affecting the SB onset time. Depending on the arrival time of the maritime flow, the consequences of the frontal passage in the ABL are different. In our study, we were able to identify for the first time three regimes:

  - When local conditions are convective, the convection itself weakens the frontal disturbance and surface turbulence remains almost unchanged by the SBF. Over complex terrain and closer from the coastline, however, strong updraughts and turbulence enhancement can be expected due to the passage of abrupt SBFs.
  - During the AT, the average wind speed and surface turbulence increase sharply when the SBF arrives, and the convective boundary layer decays faster. An acceleration of the transition towards nocturnal stable conditions is quantified.
  - When local conditions are stable, the frontal disruption brings the wind profile out of equilibrium with surface turbulence, so that MOST is not able to reproduce the profile in the surface layer until 1–2 h later, when the equilibrium is restored.

- The intensity of the katabatic winds is closely linked with the encountered local turbulence above the surface and the associated thermal stratification within the NBL:

  - Weak katabatics occur when their onset takes place close to sunset, when the stratification is neutral or stable. They are driven by a positive feedback between weak turbulence and the progressive cooling of the surface, giving rise to a corresponding very stable boundary layer.
  - Intense katabatics develop when their onset occurs 2–4 h earlier than sunset and the stratification is still unstable. They are associated with a continuous strong shear that gives rise to near-neutral conditions and the onset of a weakly stable boundary layer.
  - The transition from the weakly stable boundary layer to the very stable boundary layer or *vice versa* is particularly ruled by the katabatic intensity and the associated wind shear, as described by the HOST concept. Above a certain wind-speed threshold, the bulk shear dominates the turbulent production and the thermal inversion is significantly eroded, giving rise to a regime transition in the nocturnal boundary layer.

IMPACTS ON ABL DYNAMICS AND SCALAR TRANSPORT (OBJECTIVE 3)

- The impact of thermally-driven flows on the variability of the CO_2 is mainly explained by changes in turbulent fluxes caused by the disruptive frontal passage and by horizontal transport, which can be significantly large for intense katabatic winds. In the case of SB flows, sudden variations in the CO_2 mixing ratio are explained by the return of continental air masses within the mesoscale circulation.

- Understanding the variability of the ^{222}Rn is more challenging compared with the CO_2. We find considerable decreases and increases of this gas at different levels for distinct SB directions.

PERFORMANCE OF THE WRF MODEL (OBJECTIVE 4)

- Over complex terrain, discrepancies in the SB intensity and direction result from an incorrect simulation of the interaction with diurnal mountain winds. Over flat terrain discrepancies are smaller, but the onset time is biased substantially without no clear indication that the frontal arrival is before or after the observations.

- Substantial divergence is found when applying the mesoscale algorithm directly to the variables simulated from WRF, which indicates that the large-scale and local forcings giving rise to SB formation are biased in the model.

- WRF reproduces the impacts of SBFs on local turbulence for each ABL regime studied. However, the great overestimation of the SH flux associated with prescribed land-use properties produces stronger frontal disturbances. On the other hand, an acceleration of the afternoon and evening transition is simulated comparing with observations.

7.2 FINAL THOUGHT AND FUTURE PROSPECTS

In this thesis we have provided responses to matters regarding the understanding of the thermally-driven flows and their physical interconnection with the smaller (micro) and larger (synoptic) scales. The gained knowledge allows us to place in context our findings, and to raise future prospects in relation to new possible research lines and the practical application of the learning acquired. The next lines intend to be a small sample of the relevance of this thesis, and an invitation for further investigation on this topic.

One of the key aspects of the investigation carried out along the completion of the doctoral thesis has been the development of an objective and systematic algorithm to select the mesoscale phenomena of interest. The algorithm can be extended to various emplacements and be easily adapted for selecting different thermally-driven flows. We strongly encourage the use of this algorithm, so that the observed characteristics of thermally-driven winds in different emplacements can be objectively contrasted. For that, it is advisable to employ common criteria in their selection, and the alterations in the filters must be physically justified, e.g. changing the level of the large-scale wind in mountainous areas from 850 hPa to lower-pressure levels and adapting the wind-speed threshold correspondingly. Future studies should also be focused on carrying out a sensitivity analysis of the thresholds employed in each of the filters for an optimum use of this algorithm, and a validation of its performance should be carried out to further show its strength.

Additionally, the use and investigation of this algorithm can have a positive impact on the improvement of the forecasting of these phenomena. By applying the algorithm to the numerical simulations from the WRF model, we have learnt that it shows deficiencies on representing the forcings favourable to the development of SB circulations. Revising the representation of the large-scale conditions and the performance of the parameterisations related with the land use and the surface layer, could give rise to a better simulation of the influencing forcings such as the sea-land thermal contrast. However, we discourage the use of the grid analysis nudging to reduce modelling biases, since it can give rise to an incorrect phenomenological simulation. An improved forecast of SB phenomena is necessary for better estimates of the maximum temperatures, more importantly during hot spells, and air quality in coastal urban areas. In addition, an improved representation of SB and mountain-breeze characteristics in terms of wind speed and direction is fundamental for choosing the suitable location

of future wind farms. In this thesis in particular we have found that the SB direction and intensity are poorly reproduced over complex terrain, due mainly to the incorrect interaction with the daytime mountain breezes. Efforts should also be dedicated to better representing the topographic features –which tend to be smoothed even with a grid resolution of 1 km–, and their influence on the simulated flow.

Moreover, one of the factors that most importantly influences the development of the thermally-driven winds is the coupling with turbulence in the ABL. In particular, as we stressed in the introduction, little was known about that relevant interaction during the afternoon and evening transition of the ABL. In this thesis we have demonstrated and quantified how microscales and mesoscales are intimately related during this stage. In fact, we have found that the impact of the SB on the ABL is very sensitive to local-turbulent features. However, we have not explored how the distance of the location from the sea can affect that coupling. We have observed from numerical simulations the decay of the convective boundary layer over complex terrain and closer from the shore (10–15 km) due to the passage of strong SB fronts. By analysing observational measurements over flat terrain and further from the shore (50 km), instead, we have not observed such a collapse of the convective regime. Therefore, future observational and numerical investigations should focus on the sensitivity of the mesoscale-microscale interactions to the distance from the shoreline. The conclusions drawn from our emplacements, besides, should be confirmed by employing a similar research strategy in other geographical locations.

On the other hand, the performance of a mesoscale model such as WRF in reproducing the evolution of the dynamics and thermal structure of the ABL during the afternoon and evening transition need to be improved. WRF transits from convective to stable conditions depending on the value of the bulk Richardson number, whereas in reality that transition occurs in a smoother way and under different regimes. Future ABL and surface-layer parameterisations in mesoscale models should be able to represent the transition in a smoother manner, so that the impacts of mesoscale flows on the ABL are more realistic. In such a way, a better simulation of the thermal stratification and the turbulent characteristics of the SBL over complex terrain could be expected. A more precise forecasting of the minimum temperatures and relevant phenomena associated with the SBL, such as radiation fog and frost, could be accomplished. Some of the issues which remain unclear could be elucidated by carrying out large-eddy simulations which solve a large part of the spectrum associated with the microscale phemomena. In this thesis, numerical simulations have exclusively been carried out using a mesoscale model in order to capture the interconnection between large, intermediate and small scales. Large-eddy simulations could bring interesting further insight into the mesoscale-microscale interactions during the afternoon and evening transition and their implication, for instance, on the variability of the spectral gap.

In the case of katabatic winds, we have found how an external variable such as soil moisture can be highly influential for their intensity. However, the role of that factor in modulating the partitioning of the different terms from the surface energy balance is

not absolutely clear yet, since these terms show almost similar behaviour for low and high soil-moisture values. Longer observational time series and the employment of a similar research strategy from this thesis in other mountainous emplacements could shed more light on this aspect.

Finally, in this thesis we have quantified and discussed the role of the mesoscale-microscale interactions in the dynamics of the ABL and the variability of scalars such as CO_2 and ^{222}Rn. Important alterations in the concentration of these gases have been quantified due to the arrival of SB flows and katabatic winds. Understanding the sources of variability and the influence of mesoscale flows on the CO_2 budget is highly relevant for explaining the land-atmosphere exchange of this gas, which is still uncertain in the global carbon budget. Reducing that uncertainty is very important for better explaining the role of greenhouse gases in the climate change. In this thesis we have demonstrated how the return of continental air masses in the mesoscale circulation can be prone to sharp CO_2 increases. Intense katabatic winds, besides, can be responsible for significant horizontal transport compensating the loss due to the divergence of the turbulent fluxes of this gas. In the case of the ^{222}Rn, we have found important alterations in the concentration of this gas for different SB directions. This implies that the influence of mesoscale flows must be considered when analysing the history and the footprint of the air masses containing this gas. However, it is still unclear how the dynamics of the SB circulation rules iTs variability, which suggests the necessity of further studies on this topic. In particular, observational campaigns measuring ^{222}Rn concentrations at different distances from the coast, various vertical levels and at distinct times of day, could elucidate the role of mesoscale circulations in the variability of this gas. In addition to the non-local contribution, by measuring surface turbulent fluxes the impact of the mesoscale on local variability could be better explained.

REFERENCES

AEMET: Summary of Summer 2017, Spanish Meteorological Agency, URL http://www.aemet.es/en/noticias/2017/09/Verano_2017, 2017.

Ahmadov, R., Gerbig, C., Kretschmer, R., Koerner, S., Neininger, B., Dolman, A. J., and Sarrat, C.: Mesoscale covariance of transport and CO2 fluxes: Evidence from observations and simulations using the WRF-VPRM coupled atmosphere-biosphere model, J. Geophys. Res., 112, D22 107–, URL https://doi.org/10.1029/2007JD008552, 2007.

Alonso, L., Gangoiti, G., Navazo, M., Millán, M., and Mantilla, E.: Transport of tropospheric ozone over the bay of Biscay and the eastern Cantabrian coast of Spain, J. Appl. Meteorol., 39, 475–486, 2000.

Anthes, R.: The height of the PBL and the production of circulation in a sea-breeze model, J. Atmos. Sci., 35, 1231–1239, 1978.

Antonelli, M. and Rotunno, R.: Large-Eddy Simulation of the Onset of the Sea Breeze, J. Atmos. Sci., 64, 4445–4457, URL https://doi.org/10.1175/2007JAS2261.1, 2007.

Archer, C., Colle, B., Monache, L., Dvorak, M., Lundquist, J., Bailey, B., Beaucage, P., Churchfield, M., Fitch, A., Kosovic, B., Lee, S., Moriarty, P., Simao, H., Stevens, R., Veron, D., and Zack, J.: Meteorology for coastal/offshore wind energy in the United States: recommendations and research needs for the next 10 years, Bull. Amer. Meteor. Soc., 13, 515–519, 2014.

Arnold, D., Vargas, A., and Ortega, X.: Analysis of outdoor radon progeny concentration measured at the Spanish radioactive aerosol automatic monitoring network, Appl. Radiat. Isot., 67, 833 – 838, URL http://dx.doi.org/10.1016/j.apradiso.2009.01.042, 5th International Conference on Radionuclide Metrology - Low-Level Radioactivity Measurement Techniques ICRM-LLRMT'08, 2009.

Arrillaga, J. A., Yagüe, C., Sastre, M., Román-Cascón, C., Maqueda, G., Inclán, R., González-Roúco, J., Santolaria, E., Durán, L., and Navarro., J.: WRF simulations of upslope and downslope flows over the Guadarrama Mountain Range (Spain), in: 32nd Conference on Agricultural and Forest Meteorology, Salt Lake City (UT, USA), 2016a.

Arrillaga, J. A., Yagüe, C., Sastre, M., and Román-Cascón, C.: A characterisation of sea-breeze events in the eastern Cantabrian coast (Spain) from observational data and {WRF} simulations, Atmos. Res., 181, 265 – 280, URL http://dx.doi.org/10.1016/j.atmosres.2016.06.021, 2016b.

Arrillaga, J. A., Vilà-Guerau de Arellano, J., Bosveld, F., Baltink, H. K., Yagüe, C., Sastre, M., and Román-Cascón, C.: Impacts of afternoon and evening sea-breeze fronts on local turbulence, and on CO2 and radon-222 transport, Q. J. R. Meteorol. Soc., 144, 990–1011, URL https://doi.org/10.1002/qj.3252, 2018.

Arrillaga, J. A., Yagüe, C., Román-Cascón, C., Sastre, M., Maqueda, G., and Vilà-Guerau de Arellano, J.: Weak and intense katabatic winds: impacts on turbulent characteristics in the stable boundary layer and CO2 transport., URL https://doi.org/10.5194/acp-2018-944, atmos. Chem. Phys. Discuss., in review, 2018b.

Arrillaga, J. A., Vilà-Guerau de Arellano, J., Jiménez, P., and Yagüe, C.: The role of local turbulence and synoptic scales on sea-breeze features: using 10-year WRF and observations, in preparation to be submitted to J. Geophys. Res. Atmos., 2018c.

Arritt, R.: Effects of the large-scale flow on characteristic features of the sea breeze, J. Appl. Meteorol., 32, 116–125, 1993.

Arya, P.: Introduction to micrometeorology, International Geophysics Series, Academic Press, London, 2001.

Asai, T. and Mitsumoto, S.: Effects of an Inclined Land Surface on the Land and Sea Breeze Circulation: A Numerical Experiment, J. Meteorol. Soc. Jpn., 56, 559–570, URL https://doi.org/10.2151/jmsj1965.56.6_559, 1978.

Atkins, N. T. and Wakimoto, R. M.: Influence of the Synoptic-Scale Flow on Sea Breezes Observed during CaPE, Mon. Wea. Rev., 125, 2112–2130, URL https://doi.org/10.1175/1520-0493(1997)125<2112:IOTSSF>2.0.CO;2, 1997.

Atkinson, B.: Meso-Scale Atmospheric Circulations, Academic Press, London, 1981.

Azorin-Molina, C. and Lopez-Bustins, J.-A.: An automated sea breeze selection technique based on regional sea-level pressure difference: WeMOi, Int. J. Climatol., 28, 1681–1692, URL https://doi.org/10.1002/joc.1663, 2008.

Azorin-Molina, C., Tijm, S., and Chen, D.: Development of selection algorithms and databases for sea breeze studies, Theor. Appl. Climatol., 106, 531–546, URL https://doi.org/10.1007/s00704-011-0454-4, 2011.

Azorín-Molina, C. and Chen, D.: A climatological study of the influence of synoptic-scale flows on sea-breeze evolution in the Bay of Alicante (Spain), Theor. Appl. Climatol., 96, 249–260, 2009.

Azorín-Molina, C., Tijm, S., Ebert, E., Vicente-Serrano, S., and Estrela, M.: Sea breeze thunderstorms in the eastern Iberian Peninsula. Neighborhood verification of HIRLAM and HARMONIE precipitacion forecasts., Atmos. Res., 139, 101–115, 2014.

Babić, N., Večenaj, Z., and De Wekker, S. F. J.: Spectral gap characteristics in a daytime valley boundary layer, Q. J. R. Meteorol. Soc., 143, 2509–2523, URL https://doi.org/10.1002/qj.3103, 2017.

Baklanov, A. A., Grisogono, B., Bornstein, R., Mahrt, L., Zilitinkevich, S. S., Taylor, P., Larsen, S. E., Rotach, M. W., and Fernando, H. J. S.: The Nature, Theory, and Modeling of Atmospheric Planetary Boundary Layers, Bull. Amer. Meteor. Soc., 92, 123–128, URL https://doi.org/10.1175/2010BAMS2797.1, 2011.

Banta, R., Olivier, L., and D.H., L.: Evolution of the Monterey Bay sea-breeze layer as observed by pulsed Doppler radar, J. Atmos. Sci., 50, 3959–3982, 1993.

Banta, R. M. and Gannon, P. T.: Influence of soil moisture on simulations of katabatic flow, Theor. Appl. Climatol., 52, 85–94, URL https://doi.org/10.1007/BF00865509, 1995.

Barry, R. G.: Mountain Weather and Climate, Cambridge University Press, 3rd edn., 2008.

Baumbach, G. and Vogt, U.: Experimental determination of the effect of mountain-valley breeze circulation on air pollution in the vicinity of Freiburg, Atmos. Environ., 33, 4019 – 4027, URL https://doi.org/10.1016/S1352-2310(99)00143-0, 1999.

Bechtold, P., Pinty, J., and Mascart, P.: A numerical investigation of the Influence of large-scale wind on sea-breeze- and inland-breeze-type circulations, J. Appl. Meteorol., 30, 1268–1279, 1991.

Beljaars, A.: The parameterization of surface fluxes in large-scale models under free convection, Q. J. R. Meteorol. Soc., 121, 255–270, 1994.

Beljaars, A. C. M. and Bosveld, F. C.: Cabauw Data for the Validation of Land Surface Parameterization Schemes, J. Climate, 10, 1172–1193, URL https://doi.org/10.1175/1520-0442(1997)010<1172:CDFTVO>2.0.CO;2, 1997.

Blackadar, A. K.: The vertical distribution of wind and turbulent exchange in a neutral atmosphere, J. Geophys. Res., 67, 3095–3102, URL https://doi.org/10.1029/JZ067i008p03095, 1962.

Blay-Carreras, E., Pardyjak, E. R., Pino, D., Hoch, S. W., Cuxart, J., Martínez, D., and Reuder, J.: Lifted temperature minimum during the atmospheric evening transition, Atmos. Chem. Phys., 15, 6981–6991, URL https://doi.org/10.5194/acp-15-6981-2015, 2015.

Bodine, D., Klein, P. M., Arms, S. C., and Shapiro, A.: Variability of Surface Air Temperature over Gently Sloped Terrain, J. Appl. Meteor. Climatol., 48, 1117–1141, URL https://doi.org/10.1175/2009JAMC1933.1, 2009.

Bonin, T., Chilson, P., Zielke, B., and Fedorovich, E.: Observations of the Early Evening Boundary-Layer Transition Using a Small Unmanned Aerial System, Boundary-Layer Meteorol., 146, 119–132, URL https://doi.org/10.1007/s10546-012-9760-3, 2013.

Borge, R., Alexandrov, V., José del Vas, J., Lumbreras, J., and Rodríguez, E.: A comprehensive sensitivity analysis of the WRF model for air quality applications over the Iberian Peninsula, Atmos. Environ., 42, 8560–8574, 2008.

Borge, R., Narros, A., Artíñano, B., Yagüe, C., Gómez-Moreno, F. J., de la Paz, D., Román-Cascón, C., Díaz, E., Maqueda, G., Sastre, M., Quaassdorff, C., Dimitroulopoulou, C., and Vardoulakis, S.: Assessment of microscale spatio-temporal variation of air pollution at an urban hotspot in Madrid (Spain) through an extensive field campaign, Atmos. Environ., 140, 432 – 445, URL https://doi.org/10.1016/j.atmosenv.2016.06.020, 2016.

Borge, R., Artíñano, B., Yagüe, C., Gomez-Moreno, F. J., Saiz-Lopez, A., Sastre, M., Narros, A., García-Nieto, D., Benavent, N., Maqueda, G., Barreiro, M., de Andrés, J. M., and Ángeles Cristóbal: Application of a short term air quality action plan in Madrid (Spain) under a high-pollution episode - Part I: Diagnostic and analysis from observations, Sci. Total Environ., 635, 1561 – 1573, URL https://doi.org/10.1016/j.scitotenv.2018.03.149, 2018.

Borne, K., Chen, D., and Nunez, M.: A method for finding sea breeze days under stable synoptic conditions and its application to the Swedish west coast, Int. J. Climatol., 18, 901–914, URL https://doi.org/10.1002/(SICI)1097-0088(19980630)18:8<901::AID-JOC295>3.0.CO;2-F, 1998.

Bosveld, F.: Dataset-description document of the datasets in the Cesar database, Tech. rep., KNMI, URL http://projects.knmi.nl/cabauw/insitu/observations/documentation/Cabauw_TR/Cabauw_TR.pdf, 2017.

Calmet, I. and Mestayer, P.: Study of the thermal internal boundary layer during sea-breeze events in the complex coastal area of Marseille, Theor. Appl. Climatol., 123, 801–826, URL https://doi.org/10.1007/s00704-015-1394-1, 2016.

Casso-Torralba, P., Vilà-Guerau de Arellano, J., Bosveld, F., Soler, M. R., Vermeulen, A., Werner, C., and Moors, E.: Diurnal and vertical variability of the sensible heat and carbon dioxide budgets in the atmospheric surface layer, J. Geophys. Res. Atmos., 113, n/a–n/a, URL https://doi.org/10.1029/2007JD009583, d12119, 2008.

Challa, V. S., Indracanti, J., Rabarison, M. K., Patrick, C., Baham, J. M., Young, J., Hughes, R., Hardy, M. G., Swanier, S. J., and Yerramilli, A.: A simulation study of mesoscale coastal circulations in Mississippi Gulf coast, Atmos. Res., 91, 9 – 25, URL https://doi.org/10.1016/j.atmosres.2008.05.004, 2009.

Chang, L., Takle, E., and Sani, R.: Development of a two-dimensional finite-element PBL Model and two preliminary model applications, Mon. Wea. Rev., 110, 2025–2037, 1982.

Chapin, F., Matson, P., and Vitousek, P.: Principles of Terrestrial Ecosystem Ecology, Springer, 2011.

Charuchittipan, D., Babel, W., Mauder, M., Leps, J.-P., and Foken, T.: Extension of the Averaging Time in Eddy-Covariance Measurements and Its Effect on the Energy Balance Closure, Boundary-Layer Meteorol., 152, 303–327, URL https://doi.org/10.1007/s10546-014-9922-6, 2014.

Chemel, C. and Sokhi, R.: Response of London's urban heat island to a marine air intrusion in an easterly wind regime, Boundary-Layer Meteorol., 144, 65–81, 2012.

Clappier, A., Martilli, A., Grossi, P., Thunis, P., Pasi, F., Krueger, B., Calpini, B., Graziani, G., and van der Bergh, H.: Effect of sea breeze on air pollution in the greater Athens area. Part I: numerical simulations and field observations, J. Appl. Meteorol, 39, 546–562, 2000.

Cohn, S. A. and Angevine, W. M.: Boundary Layer Height and Entrainment Zone Thickness Measured by Lidars and Wind-Profiling Radars, J. Appl. Meteorol., 39, 1233–1247, URL https://doi.org/10.1175/1520-0450(2000)039<1233:BLHAEZ>2.0.CO;2, 2000.

Comin, A. N., Miglietta, M. M., Rizza, U., Acevedo, O. C., and Degrazia, G. A.: Investigation of sea-breeze convergence in Salento Peninsula (southeastern Italy), Atmos. Res., 160, 68 – 79, URL https://doi.org/10.1016/j.atmosres.2015.03.010, 2015.

Couvreux, F., Bazile, E., Canut, G., Seity, Y., Lothon, M., Lohou, F., Guichard, F., and Nilsson, E.: Boundary-layer turbulent processes and mesoscale variability represented by numerical weather prediction models during the BLLAST campaign, Atmos. Chem. Phys., 16, 8983–9002, URL https://doi.org/10.5194/acp-16-8983-2016, 2016.

Cristofanelli, P., Calzolari, F., Bonafè, U., Lanconelli, C., Lupi, A., Busetto, M., Vitale, V., Colombo, T., and Bonasoni, P.: Five-year analysis of background carbon dioxide and ozone variations during summer seasons at the Mario Zucchelli station (Antarctica), Tellus B, 63, 831–842, URL https://doi.org/10.1111/j.1600-0889.2011.00576.x, 2011.

Crosman, E. T. and Horel, J. D.: Sea and Lake Breezes: A Review of Numerical Studies, Boundary-Layer Meteorol., 137, 1–29, URL https://doi.org/10.1007/s10546-010-9517-9, 2010.

Cuxart, J., Jiménez, M. A., Prtenjak, M. T., and Grisogono, B.: Study of a Sea-Breeze Case through Momentum, Temperature, and Turbulence Budgets, J. Appl. Meteor. Climatol., 53, 2589–2609, URL https://doi.org/10.1175/JAMC-D-14-0007.1, 2014.

Darbieu, C., Lohou, F., Lothon, M., Vilà-Guerau de Arellano, J., Couvreux, F., Durand, P., Pino, D., Patton, E. G., Nilsson, E., Blay-Carreras, E., and Gioli, B.: Turbulence vertical structure of the boundary layer during the afternoon transition, Atmos. Chem. Phys., 15, 10 071–10 086, URL https://doi.org/10.5194/acp-15-10071-2015, 2015.

de Haij, M., Wauben, W., and Klein Baltink, H.: Continuous mixing layer height determination using the LD-40 ceilometer: a feasibility study, Royal Netherlands Meteorological Institute (KNMI), De Bilt, 2007.

De Tomasi, F., Miglietta, M. M., and Perrone, M. R.: The Growth of the Planetary Boundary Layer at a Coastal Site: a Case Study, Boundary-Layer Meteorol., 139, 521–541, URL https://doi.org/10.1007/s10546-011-9592-6, 2011.

De Wekker, S. F. J., Kossmann, M., Knievel, J. C., Giovannini, L., Gutmann, E. D., and Zardi, D.: Meteorological Applications Benefiting from an Improved Understanding of Atmospheric Exchange Processes over Mountains, Atmosphere, 9, URL https://doi.org/10.3390/atmos9100371, 2018.

Deardorff, J. W.: Numerical Investigation of Neutral and Unstable Planetary Boundary Layers, J. Atmos. Sci., 29, 91–115, URL https://doi.org/10.1175/1520-0469(1972)029<0091:NIONAU>2.0.CO;2, 1972.

Di Giuseppe, F., Riccio, A., Caporaso, L., Bonafé, G., Gobbi, G. P., and Angelini, F.: Automatic detection of atmospheric boundary layer height using ceilometer backscatter data assisted by a boundary layer model, Q. J. R. Meteorol. Soc., 138, 649–663, URL https://doi.org/10.1002/qj.964, 2012.

Doran, J. C.: The effects of ambient winds on valley drainage flows, Boundary-Layer Meteorol., 55, 177–189, URL https://doi.org/10.1007/BF00119333, 1991.

Duine, G.-J., Hedde, T., Roubin, P., Durand, P., Lothon, M., Lohou, F., Augustin, P., and Fourmentin, M.: Characterization of valley flows within two confluent valleys under stable conditions: observations from the KASCADE field experiment, Q. J. R. Meteorol. Soc., 143, 1886–1902, URL https://doi.org/10.1002/qj.3049, 2017.

Durán, L., Sánchez, E., and Yagüe, C.: Climatology of precipitation over the Iberian Central System mountain range, Int. J. Climatol., 33, 2260–2273, URL https://doi.org/10.1002/joc.3602, 2013.

Dyer, A. J. and Hicks, B. B.: Flux-gradient relationships in the constant flux layer, Q. J. R. Meteorol. Soc., 96, 715–721, URL https://doi.org/10.1002/qj.49709641012, 1970.

Fernando, H. J. S., Verhoef, B., Di Sabatino, S., Leo, L. S., and Park, S.: The Phoenix Evening Transition Flow Experiment (TRANSFLEX), Boundary-Layer Meteorol., 147, 443–468, URL https://doi.org/10.1007/s10546-012-9795-5, 2013.

Fitzjarrald, D. R.: Katabatic Wind in Opposing Flow, J. Atmos. Sci., 41, 1143–1158, URL https://doi.org/10.1175/1520-0469(1984)041<1143:KWIOF>2.0.CO;2, 1984.

Flocas, H. A., Helmis, C. G., Blikas, S. N., Asimakopoulos, D. N., Bartzis, J. G., and Deligiorgi, D. G.: Mean Characteristics of the Katabatic Flow of a 1024 m High Knife Edge Mountain, Theor. Appl. Climatol., 59, 237–249, URL https://doi.org/10.1007/s007040050027, 1998.

Foken, T.: 50 Years of the Monin–Obukhov Similarity Theory, Boundary-Layer Meteorol., 119, 431–447, URL https://doi.org/10.1007/s10546-006-9048-6, 2006.

Foken, T.: The energy balance closure problem: an overview, Ecol. Appl., 18, 1351–1367, URL https://doi.org/10.1890/06-0922.1, 2008.

Foken, T., Göockede, M., Mauder, M., Mahrt, L., Amiro, B., and Munger, W.: Post-Field Data Quality Control, pp. 181–208, Springer Netherlands, Dordrecht, URL https://doi.org/10.1007/1-4020-2265-4_9, 2005.

Font Tullot, I.: Climatología de España y Portugal, Ediciones Universidad de Salamanca, in Spanish, 2000.

Frizzola, J. and Fisher, E.: A series of sea-breeze Observations in the New York City area., J. Appl. Meteorol., 2, 722–739, 1963.

Gahmberg, M., Savijärvi, H., and Leskinen, M.: The influence of synoptic scale flow on sea breeze induced surface winds and calm zones, Tellus A, 62, 209–217, URL https://doi.org/10.1111/j.1600-0870.2009.00423.x, 2010.

Gangoiti, G., Millán, M. M., Salvador, R., and Mantilla, E.: Long-range transport and re-circulation of pollutants in the western Mediterranean during the project Regional Cycles of Air Pollution in the West-Central Mediterranean Area, Atmos. Environ., 35, 6267 – 6276, URL http://dx.doi.org/10.1016/S1352-2310(01)00440-X, 2001.

Grachev, A. A., Leo, L. S., Sabatino, S. D., Fernando, H. J. S., Pardyjak, E. R., and Fairall, C. W.: Structure of Turbulence in Katabatic Flows Below and Above the Wind-Speed Maximum, Boundary-Layer Meteorol., 159, 469–494, URL https://doi.org/10.1007/s10546-015-0034-8, 2016.

Grisogono, B., Ström, L., and Tjernström, M.: Small-Scale Variability in the Coastal Atmospheric Boundary Layer, Boundary-Layer Meteorol., 88, 23–46, URL https://doi.org/10.1023/A:1000933822432, 1998.

GuMNet: www.ucm.es/gumnet/, URL www.ucm.es/gumnet/, 2018.

Hang, C., Nadeau, D. F., Gultepe, I., Hoch, S. W., Román-Cascón, C., Pryor, K., Fernando, H. J. S., Creegan, E. D., Leo, L. S., Silver, Z., and Pardyjak, E. R.: A Case Study of the Mechanisms Modulating the Evolution of Valley Fog, Pure Appl. Geophys., 173, 3011–3030, URL https://doi.org/10.1007/s00024-016-1370-4, 2016.

Helmis, C., Asimakopoulos, D., Deligiorgi, D., and Lalas, D.: Observations of sea-breeze fronts near the shoreline, Boundary-Layer Meteorol., 38, 395–410, 1987.

Hernández-Ceballos, M., Vargas, A., Arnold, D., and Bolívar, J.: The role of mesoscale meteorology in modulating the 222Rn concentrations in Huelva (Spain) – impact of phosphogypsum piles, J. Environ. Radioact., 145, 1 – 9, URL http://dx.doi.org/10.1016/j.jenvrad.2015.03.023, 2015.

Hess, G. D. and Clarke, R. H.: Time spectra and cross-spectra of kinetic energy in the planetary boundary layer, Q. J. R. Meteorol. Soc., 99, 130–153, URL https://doi.org/10.1002/qj.49709941912, 1973.

Hewson, T. D.: Objective fronts, Meteorol. Appl., 5, 37–65, URL https://doi.org/10.1017/S1350482798000553, 1998.

Ho, E. C. and Measday, D. F.: A simple model for describing the concentration of 212Pb in the atmosphere, J. Environ. Radioact., 78, 289 – 309, URL http://dx.doi.org/10.1016/j.jenvrad.2004.05.008, 2005.

Högström, U.: Review of some basic characteristics of the atmospheric surface layer, Boundary-Layer Meteorol., 78, 215–246, URL https://doi.org/10.1007/BF00120937, 1996.

Holtslag, A. A. M. and Bruin, H. A. R. D.: Applied Modeling of the Nighttime Surface Energy Balance over Land, J. Appl. Meteorol., 27, 689–704, URL https://doi.org/10.1175/1520-0450(1988)027<0689:AMOTNS>2.0.CO;2, 1988.

Hong, S.-Y.: A new stable boundary-layer mixing scheme and its impact on the simulated East Asian summer monsoon, Q. J. R. Meteorol. Soc., 136, 1481–1496, URL https://doi.org/10.1002/qj.665, 2010.

Hong, S.-Y. and Pan, H.-L.: Nonlocal Boundary Layer Vertical Diffusion in a Medium-Range Forecast Model, Mon. Wea. Rev., 124, 2322–2339, URL https://doi.org/10.1175/1520-0493(1996)124<2322:NBLVDI>2.0.CO;2, 1996.

Hong, S.-Y., Noh, Y., and Dudhia, J.: A New Vertical Diffusion Package with an Explicit Treatment of Entrainment Processes, Mon. Wea. Rev., 134, 2318–2341, 2006.

Horst, T. W. and Doran, J. C.: Nocturnal drainage flow on simple slopes, Boundary-Layer Meteorol., 34, 263–286, URL https://doi.org/10.1007/BF00122382, 1986.

Hu, X.-M. and Xue, M.: Influence of Synoptic Sea-Breeze Fronts on the Urban Heat Island Intensity in Dallas–Fort Worth, Texas, Mon. Wea. Rev., 144, 1487–1507, URL https://doi.org/10.1175/MWR-D-15-0201.1, 2016.

Jacobs, A. F. G., Heusinkveld, B. G., and Holtslag, A. A. M.: Seasonal and interannual variability of carbon dioxide and water balances of a grassland, Clim. Change, 82, 163–177, URL https://doi.org/10.1007/s10584-006-9182-7, 2007a.

Jacobs, C. M. J., Jacobs, A. F. G., Bosveld, F. C., Hendriks, D. M. D., Hensen, A., Kroon, P. S., Moors, E. J., Nol, L., Schrier-Uijl, A., and Veenendaal, E. M.: Variability of annual CO_2 exchange from Dutch grasslands, Biogeosciences, 4, 803–816, URL https://doi.org/10.5194/bg-4-803-2007, 2007b.

Janjić, Z. I.: The Step-Mountain Eta Coordinate Model: Further Developments of the Convection, Viscous Sublayers and Turbulence Closure Schemes, Mon. Wea. Rev., 122, 927–945, 1994.

Janjić, Z. I.: The surface layer in the NCEP Eta Model, in: Eleventh Conference on Numerical Weather Prediction, pp. 354–355, Amer. Meteor. Soc., Norfolk, VA, 1996.

Jensen, Derek D, ., Nadeau, F., D., Hoch, Sebastian W, ., and Pardyjak, E. R.: The evolution and sensitivity of katabatic flow dynamics to external influences through the evening transition, Q. J. R. Meteorol. Soc., 143, 423–438, URL https://doi.org/10.1002/qj.2932, 2017a.

Jensen, D. D., Price, T. A., Nadeau, D. F., Kingston, J., and Pardyjak, E. R.: Coastal Wind and Turbulence Observations during the Morning and Evening Transitions over Tropical Terrain, J. Appl. Meteor. Climatol., 56, 3167–3185, URL https://doi.org/10.1175/JAMC-D-17-0077.1, 2017b.

Jiménez, M., Simó, G., Wrenger, B., Telisman-Prtenjak, M., Guijarro, J., and Cuxart, J.: Morning transition case between the land and sea breeze regimes, Atmos. Res., 172-173, 95–108, URL https://doi.org/10.1016/j.atmosres.2015.12.019, 2016a.

Jiménez, M. A. and Cuxart, J.: A study of the nocturnal flows generated in the north side of the Pyrenees, Atmos. Res., 145-146, 244 – 254, https://doi.org/https://doi.org/10.1016/j.atmosres.2014.04.010, 2014.

Jiménez, P. A. and Dudhia, J.: On the ability of the WRF model to reproduce the surface wind direction over complex terrain, J. Appl. Meteor. Climatol., 52, 1610–1617, 2013.

Jiménez, P. A., de Arellano, J. V.-G., Dudhia, J., and Bosveld, F. C.: Role of synoptic- and meso-scales on the evolution of the boundary-layer wind profile over a coastal region: the near-coast diurnal acceleration, Meteorol. Atmos. Phys., 128, 39–56, URL https://doi.org/10.1007/s00703-015-0400-6, 2016b.

Johansson, C., Smedman, A.-S., Högström, U., Brasseur, J. G., and Khanna, S.: Critical Test of the Validity of Monin–Obukhov Similarity during Convective Conditions, J. Atmos. Sci., 58, 1549–1566, URL https://doi.org/10.1175/1520-0469(2001)058<1549:CTOTVO>2.0.CO;2, 2001.

Kalthoff, N., Lohou, F., Brooks, B., Jegede, G., Adler, B., Babić, K., Dione, C., Ajao, A., Amekudzi, L. K., Aryee, J. N. A., Ayoola, M., Bessardon, G., Danuor, S. K., Handwerker, J., Kohler, M., Lothon, M., Pedruzo-Bagazgoitia, X., Smith, V., Sunmonu, L., Wieser, A., Fink, A. H., and Knippertz, P.: An overview of the diurnal cycle of the atmospheric boundary layer during the West African monsoon season: results from the 2016 observational campaign, Atmos. Chem. Phys., 18, 2913–2928, URL https://doi.org/10.5194/acp-18-2913-2018, 2018.

Lampert, A., Pätzold, F., Jiménez, M. A., Lobitz, L., Martin, S., Lohmann, G., Canut, G., Legain, D., Bange, J., Martínez-Villagrasa, D., and Cuxart, J.: A study of local turbulence and anisotropy during the afternoon and evening transition with an unmanned aerial system and mesoscale simulation, Atmos. Chem. Phys., 16, 8009–8021, URL https://doi.org/10.5194/acp-16-8009-2016, 2016.

Lee, S.-M., Fernando, H. J. S., and Grossman-Clarke, S.: MM5-SMOKE-CMAQ as a modeling tool for 8-h ozone regulatory enforcement: application to the state of Arizona, Environ. Model. Assess., 12, 63–74, URL https://doi.org/10.1007/s10666-006-9053-7, 2007.

Legrand, M., Preunkert, S., Savarino, J., Frey, M. M., Kukui, A., Helmig, D., Jourdain, B., Jones, A. E., Weller, R., Brough, N., and Gallée, H.: Inter-annual variability of surface ozone at coastal (Dumont d'Urville, 2004–2014) and inland (Concordia, 2007–2014) sites in East Antarctica, Atmos. Chem. Phys., 16, 8053–8069, URL https://doi.org/10.5194/acp-16-8053-2016, 2016.

Lehner, M., Whiteman, C. D., Hoch, S. W., Jensen, D., Pardyjak, E. R., Leo, L. S., Di Sabatino, S., and Fernando, H. J. S.: A Case Study of the Nocturnal Boundary Layer Evolution on a Slope at the Foot of a Desert Mountain, J. Appl. Meteor. Climatol., 54, 732–751, URL https://doi.org/10.1175/JAMC-D-14-0223.1, 2015.

Lenschow, D. H., Wyngaard, J. C., and Pennell, W. T.: Mean-Field and Second-Moment Budgets in a Baroclinic, Convective Boundary Layer, J. Atmos. Sci., 37, 1313–1326, URL https://doi.org/10.1175/1520-0469(1980)037<1313:MFASMB>2.0.CO;2, 1980.

Liu, P., Tsimpidi, A., Hu, Y., Stone, B., Russell, A., and Nenes, A.: Differences between downscaling with spectral and grid nudging using WRF, Atmos. Chem. Phys., 12, 3601–3610, 2012.

Lloyd, J. and Taylor, J.: On the Temperature Dependence of Soil Respiration, Funct. Ecol., 8, 315–323, 1994.

Lothon, M., Lohou, F., Pino, D., Couvreux, F., Pardyjak, E. R., Reuder, J., Vilà-Guerau de Arellano, J., Durand, P., Hartogensis, O., Legain, D., Augustin, P., Gioli, B., Lenschow, D. H., Faloona, I., Yagüe, C., Alexander, D. C., Angevine, W. M., Bargain, E., Barrié, J., Bazile, E., Bezombes, Y., Blay-Carreras, E., van de Boer, A., Boichard, J. L., Bourdon, A., Butet, A., Campistron, B., de Coster, O., Cuxart, J., Dabas, A., Darbieu, C., Deboudt, K., Delbarre, H., Derrien, S., Flament, P., Fourmentin, M., Garai, A., Gibert, F., Graf, A., Groebner, J., Guichard, F., Jiménez, M. A., Jonassen, M., van den Kroonenberg, A., Magliulo, V., Martin, S., Martinez, D., Mastrorillo, L., Moene, A. F., Molinos, F., Moulin, E., Pietersen, H. P., Piguet, B., Pique, E., Román-Cascón, C., Rufin-Soler, C., Saïd, F., Sastre-Marugán, M., Seity, Y., Steeneveld, G. J., Toscano, P., Traullé, O., Tzanos, D., Wacker, S., Wildmann, N., and Zaldei, A.: The BLLAST field experiment: Boundary-Layer Late Afternoon and Sunset Turbulence, Atmos. Chem. Phys., 14, 10 931–10 960, URL https://doi.org/10.5194/acp-14-10931-2014, 2014.

Lyons, W.: The climatology and prediction of the Chicago lake breeze, J. Appl. Meteorol., 11, 1259–1270, 1972.

Mahrt, L.: Nocturnal Boundary-Layer Regimes, Boundary-Layer Meteorol., 88, 255–278, URL https://doi.org/10.1023/A:1001171313493, 1998.

Mahrt, L.: Stably Stratified Atmospheric Boundary Layers, Annu. Rev. Fluid Mech., 46, 23–45, URL https://doi.org/10.1146/annurev-fluid-010313-141354, 2014.

Mahrt, L. and Larsen, S.: Relation of slope winds to the ambient flow over gentle terrain, Boundary-Layer Meteorol., 53, 93–102, URL https://doi.org/10.1007/BF00122465, 1990.

Mahrt, L., Vickers, D., Nakamura, R., Soler, M. R., Sun, J., Burns, S., and Lenschow, D.: Shallow Drainage Flows, Boundary-Layer Meteorol., 101, 243–260, URL https://doi.org/10.1023/A:1019273314378, 2001.

Mathews, J.: The sea-breeze - Forecasting aspects, Aust. Meteor. Mag., 30, 205–209, 1982.

Mauritsen, T. and Svensson, G.: Observations of Stably Stratified Shear-Driven Atmospheric Turbulence at Low and High Richardson Numbers, J. Atmos. Sci., 64, 645–655, URL https://doi.org/10.1175/JAS3856.1, 2007.

Meir, T., Orton, P., Pullen, J., Holt, T., Thompson, W., and Arend, M.: Forecasting the New York City urban heat island and sea breeze during extreme heat events, Wea. Forecasting, 28, 1460–1477, 2013.

Mellor, G. L. and Yamada, T.: Development of a turbulence closure model for geophysical fluid problems, Rev. Geophys., 20, 851–875, URL https://doi.org/10.1029/RG020i004p00851, 1982.

Mestayer, P. G., Calmet, I., Herlédant, O., Barré, S., Piquet, T., and Rosant, J.-M.: A Coastal Bay Summer Breeze Study, Part 1: Results of the Quiberon 2006 Experimental Campaign, Boundary-Layer Meteorol., 167, 1–26, URL https://doi.org/10.1007/s10546-017-0314-6, 2018.

Miao, J.-F., Kroon, L., Vilà-Guerau de Arellano, J., and Holtslag, A.: Impacts of topography and land degradation on the sea breeze over eastern Spain, Meteorol. Atmos. Phys., 84, 157–170, 2003.

Miller, S. T. K., Keim, B. D., Talbot, R. W., and Mao, H.: Sea breeze: Structure, forecasting, and impacts, Rev. Geophys., 41, n/a–n/a, URL https://doi.org/10.1029/2003RG000124, 1011, 2003.

Millán, Millán, M., Artíñano, B., Palomino, I., Bezares, J. C., Martín, M., and Salvador, R.: Meso-Meteorological Studies in the Iberian Peninsula and Western Mediterranean Area, pp. 371–379, Springer US, Boston, MA, URL https://doi.org/10.1007/978-1-4615-3720-5_32, 1991.

Moeng, C.-H. and Sullivan, P. P.: A Comparison of Shear- and Buoyancy-Driven Planetary Boundary Layer Flows, J. Atmos. Sci., 51, 999–1022, URL https://doi.org/10.1175/1520-0469(1994)051<0999:ACOSAB>2.0.CO;2, 1994.

Monin, A. and Obukhov, A.: Basic laws of turbulent mixing in the surface layer of the atmosphere (in Russian), Contrib. Geophys. Inst. Acad. Sci. USSR, 151, 163–187, 1954.

Mooij, W., Domis, L. D. S., and Hülsmann, S.: The impact of climate warming on water temperature, timing of hatching and young-of-the-year growth of fish in shallow lakes in the Netherlands, J. Sea Res., 60, 32 – 43, URL http://dx.doi.org/10.1016/j.seares.2008.03.002, 2008.

Muppa, S., Anandan, V., Kesardar, K., Rao, S., and Reddy, P.: Study on deep inland penetration of sea breeze over complex terrain in the tropics, Atmos. Res., 104, 209–216, 2012.

Nadeau, D., Pardyjak, E. R., Higgins, C. W., Huwald, H., and Parlange, M. B.: Flow during the evening transition over steep Alpine slopes, Q. J. R. Meteorol. Soc., 139, 607–624, 2013.

Nadeau, D. F., Pardyjak, E. R., Higgins, C. W., Fernando, H. J. S., and Parlange, M. B.: A Simple Model for the Afternoon and Early Evening Decay of Convective Turbulence Over Different Land Surfaces, Boundary-Layer Meteorol., 141, 301, URL https://doi.org/10.1007/s10546-011-9645-x, 2011.

Nilsson, E., Lohou, F., Lothon, M., Pardyjak, E., Mahrt, L., and Darbieu, C.: Turbulence kinetic energy budget during the afternoon transition – Part 1: Observed surface TKE budget and boundary layer description for 10 intensive observation period days, Atmos. Chem. Phys., 16, 8849–8872, URL https://doi.org/10.5194/acp-16-8849-2016, 2016.

Oldroyd, H. J., Pardyjak, E. R., Higgins, C. W., and Parlange, M. B.: Buoyant Turbulent Kinetic Energy Production in Steep-Slope Katabatic Flow, Boundary-Layer Meteorol., 161, 405–416, URL https://doi.org/10.1007/s10546-016-0184-3, 2016.

Panofsky, H. A.: Spectra of Atmospheric Variables in the Boundary Layer, Radio Sci., 4, 1101–1109, URL https://doi.org/10.1029/RS004i012p01101, 1969.

Papadopoulos, K. H. and Helmis, C. G.: Evening and Morning Transition of Katabatic Flows, Boundary-Layer Meteorol., 92, 195–227, URL https://doi.org/10.1023/A:1002070526425, 1999.

Papanastasiou, D., Melas, D., and Lissaridis, I.: Study of wind field under sea breeze conditions; an application of WRF model, Atmos. Res., 98, 102 – 117, URL https://doi.org/10.1016/j.atmosres.2010.06.005, clouds, Aerosols and Radiation, 2010.

Pardyjak, E. R., Fernando, H., Joseph S. Hunt, J. C. G., and Anderson, J.: A case study of the development of nocturnal slope flows in a wide open valley and associated air quality implications, Meteorol. Z., 18, 85–100, URL https://doi.org/10.1127/0941-2948/2009/362, 2009.

Paulson, C. A.: The Mathematical Representation of Wind Speed and Temperature Profiles in the Unstable Atmospheric Surface Layer, J. Appl. Meteorol., 9, 857–861, URL https://doi.org/10.1175/1520-0450(1970)009<0857:TMROWS>2.0.CO;2, 1970.

Pearson, R. A.: On the asymmetry of the land-breeze sea-breeze circulation, Q. J. R. Meteorol. Soc., 101, 529–536, URL https://doi.org/10.1002/qj.49710142909, 1975.

Pérez-Landa, G., Ciais, P., Sanz, M. J., Gioli, B., Miglietta, F., Palau, J. L., Gangoiti, G., and Millán, M. M.: Mesoscale circulations over complex terrain in the Valencia coastal region, Spain – Part 1: Simulation of diurnal circulation regimes, Atmos. Chem. Phys., 7, 1835–1849, URL https://doi.org/10.5194/acp-7-1835-2007, 2007.

Plaza, J., Pujadas, M., and Artíñano, B.: Formation and Transport of the Madrid Ozone Plume, J. Air Waste Manag. Assoc., 47, 766–774, URL https://doi.org/10.1080/10473289.1997.10463938, 1997.

Ponce de León, S. and Orfila, A.: Numerical study of the marine breeze around Mallorca island, Appl. Ocean Res., 40, 26–34, 2013.

Poulos, G. and Zhong, S.: An Observational History of Small-Scale Katabatic Winds in Mid-Latitudes, Geography Compass, 2, 1798–1821, URL https://doi.org/10.1111/j.1749-8198.2008.00166.x, 2008.

Poulos, G. S., Blumen, W., Fritts, D. C., Lundquist, J. K., Sun, J., Burns, S. P., Nappo, C., Banta, R., Newsom, R., Cuxart, J., Terradellas, E., Balsley, B., and Jensen, M.: CASES-99: A Comprehensive Investigation of the Stable Nocturnal Boundary Layer, Bull. Amer. Meteor. Soc., 83, 555–582, URL https://doi.org/10.1175/1520-0477(2002)083<0555:CACIOT>2.3.CO;2, 2002.

Prtenjak, M. T., Klaić, M., Jeričević, A., and Cuxart, J.: The interaction of the downslope winds and fog formation over the Zagreb area, Atmos. Res., 214, 213 – 227, URL https://doi.org/10.1016/j.atmosres.2018.08.001, 2018.

Ramis, C. and Romero, C.: A first numerical simulation of the development and structure of the sea breeze on the island of Mallorca, Ann. Geophys., 13, 981–994, 1995.

Raynor, G., Sethuraman, S., and Brown, R.: Formation and characteristics of coastal internal boundary layers during onshore flows, Boundary-Layer Meteorol., 16, 487–514, 1979.

Ribeiro, F. N., de Oliveira, A. P., Soares, J., de Miranda, R. M., Barlage, M., and Chen, F.: Effect of sea breeze propagation on the urban boundary layer of the metropolitan region of Sao Paulo, Brazil, Atmos. Res., 214, 174 – 188, URL https://doi.org/10.1016/j.atmosres.2018.07.015, 2018.

Román-Cascón, C., Yagüe, C., Mahrt, L., Sastre, M., Steeneveld, G.-J., Pardyjak, E., van de Boer, A., and Hartogensis, O.: Interactions among drainage flows, gravity waves and turbulence: a BLLAST case study, Atmos. Chem. Phys., 15, 9031–9047, URL https://doi.org/10.5194/acp-15-9031-2015, 2015.

Román-Cascón, C., a. S. G. J., Yagüe, C., Sastre, M., Arrillaga, J. A., and Maqueda, G.: Forecasting radiation fog at climatologically contrasting sites: evaluation of statistical methods and WRF, Q. J. R. Meteorol. Soc., 142, 1048–1063, URL https://doi.org/10.1002/qj.2708, 2016a.

Román-Cascón, C., Yagüe, C., Sastre, M., Maqueda, G., Salamanca, F., and Viana, S.: Observations and WRF simulations of fog events at the Spanish Northern Plateau, Adv. Sci. Res., 8, 11–18, 2012.

Román-Cascón, C., Yagüe, C., Steeneveld, G.-J., Sastre, M., Arrillaga, J. A., and Maqueda, G.: Estimating fog-top height through near-surface micrometeorological measurements, Atmos. Res., 170, 76 – 86, URL https://doi.org/10.1016/j.atmosres.2015.11.016, 2016b.

Rotach, M. W., Wohlfahrt, G., Hansel, A., Reif, M., Wagner, J., and Gohm, A.: The World is Not Flat: Implications for the Global Carbon Balance, Bull. Amer. Meteor. Soc., 95, 1021–1028, URL https://doi.org/10.1175/BAMS-D-13-00109.1, 2014.

Sastre, M., Steeneveld, G., Yagüe, C., Román-Cascón, C., and Maqueda, G.: WRF sensitivity to boundary-layer and land-surface schemes during the evening transition: validation with BLLAST case study., in: 21st Symposium on Boundary Layers and Turbulence, Leeds (UK), 2014.

Sastre, M., Yagüe, C., Román-Cascón, C., and Maqueda, G.: Atmospheric Boundary-Layer Evening Transitions: A Comparison Between Two Different Experimental Sites., Boundary-Layer Meteorol., 157, 375 – 399, 2015.

Schalkwijk, J., Jonker, H. J. J., Siebesma, A. P., and Bosveld, F. C.: A Year-Long Large-Eddy Simulation of the Weather over Cabauw: An Overview, Mon. Wea. Rev., 143, 828–844, URL https://doi.org/10.1175/MWR-D-14-00293.1, 2015.

Seibert, P., Beyrich, F., Gryning, S.-E., Joffre, S., Rasmussen, A., and Tercier, P.: Review and intercomparison of operational methods for the determination of the mixing height, Atmos. Environ., 34, 1001 – 1027, URL https://doi.org/10.1016/S1352-2310(99)00349-0, 2000.

Simpson, J.: Sea Breeze and Local Winds, Cambridge University Press, 1994.

Skamarock, W., Rotunno, R., and Klemp, J.: Models of coastally trapped disturbances, J. Atmos. Sci., 56, 3349–3365, 1999.

Skamarock, W., Klemp, J., Dudhia, J., Gill, D., Barker, D., Wang, W., and Powers, J.: A description of the Advanced Research WRF version 3, Tech. rep., NCAR: Boulder, CO, 2008.

Sluijter, R., Instituut, K. N. M., Leenaers, H., Camarasa, M., and Atlasproducties, N.: De Bosatlas van het klimaat, De Bosatlas, Noordhoff Uitgevers, URL https://books.google.es/books?id=zACIpwAACAAJ, 2011.

Smedman-Högström, A.-S. and Högström, U.: Spectral gap in surface-Layer measurements, J. Atmos. Sci., 32, 340–350, URL https://doi.org/10.1175/1520-0469(1975)032<0340:SGISLM>2.0.CO;2, 1975.

Soler, M., Infante, C., Buenestado, P., and Mahrt, L.: Observations Of Nocturnal Drainage Flow In A Shallow Gully, Boundary-Layer Meteorol., 105, 253–273, URL https://doi.org/10.1023/A:1019910622806, 2002.

Soler, M., Arasa, R., Merino, M., Olid, M., and Ortega, S.: Modelling local sea-breeze flow and associated dispersion patterns over a coastal area in north-east Spain: a case study., Boundary-Layer Meteorol., 140, 37–56, 2011.

Soler, M. R., Udina, M., and Ferreres, E.: Observational and Numerical Simulation Study of a Sequence of Eight Atmospheric Density Currents in Northern Spain, Boundary-Layer Meteorol., 153, 195–216, URL https://doi.org/10.1007/s10546-014-9942-2, 2014.

Stauffer, D. and Seaman, N.: Use of four-dimensional data assimilation in a limited-area mesoscale model, Part I: Experiments with synoptic-scale data, Mon. Wea. Rev., 118, 1250–1277, 1990.

Stauffer, D., Seaman, N., and Binkowski, F. S.: Use of four-dimensional data assimilation in a limited-area mesoscale model, Part II: effects of data assimilation within the planetary boundary layer, Mon. Wea. Rev., 119, 734–754, 1991.

Steele, C., Dorling, S., von Glasow, R., and Bacon, J.: Idealized WRF model sensitivity simulations of sea breeze types and their effects on offshore windfields, Atmos. Chem. Phys., 13, 443–461, 2013.

Steeneveld, G. J., Holtslag, A. A. M., and Debruin, H. A. R.: Fluxes and Gradients in the Convective Surface Layer and the Possible Role of Boundary-Layer Depth and Entrainment Flux, Boundary-Layer Meteorol., 116, 237–252, URL https://doi.org/10.1007/s10546-004-2730-7, 2005.

Steeneveld, G. J., Tolk, L. F., Moene, A. F., Hartogensis, O. K., Peters, W., and Holtslag, A. A. M.: Confronting the WRF and RAMS mesoscale models with innovative observations in the Netherlands: Evaluating the boundary layer heat budget, J. Geophys. Res. Atmos., 116, URL https://doi.org/10.1029/2011JD016303, 2011.

Stiperski, I. and Rotach, M. W.: On the Measurement of Turbulence Over Complex Mountainous Terrain, Boundary-Layer Meteorol., 159, 97–121, URL https://doi.org/10.1007/s10546-015-0103-z, 2016.

Stull, R.: An Introduction to Boundary Layer Meteorology, Atmospheric and Oceanographic Sciences Library, Springer Netherlands, 1988.

Sun, H., Clark, T. L., Stull, R. B., and Black, T. A.: Two-dimensional simulation of airflow and carbon dioxide transport over a forested mountain: Part II. Carbon dioxide budget analysis and advection effects, Agric. For. Meteorol., 140, 352 – 364, URL https://doi.org/10.1016/j.agrformet.2006.03.016, 2006.

Sun, J., Burns, S. P., Delany, A. C., Oncley, S. P., Turnipseed, A. A., Stephens, B. B., Lenschow, D. H., LeMone, M. A., Monson, R. K., and Anderson, D. E.: CO2 transport over complex terrain, Agric. For. Meteorol., 145, 1 – 21, URL https://doi.org/10.1016/j.agrformet.2007.02.007, 2007.

Sun, J., Mahrt, L., Banta, R. M., and Pichugina, Y. L.: Turbulence Regimes and Turbulence Intermittency in the Stable Boundary Layer during CASES-99, J. Atmos. Sci., 69, 338–351, URL https://doi.org/10.1175/JAS-D-11-082.1, 2012.

Sun, J., Mahrt, L., Nappo, C., and Lenschow, D. H.: Wind and Temperature Oscillations Generated by Wave–Turbulence Interactions in the Stably Stratified Boundary Layer, J. Atmos. Sci., 72, 1484–1503, URL https://doi.org/10.1175/JAS-D-14-0129.1, 2015.

Sun, J., Lenschow, D. H., LeMone, M. A., and Mahrt, L.: The Role of Large-Coherent-Eddy Transport in the Atmospheric Surface Layer Based on CASES-99 Observations, Boundary-Layer Meteorol., 160, 83–111, URL https://doi.org/10.1007/s10546-016-0134-0, 2016.

Super, I., van der Gon, H. D., Visschedijk, A., Moerman, M., Chen, H., van der Molen, M., and Peters, W.: Interpreting continuous in-situ observations of carbon dioxide and carbon monoxide in the urban port area of Rotterdam, Atmos. Pollut. Res., 8, 174 – 187, URL http://dx.doi.org/10.1016/j.apr.2016.08.008, 2017.

Talbot, C., Augustin, P., Leroy, C., Willart, V., Delbarre, H., and Khomenko, G.: Impact of a sea breeze on the boundary-layer dynamics and the atmospheric stratification in a coastal area of the North Sea, Boundary-Layer Meteorol,, 125, 133–154, URL https://doi.org/10.1007/s10546-007-9185-6, 2007.

Tang, Y.: The Effect of Variable Sea Surface Temperature on Forecasting Sea Fog and Sea Breezes: A Case Study, J. Appl. Meteor. Climatol., 51, 986–990, URL https://doi.org/10.1175/JAMC-D-11-0253.1, 2012.

Terradellas, E. and Cano, D.: Implementation of a Single-Column Model for Fog and Low Cloud Forecasting at Central-Spanish Airports, Pure Appl. Geophys., 164, 1327–1345, 2007.

Thorpe, A. J., Volkert, H., and Ziemiański, M. J.: The Bjerknes' Circulation Theorem: A Historical Perspective, Bull. Amer. Meteor. Soc., 84, 471–480, URL https://doi.org/10.1175/BAMS-84-4-471, 2003.

Tijm, A. B. C., Holtslag, A. A. M., and van Delden, A. J.: Observations and Modeling of the Sea Breeze with the Return Current, Mon. Wea. Rev., 127, 625–640, URL https://doi.org/10.1175/1520-0493(1999)127<0625:OAMOTS>2.0.CO;2, 1999.

Van de Wiel, B. J. H., Moene, A. F., Steeneveld, G., Baas, P., Bosveld, F., and Holtslag, A. A. M.: Intermittent Turbulence and Oscillations in the Stable Boundary Layer over Land. Part III: A classification for observations during CASES-99, J. Atmos. Sci., 60, 2509–2522, URL https://doi.org/10.1175/1520-0469(2002)059<2567:ITAOIT>2.0.CO;2, 2003.

Van de Wiel, B. J. H., Moene, A. F., Jonker, H. J. J., Baas, P., Basu, S., Donda, J. M. M., Sun, J., and Holtslag, A. A. M.: The Minimum Wind Speed for Sustainable Turbulence in the Nocturnal Boundary Layer, J. Atmos. Sci., 69, 3116–3127, URL https://doi.org/10.1175/JAS-D-12-0107.1, 2012a.

Van de Wiel, B. J. H., Moene, A. F., and Jonker, H. J. J.: The Cessation of Continuous Turbulence as Precursor of the Very Stable Nocturnal Boundary Layer, J. Atmos. Sci., 69, 3097–3115, URL https://doi.org/10.1175/JAS-D-12-064.1, 2012b.

Van der Hoven, I.: Power spectrum of horizontal wind speed in the frequency range from 0.0007 to 900 cycles per hour, J. Meteor., 14, 160–164, URL https://doi.org/10.1175/1520-0469(1957)014<0160:PSOHWS>2.0.CO;2, 1957.

van der Laan, S., Manohar, S., Vermeulen, A., Bosveld, F., Meijer, H., Manning, A., van der Molen, M., and van der Laan-Luijkx, I.: Inferring ^{222}Rn soil fluxes from ambient ^{222}Rn activity and eddy covariance measurements of CO_2, Atmos. Meas. Tech., 9, 5523–5533, URL https://doi.org/10.5194/amt-9-5523-2016, 2016.

van der Linden, S. J. A., Baas, P., Antoon van Hooft, J., van Hooijdonk, I. G. S., Bosveld, F. C., and van de Wiel, B. J. H.: Local Characteristics of the Nocturnal Boundary Layer in Response to External Pressure Forcing, J. Appl. Meteor. Climatol., 56, 3035–3047, URL https://doi.org/10.1175/JAMC-D-17-0011.1, 2017.

van Hooijdonk, I. G. S., Donda, J. M. M., Clercx, H. J. H., Bosveld, F. C., and van de Wiel, B. J. H.: Shear Capacity as Prognostic for Nocturnal Boundary Layer Regimes, J. Atmos. Sci., 72, 1518–1532, URL https://doi.org/10.1175/JAS-D-14-0140.1, 2015.

Van Ulden, A. P. and Wieringa, J.: Atmospheric boundary layer research at Cabauw, Boundary-Layer Meteorol., 78, 39–69, URL https://doi.org/10.1007/BF00122486, 1996.

Vargas, A., Arnold, D., Adame, J., Grossi, C., Hernández-Ceballos, M., and Bolivar, J.: Analysis of the vertical radon structure at the Spanish "El Arenosillo" tower station, J. Environ. Radioact., 139, 1 – 17, URL http://dx.doi.org/10.1016/j.jenvrad.2014.09.018, 2015.

Verkaik, J. W. and Holtslag, A. A. M.: Wind profiles, momentum fluxes and roughness lengths at Cabauw revisited, Boundary-Layer Meteorol., 122, 701–719, URL https://doi.org/10.1007/s10546-006-9121-1, 2007.

Večenaj, v., Belušić, D., and Grisogono, B.: Characteristics of the near-surface turbulence during a bora event, Ann. Geophys., 28, 155–163, URL https://doi.org/10.5194/angeo-28-155-2010, 2010.

Vinnichenko, N. K. and Dutton, J. A.: Empirical studies of atmospheric structure and spectra in the free stmosphere, Radio Sci., 4, 1115–1126, URL https://doi.org/10.1029/RS004i012p01115, 1969.

Wang, J., Yang, Z., Hyer, E., Reid, J., Chew, B-N., M. M., Zhang, Y., and Zhang, M.: Mesoscale modeling of smoke transport over the Southeast Asian Maritime Continent: Interplay of sea breeze, trade wind, typhoon, and topography, Atmos. Res., 122, 486–503, 2013.

Webb, E. K.: Profile relationships: The log-linear range, and extension to strong stability, Q. J. R. Meteorol. Soc., 96, 67–90, URL https://doi.org/10.1002/qj.49709640708, 1970.

White, A. B., Fairall, C. W., and Thomson, D. W.: Radar Observations of Humidity Variability in and above the Marine Atmospheric Boundary Layer, J. Atmos. Oceanic Technol., 8, 639–658, URL https://doi.org/10.1175/1520-0426(1991)008<0639:ROOHVI>2.0.CO;2, 1991.

Whiteman, C.: Mountain Meteorology: Fundamentals and Applications, Oxford University Press, URL https://books.google.es/books?id=Mz_7qLK5hQcC, 2000.

Whiteman, C. D.: Breakup of Temperature Inversions in Deep Mountain Valleys: Part I. Observations, J. Appl. Meteorol., 21, 270–289, URL https://doi.org/10.1175/1520-0450(1982)021<0270:BOTIID>2.0.CO;2, 1982.

Wichink Kruit, R. J., Holtslag, A. A. M., and Tijm, A. B. C.: Scaling of the Sea-Breeze Strength with Observations in the Netherlands, Boundary-Layer Meteorol., 112, 369–380, URL https://doi.org/10.1023/B:BOUN.0000027904.18874.75, 2004.

Wyngaard, J.: Turbulence in the Atmosphere, Cambridge University Press, 2010.

Zahorowski, W., Williams, A. G., Vermeulen, A. T., Chambers, S. D., Crawford, J., and Sisoutham, O.: Diurnal boundary layer mixing patterns characterised by radon-222 gradient observations at Cabauw, in: Extended Abstracts, 18th Conf. on Boundary Layers and Turbulence, Stockholm, Sweden, American Meteorological Society, 2008.

Zardi, D. and Whiteman, C.: Mountain Weather Research and Forecasting: Recent Progress and Current Challenges, vol. XIII of *Springer Atmospheric Sciences*, chap. Diurnal Mountain WInd Systems., pp. 35–119, Springer Netherlands, 1 edn., 2013.

Zhong, S. and Takle, E. S.: An Observational Study of Sea- and Land-Breeze Circulation in an Area of Complex Coastal Heating, J. Appl. Meteorol., 31, 1426–1438, URL https://doi.org/10.1175/1520-0450(1992)031<1426:AOSOSA>2.0.CO;2, 1992.

APPENDIX A

Ceilometer

We use the Haar wavelet transform to estimate the MLH from the LD40 ceilometer (Cohn and Angevine, 2000). From the convolution of the aerosol backscatter profile *B(z)* and the Haar wavelet function, integrated between the altitudes z_b and z_t of the profile, and with a the dilation and b the translation of the wavelet, we obtain the wavelet power spectrum coefficients:

$$W_B(a,b) = \frac{1}{a}\int_{z_b}^{z_t} B(z)h(\frac{z\text{-}b}{a})dz. \tag{A1}$$

Positive values of $W_B(a,b)$ are generally coincident with the top of aerosol layers. However, this method presents problems under certain conditions: e.g. it is reported to have difficulties in both discerning the evening SBL close to the surface from the remaining residual layer (Di Giuseppe et al., 2012), and in the case of the LD40 ceilometer, in detecting the well-mixed CBL. In fact, since some MLH detections can be doubtful, we discarded detections with a quality index below a specific value. For further details about this procedure we refer the reader to de Haij et al. (2007).

The LD40 ceilometer at Cabauw was not continuously operational before April 2006 (see Table 6.1). Data from the CT75 ceilometer are available before that date, but these have a poorer resolution and the wavelet transform has not yet been tested for them. On the other hand, continuous data from the LD40 ceilometer at De Bilt, which is approximately 25 km NE of Cabauw (see Fig. 2.3), are available for the whole period (2001-2010). In order to check whether MLH estimates from De Bilt can be used as a proxy for Cabauw, we analysed the correlation of the average daily evolution of the MLH for complete overlapping months in Fig. A1. Specifically, we chose January and July 2009 since the local forcings in these months are contrasting. Despite some slight differences, such as the higher values of the MLH during nighttime in De Bilt especially in July, most probably as a consequence of urban influence, both emplacements are quite well correlated. We therefore used MLH estimates from De Bilt for the whole 10-year period.

Wind profiler

The MLH during convective conditions was estimated from the maximum value in the vertical profile of the structure parameter $C_n{}^2$. The backscatter intensity of the electromagnetic signal measured by the wind profiler is proportional to this parameter. Further specifications are given in White et al. (1991). The algorithm employed to

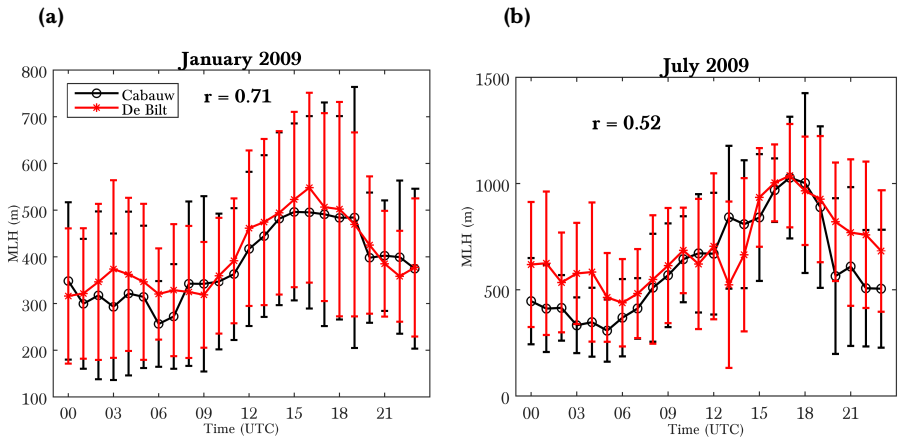

Figure A1: Mean diurnal evolution of the estimated MLH from the LD40 ceilometer at Cabauw and De Bilt for complete overlapping months: (a) January 2009 and (b) July 2009. The error bars indicate the standard deviation of the estimated MLH during each month. The value of the linear-correlation coefficient is also included.

estimate the MLH from the maximum in the wind-profiler vertical-backscatter profiles, was modified and extended. Instead of only using the vertical beam, a time-averaged backscatter profile from the four oblique beams at profiler vertical sampling resolution was calculated and fitted with a spline function before the maxima were determined. At the most, two maxima from each profile were selected. The most likely MLH was selected automatically on the basis of certain additional criteria, such as time-height continuity and the spectral width of the Doppler spectrum.

The wind profiler is a very powerful tool for detecting the MLH in deep CBLs, but not for the stable ABLs. The most reliable estimates were selected from a manual editing of the first-guess estimates made by the algorithm.

APPENDIX B

The thermal profile within the first 10 m over the surface is fitted to a logarithmic profile by the method of least squares following Eq. 2.4. The fit is carried out employing four vertical values of the virtual potential temperature calculated from measurements in La Herrería at the surface, and at 3, 6 and 10 m, in the subsequent manner:

$$\theta_v(z,t) = \alpha(t) + \beta(t)\ln(z) + \gamma(t)\ln^2(z) + \delta(t)\ln^3(z). \tag{B1}$$

We find that from the instantaneous value of $\delta(t)$, which provides information about the curvature of the profile in its lowest part, we can infer the static stability of the thermal profile. We illustrate the thermal profile at three different times of day in Fig. B1, each time associated with a different static stability for a moderate katabatic event: 25 July. The use of four vertical levels allows the fit to a cubic polynomial and as a consequence more realistic near-surface profiles. Given also the limited number of measurements, the fit is exact (note that $r^2 = 1$), which would not occur in case of having a greater number of vertical measurements.

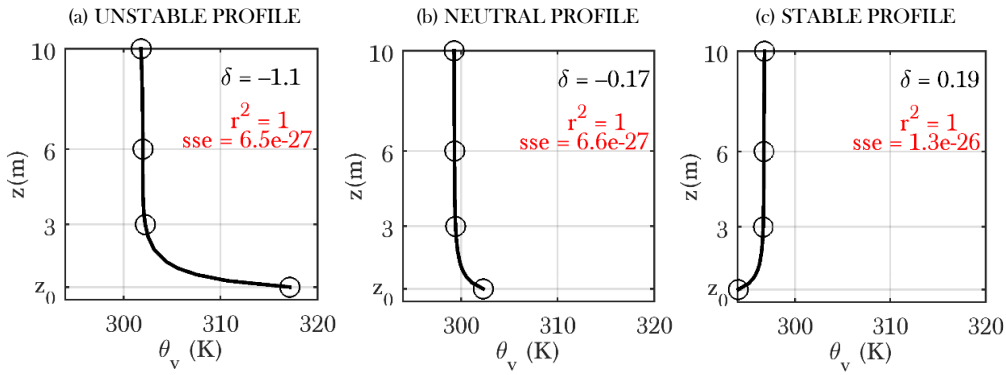

Figure B1: Vertical profiles of the virtual potential temperature (θ_v) for different static stabilities. Values are taken from a moderate katabatic event (25 July) at (a) 1600 UTC, (b) 1830 UTC and (c) 2130 UTC. The instantaneous value of δ is shown in black, and the square of the multiple correlation coefficient (r^2) and the sum of the squares due to error (*sse*) are shown in red, as a measure of the goodness of fit.

From a careful inspection of $\delta(t)$ for different events at various times of day and employing θ_v in K and z in m, we classify the static stability of the lowest 10-m atmospheric layer into the three subsequent groups according to the value of $\delta(t)$:

$$\begin{aligned} &\textit{Unstable}: && \delta(t) < -0.3, \\ &\textit{Neutral}: && -0.3 \leqslant \delta(t) \leqslant 0, \\ &\textit{Stable}: && \delta(t) > 0. \end{aligned} \tag{B2}$$

ACRONYMS

ABL atmospheric boundary layer
AEMET *Agencia Estatal de Meteorología* (Spanish Meteorological Agency)
AET afternoon and evening transition
agl above ground level
asl above sea level
AT afternoon transition
CBL convective boundary layer
CESAR Cabauw Experimental Site for Atmospheric Research
E east
EC eddy covariance
ERA-Interim ECMWF Re-Analysis–Interim
ET evening transition
GuMNet Guadarrama Monitoring Network
HFD heat-flux demand
HOST hockey-stick transition
IRGASON Integrated CO_2 and H_2O Open-Path Gas Analyser and 3D Sonic Anemometer
KNMI *Koninklijk Nederlands Meteorologisch Instituut* (Royal Netherlands Meteorological Institute)
LB land breeze
LES large-eddy simulations
LH latent heat
LIDAR Light Detection and Ranging / Laser Imaging Detection and Ranging
LSB late sea breeze
LSM land-surface model
LT local time
MB mountain breeze
MBE mean bias error
ML mixed layer
MLH mixing-layer height
MOST Monin-Obukhov Similarity Theory
MYJ Mellor-Yamada-Janjic
N north
NBL nocturnal boundary layer
NCDA near-coastal diurnal acceleration
NCEP National Centers for Environmental Prediction

NE north-east
NSB non-sea breeze
NW north-west
PGF pressure gradient force
RMSE root mean square error
RQ research question
S south
SB sea breeze
SBF sea-breeze front
SBL stable boundary layer
SC shear capacity
SE south-east
SEB surface energy balance
SH sensible heat
SM_i soil-moisture index
SW south-west
TIBL thermal internal boundary layer
TKE turbulent kinetic energy
UCM Universidad Complutense de Madrid
UTC universal time coordinated
VSBL very stable boundary layer
W west
WRF Weather Research & Forecasting
WSBL weakly stable boundary layer
YSU Yonsei State University

SCIENTIFIC NOTATION

B_*: buoyancy term (Eq. 4.4)
c_{pd}: specific heat of the dry air at constant pressure
CO_2: carbon dioxide
$\overline{e}$: TKE (Eq. 2.3)
g: gravity acceleration
G: soil-heat flux
H: SH flux (Eq. 2.1)
K_C: eddy diffusivity for variable C
K_H: eddy diffusivity for heat
K_M: eddy diffusivity for momentum
l_v: latent heat of vaporisation of the dry air at constant pressure
L: Obukhov length (Eq. 4.8)
LWD: downward longwave radiation
LWU: upward longwave radiation
p: atmospheric pressure
pp: precipitation
q: specific humidity
r: water-vapour mixing ratio
R_B: bulk Richardson number $\left(R_B = \frac{g\Delta\overline{\theta_v}\Delta z}{\overline{\theta_v}[(\Delta\overline{u})^2+(\Delta\overline{v})^2]}\right)$
R_c: critical bulk Richardson number
R_{net}: net radiation (R_{net} = SWD - SWU + LWD - LWU)
R_s: soil-respiration flux (Eq. 6.2)
Ri_c: critical gradient Richardson number
^{222}Rn: the most stable isotope of radon.
S_*: shear term (Eq. 4.5)
SM_i: soil-moisture index (SM_i = SM/SM_{max})
SWD: downward shortwave radiation
SWU: upward shortwave radiation
t: time
t_*: representative time scale of the eddies ($t_* = Z_i/w_*$ *or* $t_* = Z_i/u_*$)
T: air temperature
T_v: virtual air temperature (T_v = $T(1+0.61q)$)
u: velocity component in the x direction
u_{SB}: SB intensity (Eq. 3.2)
u_*: friction velocity (Eq. 2.2)
U: horizontal wind speed ($U = \sqrt{u^2 + v^2}$)

v: velocity component in the y direction
V_{850}: reanalysis wind speed at 850 hPa
V_{TKE}: turbulent velocity scale (V_{TKE} = TKE$^{1/2}$)
w: velocity component in the z direction
w_*: convective velocity scale (Eq. 4.14)
z: height agl
Z_i: estimation of the MLH
α: wind direction
β: Bowen ratio ($\beta = H/\mathrm{LH}$)
ζ: stability parameter in the surface layer ($\zeta = z/L$)
θ: potential temperature ($\theta \simeq T + gz/c_{pd}$)
θ_e: equivalent potential temperature ($\theta_e = \theta + (l_v\theta/c_{pd}T)r$)
θ_v: virtual potential temperature ($\theta_v \simeq \theta(1 + 0.61q)$)
κ: Von Kármán constant
ρ: density of the air
σ_w: standard deviation of the vertical velocity
Φ_M: dimensionless wind shear in the surface layer (Eq. 4.10)
Ψ_M: stability profile function in the surface layer (Eq. 4.12)

LIST OF JOURNAL PUBLICATIONS AND CONFERENCE PRESENTATIONS

JOURNAL PUBLICATIONS

PUBLICATIONS OF THIS THESIS

[1] Arrillaga, J.A., Yagüe, C., Sastre, M, and Román-Cascón, C. (2016). A characterisation of sea-breeze events in the eastern Cantabrian coast (Spain) from observational data and WRF simulations. *Atmos. Res.*, 181:265-280, http://dx.doi.org/10.1016/j.atmosres.2016.06.021.

[2] Arrillaga, J.A., Vilà-Guerau de Arellano, J., Bosveld, F., Baltink, H.K., Yagüe, C., Sastre, M, and Román-Cascón, C. (2018). Impacts of afternoon and evening sea-breeze fronts on local turbulence, and on CO_2 and radon-222 transport. *Q. J. R. Meteorol. Soc.*, 144:990-1011, https://doi.org/10.1002/qj.3252.

[3] Arrillaga, J.A., Yagüe, C., Román-Cascón, C., Sastre, M., Maqueda, G., and Vilà-Guerau de Arellano, J. (2018). Weak and intense katabatic winds: impacts on turbulent characteristics in the stable boundary layer and CO_2 transport. *Atmos. Chem. Phys. Discuss, in review*, https://doi.org/10.5194/acp-2018-944.

[4] Arrillaga, J.A., Vilà-Guerau de Arellano, J., Jiménez, P, and Yagüe, C. (2018). The role of local turbulence and synoptic scales on sea-breeze features: using 10-year WRF and observations. *To be submitted to Journal of Geophysical Research-Atmospheres*.

OTHER PUBLICATIONS

[5] Román-Cascón, C., Yagüe, C., Steeneveld, G.J., Sastre, M., **Arrillaga, J.A.**, and Maqueda, G. (2016). Estimating fog-top height through near-surface micrometeorological measurements. *Atmos. Res.*, 170:76-86, https://doi.org/10.1016/j.atmosres.2015.11.016.

[6] Román-Cascón, C., Steeneveld, G.J., Yagüe, C., Sastre, M., **Arrillaga, J.A.**, and Maqueda, G. (2016). Forecasting radiation fog at climatologically contrasting sites: evaluation of statistical methods and WRF. *Q. J. R. Meteorol. Soc.*, 142:1048-1063, https://doi.org/10.1002/qj.2708.

[7] Román-Cascón, C., Yagüe, C., **Arrillaga, J.A.**, Lothon, M., Pardyjak, E.R., Lohou, F., Inclán, R.M., Sastre, M., Maqueda, G., Derrien, S., Meyerfeld, Y., Hang, C., Cam-

parguez, P., and Turki, I. (2018). Observational characterization of diurnal mountain winds and their impacts on CO_2 mixing ratios at three contrasting sites. *Under review in Atmos. Res.*

CONFERENCE PRESENTATIONS

Total contributions throughout the doctorate: **19 oral** and **23 poster** communications. Among those, the ones related to this thesis and presented as first author are listed below.

POSTER CONTRIBUTIONS

[1] Arrillaga, J.A., Yagüe, C., Sastre, M., and Román-Cascón, C. An observational and numerical study of the sea breeze in the eastern Cantabrian coast (Spain). *European Geosciences Union - General Assembly 2015*, Vienna (Austria) 12-17 April 2015.

Published in: Geophysical Research Abstracts, 17, 268. ISSN: 1607-7962.

Awarded: Outstanding Student Poster Award.

[2] Arrillaga, J.A., Yagüe, C., Román-Cascón, C., Sastre, M. Study of the origin and structure of a nocturnal atmospheric density current from observations and numerical simulations. *European Geosciences Union - General Assembly 2016*, Vienna (Austria) 17-22 April 2016.

Published in: Geophysical Research Abstracts, 18, 6019. ISSN: 1607-7962.

[3] Arrillaga, J.A. and The GuMNet Consortium Team. GuMNet – A High Altitude Monitoring Network in The Guadarrama Mountain Range. *32nd Conference on Agricultural and Forest Meteorology, 22nd Symposium on Boundary Layers and Turbulence, and Third Conference on Biogeosciences*, Salt Lake City (UT, USA) 20-24 June 2016.

[4] Arrillaga, J.A., Yagüe, C., Sastre, M., Román-Cascón, C., Maqueda, G., Inclán, R.M., González-Roúco, J.F., Santolaria, E., Durán, L., and Navarro, J. WRF simulations of upslope and downslope flows over the Guadarrama Mountain Range (Spain). *32nd Conference on Agricultural and Forest Meteorology, 22nd Symposium on Boundary Layers and Turbulence, and Third Conference on Biogeosciences*, Salt Lake City (UT, USA) 20-24 June 2016.

Awarded: Student Honorable Mention.

[5] Arrillaga, J.A., Vilà-Guerau de Arellano, J., Bosveld, F., Jiménez, P., Baltink, H.K., Yagüe, C., Dudhia, J., Zhao, W. A 10-Yr Climatological Study of the Atmospheric Boundary Layer in Cabauw. *BBOS Autumn Symposium 2016*, Oranjewoud (Netherlands) 26-28 October 2016.

[6] Arrillaga, J.A, Cano, D., Sastre, M., Román-Cascón, C., Maqueda, G., Morales, G., Viana, S., Inclán, R.M., González Roúco, J.F., Santolaria, E., Durán, L., and Yagüe, C. Local and regional characterisation of the diurnal mountain wind systems in the Guadarrama mountain range (Spain). *European Geosciences Union - General Assembly 2017*, Vienna (Austria) 23-28 April 2017.

Published in: Geophysical Research Abstracts, 17, 14802. ISSN: 1607-7962.

[7] Arrillaga, J.A., Yagüe, C., Vilà-Guerau de Arellano, J., Sastre, M., and Román-Cascón, C. The role of diurnal mountain winds during severe drying out conditions: impacts at Madrid-Barajas airport. *PhDay Físicas 2017*, Universidad Complutense de Madrid, Madrid (Spain) 15 December 2017.

[8] Arrillaga, J.A., Yagüe, C., Román-Cascón, C., Sastre, M., Vilà-Guerau de Arellano, J., and Maqueda, G. Nature and characteristics of weak and intense katabatic flows. *European Geosciences Union - General Assembly 2018*, Vienna (Austria) 09-13 April 2018.

Published in: Geophysical Research Abstracts, 20, 8295. ISSN: 1607-7962.

[9] Arrillaga, J.A., Yagüe, C., Román-Cascón, C., Sastre, M., Vilà-Guerau de Arellano, J., Maqueda, G. Nature and characteristics of weak and intense katabatic flows. *23rd Symposium on Boundary Layers and Turbulence, 21st Conference on Air-Sea Interaction*, Oklahoma City (OK, USA) 11-15 June 2018.

Awarded: Outstanding Student Poster Presentation.

ORAL CONTRIBUTIONS

[1] Arrillaga, J.A., Yagüe, C., Sastre, M., Román-Cascón, C. Evaluación de las características de la brisa marina en la costa cantábrica oriental mediante observaciones y simulaciones con el modelo WRF. *XXXIV Jornadas Científicas de la Asociación Meteorológica Española y 17º encuentro Hispano Luso de Meteorología*, Teruel (Spain) 29 February-02

March 2016.

Published in: XXXIV Jornadas Científicas de la Asociación Meteorológica Española, ISBN 978-84-617-5240-9.

Awarded: Bolsa de Viaje para Jóvenes Investigadores.

[2] Arrillaga, J.A., Yagüe, C., Sastre, M., Román-Cascón, C. Sea-breeze characteristics over complex terrain: an evaluation from observational data and WRF simulations. *32nd Conference on Agricultural and Forest Meteorology, 22nd Symposium on Boundary Layers and Turbulence, and Third Conference on Biogeosciences*, Salt Lake City (UT, USA) 20-24 June 2016.

[3] Arrillaga, J.A., Vilà-Guerau de Arellano, J., Yagüe, C., Bosveld, F., Jiménez, P., Baltink, H.K., Dudhia, J., Zhao, W. A 10-Yr Climatological Study of the Atmospheric Boundary Layer in Cabauw. *Boundary Layer and Turbulence BBOS workshop*, Universitat Politècnica de Catalunya, Barcelona (Spain) 14 October 2016.

[4] Arrillaga, J.A., Bosveld, F., Jiménez, P., Baltink, H.K., Yagüe, C., Hensen, A., van Dinther, D., Frumau, A., Dudhia, J., Zhao, W., Vilà-Guerau de Arellano, J. Integrating surface, entrainment and mesoscale in the Atmospheric Boundary Layer dynamics: a 10-year study in Cabauw (Netherlands). *European Geosciences Union - General Assembly 2017*, Vienna (Austria) 23-28 April 2017.

Published in: Geophysical Research Abstracts, 19, 888. ISSN: 1607-7962.

[5] Arrillaga, J.A., Vilà-Guerau de Arellano, J., Bosveld, F., Baltink, H.K., Yagüe, C., Hensen, A., van Dinther, D., Frumau, A., Sastre, M., and Román-Cascón, C. Sea-breeze occurrences in Cabauw: implications for the scalar-transport and dynamics of the boundary layer. *CESAR Science Day 2017*, KNMI (De Bilt, Netherlands) 09 June 2017.

[6] Arrillaga, J.A., Bosveld, F., Baltink, H.K., Yagüe, C., Hensen, A., van Dinther, D., Frumau, A., Sastre, M., Román-Cascón, C., Vilà-Guerau de Arellano, J. Mesoscale-turbulence interactions in the ABL dynamics: a 10 year-study in Cabauw (Netherlands). *EMS Annual Meeting: European Conference for Applied Meteorology and Climatology 2017*, Dublin (Ireland) 04-08 September 2017.

Published in: EMS Annual Meeting Abstracts Vol. 14, EMS2017-24-1 2017.

Awarded: Young Scientist Travel Award.

[7] Arrillaga, J.A., Bosveld, F., Baltink, H.K., Yagüe, C., Jiménez, P., Hensen, A., Van Dinther, D., Frumau, A., Dudhia, J., Sastre, M., Román-Cascón, C., Zhao, W., and Vilà-Guerau de Arellano, J. 10-years analysis of sea-breeze phenomena: implications for scalar transport and challenging interaction with local turbulence. *Meteorology and Climate – Modeling for Air Quality 2017*, University of California Davis (CA, USA), 13-15 September 2017.

[8] Arrillaga, J.A., Yagüe, C., Román-Cascón, C., Sastre, M., Vilà-Guerau de Arellano, J., and Maqueda, G. Los vientos catabáticos y su impacto en el régimen estable nocturno durante el verano de 2017 en el Bosque de la Herrería (Madrid). *XXXV Jornadas Científicas de la Asociación Meteorológica Española y 19^0 Encuentro Hispano-Luso de Meteorología*, León (Spain) 05-07 March 2018.

Published in: XXXV Jornadas Científicas de la Asociación Meteorológica Española, ISBN 978-84-617-5240-9.

Awarded: Bolsa de Viaje para Jóvenes Investigadores.

[9] Arrillaga, J.A., Vilà-Guerau de Arellano, J., Yagüe, C., Bosveld, F., Jiménez, P., Baltink, H.K., Dudhia, J., Sastre, M., Román-Cascón, C. On the complex interaction between the sea breeze and boundary-layer turbulence before, during, and after the afternoon transition. *23rd Symposium on Boundary Layers and Turbulence, 21st Conference on Air-Sea Interaction*, Oklahoma City (OK, USA) 11-15 June 2018.